EXPLORING THE BIOFLUIDDYNAMICS OF SWIMMING AND FLIGHT

David Lentink

Promotor	prof. dr. ir. Johan L. van Leeuwen Hoogleraar in de Experimentele Zoölogie, Wageningen Universiteit.
Copromotoren	prof. dr. Michael H. Dickinson Esther M. and Abe M. Zarem Professor of Bioengineering, California Institute of Technology, United States of America.
	prof. dr. ir. GertJan F. van Heijst Hoogleraar in de Transportfysica, Technische Universiteit Eindhoven.
Overige leden promotiecommissie	prof. dr. Peter Aerts University of Antwerp, Belgium.
	prof. dr. Thomas L. Daniel University of Washington, United States of America.
	prof. dr. Anders Hedenström Lund University, Sweden.
	prof. dr. Jaap Molenaar Wageningen Universiteit.

EXPLORING THE BIOFLUIDDYNAMICS OF SWIMMING AND FLIGHT

David Lentink

Proefschrift
ter verkrijging van de graad van doctor
op gezag van de rector magnificus
van Wageningen Universiteit,
prof. dr. M.J. Kropff
in het openbaar te verdedigen
op dinsdag 9 september 2008
des namiddags te vier uur in de Aula.

Lentink, D. (2008) Exploring the biofluiddynamics of swimming and flight.

PhD thesis, Experimental Zoology Group, Wageningen University.
P.O. Box 338, 6700 AH Wageningen, the Netherlands.

Subject headings: biofluiddynamics/vortex/stability/chaos/scaling/swimming/flight/design.

ISBN 978-90-8504-971-5

Summary

Many organisms must move through water or air in order to survive and reproduce. Therefore both the development of these individuals and the evolution of their species are shaped by the physical interaction between organism and surrounding fluid. One characteristic of macroscopic animals moving at typical speeds is the appearance of vortices, or distinct whorls of fluid. These vortices are created close to the body as it is driven by the action of muscles or gravity, then are 'shed' to form a wake (in effect a trackway left behind in the fluid), and ultimately are dissipated as heat. It is useful to analyze fluid motion as a collection of vortices, yet the dynamics are complex: vortices interact with the moving organism, interact with each other, and evolve independently in time.

This research examines two flow phenomena that are central to the locomotory performance of certain organisms. The first of these is leading-edge vortex stability. A tornado-shaped vortex has been observed above insect wings, parallel to the leading edge. The leading edge vortex substantially augments lift and is integral to insect flight. Here I consider in detail the conditions that stabilize this flow pattern. The second dynamical phenomenon is vortex wake periodicity. Depending on conditions, the wake structure behind a moving organism can be regular and predictable, or chaotic. Although the fluid flow is always deterministic, in the latter case its exact structure becomes hypersensitive to small disturbances. This can reduce the 'forecast horizon' within which fluiddynamic forces acting on the body can be reliably predicted. Here I describe the onset of chaotic vortex interactions in biologically relevant models, and consider the consequences for feedback-mediated neural control.

These studies were carried out using models that represent swimming fish, flying insects, autorotating plant seeds, and birds. The flow patterns and forces were observed using (in order of increasing realism) a two-dimensional flapping foil in a soap film tunnel, a dynamically scaled three-dimensional robotic fly and seed wing in oil, and freeze-dried swift wings in a wind tunnel. The measurements were designed and understood by means of dimensional analysis: dimensionless parameters can identify the fluid accelerations and stresses that dominate the flow; when mapped as a function of morphological and kinematic variables that produce the flow, they yield an overview of the biofluid-dynamical parameter space. Using this framework we were able to show that: (1) Symmetric and periodic flapping fins and wings can produce asymmetric and chaotic vortex wakes. (2) Rotational accelerations stabilize leading edge vortices on revolving wings of insects and other organisms. (3) Stable leading edge vortices augment lift in both animal and plant flight. (4) Wing morphing in birds drastically improves glide performance. (5) Flapping insect wings are less efficient than spinning and translating insect wings.

This reverse-engineering analysis of biofluidic locomotion has furthermore helped us to forward-engineer two micro-air vehicles. We have designed, built, and flown a robotic flapper (DelFly) and a morphing model swift (RoboSwift). Clearly the formal methods and findings presented here can lead directly to novel technological products.

Exploring the biofluiddynamics of swimming and flight

2 Designing a map for exploration

4 Take-off into the third dimension

6 Escape into thin air

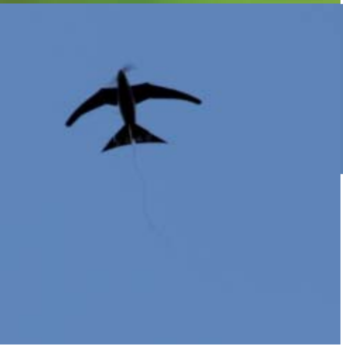

8 Back to the future

As an inspiration for design

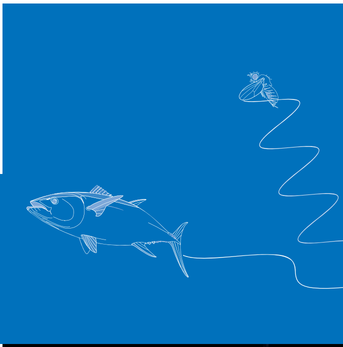

Introduction 1

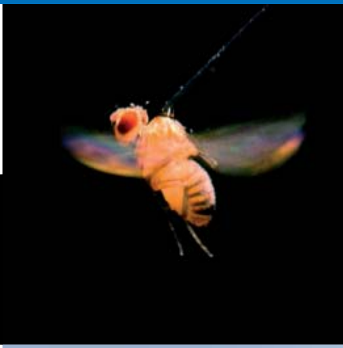

A Journey through flatland 3

Swirling down to earth 5

Synthesis 7

1 Introduction

1.1

EXPLORING THE BIOFLUIDDYNAMICS OF SWIMMING AND FLIGHT

David Lentink

Adaptations for locomotion

We are surrounded by organisms that seem to walk, swim and fly effortlessly while traveling long distances. In fact, we are proficient long distance runners ourselves and adaptations like sweating help us to stay cool. Presumably we can run marathons today because our predecessors used to catch prey on the African savannah by chasing them down for hours, until the prey was exhausted and could be caught easily (Bramble and Lieberman, 2004). Even these days, some of us enjoy chasing down animals. Such as Huw Lobb, who is the first man ever to beat a horse in the annual 'man against horse race' of 2004 over 22 miles at Llanwrtyd Wells in mid Wales. While it was a triumph for Huw, who won one of the biggest unclaimed prizes in British athletics of £25,000, Bookie William Hill had to pay out on scores of bets struck at odds of 16/1 (BBC News, 13-06-2004). This illustrates how we are fascinated with the locomotory capabilities of other organisms, and that we are willing to pay the price just to outperform them. Perhaps we especially admire organisms that swim and fly, for which we are poorly adapted. Most of us have learned about our poor adaptations for swimming and flight as kids, when trying to swim in deep water and falling from heights. How can we better understand the adaptations needed for swimming and flying?

Swimming and flight is constrained by fluid dynamics

The habitats on earth can be divided in land, water, air and their interfaces. The physical properties of these habitats constrain the locomotion of organisms. Just think of us running; we not only depend on friction to push off; the deformational properties of the material on which we run directly affects running efficiency. We experience these different efficiencies when running on streets consisting of solid materials versus sand, which is a granular material that shares material properties of both solids and fluids. Understanding the differences in dynamical properties between solids and fluids gives insight in how these properties can constrain locomotion. Fluids behave very differently compared with solid and granular materials, they cannot resist a load without deforming continuously. We experience this difference in material properties of land versus water when we attempt to walk over water and sink straight to the bottom. When we swim back to land, we are moving packets of water backwards with our hands, arms and legs. These packets of water resist being moved, which enables us to push off against these packets and swim forward. Hence we rely on the dynamic properties of water to move through it. From a physical point of view, the dynamics of water and air are similar irrespective of their different material properties, such as density and viscosity. They are both fluids because they only resist rate of deformation, but not deformation itself. This particular dynamical property of fluids is captured by the Navier-Stokes equation, which describes the dynamics of fluid motion. Compared to our humble swimming performance and our inability to fly, many organisms have evolved into specialists with adapted morphology and body kinematics tuned to match the dynamical properties of fluids, which enables them to swim and fly well. E.g. half of all vertebrates are fish, moving through water, roughly a quarter of all mammals are bats flying through the air, and the majority of insects and birds can fly. How do all these organisms manage to move so well through water and air, and how do they bring the fluid in motion to accomplish this?

Organisms can generate fluid vortices

The fluid very close to the body of an organism is forced to follow the body's motion, irrespective of the fluid's inertia, because fluid cannot flow through the body and viscosity makes it

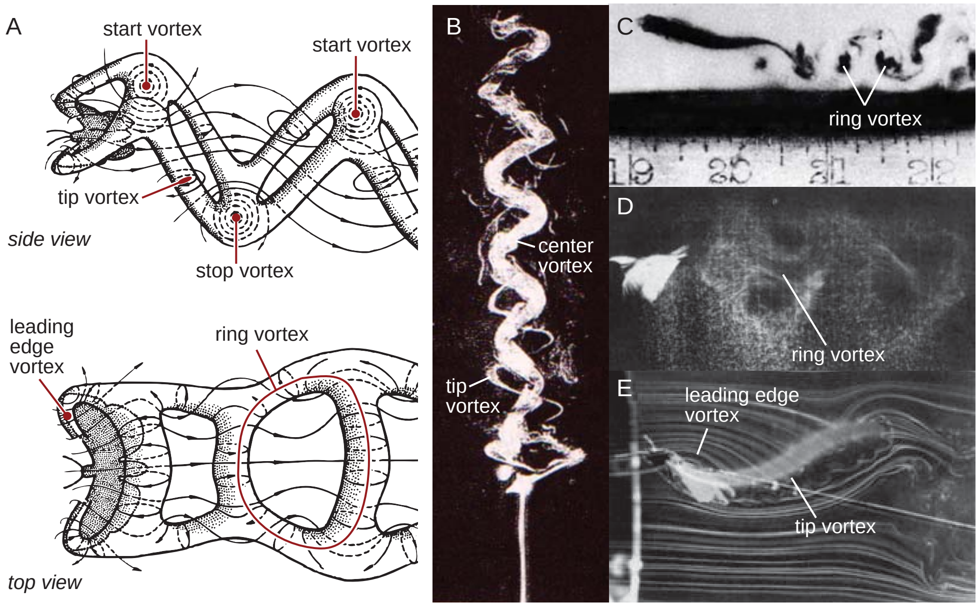

Fig. 1 | Many macroscopic animals generate large vortices which they shed in their wake. Such a wake is illustrated for a butterfly in (A), taken from Brodsky (1996). Top; the vortex wake of this particular butterfly consist of a 'folded ladder' composed out of start and stop vortices that are generated at the start and end of each stroke. These start and stop vortices are connected through the tip vortex, that is connected with the wing tip. Bottom; together the start, stop and tip vortices form interconnected ring vortices that build up the 'folded ladder' vortex wake. For several organisms, such as butterflies, the vortex 'ladder' starts at the leading edge of the wing with a so called 'leading edge vortex'. There exists no blueprint of an organism's vortex wake, its shape and dynamics depend on both the morphology and the kinematics of an organism. There exist, however, many similarities among vortex wakes of different organisms. This is illustrated by several photographs of vortex trails of swimming and flying organisms: (B) Smoke visualization of flow around a maple seed (Onda *et al.* 1986), (C) Ink visualization of flow around a pearl danio (Rosen, 1959), (D) Saw dust visualization of flow around a Shaffinch (Kokshaysky, 1979) and (E) Smoke visualization of flow around a hawkmoth (Ellington *et al.*, 1996).

stick to the body. The fluid that sticks to the body continuously shears and forms shear layers, which are left behind in the wake of the organism. These shear layers are unstable when the inertia of the fluid dominates its viscosity. As a result, shear layers can roll-up into packets of rotating fluid, vortices, as soon as they separate from the body. Many macroscopic swimming and flying organisms such as animals and plant seeds create large vortices with their fins and wings when they move through water and air. These vortices are shed in their wake, and together they form the footprint of the organism in the fluid, Fig. 1 (e.g. Alexander, 1999).

Leading edge vortex stability

We have all heard the apocryphal story that bumble bees cannot generate enough lift to hover with their wings according to the aerodynamic theory of aircraft, pioneered by Lanchester (1907), and later Prandtl (1918, 1919). This mystery was solved through the discovery of a stable leading edge vortex on top of the wing of a hawkmoth, which augments lift beyond predicted values, because the low pressure core of the vortex sucks the wing upward (Ellington *et al.*, 1996), Fig. 2A, B. Ever since we have a mental picture of how hawkmoths, bumble bees and other insects can generate enough lift, but we are left with the mystery why this tornado-like vortex rests stably on top of insect wings (Ellington *et al.*, 1996; Birch and Dickinson, 2001). Currently, the stable leading edge vortex has become a fluid dynamic mechanism that potentially can also explain the elevated swimming and flight forces of many other organisms. Swept model wings of gliding swifts, for example, generate a stable leading edge vortex

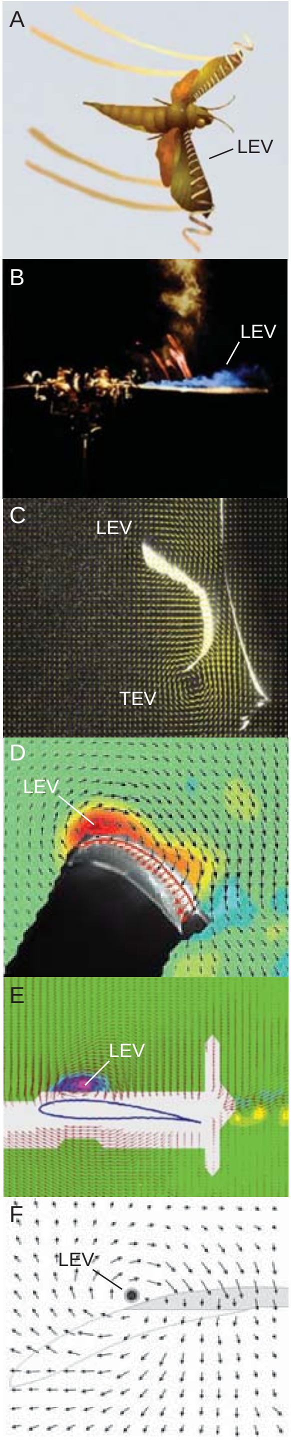

Fig. 2 | Leading edge vortices (LEVs) on the wings and fins of animals. (A) Artistic impression of leading edge vortices on hawkmoth wings (George Hayhurst in Dalton, 1999, after Ellington *et al.*, 1996). Experimental observations of leading edge vortices: (B) Front view of a model flapping hawkmoth wing. The LEV is visualized with smoke (Ellington *et al.*, 1996). (C) Hind view of the pectoral fin of a sunfish, which generates both a leading and trailing edge vortex (TEV). Both vortices are visualized using velocity vectors measured with particle image velocimetry (PIV). (Bandyopadhyay *et al.*, 2008). (D) Side view of the wing of Pallas' long-tongued bat. The LEV is visualized using velocity vectors and colors that represent the vorticity field, which is a measure of the fluids rotation. (Muijres *et al.*, 2008). (E) Side view of a flapping goose wing model. The LEV is visualized using velocity vectors and colors that represent the vorticity field. (Hubel, 2006). (F) Hind view of a model gliding swift wing that is swept back. The LEV is visualized with velocity vectors (Videler *et al.*, 2004).

(Videler *et al.*, 2004). Using a flapping goose model, Hubel and colleagues found a stable leading edge vortex in forward flapping flight (Hubel, 2006). Recent in-flight measurements have revealed that Pallas' long-tongued bat also generates a stable leading edge vortex when it hovers, like insects do (Muijres *et al.*, 2008). There is even evidence that suggests that sun fish generate both a stable leading and trailing edge vortex, which could augment force generation (Lauder and Madden in: Bandyopadhyay *et al.*, 2008), Fig. 2. Why, and under which conditions leading edge vortices are stable on fins or wings is, however, still unclear.

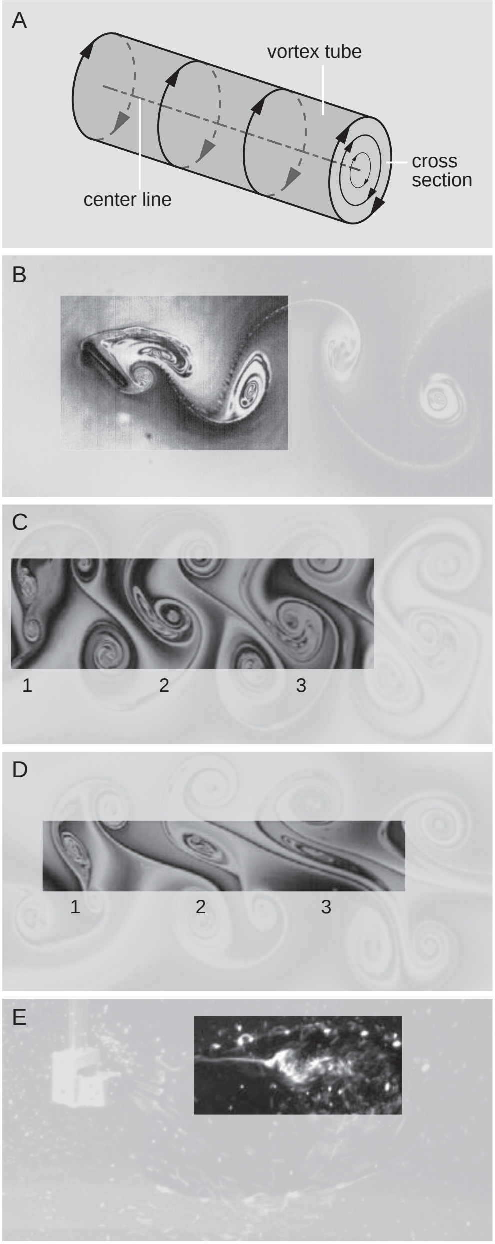

Fig. 3 | Vortices have their own dynamics. (A) A sketch of a three-dimensional vortex tube in a fluid. The vortex tube represents a local region in the fluid that rotates around its centerline. A two-dimensional vortex is simply the cross-section of the three-dimensional vortex tube. (B) Two-dimensional vortex shedding of a translating foil in a soap film. The foil represents a streamwise cross-section of a wing or fin set at an angle of attack with respect to the flow, in this case 45°. At such high angles, the flow around the wing separates from the surface at the leading and trailing edge. These separating 'shear layers' roll up into leading and trailing edge vortices that are unstable and start to shed from the foil. Due to the vortex shedding, the fluid force exerted on the foil (i.e. lift and drag) fluctuates. (C) Co-rotating vortices can merge when they get close enough to influence each other's path in the fluid. The two high-lighted two-dimensional vortices in a soap film merge in three successive (time) steps downstream of a flapping foil. (D) The shear field of vortices can elongate and tear other vortices apart. The high-lighted two-dimensional vortex in a soap film is torn apart by neighboring vortices in three successive (time) steps downstream of a flapping foil. (E) The laminar structure of three-dimensional vortices can break apart, burst, when axial flow in the vortex core ('centerline') decelerates; shown is spiral bursting of a leading edge vortex attached to a flapping wing. (The Reynolds number, a measure of the relative importance of inertial acceleration versus viscous stress, is of order 1000 in all cases.)

Vortex wake periodicity

The shape and dynamics of a vortex wake are not simply a consequence of the order in which an organism sheds the vortices it creates in the wake. Vortices have their own dynamics – vortices can shed, merge, tear, burst and interact with each other and with the organism in all kinds of manners that are co-determined by vortex dynamics, Fig. 3. In some cases, these interactions are beneficial to an animal's locomotory performance. Insects, for example, can recapture their vortex wake and generate extra lift (Dickinson *et al.*, 1999) while birds fly in formation to capture energy from each other's wake (Lissaman and Schollenberg, 1970). Trouts even adopt a special Kármán gait when swimming in the vortex wake of a half-cylinder to save energy (Liao *et al.*, 2003).

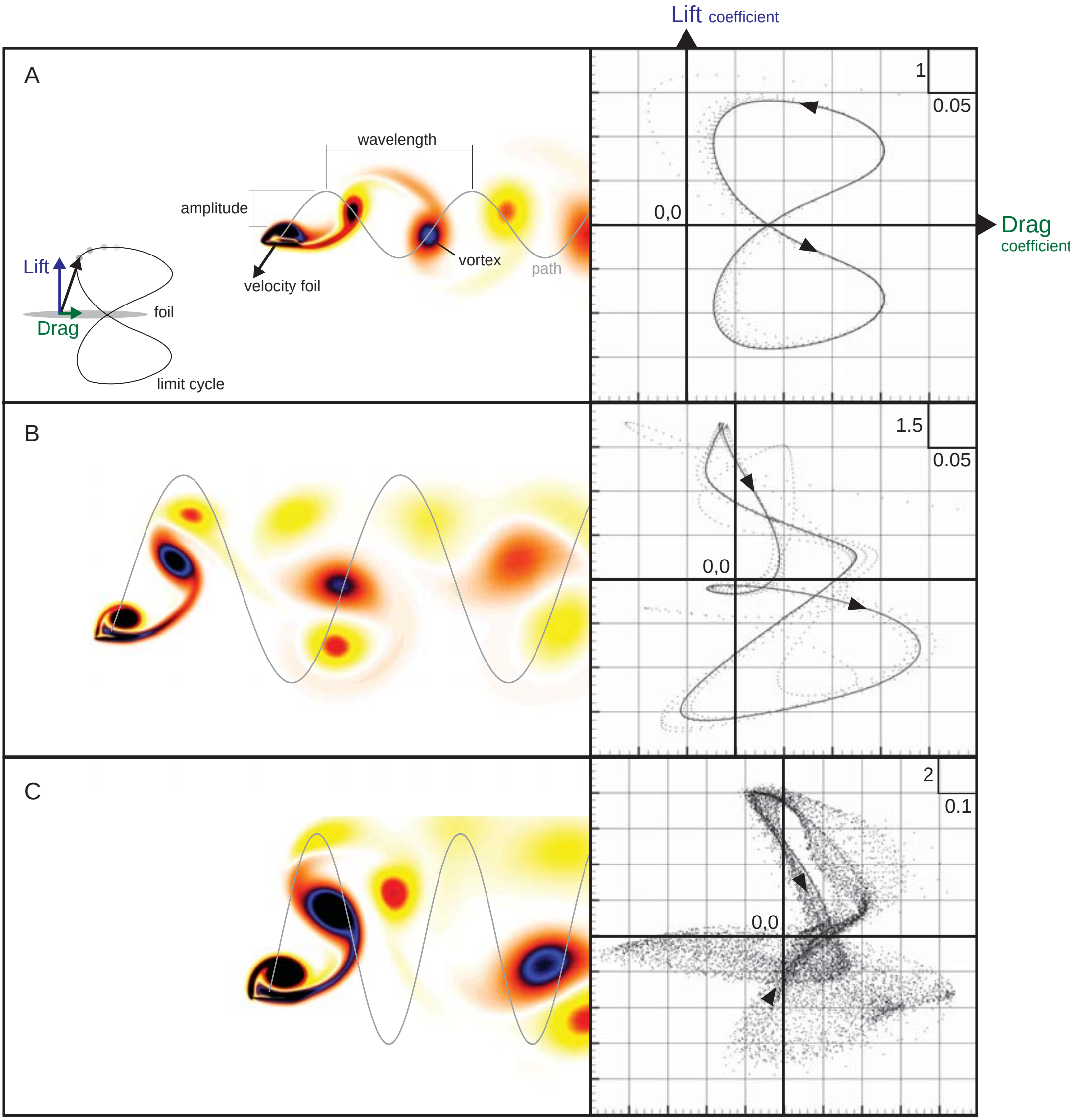

The lateral line of fish enables them to sense these vortices (Chagnaud *et al.*, 2006) and tune into their dynamics. This illustrates that some animals explicitly adapt their behavior to vortex dynamics using their sensory system. This raises the question how difficult it is for an animal to predict vortex dynamics based on its sensory information, such that it can tune its fin or wing kinematics to exploit vortices.

Vortex wakes of animals are typically interpreted and illustrated as a periodic row of alternating vortices, Fig. 1. This is contrasted by two basic numerical studies of two-dimensional heaving foils that model the fins and wings of animals (Lewin and Haj-Hariri, 2003; Lentink and Gerritsma, 2003). Although several periodic vortex wakes have been found as a function of flapping kinematics, compelling evidence was found for a specific set of foil kinematics that cause the vortex wake and lift and drag forces to be chaotic (Lentink and Gerritsma, 2003), Fig. 4.

Chaos (Lorenz, 1963) significantly limits the forecast horizon of the dynamics of vortices and corresponding fluid dynamic forces. If animals would actually have to cope with chaotic vortices and forces, it might well constrain both their ability to exploit vortices and their neural control of body motion. However, we do not know yet whether chaotic vortex wakes are exceptional or common in the parametric space of a flapping foil.

Biofluiddynamics as an inspiration for design

Swimming and flying organisms have inspired us long before we realized that they juggle with vortices to move well. They made us dream of exploring the oceans and taking off into thin air ourselves. Engineers have provided us with an array of ingenious devices, high-tech ‘ortheses’, to accomplish this; from submarines and aircrafts to spacecrafts. Yet, after we descended to the ocean floor, flew non-stop around the world, and landed on the moon, the discoveries of biologists and climate researchers woke us up again. Nowadays we are constantly reminded that our technology is often not sustainable, and that many of our designs are still primitive compared with nature. To find new ways to make our vehicle designs more effective, engineers now again look for inspiration in nature – bio-inspired design (e.g. French, 1988; Dickinson, 1999; Nachtigall and Blüchel, 2000; Pfeifer *et al.*, 2007). But for such designs we need to understand how exactly the locomotion of organisms works in order to prevent us from copy-pasting designs that do not make our vehicles more effective. An integrated approach that

Fig. 4 | Computational fluid dynamic simulations of the flow and forces generated by a thin two-dimensional heaving foil at the scale of a fruit fly (Lentink, 2003; Lentink and Gerritsma, 2003). The colors represent the vorticity field; yellow vortices spin clockwise, whereas orange vortices spin anti-clockwise. (A) An amplitude of 0.5 chord lengths in combination with a wave length of 4 chord lengths results in a symmetric and periodic vortex wake and a corresponding limit cycle in the lift-drag phase diagram. Note that the limit cycle is the ultimate path of the resultant force vector that is composed of a drag and a lift component. The dots indicate the force vector path before the limit cycle kicks in. (B) Increasing the amplitude to 1.5 chord lengths and the wave length to 6 chord lengths results in an asymmetric vortex wake and corresponding asymmetric lift-drag phase diagram. The flow is, however, still periodic. (C) When we keep the amplitude constant, set at 1.5 chord lengths, and decrease the wave length to 4 chord lengths, we find a vortex wake that never repeats itself over the 167 simulated periods. The corresponding lift-drag phase diagram shows a limit cycle of which the shape changes every period and never repeats itself, which results in a so-called ‘strange attractor’. A further analysis has shown that this flow is initial-condition sensitive and that the frequency spectrum of lift and drag forces is broad; these are all hallmarks of chaos (Lorenz, 1963).

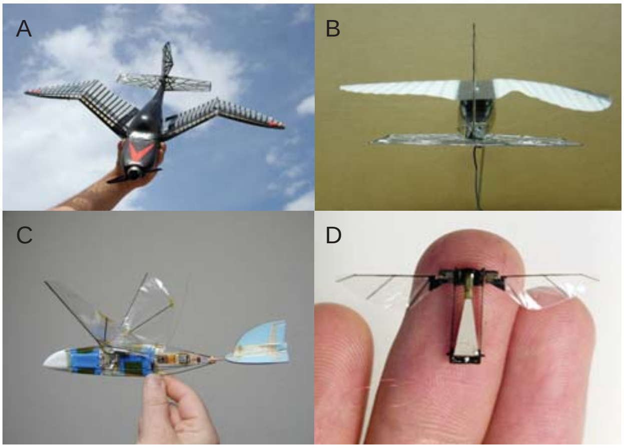

Fig. 5 | Examples of successful morphing and flapping micro air vehicles. (A) Gull-like variable wing dihedral for enhanced stability versus maneuverability (Lind *et al.*, 2004). (B) Bird-like wing twist for enhanced roll-performance (Lind *et al.*, 2004). (C) Insect-like flapping wings that generate both lift and thrust (Pornsin-Sirirak *et al.*, 2001) (D) Prototype robotic fly that can take-off guided by wires (Wood, 2008).

includes both fundamental biofluiddynamic research and engineering design has the potential to provide us with new insights into swimming and flight mechanisms in nature, and novel bio-inspired designs that work. This thesis is the result of such an approach. I integrated biofluid-dynamic research and aerospace engineering design, which resulted in inspiration for designing new flapping and morphing micro air vehicles (Fig. 5).

Thesis aim and outline

The locomotion of most macroscopic organisms that swim or fly depends on caudal fins, pectoral fins, or wings. The swimming and flying animals and plant seeds that I will study here create vortices with their fins and wings that are shed in a wake. These vortices have their own dynamics, which the organisms have to cope with to move effectively through their surrounding fluid. *The aim of this thesis is, therefore, to explore how the swimming and flight apparatus of organisms is constrained by vortex dynamics. I focus on how principal morphological and kinematic parameters of fins and wings co-determine leading edge vortex stability and vortex wake periodicity, which mediate fluid force augmentation and forecast horizon, respectively. The principal findings of this thesis will serve as an inspiration for the design of new micro air vehicles.* To answer these questions, I need to mount a systematic exploration of these morphological and kinematic parameters. And this can be achieved most effectively by first gaining a rough overview over the most relevant parameters with the help of so-called dimensionless numbers. In fluid dynamics, these numbers map out which fluid accelerations and stresses dominate a flow as a function of the shape and kinematic parameters that cause the flow to exist, e.g. the flow generated by an airplane. However, no coherent framework of dimensionless numbers exists for studying the biofluiddynamics of fins and wings.

In this study, we start out with a dimensional analysis of the Navier-Stokes equation to derive a coherent framework of dimensionless numbers for the flow generated by translating, spinning and flapping fins and wings. This framework enables us to determine which fluid accelerations and stresses dominate the flows dynamics as a function of fin and wing morphology and kinematics. We used this framework for designing all our experiments and therefore derive and illustrate it in Chapter 2: *Designing a map for exploration*.

Based on this dimensionless map we explored both leading edge vortex stability and vortex wake periodicity as a function of foil kinematics using a two-dimensional flapping foil in a soap film. Like others before us, we find that the leading edge vortex is unstable on two-dimensional flapping foils. More significantly this study provides the first experimental confirmation that chaotic vortex wakes can be generated by a periodically and symmetrically flapping foil. Surprisingly we find that chaotic wakes are common, which is shown in Chapter 3: *A journey through flatland*.

Leading edge vortices are unstable on two-dimensional flapping foils, whereas they are stably attached to the three-dimensional flapping wings of hovering insects. The dimensionless Rossby number, which we derived in Chapter 2 for three-dimensional flapping wings, predicts that the rotational centripetal and Coriolis accelerations could mediate leading edge vortex stability. According to the prediction this works both for flapping and spinning wings, provided that the Rossby number is close to one. To test this we performed systematic experiments with a three-dimensional robotic model of a dynamically scaled fly wing that can translate, spin and flap at various Rossby numbers. These experiments confirm our theoretical prediction that rotational accelerations stabilize leading edge vortices on revolving wings for Rossby numbers close to one, which we describe in Chapter 4: *Take-off into the third dimension*.

Based on the previous study it became evident that autorotating seeds might also augment their lift with a stable leading edge vortex, because their Rossby number is close to one. We investigate this prediction by measuring the flow generated by dynamically-scaled models of maple and hornbeam seeds. Our flow measurements show that these seeds indeed generate a stable leading edge vortex. This result suggests that the leading edge vortex represents a convergent aerodynamic solution in the evolution of flight performance in both animals and plants, which we discuss in Chapter 5: *Swirling down to earth*.

Finally, we study the lift augmentation of the stable leading edge vortex generated by swept swift wings and compare it to the lift of fully extended wings. For this we mounted freeze-dried swift wings to a balance system in a low-speed wind tunnel. These experiments not only show that the lift augmentation of a leading edge vortex on swept swift wings is insignificant compared to the lift augmentation found for flapping and spinning wings. It also provides us with a functional perspective of the unique morphing wings of birds, which allows them to adapt the shape of their wings to obtain maximal glide performance at both low and high speeds by varying wing sweep, which we describe in Chapter 6: *Escape into thin air*.

After all these studies I synthesize my findings into 5 biofluiddynamic conclusions and two designs of micro air vehicles inspired by these conclusions: A morphing micro air vehicle inspired by swifts and a flapping micro air vehicle inspired by insect flight. Through this synthesis we found that micro air vehicles that flap their wings do not hover very efficiently. Therefore, I close my synthesis by describing a future experiment with spinning hummingbird-inspired wings, which can provide inspiration for designing more efficient hovering micro air vehicles in Chapter 7: *Biofluiddynamics as an inspiration for design*.

The research outlined here got me really excited about the comparative biofluiddynamics of swimming and flight. This motivated me to write an NWO-ALW grant proposal for comparing the aerodynamics of fruit flies with the hydrodynamics of zebra fish larvae, which are both high performance locomotors in the same flow regime. For this comparison between fly and fish we developed new experimental setups to quantify the swimming performance of zebra fish as a function of swimming speed and age. This future work is illustrated in Chapter 8: *Back to the future*.

Acknowledgements

Steven Prins, Ulrike Müller, Sander Kranenbarg and Johan van Leeuwen critically read several versions of the manuscript.

References

Alexander, R. McN. (1999). Energy for animal life. Oxford University Press.

Bandyopadhyay, P. R., Beal, D. N. and Menozzi, A. (2008). Biorobotic insights into how animals swim. *J. Exp. Biol.* **211**, 206-214.

Birch, J. M. and Dickinson, M. H. (2001). Spanwise flow and the attachment of the leading-edge vortex on insect wings. *Nature* **412,** 729-733.

Brodsky, A. K. (1996). *The evolution of insect flight.* Oxford University Press.

Bramble, D. M. and Lieberman, D. E. (2004). Endurance running and the evolution of Homo. *Nature* **432**, 345-352.

Chagnaud, B. P., Bleckmann, H. and Engelmann J. (2006). Neural responses of goldfish lateral line afferents to vortex motions. *J. Exp. Biol.* **209**, 327-342.

Dalton, S. (1999). *The miracle of flight.* Firefly Books Limited.

Dickinson, M. H. (1999). Bionics: Biological insight into mechanical design. *PNAS* **96**, 14208-14209.

Dickinson, M. H., Lehmann, F. O. and Sane, S. P. (1999). Wing rotation and the aerodynamic basis of insect flight. *Science* **284**, 1954-1960.

Ellington, C. P., Van den Berg, C., Willmott, A. P. and Thomas, A. L. R. (1996). Leading-edge vortices in insect flight. *Nature* **384**, 626-630.

French, M. J. (1988). *Invention and evolution. Design in nature and engineering.* Cambridge University Press.

Hubel, T. (2006). Untersuchungen zur instationären Aerodynamik an einem vogelähnlichen Flügelschlagmodell, PhD thesis, *TU Darmstadt, Fachbereich Biologie*.

Kokshaysky, N. V. (1979). Tracing the wake of a bird. *Nature* **179**, 146-148.

Lancaster, F. W. (1907). *Aerodynamics*. A. Constable & Co, London.

Lentink, D. (2003). *Influence of airfoil shape on performance in insect flight.* MSc. Thesis, Delft University of Technology (fac. AE).

Lentink, D. and Gerritsma, M. I. (2003). Influence of airfoil shape on performance in insect flight. *AIAA* 2003-3447.

Lewin, G. C. and Haj-Hariri, H. (2003). Modelling thrust generation of a two-dimensional heaving airfoil in a viscous flow. *J. Fluid Mech.* **492**, 339-362.

Liao, J. C., Beal, D. N., Lauder, G. V. and Triantafyllou, M. S. (2003). Fish exploiting vortices decrease muscle activity. *Science* **302**, 1566-1569.

Lind, R., Abdulrahim, M., Boothe, K. and Ifju, P. (2004). Morphing for flight control of micro air vehicles. *European Micro Air Vehicle Conference*, Braunschweig, Germany.

Lissaman, P. B. S. and C. A. Schollenberg. (1970). Formation flight of birds. *Science* **168**, 1003-1005.

Lorenz, E. N. (1963). Deterministic nonperiodic flow. *J. Atmospher. Sci.* **20**, 130-141.

Muijres, F. T., Johansson, L. C., Barfield, R., Wolf, M., Spedding, G. R. and Hedenström, A. (2008). Leading-Edge Vortex Improves Lift in Slow-Flying Bats. *Science* **319**, 1250–1253.

Nachtigall, W. and Blüchel, K. G. (2000). *Das große buch der bionik. Neue technologien nach dem vorbild der natur.* Deutsche Verlags-Anstalt.

Onda, Y., Azuma, A. and Yasuda, K. (1986). The wake structure trailed from samara in autorotation. *Special issue of 14th Symposium on Flow Visualization* **6** (22) Flow Visual Soc. Japan, 311-314.

Pfeifer, R., Lungarella, M. and Iida, F. (2007). Self-organization, embodiment, and biologically inspired robotics. *Science* **318,** 1088-1093.

Pornsin-Sirirak, T. N., Tai, Y. C., Ho, C. H. and Keenon, M. (2001). Microbat-a palm-sized electrically powered omithopter. *NASA/JPL Workshop on Biomorphic Robotics*, Pasadena, USA.

Prandtl, L. (1918).*Tragflächentheorie. I.* Mitteilungen, Nachrichten der K. Gesellschaft der wissenschaften zu Göttingen, Math-phys. Klasse.

Prandtl, L. (1919).*Tragflächentheorie. II.* Mitteilungen, Nachrichten der K. Gesellschaft der wissenschaften zu Göttingen, Math-phys. Klasse.

Rosen, M. W. (1959). Water flow about a swimming fish. *NOTS Technical Publication*. China Lake, CA: U.S. Naval Ordnance Test Station.

Videler, J. J., Stamhuis, E. J. and Povel, G. D. E. (2004). Leading-edge vortex lifts swifts. *Science* **306**, 1960-1962.

Wood, R. J. (2008). The first takeoff of a biologically-inspired at-scale robotic insect. *IEEE Trans. on Robotics* **24**, 341-347.

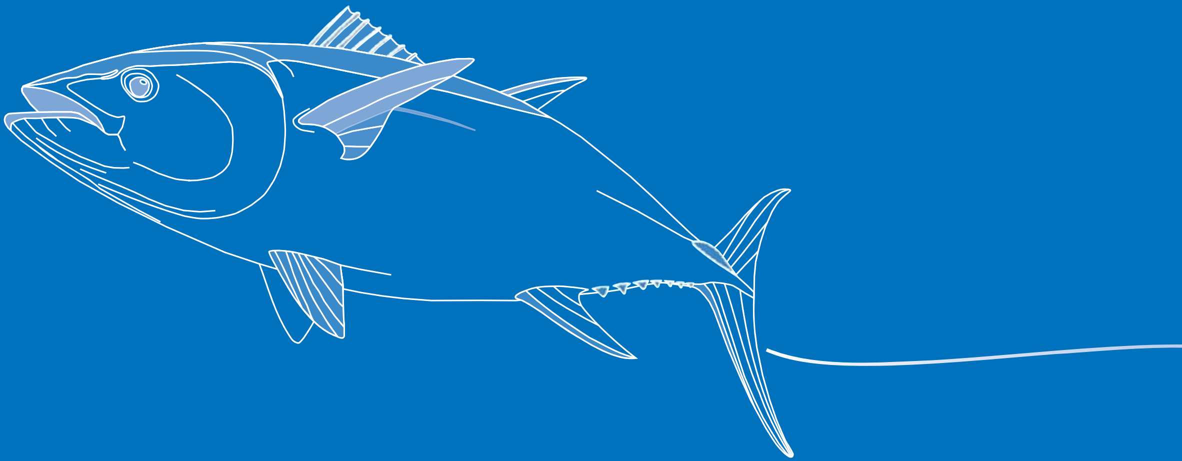

2 Designing a map for exploration

2.1

BIOFLUIDDYNAMIC SCALING OF FLAPPING, SPINNING AND TRANSLATING FINS AND WINGS

David Lentink* and Michael H. Dickinson

Summary

Organisms that swim or fly with wings and fins physically interact with the surrounding water and air. The interactions are governed by the morphology and kinematics of the locomotory system that form boundary conditions to the Navier-Stokes (NS) equations. These equations represent Newton's law of motion for the fluid surrounding the organism. Several dimensionless numbers, such as the Reynolds number and Strouhal number, measure the influence of morphology and kinematics on the biofluiddynamics of swimming and flight. There exists, however, no coherent theoretical framework that shows how such dimensionless numbers of organisms are linked to the NS-equation.

Here we present an integrated approach to scale the biological fluid dynamics of a wing that either flaps, spins or translates. Both the morphology and kinematics of the locomotory system are coupled to the NS-equation through which we find independent dimensionless numbers that represent rotational accelerations in the flow due to wing kinematics and morphology. The three corresponding dimensionless numbers are the (1) angular acceleration number, (2) centripetal acceleration number, and (3) the Rossby number which measures Coriolis acceleration. These dimensionless numbers consist of length scale ratios, which facilitate their geometric interpretation. This approach gives fundamental insight into the physical mechanisms that explain the differences in performance among flapping, spinning, and translating wings. Although we derived this new framework for the special case of a model fly wing, the method is general enough to make it applicable to other organisms that swim or fly using wings or fins.

Introduction

The use of dimensionless numbers for understanding complex biological flows has helped us enormously to better understand adaptations for swimming and flight in nature, as well as the corresponding flow phenomena. For example, the Reynolds number, *Re*, is the ratio of convective acceleration times density over viscous stress in the fluid (e.g. Tritton, 2005). It not only dictates what kind of propulsive mechanism the organism has at hand (viscous vs. inertial) it also determines whether the flow is reversible or irreversible, or whether it is laminar or can become turbulent. Such dimensionless numbers can be interpreted in at least three ways: as ratios of force, time, or length (e.g. Tennekes and Lumley, 1983). For example, although the Reynolds number is often described as the ratio of inertial to viscous forces, it can be interpreted as the ratio of convection length (or time) over diffusion length (or time) for a standard transport time

Submitted

(or distance) (e.g. Tennekes and Lumley, 1983). The wide-ranging use of the Reynolds number in biologically-relevant flows is well illustrated in Steven Vogel's book 'Life in moving fluids' (Vogel, 1996).

The Strouhal number St is another important dimensionless number, which has been used extensively in the biological fluid dynamics literature. It is typically defined as $St = fA/U$ where f is flapping frequency, A is flapping amplitude, and U is mean flow velocity. Its original context was as a measure of dimensionless shedding frequency for a bluff body undergoing von Kármán shedding in a constant flow (e.g. Guyon *et al.*, 2001), but is has additional uses in biological fluid dynamics (Triantafyllou, 1993; Taylor, 2003). For example, it is proportional to the tangent of maximal induced angle of attack by a flapping wing or fin when the stroke plane is perpendicular to the direction of motion (Taylor, 2003, Lentink *et al.*, 2008). This amplitude-based Strouhal number closely resembles the inverse of the advance ratio $J = U/2\Phi fR$ as defined by Ellington (Ellington, 1984), where Φ is total wing beat amplitude in radians, f is flapping frequency, and R is root-to-tip wing length. Note that $2\Phi R$ is actually the total wingtip excursion in the stroke plane (down stroke plus upstroke), whereas U/f measures wingbeat wavelength λ, the distance traveled during one stroke cycle. The advance ratio is therefore a measure of the pitch of a flapping wing; very much like the pitch of a propeller (and the pitch of a screw) provided that the stroke plane is normal to body speed. Dickinson (1994) and Wang (2000b) defined a chord-based Strouhal number, $St_c = fc/U$ where c is chord length. This number closely resembles the reduced frequency k defined by Daniel and Webb (1987) for swimming $k = \pi fc/U$, which is usually defined as a ratio of velocities due to flapping to velocity due to forward motion. It should be noted that, in engineering fluid dynamics, Strouhal numbers are often reserved to their original purpose - to describe natural vortex shedding processes (e.g. Green, 1995) - whereas reduced frequencies (or the analogues dimensionless wavelength) are more appropriate for forced vibrations, such as flapping wings (e.g. Tobalske *et al.* 2007).

From our brief overview it becomes clear that different points of view exist in the biomechanics field on how to best define and use dimensionless numbers to study swimming and flight. Further, the interpretation of these dimensionless numbers is not always straightforward, or perhaps more importantly, similarly defined throughout the field. Our goal is to improve this for flapping studies by deriving a new set of dimensionless numbers. These numbers are not only directly linked to the Navier-Stokes (NS) equations, but can also be interpreted more easily based on the morphology and kinematics of the wing (or fin). For this we choose to use morphological and kinematic length scale ratios, because they are most easy to interpret and illustrate geometrically.

For simplicity we focus our analysis on fly wings. In the discussion we will indicate how to apply the theory to the wings and fins of other organisms such as insects, birds, fish, and samara seeds. First we derive the dimensionless NS-equation with respect to the surface of the flapping wing of a forward flying fly. Next we show that the angle between the body velocity vector of a fly and its (approximate) stroke plane can be neglected for estimating the correct order of magnitude of the dimensionless numbers that depend on speed. We then further simplify the NS-equation for hover conditions. Next we simplify the NS equations even further for spinning and translating fly wings. These more simplified forms of the NS-equation and the corresponding dimensionless numbers are illustrated graphically for three-dimensional wings. Our frame work can therefore be readily applied to the design of appropriate parameter spaces for complex biofluiddynamic studies of flapping, spinning and translating wings and fins. Finally we discuss how three-dimensional and two-dimensional wing kinematics are related and can potentially

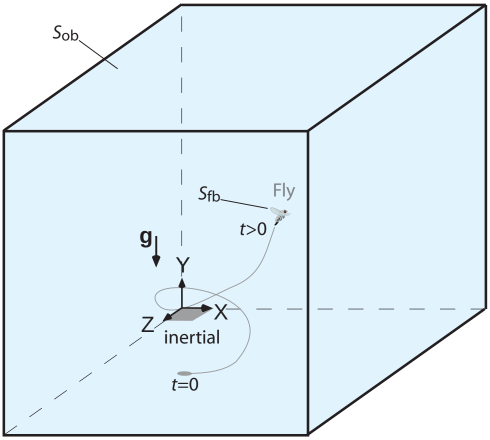

Fig. 1 | Boundary and initial conditions of the Navier-Stokes (NS) equations of air around a fly. The fly flies with respect to an inertial coordinate system (X,Y,Z) fixed to earth in a volume bounded by the outer surface S_{ob} where the air remains at rest (outer boundary condition). The fly takes off at $t=0$ when the fly and fluid is at rest (initial condition). The air at the surface of the fly S_{fb} adopts the same velocity as the fly's body surface (inner boundary condition). Gravity is indicated with **g**.

mediate the stall characteristics of a wing. Experimental tests of the efficacy of this new approach in characterizing salient features of biologically-relevant forces and flows are presented elsewhere (Lentink and Dickinson, 2008).

Materials and methods

NS-equation of a fly in forward flapping flight

For problems related to flying and swimming, the relevant external media (air and water) are incompressible to within a good approximation. This significantly simplifies the governing equations such as those describing the conservation of mass (Eqn. 1) and momentum (Eqn. 2) (e.g. Anderson, 1991; White, 1991; Guyon *et al.*, 2001; Tritton, 2005):

$$\nabla \cdot \mathbf{u} = 0, \tag{1}$$

$$\rho \frac{D\mathbf{u}}{Dt} = -\nabla p + \mu \nabla^2 \mathbf{u}, \tag{2}$$

in which $\nabla = [\partial/\partial x, \partial/\partial y, \partial/\partial z]^T$ is the gradient (del) operator, **u** velocity, ρ density, t time, p pressure and μ dynamic viscosity. Note that ρ and μ are constant (incompressible air and water). These equations are necessarily derived with respect to an inertial reference frame attached to earth. We can compute the time-dependent flow field, $\mathbf{u}(\mathbf{x},t)$, around a flying fly using this system of time-dependent and non-linear partial differential equations ($\mathbf{x}$ is the position vector in space). In order to solve the equations, we need to specify an initial velocity condition to start up the solution, and we need velocity boundary conditions to keep the solution within bounds, Fig. 1. An appropriate and simple initial condition is that the fly starts ($t=0$) at rest in still air:

$$\mathbf{u}(t=0) = \mathbf{0}. \tag{3}$$

While we can further assume that the air far away from the fly remains practically unaffected by the fly's movement, on the outer boundary S_{ob}:

$$\mathbf{u}(\mathbf{x} \in S_{\mathrm{ob}}) = \mathbf{0}. \tag{4}$$

Finally the air extremely close to the fly's outer surface S_{fb} can neither flow though, nor slip with respect to the fly's surface; the air adopts therefore the same velocity as the fly's surface (e.g. White, 1991):

$$\mathbf{u}(\mathbf{x} \in S_{\mathrm{fb}}) = \mathbf{u}_{\mathrm{fly}}. \tag{5}$$

Although the initial condition (Eqn. 3) and the boundary condition far away of the fly (Eqn. 4) are simple because they are zero (homogeneous), the boundary condition at the fly's surface (Eqn. 5) is not. The mathematical expression of the velocity boundary condition on the fly surface must describe the fly's velocity distribution over its (microscopic) surface architecture, while tracking its position in space as the fly flies around. This formidable problem can be solved numerically using Computational Fluid Dynamics (CFD) techniques (e.g. Liu. and Kawachi, 1998; Wang, 2000a; Sun and Tang, 2002), or experimentally through building physical models of flying insects in the lab (Maxworthy, 1979; Dickinson, 1994; Ellington, 1996; Dickinson, 1999).

Coordinate transformation that simplifies the fly's velocity boundary condition

A complementary approach is to first transform the governing equations and boundary conditions (Eqn. 1-5) such that the velocity boundary condition on the surface of interest is simplified. Preferably, the velocity boundary condition becomes zero such that we do not need to track the surface explicitly, but implicitly through the coordinate transformation (e.g. Anderson, 1991;

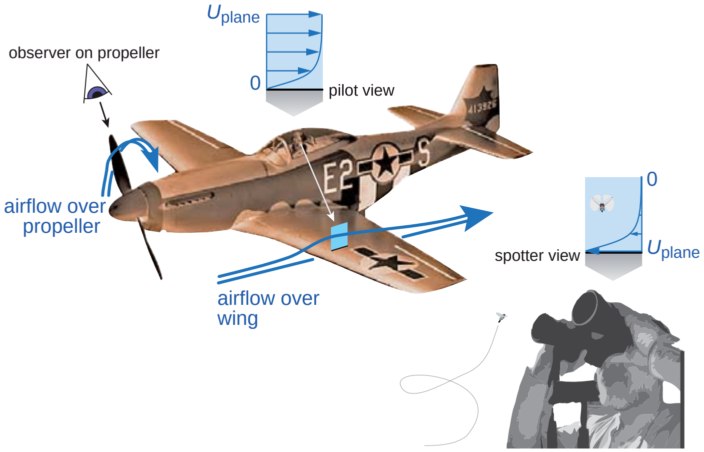

Fig. 2 | The velocity profile in the boundary layer around an airplane wing depends on the observer; airplane spotter (inertial observer) versus pilot (local observer). In engineering problems the reference frame (analogous to the observer) is customary attached to the wing (like the pilot is). This transformation simplifies mathematical analysis, numerical simulations and experiments, e.g. through the use of wind tunnels. The main advantage is that the surface of interest remains stationary with respect to the reference frame. A similar approach can be used for propellers; in this case the reference frame (or unfortunate observer) is fixed to the spinning and forward moving propeller, which again simplifies analysis. Here we propose to use a similar approach for studying the aerodynamics of the even more complicated motion of flapping fly wings.

White, 1991; Vanyo, 1993; Guyon *et al.*, 2001; Greitzer, 2004; Tritton, 2005). Such an approach is standard for studying cars, airplanes and even weather patterns on earth (e.g. Anderson, 1991; Batchelor, 1998). Transformation of the NS-equation by placing the reference frame on a moving object such as an airplane, Fig. 2, seems almost trivial through its common use, e.g. in wind tunnels. Transformations of coordinate systems are similarly helpful when studying the flow around a propeller (Fig. 2) or turbine blade (e.g. Du and Selig, 1998; Dumitrescu and Cardos, 2003). Such an approach simplifies the mathematical analysis of the boundary layer flow, which mediates the shear stress and pressure distribution on the surface, and therefore the net aerodynamic force and moment.

Here we attach our local frame of reference (x, y, z) to a flapping wing, at the wing's joint Fig. 3. To simplify our analysis we assume that the fly flies along a straight path at constant speed in an arbitrary direction. In this transformation we neglect possible morphological undulations such as traveling waves in the wing, which holds because the amplitudes of undulations in a fly wing are typically small compared to the wings stroke amplitude. The kinematics of the wing, to which we attached our reference frame, consists of three rotational components; stroke (ϕ), deviation (φ) and angle of attack (α), generate velocity gradients along the wing, Fig. 3A. The velocity transformation (Baruh, 1999) needed to make the velocity boundary condition identical to zero is (Vanyo, 1993; Greitzer *et al.*, 2004):

$$\mathbf{u}_{\text{inert}} = \mathbf{u}_{\text{loc}} + [\,\mathbf{u}_{\text{body}} + \mathbf{\Omega}_{\text{wing}} \times \mathbf{r}]. \tag{6}$$

The resulting transformed boundary conditions are:

$$\mathbf{u}_{\text{loc}}(t = 0) = \mathbf{0}, \tag{7}$$

$$\mathbf{u}_{\text{loc}}(\mathbf{x} \in S_{ob}) = -[\,\mathbf{u}_{\text{body}} + \mathbf{\Omega}_{\text{wing}} \times \mathbf{r}], \tag{8}$$

$$\mathbf{u}_{\text{loc}}(\mathbf{x} \in S_{fb}) = \mathbf{0}. \tag{9}$$

The fluid acceleration with respect to the inertial frame (X, Y, Z), $\mathbf{a}_{\text{inert}}$ is related to that in the rotating frame $\mathbf{a}_{\text{loc}}$ by the following transformation (Baruh, 1999; Vanyo, 1993; Greitzer *et al.*, 2004):

$$\mathbf{a}_{\text{inert}} = \mathbf{a}_{\text{loc}} + [\,\mathbf{a}_{\text{ang}} + \mathbf{a}_{\text{cen}} + \mathbf{a}_{\text{Cor}}], \text{ where} \tag{10}$$

$$\mathbf{a}_{\text{ang}} = \dot{\mathbf{\Omega}} \times \mathbf{r}, \tag{11}$$

$$\mathbf{a}_{\text{cen}} = \mathbf{\Omega} \times (\mathbf{\Omega} \times \mathbf{r}), \tag{12}$$

$$\mathbf{a}_{\text{Cor}} = 2\mathbf{\Omega} \times \mathbf{u}_{\text{loc}}. \tag{13}$$

Here $\mathbf{\Omega}$ is the angular velocity and $\dot{\mathbf{\Omega}}$ is the angular acceleration of the rotating frame, and $\mathbf{r}$ and $\mathbf{u}_{\text{loc}}$ are the position and velocity of a fluid volume in the rotating frame, respectively. The three terms enclosed in brackets in Eqn. 10 are the angular ($\mathbf{a}_{\text{ang}}$), centripetal ($\mathbf{a}_{\text{cen}}$) and Coriolis ($\mathbf{a}_{\text{Cor}}$) accelerations (note that we neglected the accelerations of the body itself because we assume steady flight. We now substitute the coordinate transformation described by Eqn. 10 into the NS-equation, Eqn. 2, and obtain its form with respect to the local coordinate system (x,y,z) fixed to the wing (Eqn. 14). Note that $\frac{D\mathbf{u}}{Dt}=\mathbf{a}_{\text{inert}}$ in Eqn. 2, whereas $\frac{D\mathbf{u}}{Dt}=\mathbf{a}_{\text{loc}}$ in Eqn. 14, because we drop the 'inert' and 'loc' subscripts in the NS-equation for easy notation in every subsequent NS-equation.

$$\rho\frac{D\mathbf{u}}{Dt}+\rho\dot{\mathbf{\Omega}}\times\mathbf{r}+\rho\mathbf{\Omega}\times(\mathbf{\Omega}\times\mathbf{r})+\rho2\mathbf{\Omega}\times\mathbf{u}=-\nabla p+\mu\nabla^2\mathbf{u}\,. \tag{14}$$

This equation captures the (relative) accelerations and stresses that a 'fluid particle' with *local* velocity $\mathbf{u}$ experiences close to the wing (i.e. in its boundary layer). We consider accelerations (Eqns. 10-13) instead of the analogous "fictitious forces", which point in the opposite direction (e.g. Vanyo, 1993; Greitzer *et al.*, 2004).

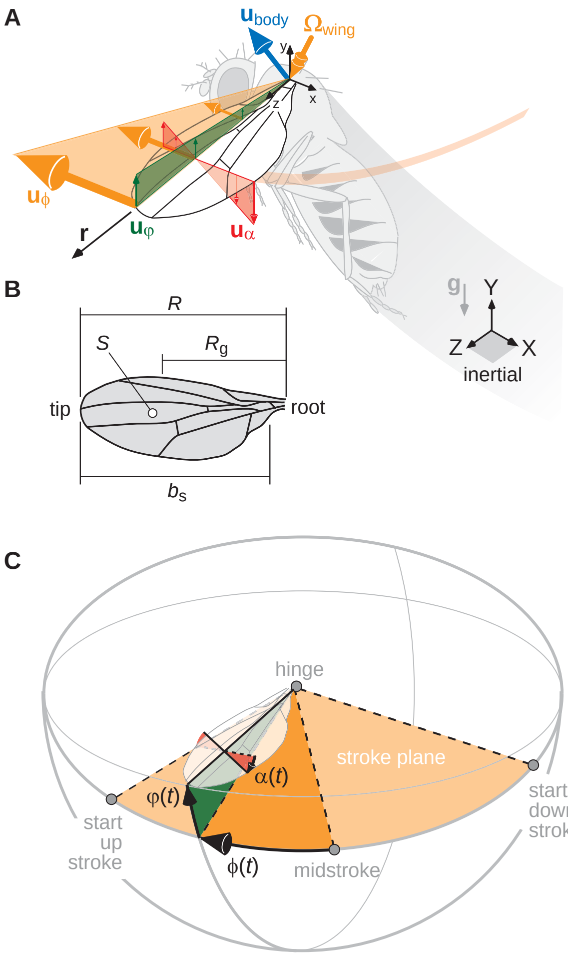

Fig. 3 | The kinematics and morphology of a forward flying fly. (A) The fly flies with velocity $\mathbf{u}_{\text{body}}$ while flapping its wings with angular velocity Ω_{wing}. The cross product of the wings angular velocity vector and the local radius $\mathbf{r}$ induces three velocity gradients along the wing; a velocity gradient due to deviation $\mathbf{u}_\varphi$, stroke $\mathbf{u}_\phi$, and angle of attack variation $\mathbf{u}_\alpha$. There are two reference frames, the inertial reference frame (X,Y,Z) attached to earth and the local reference frame (x,y,z) attached to the fly's wing at the joint. (B) Wing morphology. Wing radius is the radial distance between the wings root and tip; R. The wings radius of gyration R_g can be calculated using a blade element method and is roughly equal to half the wings radius (Ellington, 1984). The average chord length of the wing can be calculated by dividing single wing area S by single wing span b_s. We define the single wing aspect ratio as R/c. (C) The definition of wing deviation φ, stroke ϕ, and angle of attack α which depend on time t (Sane and Dickinson, 2001).

Scaling the NS-equation in the reference frame attached to the fly's wing

To find out how these acceleration and stress terms influence the physical phenomena around a fly wing, we scale all terms in Eqn. 14 with respect to their orders of magnitude:

$$\mathbf{u}^* = \frac{\mathbf{u}}{U},\ t^* = \frac{Ut}{c},\ \boldsymbol{\nabla}^* = c \cdot \nabla,\ \dot{\boldsymbol{\Omega}}^* = \frac{\dot{\boldsymbol{\Omega}}}{\dot{\Omega}},\ \boldsymbol{\Omega}^* = \frac{\boldsymbol{\Omega}}{\Omega},\ \mathbf{r}^* = \frac{\mathbf{r}}{R},\ p^* = \frac{p}{p_0}\ , \qquad (15\text{-}21)$$

in which '*' indicates a scaled, dimensionless, variable. The velocity **u** scales with the (absolute) time-averaged speed of the flapping wing at its wingtip U. The del operator $\boldsymbol{\nabla}$ scales with the average chord length as $1/c$, for which we divided the wing's single wing area S by its single wing span b_s ($c = S/b_s$), Fig. 3B Time t scales with the time it takes the fluid to travel over the wings chord c/U (e.g. Anderson, 1991; Tritton, 2005). The angular acceleration $\dot{\boldsymbol{\Omega}}$ and velocity $\boldsymbol{\Omega}$ scale with the (absolute) time-averaged angular acceleration amplitude $\dot{\Omega}$ and time-averaged angular velocity amplitude Ω of the wing, respectively. The local radius **r** scales with the wing tip radius, R, and the pressure p scales with the ambient (atmospheric) pressure p_0. After substituting Eqns. 15-21 in Eqn. 14 we normalize the resulting equation by dividing it with the order of magnitude of the convective acceleration term of the fluid $\rho U^2/c$ (e.g. Anderson, 1991; Tritton, 2005; Greitzer *et al.*, 2004). The resulting equation is dimensionless, for simplicity we omit '*':

$$1 \cdot \frac{D\mathbf{u}}{Dt} + \frac{\dot{\Omega} Rc}{U^2} \cdot \dot{\boldsymbol{\Omega}} \times \mathbf{r} + \frac{\Omega^2 Rc}{U^2} \cdot \boldsymbol{\Omega} \times (\boldsymbol{\Omega} \times \mathbf{r}) + \frac{\Omega c}{U} \cdot 2\boldsymbol{\Omega} \times \mathbf{u} = -\frac{p_0}{\rho U^2} \cdot \boldsymbol{\nabla} p + \frac{\mu}{\rho U c} \cdot \boldsymbol{\nabla}^2 \mathbf{u}, \quad (22)$$

The scale factors in this equation give the relative order of magnitude of all accelerations and stresses acting on an infinitesimal volume of fluid, compared to the convective acceleration. Hence these scale factors enable us to pin point how dominant the corresponding terms are and allow us to identify the dominant physical mechanisms that scale with these dimensionless numbers.

Results

Basic kinematic model of a fly wing in forward flight

The dimensionless numbers that scale the aerodynamics of a fly wing can be derived easier without loss of generality if we simplify the flight conditions and kinematics. This works because the order of magnitude of the scale factors are more important than their precise value. Mathematically our insect flight model is simplified in three steps: (1) Flight without sideslip, Fig. 4A. (2) Straight flight at constant speed U_∞ in an arbitrary direction with respect to gravity, Fig. 4B. (3) Zero wing deviation φ (Eqn. 23) and sinusoidal wing stroke ϕ (Eqn. 24) and angle of attack α (Eqn. 25) kinematics:

$$\varphi = 0, \qquad (23)$$

$$\phi = \Phi_0 \sin(2\pi f t), \qquad (24)$$

$$\alpha = \alpha_0 \cos(2\pi f t), \qquad (25)$$

in which the wing stroke and angle of attack flap 90° out of phase at the same frequency f. Note that Φ_0 is stroke amplitude, which is half the full amplitude defined by Ellington (Ellington, 1984), and α_0 is angle of attack amplitude (the ranges found for insects are $0° < \Phi_0 < 90°$ and $0° < \alpha_0 < 90°$). In our simplification we use Ellington's observation that the wing kinematics of many insects can be approximated well with sinusoidal stroke kinematics, and that wing deviation with respect to the stroke plane is typically small (Ellington, 1984). This has also been found by Fry and co-workers for fruit flies (Fry *et al.*, 2003). Based on Eqn. 23-25 we calculated the resulting angular velocities and accelerations as:

$$\dot{\phi} = \Phi_0 2\pi f \cos(2\pi f t), \tag{26}$$

$$\ddot{\phi} = -\Phi_0 (2\pi f)^2 \sin(2\pi f t), \tag{27}$$

$$\dot{\alpha} = -\alpha_0 2\pi f \sin(2\pi f t), \tag{28}$$

$$\ddot{\alpha} = -\alpha_0 (2\pi f)^2 \cos(2\pi f t). \tag{29}$$

Visualizing rotational flow accelerations due to wing stroke

For many insects, including flies, the velocity and acceleration due to wing stroke are larger than the velocity and acceleration due to angle of attack variation, because $\Phi_0 R > \alpha_0 c$ holds. Using Eqns. 11-13 we can draw and interpret the rotational accelerations that result from the wing

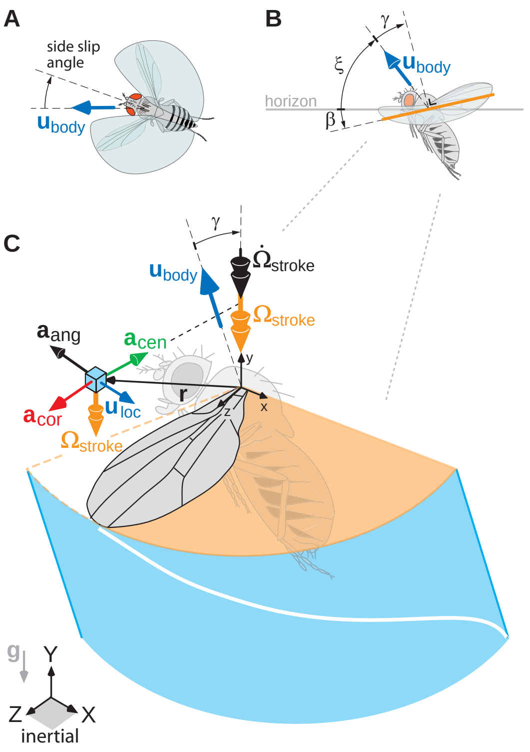

Fig. 4 | Simplified forward flight model of a fly. (A) We first assume that the side slip angle of the fly, with respect to its body velocity, is zero. (B) Definition of the stroke plane angle β (Ellington, 1984), flight path angle ξ (Ellington, 1984), and the angle between the normal vector of the stroke plane and the body velocity γ. (C) A hovering fly induces three rotational accelerations in the flow due to stroke (down stroke shown). Shown are the angular $\mathbf{a}_{ang}$, centripetal $\mathbf{a}_{cen}$, and Coriolis $\mathbf{a}_{cor}$ accelerations that are induced in the fluid near the wing and result from the wings stroke, its propeller-like swing. The angular velocity of the wing stroke is Ω_{stroke} and its angular acceleration is $\dot{\mathbf{\Omega}}_{stroke}$. The local velocity of fluid with respect to the local reference frame (x,y,z) is $\mathbf{u}_{loc}$. We color coded the stroke plane of the wing orange and the 'outer shell' blue, which features the white wingtip path. (Note that the depicted direction of angular acceleration was chosen to prevent image clutter).

stroke and act on the fluid near the wing, Fig. 4C. The first component $\mathbf{a}_{\mathrm{ang}}$ is the manifestation of the angular acceleration of the wing around its base, which results locally in a chord-wise acceleration (Fig. 4C). The second term $\mathbf{a}_{\mathrm{cen}}$ represents the centripetal acceleration, which is directed spanwise towards the wing's base (Fig. 4C). The third term $\mathbf{a}_{\mathrm{Cor}}$, represents the Coriolis acceleration, its direction depends on the direction of local fluid velocity $\mathbf{u}_{\mathrm{loc}}$ (Fig. 4C). Both the centripetal and Coriolis accelerations ($\mathbf{a}_{\mathrm{cen}}$ and $\mathbf{a}_{\mathrm{Cor}}$) are 'quasi-steady' in that they depend on the instantaneous value of the angular velocity $\boldsymbol{\Omega}$ of the wing (Eqns. 12, 13.), in contrast to the angular acceleration ($\mathbf{a}_{\mathrm{ang}}$), which depends on the rate of change of angular velocity $\dot{\boldsymbol{\Omega}}$ (Eqn. 11). These rotational accelerations arise in the fluid because the 'fluid particles' on the wings surface are forced to rotate with the same angular velocity and angular acceleration, as the wing. The angular velocity and acceleration acquired by the 'fluid particles' on the surface then diffuse into the flow and form the boundary layer around the wing in which the Coriolis acceleration acts on the fluid when it moves with respect to the rotating wing.

Scaling rotational accelerations due to wing stroke

We now simplify and interpret the dimensionless scale factors of the rotational accelerations (Eqn. 22) Using Eqns. 26 and 27, we can calculate the (absolute) time-averaged values for $\boldsymbol{\Omega}$ and $\dot{\boldsymbol{\Omega}}$ based on stroke kinematics:

$$\Omega = \frac{1}{T}\int_0^T \left|\dot{\phi}\right| \mathrm{d}t = \frac{1}{T}\int_0^T \left|\Phi_0 2\pi f \cdot \cos(2\pi f t)\right| \mathrm{d}t = 4\Phi_0 f, \tag{30}$$

$$\dot{\Omega} = \frac{1}{T}\int_0^T \left|\ddot{\phi}\right| \mathrm{d}t = 2\pi f \Omega, \tag{31}$$

in which T is the flap period, with $T = 1/f$. The wingtip path is illustrated in Fig. 5. The tip speed consists of a component in the direction of flight u_{t} and normal to it u_{n} from which we can calculate the absolute, time aver-

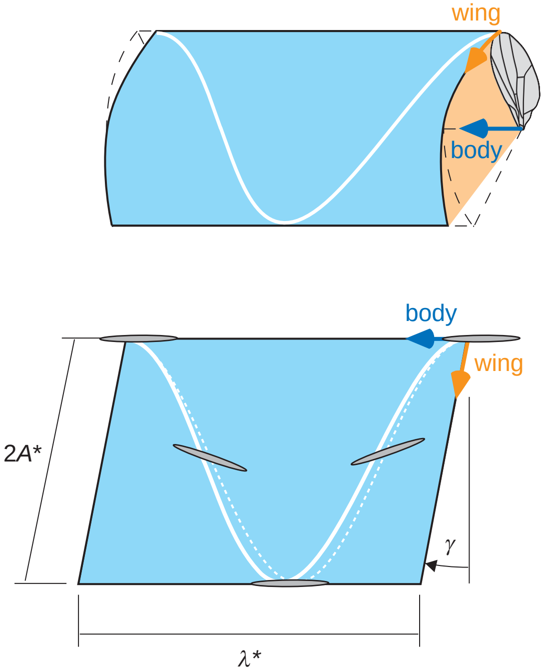

Fig. 5 | Flapping wing in forward flight. Graphical representation of the dimensionless numbers in the NS-equation that describe the wingtip kinematics; A^* the dimensionless stroke amplitude and λ^* the dimensionless wavelength. The body and wingtip speed are indicated with blue and orange vectors respectively. The dashed line is the wingtip path for $\gamma = 0°$ (fast forward or climbing flight). This figure holds for arbitrary flight direction with respect to gravity.

aged, wing tip speed:

$$U = \frac{1}{T}\int_0^T \left|\mathbf{u}(R)\right| \mathrm{d}t = \frac{1}{T}\int_0^T \sqrt{u_\mathrm{t}^2 + u_\mathrm{n}^2}\, \mathrm{d}t. \tag{32}$$

It is essential that both wing and body speed are included in the average speed U, so that it represents the right magnitude and ensures that we can continuously scale the NS-equation from fast-forward to hovering flight (Lentink and Gerritsma, 2003). We now insert Eqn. 26 in Eqn. 32 and calculate the tangential and normal velocity components due to the angle between the stroke plane and direction of flight γ, Fig. 4B:

$$U = \frac{1}{T}\int_0^T \sqrt{\left(U_\infty + R\cdot\Phi_0 2\pi f\cdot\cos(2\pi f t)\cdot\sin(\gamma)\right)^2 + \left(R\cdot\Phi_0 2\pi f\cdot\cos(2\pi f t)\cdot\cos(\gamma)\right)^2}\, \mathrm{d}t, \tag{33}$$

in which U_∞ is the body speed. We found in an earlier study (Lentink and Gerritsma, 2003) that this equation can be approximated with an error less than 5% for $\gamma = 0°$ and $0° \leq \arctan(J) \leq 90°$, in which $J = U_\infty / 4\Phi_0 R f$ is the advance ratio:

$$U \approx \sqrt{U_\infty^2 + (4\Phi_0 R f)^2}. \tag{34}$$

This approximation is derived such that it is exact for both hovering ($U_\infty = 0$) and non flapping flight ($f = 0$). In Fig. 6 we show that this approximation also holds for $0° \leq \gamma \leq 90°$ and we will therefore incorporate it in our model. We now substitute the expressions for Ω (Eqn. 30), $\dot{\Omega}$ (Eqn. 31) and U (Eqn. 34) into the scaled NS-equation (Eqn. 22) and obtain an easier to interpret dimensionless NS-equation for a flapping fly wing in forward flight (see Appendix I):

$$\frac{D\mathbf{u}}{Dt} + \frac{1}{J^2+1}\frac{1}{A^*}\cdot\dot{\mathbf{\Omega}}\times\mathbf{r} + \frac{1}{J^2+1}\frac{1}{AR_s}\cdot\mathbf{\Omega}\times(\mathbf{\Omega}\times\mathbf{r}) + \frac{1}{\sqrt{J^2+1}}\frac{1}{AR_s}\cdot 2\mathbf{\Omega}\times\mathbf{u} = -Eu\cdot\nabla p + \frac{1}{Re}\cdot\nabla^2\mathbf{u}, \tag{35}$$

in which J is the advance ratio, A^* the dimensionless amplitude of the wing, AR_s the single wing aspect ratio, Eu the Euler number, which is irrelevant for incompressible flow around insects (White, 1991), and Re the Reynolds number.

The definitions of the dimensionless numbers in Eqn. 35 are as follows:

$$J = U_\infty / 4\Phi_0 R f = \lambda^* / 4A^*, \tag{36}$$

$$A^* = \frac{\Phi_0 R}{c}, \tag{37}$$

$$AR_s = \frac{R}{c}, \tag{38}$$

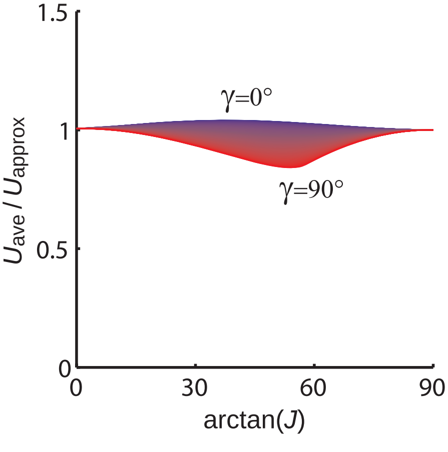

Fig. 6 | Approximation average wing tip velocity. The absolute average of the wing tip velocity (U_ave) can be approximated well (U_approx) within the same order of magnitude using Eqn. 34 for any combination of γ and J (advance ratio).

$$Re = \sqrt{\left(\frac{U_\infty c}{\nu}\right)^2 + \left(\frac{4\Phi_0 Rfc}{\nu}\right)^2} = \sqrt{Re_b^2 + Re_s^2} = \sqrt{J^2+1}\cdot Re_s. \qquad (39)$$

Note that the Reynolds number consists of two components; the first is due to body speed, Re_b, and the second due to wings stroke, Re_s.

Graphical representation of dimensionless numbers

To better understand how the dimensionless numbers in the NS-equation of a flapping wing relate to wing kinematics and morphology we represent them graphically. The advance ratio (Eqn. 36) is equal to dimensionless wavelength $\lambda^* = U_\infty / fc$ divided by the total wing tip excursion in the stroke plane $4A^*$, Fig. 5. The fly hovers for $J = 0$ and flies forward (or descends) in arbitrary direction when $J > 0$. For $\gamma = 0°$, which approximates fast forward and climbing flight, advance ratio is a direct measure of the average pitch of a flapping wing. The average pitch is a measure of the average induced angle of attack of the flapping wing, Fig. 7, and determines together with the geometric angle of attack amplitude (with amplitude α_0) the average effective angle of attack amplitude, Fig. 7. The effective angle of attack amplitude modulates wing lift and drag. For $0° < \gamma \leq 90°$, Fig. 5, the geometric interpretation of J is gradually modified, $\gamma = 90°$ being the extreme case. This case is relevant for slow hovering (Dickson and Dickinson, 2004), under such conditions the advance ratio also measures how much the fly moves forward along its flight path compared to its total stroke length. The average induced angle of attack is, however, zero, because it is proportional to cos(γ).

The geometric representation of the dimensionless amplitude A^* (Eqn. 37) is shown in Fig. 5 and its geometric interpretation is simple. An equivalent dimensionless total amplitude $\Lambda = 2A^*$, has been defined by Ellington (1984). The geometric interpretation of the single wing aspect ratio (Eqn. 38) is also straight forward and can be inferred from Fig. 3B by noting $AR_\mathrm{s} = R/c = Rb_\mathrm{s}/S$ (in which b_s is the semi-wing wingspan). Finally, Re can be interpreted as the ratio of convective versus diffusive transport length for a fixed time interval. It measures

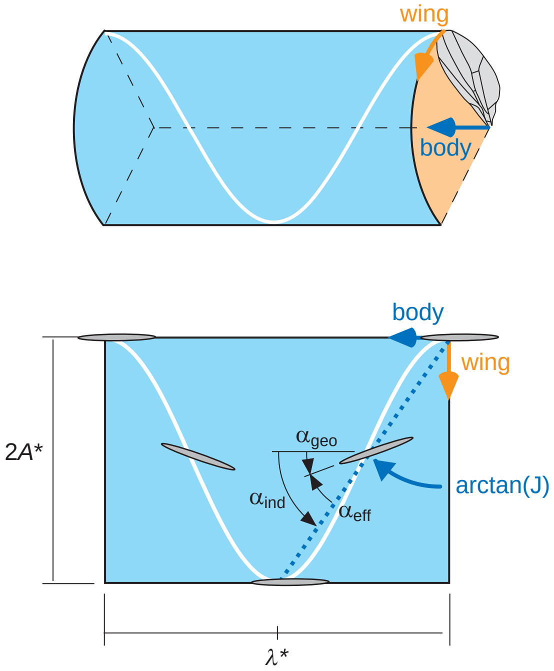

Fig. 7 | Graphical representation of A* and λ^* for $\gamma = 0°$; fast forward or climbing flight. Under these conditions arctan($1/J$) is the average induced angle of attack α_ind of the flapping wing. The maximum induced angle of attack amplitude at mid stroke can be calculated using arctan($\pi/2J$) (Lentink *et al.*, 2008). The effective angle of attack of the wing α_eff is equal to the induced angle of attack α_ind minus the geometric angle of attack α_geo.

how strongly the velocity boundary condition at the wing surface is diffused into the flow and is a measure of boundary layer thickness (e.g. Schlichting, 1979; Tennekes and Lumley, 1983), Fig. 2.

How do scale factors of the rotational accelerations in Eqn. 35 behave? The angular acceleration scales with $((J^2+1)A^*)^{-1}$, which increases for decreasing A^* at constant J and increases for decreasing J at constant A^*. When $A^*=0$ a careful analysis of the product is needed, which shows that it will become zero (non-singular) provided that $U \neq 0$; there is flow. The analysis holds for the subsequent terms discussed below, they are also non-singular provided that $U \neq 0$. The centripetal acceleration scales with $((J^2+1)AR_s)^{-1}$, which increases for decreasing AR_s at constant J and increases for decreasing J at constant AR_s. The Coriolis acceleration scales with $(\sqrt{J^2+1}AR_s)^{-1}$, which also increases for decreasing AR_s at constant J and increases for decreasing J at constant AR_s. Similar to the dimensional analysis of wind turbines (Dumitrescu and Cardos, 2003) we find that the ratio of Coriolis over centripetal acceleration is $\sqrt{J^2+1}$, the same goes for Coriolis acceleration over angular acceleration. This suggests that angular and centripetal acceleration decay faster than Coriolis acceleration for increasing advance ratio.

Hovering flight

When insects fly slowly at advance ratios less than 0.1 they hover according to the definition of Ellington (Ellington, 1984). This notion is confirmed by calculating the scale factors in Eqn. 35. The effect of forward flight is scaled by the inverse of $\sqrt{J^2+1}$ for Coriolis and the square of that for centripetal and angular acceleration, which makes them even less sensitive to low J's. Evaluating $J=0$ and 0.1 yields two scale factors that differ only 0.5 %. For such low values of J we can simplify Eqn. 35 into:

$$\frac{D\boldsymbol{u}}{Dt}+\frac{1}{A^*}\cdot\dot{\boldsymbol{\Omega}}\times\boldsymbol{r}+\frac{1}{AR_s}\cdot\boldsymbol{\Omega}\times(\boldsymbol{\Omega}\times\boldsymbol{r})+\frac{1}{AR_s}\cdot 2\boldsymbol{\Omega}\times\boldsymbol{u}=-Eu\cdot\nabla p+\frac{1}{Re}\cdot\nabla^2\boldsymbol{u} \tag{40}$$

Perhaps this equation will remain a good approximation for even higher J values. Many insects seem to perform such flights during vertical take-off and landing and slow hovering flights (Ellington, 1984), which makes Eqn. 40 particularly useful.

From flapping to spinning and translating fly wings

The aerodynamics of flapping and spinning fly wings share important traits at zero advance ratio. Dickinson and co-workers (Dickinson *et al.*, 1999) showed that a 'quasi-steady' aerodynamic model of a flapping fruit fly wing can predict the majority of lift generated based on the lift that the same wing generates when it simply spins. Ellington and collaborators showed for hawkmoths that both flapping and spinning wings generate a stable leading edge vortex (Ellington *et al.*, 1996; Usherwood and Ellington, 2002). These findings suggest that the aerodynamics of flapping and spinning insect wings could be similar to the aerodynamics of propellers (Himmelskamp, 1947) and wind turbines (e.g. Dumitrescu and Cardos, 2003; Tangler, 2004). Hence we further simplify Eqn. 35 for an insect wing spinning at constant angular velocity ($\dot{\phi}=0$) at a constant geometric angle of attack ($\dot{\alpha}=\ddot{\alpha}=0$):

$$\frac{D\mathbf{u}}{Dt}+\frac{1}{J^2+1}\frac{1}{AR_s}\cdot\mathbf{\Omega}\times(\mathbf{\Omega}\times\mathbf{r})+\frac{1}{\sqrt{J^2+1}}\frac{1}{AR_s}\cdot 2\mathbf{\Omega}\times\mathbf{u}=-Eu\cdot\nabla p+\frac{1}{Re}\cdot\nabla^2\mathbf{u}. \tag{41}$$

Because angular velocity is now constant we need to rewrite the definition of advance ratio as:

$$J = U_\infty / 2\pi R f\,, \tag{42}$$

and the Reynolds number as:

$$Re = \sqrt{\left(\frac{U_\infty c}{\nu}\right)^2 + \left(\frac{2\pi R f c}{\nu}\right)^2} = \sqrt{Re_b^2 + Re_s^2} = \sqrt{J^2 + 1} \cdot Re_s. \tag{43}$$

The corresponding graphical interpretation of the dimensionless numbers is illustrated in Fig. 8. During one full period the wingtip has rotated over a dimensionless circular distance equal to $D^* = 2\pi R / c$ and has moved forward through the air over a linear distance of $s^* = U_\infty / cf$. Our derivation of Eqn. 41 for a spinning insect wing is similar to that for wind turbines (e.g. Dumitrescu and Cardos, 2003).

The single difference between propeller and turbine kinematics is that propellers operate at positive angles of attack generating forward pointing lift, which costs power, while turbines operate at negative angles of attack, which results in backward pointing lift and allows for harvesting power from wind (and water currents). The comparison of Eqn. 41 and 35 shows that the dimensionless numbers and accelerations involved in the aerodynamics of flappers, propellers and turbines are indeed similar, provided that unsteady effects measured by A^* do not dominate over 'quasi-steady' rotational effects measured by AR_s. By noting that $A^* = \Phi_0 AR_s$ (combining Eqn. 37 and 38) for a fly wing and that Φ_0 is typically close to one for insects (Ellington, 1984) we find that unsteady accelerations measured by $1/A^*$ and 'quasi-steady' accelerations measured by

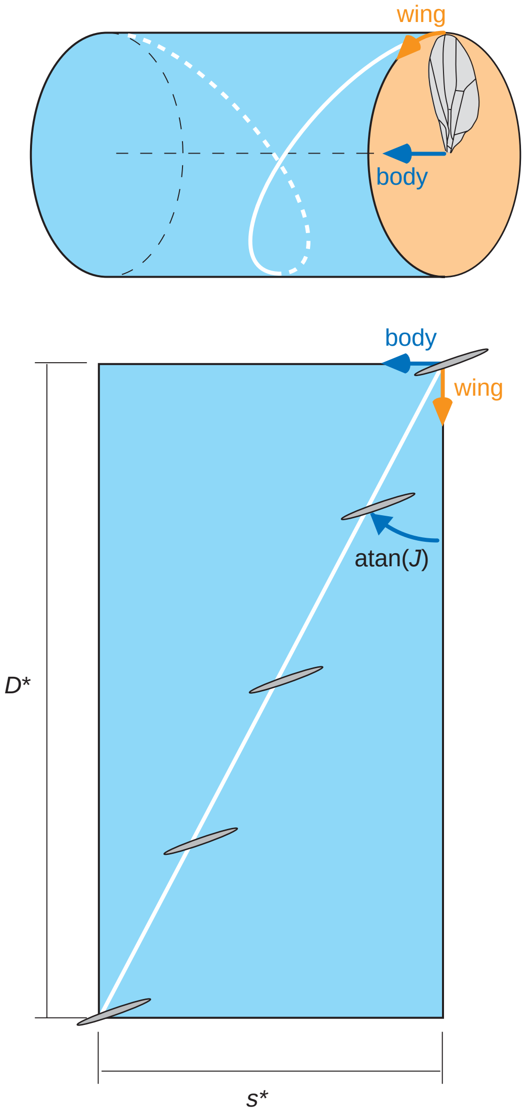

Fig. 8 | Propeller in forward flight. Graphical representation of the dimensionless numbers in the NS-equation that describe the wingtip kinematics; D^* and s^*. Note that the induced angle of attack is again $\arctan(1/J)$.

$1/AR_s$ are of the same magnitude. This might explain the physical analogy between flapping and spinning insect wings, and possibly, propellers and turbines that operate at much higher Reynolds numbers. Propellers that operate at zero advance ratio $J=0$ operate under hover conditions, such as hovering insects, which further simplifies Eqn. 41.

Although flies are not known to glide, dragonflies and many birds and bats do. When animals glide the transformed NS-equation that describes the aerodynamics of their translating wings has the same form as those for airplane wings (Fig. 2), which is obtained by setting $\mathbf{\Omega}=\mathbf{0}$ in Eqn. 41.

Two-dimensional pitch and heave wing kinematics

There are a large number of insect flight models in the literature that range from fully three-dimensional wing kinematics (e.g. Ellington *et al.*, 1996; Dickinson *et al.*, 1999) to two-dimensional pitch and heave kinematics (e.g. Dickinson , 1994, end-baffles were used to make the flow quasi-two-dimensional). A further simplification is to consider a wing cross-section; the airfoil (z-coordinate constant) (e.g. Wang 2000b; Lentink *et al.*, 2008). Although two-dimensional studies are more restrictive, they have provided valuable insight in insect wing performance. Here we focus on a three-dimensional wing that pitches sinusoidally with amplitude α_0 and heaves sinusoidally with amplitude A. Since the sinusoidal heave kinematics results in a linear acceleration of the wing, this linear acceleration term $\mathbf{a}_{\text{wing}}$ must be added to Eqn. 10. The (pitch and) heave kinematics is identical to the two-dimensional flattened stroke plane shown in Fig. 5 (lower panel). The wing stroke acceleration is derived similarly to Eqn. 27 and 29:

$$\ddot{s}_{\text{wing}} = -A(2\pi f)^2 \sin(2\pi f t), \tag{44}$$

in which s_{wing} is the stroke position of the wing in the stroke plane. The corresponding (absolute) time-averaged acceleration $\dot{U}_{\text{wing}}$ is calculated analogous to Eqns. 30 and 31 as:

$$\dot{U}_{\text{wing}} = 2\pi f \cdot 4Af. \tag{45}$$

The resulting scaled order of magnitude of the wing's heave acceleration $\mathbf{a}_{\text{wing}}$ is:

$$\frac{\dot{U}_{\text{wing}} c}{U^2} = \frac{1}{J^2+1} \cdot \frac{1}{A^*}, \tag{46}$$

This scale factor times the dimensionless wing acceleration $\mathbf{a}_{\text{wing}}$ is inserted in the dimensionless NS-equation Eqn. 22 of the pitching and heaving foil. Further the relevant radius now becomes the pitch radius, which scales with c instead of R (Appendix I):

$$\begin{gathered}\frac{D\mathbf{u}}{Dt} + \frac{1}{J^2+1} \cdot \frac{1}{A^*} \cdot \mathbf{a}_{\text{wing}} + \frac{1}{J^2+1} \frac{\alpha_0}{A^{*2}} \cdot \dot{\mathbf{\Omega}} \times \mathbf{r} + \frac{1}{J^2+1} \frac{\alpha_0^2}{A^{*2}} \cdot \mathbf{\Omega} \times (\mathbf{\Omega} \times \mathbf{r}) + \\ \frac{1}{\sqrt{J^2+1}} \frac{\alpha_0}{A^*} \cdot 2\mathbf{\Omega} \times \mathbf{u} = -Eu \cdot \nabla p + \frac{1}{Re} \cdot \nabla^2 \mathbf{u}.\end{gathered} \tag{47}$$

With the following expressions for advance ratio, which is similar to Eqn. 36:

$$J = U_{\infty}/4Af = \lambda^{*}/4A^{*}. \tag{48}$$

Note that the acceleration terms in Eqn. 47 are much simplified compared to three-dimensional kinematics, because many vector components are zero:

$$\mathbf{a}_{\mathrm{wing}} = \begin{bmatrix} \ddot{x}_{\mathrm{wing}} \\ \ddot{y}_{\mathrm{wing}} \\ 0 \end{bmatrix},\ \dot{\mathbf{\Omega}} = \begin{bmatrix} 0 \\ 0 \\ \ddot{\alpha} \end{bmatrix},\ \mathbf{\Omega} = \begin{bmatrix} 0 \\ 0 \\ \dot{\alpha} \end{bmatrix},\ \mathbf{r} = \begin{bmatrix} x \\ y \\ \mathrm{z} \end{bmatrix} \tag{49-52}$$

From inspecting Eqn. 47 we conclude that the angle of attack rotation induces rotational accelerations in the plane of the airfoil, which are proportional to the geometric angle of attack amplitude. These rotational acceleration components are also present in Eqn. 35, but are dominated by those due to the wing's stroke (its propeller-like swing). The rotational accelerations due to stroke (can) have a component normal to the z-plane which confines the wing's airfoil. The relative magnitude of the accelerations for $A^{*} = 0$ can again be inferred correctly by either reformulating the scale term as a whole or calculating the limit value, because J also depends on A^{*} (Eqn. 48). The expression for the Reynolds number is similar to Eqn. 39; it can be obtained by inserting $A = \Phi_0 R$.

Simple vibrating fly wings

Some insect wing models are even simpler and just consist of a heaving (vibrating) foil at constant geometric angle of attack ($\alpha_0 = const$) (e.g. Wang, 2000b; Lentink and Gerritsma, 2003):

$$\frac{D\mathbf{u}}{Dt} + \frac{1}{\sqrt{J^2+1}}\frac{1}{A^{*}}\cdot\mathbf{a}_{\mathrm{wing}} = -Eu\cdot\nabla p + \frac{1}{Re}\cdot\nabla^2\mathbf{u}. \tag{53}$$

Using Eqn. 48 we can simplify $\sqrt{J^2+1}A^{*}$ into:

$$1/4\sqrt{\lambda^{*2}+4^2A^{*2}}, \tag{54}$$

which relates to the synchronization bands Williamson and Roshko (Williamson and Roshko, 1988) found in experiments with a vibrating cylinder in the parameter space spanned by dimensionless wavelength (X-axis) and amplitude (Y-axis). In this elliptically-shaped synchronization band the vortex wake synchronizes with the vibrating cylinder. This occurs when the cylinder effectively vibrates at a multiple of the natural von Kármán vortex shedding wavelength λ_0^{*} of the cylinder at rest $n\lambda_0^{*} = \sqrt{\lambda^{*2}+4^2A^{*2}}$ for $\mathrm{n} = 1$ and 3 (Lentink, 2003; Ponta and Aref, 2005). The present derivation shows that this relation can be linked to the scale factor that represents the linear acceleration of the vibrating cylinder in the NS-equation (Eqn. 53). Whether or not vortex wake synchronization bands also occur for flapping wings is unclear (Lentink *et al.*, 2008).

Discussion

We derived a dimensionless form of Navier Stokes (NS) equations for a three-dimensional flapping fly wing to identify the dimensionless numbers that scale the underling physical mechanisms. This derivation showed that flapping wings induce three rotational accelerations: angular, centripetal and Coriolis in the air near to the wing's surface, which diffuse into the boundary layer of the wing. Next we simplified these equations incrementally using increasingly more restrictive assumptions. These simplifications allow us to easily interpret the dimensionless numbers geometrically for conditions that approximate both forward flight and hovering. In subsequent steps we derived the NS-equation for spinning and translating three-dimensional fly wings and for flapping and vibrating two-dimensional airfoils

Dimensionless template for parametric flapping wing studies

The dimensionless numbers that scale the NS-equation facilitate the design of the parametric space in which one can systematically investigate the fluid dynamics of flapping wings. These numbers are of additional importance to other kinematic parameters of the wing such as angle of attack amplitude α_0 and the angle between the normal vector of the average stroke plane and the direction of flight γ. When the most general conditions NS-Eqn. 22 hold, we find the following relevant scale factors:

$\frac{\dot{\Omega}Rc}{U^2} = \frac{1}{C_{\text{ang}}}$, in which C_{ang} is the angular acceleration number. (55)

$\frac{\Omega^2 Rc}{U^2} = \frac{1}{C_{\text{cen}}}$, in which C_{cen} is the centripetal acceleration number. (56)

$\frac{\Omega c}{U} = \frac{1}{Ro}$, Ro in which is the Rossby number. (57)

$\frac{\mu}{\rho Uc} = \frac{1}{Re}$, in which Re is the Reynolds number. (58)

Using this notation we are able to accommodate elegantly the definition of both Reynolds (Reynolds, 1883) and Rossby numbers (Rossby, 1936) that already exist in the biological and rotational fluid dynamics field. Three of these terms are relatively new in the biological fluid mechanic fields: (1) the angular acceleration number measures the unsteadiness of the flow induced by the rotational acceleration of the wing; (2) the centripetal acceleration number measures the centripetal acceleration due to the wings rotation, and (3) the Rossby number measures the Coriolis acceleration induced by the relative motion of fluid with respect to the rotating wing. All these rotational accelerations diminish for large values of the dimensionless numbers that represent them. Although these numbers can be readily calculated they do not give clear insight into how they represent wing kinematics and morphology, which can be critical for the design of a careful parametric study of flapping wing aerodynamics.

We developed a geometric frame work to provide insight into the dimensionless numbers that describe the aerodynamics of the flapping wings of a fly, flying at constant velocity. Within this framework we assumed sinusoidal stroke and angle of attack kinematics and zero wing deviation. Comparing Eqn. 22 and Eqn. 35 we find the following geometric interpretation for the dimensionless numbers C_{ang}, C_{cen} and Ro:

$$C_{\text{ang}} = (J^2 + 1)A^*, \tag{59}$$

$$C_{\text{cen}} = (J^2 + 1)AR_{\text{s}}, \tag{60}$$

$$Ro = \sqrt{J^2 + 1} \cdot AR_{\text{s}}. \tag{61}$$

Whereas J and A^* are measures of the wings kinematics, AR_{s} is a measure of single wing morphology. Again we note that the effect of large values of these dimensionless numbers is that it diminishes the corresponding accelerations. The effect of forward flight $J > 0$ is, therefore, that it reduces the rotational accelerations. The rotational accelerations increase for smaller stroke amplitudes and single wing aspect ratios at constant advance ratio. The extreme case is hovering flight ($J = 0$) for which the rotational accelerations are maximal. For hovering flight we also note that C_{cen} (Eqn. 60) becomes identical to the Rossby number Ro, because both are equal to a single wing spect ratio AR_{s}. Using the dimensionless scale variables J, A^* and AR_{s} we can now systematically vary the influence of rotational accelerations in parametric studies of the aerodynamics of fly wings (in forward and hovering flight). Perhaps more importantly, the graphical approach presented in Figs. 5, 7 and 8 facilitates an intuitive design of numerical and experimental studies of flapping (fly) wings with a direct link to the NS-equations.

Comparing three- and two-dimensional wing kinematics

How important are rotational accelerations for understanding the aerodynamics of a fly? Here we present an alternative approach to compare two- and three-dimensional stroke kinematics, which proved to be pivotal for designing our experiment to test how important rotational accelerations (due to stroke) are for the stability of a fly's leading edge vortex (Lentink and Dickinson, 2008). This vortex allows the fly to generate exceptionally high lift with its wing at angles of attack at which helicopter blades and airplane wings stall. There exists, however, an intriguing parallel between the lift augmentation due to the presence of a stable LEV on a fly wing and the lift augmentation found near the hub of wind turbine blades. Such blades are said to undergo 'three-dimensional stall' or 'stall-delay' near their hub, which increases lift, whereas they undergo 'two-dimensional stall' near the blade tip, which decreases lift (e.g. Tangler, 2004), Fig. 9A. For wind turbines three-dimensional stall is not observed beyond 'local aspect ratios' of three ($r/c > 3$, in which r is the local radius, see Fig. 9A, (e.g. Tangler, 2004)). Three is approximately the value of a fruit fly's aspect ratio, Fig. 9, which might explain why flapping and spinning fly wings do not seem to stall and generate extraordinary high lift like wind turbines and propellers (Himmelskamp, 1947) do near their hub. To gain insight into the possible effect of rotational accelerations we gradually transform rotational stroke kinematics into translational stroke kinematics, Fig. 9B. We do this by letting $\Phi_0 \rightarrow 0$ and $R_{\text{g}} \rightarrow \infty$ such that the wing amplitude $\Phi_0 R_{\text{g}} = A$ remains constant in the limit (at the radius of gyration R_{g}). In doing so we do not change the wing's geometry, we simply place the same wing further outward as shown in Fig. 9. Because the wing's radial distance from the center of rotation R goes to infinity ($R \rightarrow \infty$), the single wing aspect ratio based on this radial distance $AR_{\text{s}} = R/c$ also goes to infinity. The NS-equations of a flap-

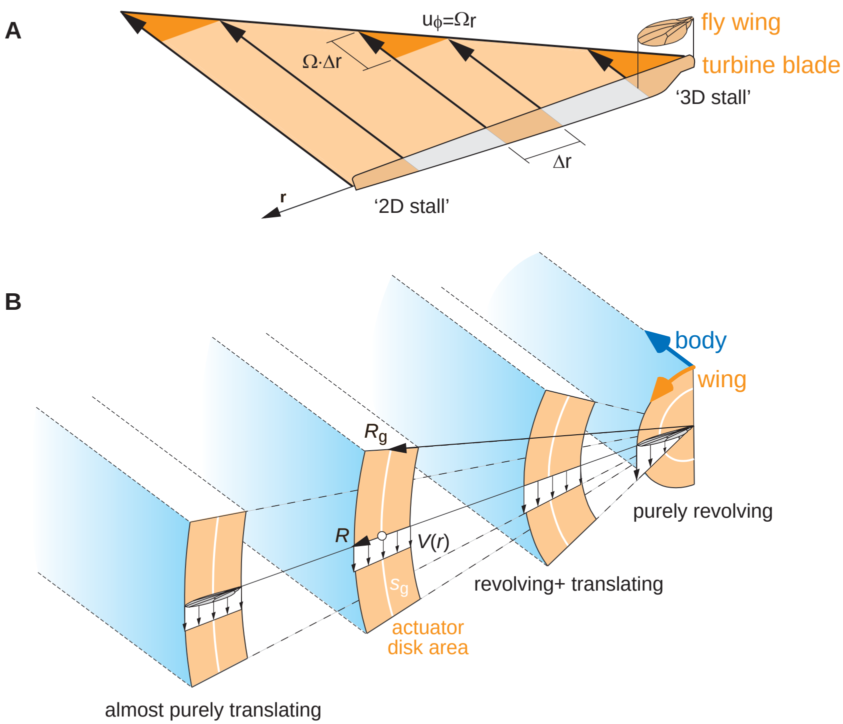

Fig. 9 | Is there an analogy between the influence of rotational accelerations on the stall characteristics of wind turbines and flapping fly wings? (A) Slender wings, such as wind turbine blades, have been found to possess distinctly different stall mechanisms near the root, for $r/c<3$ where they stall locally 'three-dimensional', and near the tip, where they stall locally 'two-dimensional'. Fly wings are much less slender than wind turbine blades, therefore their whole wing is 'submerged' in the region of 'three-dimensional stall'. Clearly the circular path (in the stroke plane) of outward wing sections become progressively less curved compared to chord length. We illustrated how the local 'rotational component' of the radial speed component $\Omega{\cdot}\Delta r$ becomes less and less important towards the tip compared to the 'linear component' of radial speed $\Omega{\cdot}r$. By taking $\Delta r = \mathrm{c}$ we find that the ratio of 'linear component' over 'rotational component' of radial speed is exactly r/c.
(B) Based on the observations in (A) we designed flapping wing kinematics that allow us to change the relative importance of rotational accelerations R/c for a fly wing, which has a constant geometric slenderness. We achieved such a gradual transition from a linear velocity distribution to a constant velocity over the wing by gradually sticking the fly wing more outward on an extension rod between the wing and its joint. In this we keep the stroke amplitude 'actuator disk' areas swept by the wing in the stroke plane constant (orange) while it travels forward (blue). It can be demonstrated that a constant actuator disk area corresponds with a nearly constant stroke amplitude along the path s_g at the radius of gyration R_g. The relative curvature of the wing sections path with respect to its chord length is again measured by R/c the single wing aspect ratio. Graphically we can directly infer that the paths traveled at more outward radii are much less curved and therefore the corresponding three-dimensional rotational accelerations will diminish.

ping (Eqn. 35) and spinning wing (Eqn. 41) show that the centripetal and Coriolis acceleration go down with aspect ratio. We have performed exactly this experiment to show that rotational accelerations mediate LEV stability in hovering insect flight (Lentink and Dickinson, 2008).

Rotational accelerations due to wing stroke versus angle of attack kinematics

The angular velocity of flapping wings consists of two significant components (1) angular velocity due to the wing's stroke and (2) angular velocity due to geometric angle of attack variation. Angular velocity due to wing stroke is approx. maximal mid-stroke, while angular velocity due to wing angle of attack variation is approx. maximal at stroke reversal. The resulting velocity magnitudes are proportional to $\Phi_0 Rf$ for stroke and $\alpha_0 cf$ for angle of attack. The ratio of both velocities is $\Phi_0 R / \alpha_0 c \approx R / c$ because $\Phi_0 \approx \alpha_0$ for most insects. For aspect ratios significantly larger than one we can assume, therefore, that rotational accelerations due to stroke dominate those due to angle of attack variation. In experimental tests, one can test if this holds by doing the experiments with and without *rotational* stroke kinematics (reciprocating revolving vs. reciprocating translating wings) for all relevant angle of attack amplitudes, which lie in the range $0° \leq \alpha_0 \leq 90°$ (Lentink and Dickinson, 2008).

Scaling the NS-equation more accurately

In some fly wing experiments more accurate dimensionless numbers are needed. For example in a careful comparison of aerodynamic forces that result from different, but related, wing kinematics. In such cases one needs to calculate the velocity and length scales more accurately by using a blade element method. For such detailed lift and drag studies, the wings radius of gyration should be chosen as the radial length scale and the accompanying velocity at the radius of gyration should be chosen as velocity scale in the NS-equation. Calculating the radius of gyration is straightforward for hovering insects (Weis-Fogh, 1973; Ellington, 1984):

$$R_g = \sqrt{\frac{1}{S}\int_0^R r^2 c(r)\, dr}, \tag{62}$$

in which R_g is the radius of gyration and S single wing area. For forward flight conditions this computation gets increasingly more complicated, e.g. see Dickson and Dickinson (Dickson and Dickinson, 2004). In practice it is therefore more convenient to consider the wing radius instead of the radius of gyration, because they can be derived much easier from lab and field data. The values of wing radius and wing speed (due to stroke) at the radius of gyration are roughly half the value calculated at the wingtip, because $R_g / R \approx 0.5$ (Ellington, 1984). This estimate helps evaluating if more precise values would change the conclusions using 'back of the envelop calculations'. Finally we note that we approximated $\pi / 2 \approx 1$ in Appendix I, this ratio could be approximated more accurately by $\pi / 2 \approx 1.5$ if needed.

Relation between existing and present dimensionless numbers

Some of the dimensionless numbers that we derived here can be related to existing dimensionless numbers. The advance ratio J is already in use (Ellington, 1984). It is equivalent to the inverse of the amplitude based Strouhal number as discussed in the Introduction. We prefer the advance ratio because it is readily interpretable geometrically and commonly used as such in aeronautics and biological fluid dynamics. Further, the Strouhal number is perhaps best reserved for its original purpose – characterizing natural shedding frequencies. The dimensionless amplitude A^* is a normal dimensionless variable, $2A^*$ represents the total dimensionless amplitude Λ introduced by Ellington (1984), we prefer A^*, because it represents the mathematical definition of amplitude. We further prefer the dimensionless wave length λ^* over the inverse, the reduced frequency k, because λ^* is a length scale ratio that can easily be drawn and interpreted graphically, e.g. Fig. 5, while the time scale ratio k cannot. The importance of the dimensionless single wing aspect ratio for calculating rotational accelerations is new in the field of insect flight. The corresponding Rossby number is, however, commonly used in the analyses of rotating fluids (Rossby, 1936; Vanyo, 1993; Greitzer, 2004; Tritton, 2005). The inverse of the single wing aspect ratio, c/r, is in use in the wind turbine literature (e.g. Lindenburg, 2004), but we prefer r/c because it corresponds to single wing aspect ratio which is easier to interpret geometrically for animal flight, and because r/c corresponds with the definition of Rossby number, which is in use in the much more elaborate literature on rotational flows (compared to wind turbines). Finally there is the Reynolds number. Our definition has the advantage that it works continuously from hovering flight to fast forward flight Eqn. 39 (Lentink and Gerritsma, 2003).

Application of dimensionless numbers in wing and fin studies

Our derivation of the dimensionless NS-equation for flapping, revolving and translating fly wings and airfoils represent the various three- and two-dimensional insect flight models in literature; from three-dimensional flapping wings to two-dimensional vibrating wings. By comparing Eqn. 35 for a three-dimensional flapping wing and Eqn. 47 for a two-dimensional flapping wing we conclude that the significant rotational accelerations due to the flapping motion in three-dimensional fly aerodynamics are neglected in two-dimensional models. The possible importance of such differences is amplified by the experimental observation that three-dimensional fly wings that either spin (e.g. Usherwood and Ellington, 2002) or flap (e.g. Birch, *et al.*, 2004; Ellington *et. al.*, 1996) around their base generate a stable leading edge vortex, while flapping two-dimensional airfoils (e.g. Dickinson, 1994; Lentink *et al.*, 2008) do not. We further note that two-dimensional vibrating insect wing models neglect all rotational accelerations (e.g. Wang, 2000b; Lentink and Gerritsma, 2003). The above insect flight models therefore increasingly incorporate the rotational accelerations induced in the flow due to the rotational kinematics of the wing's kinematics.

Two and three-dimensional models similar to those of insect flight have also been used to study the aerodynamics of birds (Hubel, 2006) and the hydrodynamics of the fins of fish (Triantafyllou *et al.*,1993; Bandyopadhyay *et al.*, 2008). The dimensionless NS-equation we derived for a flapping fly wing also represent such models, provided that care is taken that the assumptions used to derive the various equations hold. For completeness we repeat three non-trivial assumptions: (1) the fluid behaves fully Newtonian like water and air, (2) the fluid does not cavitate, and (3) the amplitudes of undulations in the body are small compared to stroke amplitude. The flow can, however, be turbulent.

Finally we note that even the abstract problem of spinning fly wings, Eqn. 41, is of direct relevance for biological fluid dynamics studies, because autorotating seeds spin with exactly such kinematics as they swirl down to earth. While doing so, autorotating seeds extract energy from the flow very much like wind turbines harvest energy from wind at much higher Reynolds numbers. This intriguing example illustrates that our theoretical approach has the potential to provide a valuable link between the fluid dynamics of translating, rotating and flapping wings & fins in nature and technology.

Acknowledgements

We gratefully acknowledge Will Dickson, Koert Lindenburg, John Dabiri for proof reading preliminary versions of the ms. We thank Johan van Leeuwen and GertJan van Heijst for heartily support, encouragement and proof reading of the various versions of the manuscript. This research is supported by NWO-ALW grant 817.02.012 to D. L. and by NSF grant IBN-0217229 to M.H.D.

Symbols

α	wing angle of attack
$\dot{\alpha}$	1st time derivative of wing angle of attack
$\ddot{\alpha}$	2nd time derivative of wing angle of attack
α_0	wing angle of attack amplitude
α_{eff}	effective angle of attack
α_{ind}	induced angle of attack
α_{geo}	geometric angle of attack
β	stroke plane angle
γ	angle between the stroke plane and direction of flight
Δr	width spanwise wing section
ϕ	wing stroke angle
$\dot{\phi}$	1st time derivative of wing stroke angle
$\ddot{\phi}$	2nd time derivative of wing stroke angle
Φ	total wing amplitude in radians
Φ_0	wing stroke amplitude (half the total stroke amplitude Φ)
φ	wing deviation with respect to stroke plane
λ	wingbeat wave length
λ^*	dimensionless wavelength
λ_0^*	natural von Kármán vortex shedding wavelength
μ	dynamic viscosity
ν	kinematic viscosity
ρ	fluid density
ξ	flight path angle with respect to horizon
Ω	absolute time-averaged angular velocity amplitude
$\dot{\Omega}$	absolute time-averaged angular acceleration amplitude
$\boldsymbol{\Omega}$	angular velocity of the rotating frame
$\dot{\boldsymbol{\Omega}}$	angular acceleration of the rotating frame
$\boldsymbol{\Omega}_{\mathrm{wing}}$	angular velocity of the fly wing

$\boldsymbol{\nabla}$	gradient (del) operator $[\partial/\partial x, \partial/\partial y, \partial/\partial z]^{\mathrm{T}}$
‘*’	dimensionless variable scaled with its order of magnitude

$\mathbf{a}_{\mathrm{ang}}$	angular acceleration
$\mathbf{a}_{\mathrm{cen}}$	centripetal acceleration
$\mathbf{a}_{\mathrm{Cor}}$	Coriolis acceleration
$\mathbf{a}_{\mathrm{inert}}$	acceleration with respect to inertial coordinate system
$\mathbf{a}_{\mathrm{loc}}$	acceleration with respect to local coordinate system

$\mathbf{a}_{\mathrm{wing}}$	linear acceleration of an airfoil
A	flap amplitude
A^*	stroke amplitude
AR_{s}	single wing aspect ratio
b_{s}	single wing span
c	average wing (or foil) chord length
C_{ang}	angular acceleration number
C_{cen}	centripetal acceleration number
D^*	dimensionless circular distance moved during one full period (propeller)
$\frac{D}{Dt}$	total differentia operator: $\frac{D}{Dt}=\frac{\partial}{\partial t}+\mathbf{u}\bullet\nabla$
Eu	Euler number
f	flap frequency
$\mathbf{g}$	gravity
J	advance ratio
k	reduced frequency
l	characteristic length
n	multiple (of λ_0^*)
p	pressure
p_0	ambient atmospheric pressure
r	magnitude of radius vector
$\mathbf{r}$	position of a fluid particle in the rotating frame
R	wing radius
R_{g}	wing radius of gyration
Re	Reynolds number
Re_{b}	Reynolds number component due to body speed
Re_{s}	Reynolds number component due to wings stroke,
Ro	Rossby number
s^*	dimensionless linear distance moved through air during one full period (propeller)
$\ddot{s}_{\mathrm{wing}}$	magnitude linear acceleration of the wing
S	single wing area
S_{fb}	outer surface of fly
S_{ob}	Outer boundary surface
St	Strouhal number
t	time
$\mathbf{u}$	velocity vector
$\mathbf{u}_{\mathrm{body}}$	velocity center of gravity of fly
$\mathbf{u}_{\mathrm{fly}}$	velocity of fly at its outer surface
$\mathbf{u}_{\mathrm{loc}}$	velocity in local coordinate system
u_{n}	component of wingtip speed normal to flight direction
u_{t}	component of wingtip speed in flight direction
$\mathbf{u}_{\alpha}$	linear velocity distribution due to angle of attack variation
$\mathbf{u}_{\phi}$	linear velocity distribution due to stroke
$\mathbf{u}_{\varphi}$	linear velocity distribution due to deviation
U	characteristic speed; absolute time-averaged speed of the wingtip
$\dot{U}_{\mathrm{wing}}$	absolute time-averaged linear acceleration of the wing

U_∞	forward flight speed (arbitrary direction with respect to gravity)
x	position vector
$\ddot{x}_\text{wing}$	x-component of $\mathbf{a}_\text{wing}$
(x, y, z)	local coordinate system
(X,Y,Z)	inertial coordinate system
$\ddot{y}_\text{wing}$	y-component of $\mathbf{a}_\text{wing}$

Appendix I: Derivation of dimensionless numbers

Three-dimensional kinematics

The dimensionless numbers in Eqn. 35 are derived by inserting the following expressions in Eqn. 22 (as explained in the main text); $U \approx \sqrt{U_\infty^2 + (4\Phi_0 Rf)^2}$, $\Omega = 4\Phi_0 f$, and $\dot{\Omega} = 2\pi f \Omega$, which results in:

$$\frac{\dot{\Omega} Rc}{U^2} = \frac{2\pi f \cdot 4\Phi_0 f \cdot Rc}{U_\infty^2 + (4\Phi_0 Rf)^2} \cdot \frac{4\Phi_0 R}{4\Phi_0 R} = \frac{1}{(U_\infty / 4\Phi_0 Rf)^2 + 1} \cdot \frac{2\pi c}{4\Phi_0 R} \approx \frac{1}{J^2+1} \cdot \frac{c}{\Phi_0 R} = \frac{1}{J^2+1} \cdot \frac{1}{A^*}, \qquad \text{(I,1)}$$

we took $\pi/2 \approx 1$ instead of the more accurate $\pi/2 \approx 1.5$, because it suffices for an order of magnitude analysis.

$$\frac{\Omega^2 Rc}{U^2} = \frac{(4\Phi_0 f)^2 \cdot Rc}{U_\infty^2 + (4\Phi_0 Rf)^2} \cdot \frac{R}{R} = \frac{1}{(U_\infty / 4\Phi_0 Rf)^2 + 1} \cdot \frac{c}{R} = \frac{1}{J^2+1} \cdot \frac{c}{R} = \frac{1}{J^2+1} \cdot \frac{1}{AR_\text{s}}, \qquad \text{(I,2)}$$

$$\frac{\Omega c}{U} = \frac{4\Phi_0 f \cdot c}{\sqrt{U_\infty^2 + (4\Phi_0 Rf)^2}} \cdot \frac{R}{R} = \frac{1}{\sqrt{(U_\infty / 4\Phi_0 Rf)^2 + 1}} \cdot \frac{c}{R} = \frac{1}{\sqrt{J^2+1}} \cdot \frac{c}{R} = \frac{1}{\sqrt{J^2+1}} \cdot \frac{1}{AR_\text{s}}, \qquad \text{(I,3)}$$

$$\frac{\mu}{\rho U c} = \frac{\nu}{Uc} = \frac{\nu}{\sqrt{U_\infty^2 + (4\Phi_0 Rf)^2}\, c} = \frac{1}{\sqrt{\left(\frac{U_\infty c}{\nu}\right)^2 + \left(\frac{4\Phi_0 Rfc}{\nu}\right)^2}} = \frac{1}{\sqrt{Re_\text{b}^2 + Re_\text{s}^2}} \qquad \text{(I,4)}$$

Two-dimensional kinematics

The dimensionless numbers is Eqn.47 are derived by inserting the following expressions in Eqn. 22 to which $\mathbf{a}_\text{wing}$ is added (as explained in the main text); $U \approx \sqrt{U_\infty^2 + (4Af)^2}$, $\dot{U}_\text{wing} = 2\pi f \cdot 4Af$, $\Omega = 4\alpha_0 f$ and $\dot{\Omega} = 2\pi f \Omega$, which results in:

$$\frac{\dot{U}_{wing} c}{U^2} = \frac{A 2\pi 4 f^2 c}{U^2} = \frac{A 2\pi 4 f^2 c}{U_\infty^2 + (4Af)^2} = \frac{1}{J^2+1} \cdot \frac{A 2\pi 4 c}{(4A)^2} \approx \frac{1}{J^2+1} \cdot \frac{1}{A^*}, \qquad \text{(I,5)}$$

$$\frac{\dot{\Omega} c^2}{U^2} = \frac{2\pi f \cdot 4\alpha_0 f \cdot c^2}{U_\infty^2 + (4Af)^2} = \frac{1}{(U_\infty / 4Af)^2 + 1} \cdot \frac{2\pi \cdot 4\alpha_0 \cdot c^2}{(4A)^2} \approx \frac{1}{J^2+1} \cdot \frac{\alpha_0 \cdot c^2}{A^2} = \frac{1}{J^2+1} \cdot \frac{\alpha_0}{A^{*2}}, \qquad \text{(I,6)}$$

again we took $\pi/2 \approx 1$ instead of the more accurate $\pi/2 \approx 1.5$, because it suffices for an order of magnitude analysis.

$$\frac{\Omega^2 c^2}{U^2} = \frac{(4\alpha_0 f)^2 \cdot c^2}{U_\infty^2 + (4Af)^2} = \frac{1}{J^2+1}\cdot\frac{\alpha_0^2 \cdot c^2}{(A)^2} = \frac{1}{J^2+1}\cdot\frac{\alpha_0^2}{A^{*2}}, \tag{I,7}$$

$$\frac{\Omega c}{U} = \frac{4\alpha_0 f \cdot c}{\sqrt{U_\infty^2 + (4Af)^2}} = \frac{1}{\sqrt{J^2+1}}\cdot\frac{\alpha_0 \cdot c}{A} = \frac{1}{\sqrt{J^2+1}}\cdot\frac{\alpha_0}{A^{*}}, \tag{I,8}$$

$$\frac{\mu}{\rho U c} = \frac{\nu}{Uc} = \frac{\nu}{\sqrt{U_\infty^2 + (4Af)^2}\,c} = \frac{1}{\sqrt{\left(\frac{U_\infty c}{\nu}\right)^2 + \left(\frac{4Afc}{\nu}\right)^2}} = \frac{1}{\sqrt{Re_\mathrm{b}^2 + Re_\mathrm{s}^2}}. \tag{I,9}$$

References

Anderson, J. D. (1991). *Fundamentals of aerodynamics.* McGraw-Hill.

Bandyopadhyay, P. R., Beal, D. N. and Menozzi, A. (2008). Biorobotic insights into how animals swim. *J. Exp. Biol.* **211**, 206-214.

Baruh, H. (1999). *Analytical dynamics*. McGraw-Hill.

Daniel, T. L. and Webb, P. W. (1987). *Comparative Physiology: Life in Water and on Land.* ed. Dejours, P., Bolis, L., Taylor, C. R. and Weibel, E. R. Fidia Research Series, IX-Liviana Press, Padova.

Dickinson, M. H. (1994). The effects of wing rotation on unsteady aerodynamic performance at low Reynolds numbers. *J. Exp. Biol.* **192**, 179-206.

Dickinson, M. H., Lehmann, F. O. and Sane, S. P. (1999). Wing rotation and the aerodynamic basis of insect flight. *Science* **284**, 1954-1960.

Dickson, W. B. and Dickinson, M. H. (2004). The effect of advance ratio on the aerodynamics of revolving wings. *J. Exp. Biol.* **207**, 4269-4281.

Du, Z. and Selig, M. S. (1998). Effect of rotation on the boundary layer of a wind turbine blade. *American Wind Energy Association*, Windpower conference, Bakersfield CA.

Dumitrescu, H. and Cardos, V. (2003). Rotational effects on the boundary-layer flow in wind turbines. *AIAA Journal* **42**, 408-411.

Ellington, C. P. (1984). The aerodynamics of insect flight I-VI. *Phil. Trans. R. Soc. Lond. B* **305,** 1-181.

Ellington, C. P., Van den Berg, C., Willmott, A. P. and Thomas, A. L. R. (1996). Leading-edge vortices in insect flight. *Nature* **384**, 626-630.

Fry, S. N., Sayaman, R. and Dickinson, M. H. (2003). The aerodynamics of free-flight maneuvers in *Drosophila. Science* **300,** 495-498.

Green, S. I. (1995). *Vortex dynamics in the wake of a cylinder*. Kluwer Academic Publishers.

Greitzer, E. M. Tan C. S. and Graf M.B. (2004). Internal flow concepts and applications. Cambridge University Press.

Guyon, E., Hulin, J. P., Petit, L. and Mitescu C.D. (2001). *Physical hydrodynamics.* Oxford University Press.

Himmelskamp, H. (1947). Profile investigations on a rotating airscrew. Dissertation Göttingen 1945, Reports and Translations No. 832.

Hubel, T. (2006) Untersuchungen zur instationären Aerodynamik an einem vogelähnlichen Flügelschlagmodell, *PhD thesis, TU Darmstadt, Fachbereich Biologie*.

Lentink, D. and Gerritsma, M. I. (2003). Influence of airfoil shape on performance in insect flight. *AIAA* 2003–3447.

Lentink, D. (2003). Influence of airfoil shape on performance in insect flight. MSc.Thesis, *Delft University of Technology* (fac. AE).

Lentink, D., Muijres, F.T., Donker-Duyvis, F. J. and van Leeuwen, J. L. (2008). Vortex-wake interactions of a flapping foil that models animal swimming and flight. *J. Exp. Biol.* **211**: 267-273.

Lentink, D. and Dickinson, M. H. (2008) Rotational accelerations stabilize leading edge vortices on revolving fly wings, *J. Exp. Biol.*, submitted.

Lindenburg, C. (2004). Modelling of rotational augmentation based on engineering considerations and measurements. *European wind energy conference*, London.

Liu, H. and Kawachi, K. (1998). A numerical study of insect flight. *J. Comput. Phys.* **146**, 124 -156.

Maxworthy, T. (1979). Experiments on the Weis-Fogh mechanism of lift generation by insects in hovering flight. Part 1. Dynamics of the 'fling'. *J. Fluid Mech.* **93**, 47-63.

Ponta, F. L. and Aref, H. (2005). Vortex synchronization regions in shedding from an oscillating cylinder. *Phys. of Fluids* **17**, 011703.

Reynolds, O. (1883). An experimental investigation of the circumstances which determine whether the motion of water shall be direct or sinuous, and of the law of resistance in parallel channels. *Philos. Trans. R. Soc. Lond.* **174**, 935-982.

Rossby, C. G. (1936). On the momentum transfer at the sea surface. Part I Papers *Phys. Oceanogr. Meteorol.* 3 no 3.

Sane, S. P. and Dickinson, M. H. (2001). The control of flight force by a flapping wing: lift and drag production. *J. Exp. Biol.* **204**, 2607-2626.

Schlichting, H. (1979) *Boundary-layer theory*. McGraw-Hill, 7th edition.

Sun, M. and Tang, J. (2002). Lift and power requirements of hovering flight in *Drosophila virilis. J. Exp. Biol.* **205**, 2413-2427.

Tangler, J. L. (2004). Insight into wind turbine stall and post-stall aerodynamics. *Wind Energy* **7**, 247-260.

Taylor, G. K., Nudds, R. L. and Thomas, A. L. R. (2003). Flying and swimming animals cruise at a Strouhal number tuned for high power efficiency. *Nature* **425**, 707-711.

Tennekes, H. and Lumley, J. L. (1983). *A first course in turbulence*. MIT Press.

Tobalske, B. W., Warrick, D. R., Clark, C. J., Powers, D. R., Hedrick, T. L., Hyder, G. A. and Biewener A. A. (2007). Three-dimensional kinematics of hummingbird flight. *J. Exp. Biol.* **210**, 2368–2382.

Triantafyllou, G. S., Triantafyllou, M. S. and Grosenbaugh, M. A. (1993). Optimal thrust development in oscillating foils with application to fish propulsion. *J. Fluids and Structures* 7, 205-224.

Tritton, D. J. (2005). *Physical fluid dynamics.* Oxford University Press.

Usherwood J. R. and Ellington C. P. (2002). The aerodynamics of revolving wings I-II. *J. Exp. Biol.* **205**, 1547-1576.

Vanyo, J. P. (1993). *Rotating fluids in engineering and science.* Dover.

Vogel, S. (1994). *Life in Moving Fluids*. Princeton University Press.

Wang, Z. J. (2000a). Two-dimensional mechanism for insect hovering. *Phys. Rev. Lett.* **85**, 2216-2218.

Wang, Z. J. (2000b). Shedding and frequency selection in flapping flight. *J. Fluid. Mech.* **410**, 323-341.

White, F. M. (1991). *Viscous fluid flow*. McGraw-Hill.
Weis-Fogh, T. (1973). Quick Estimates of Flight Fitness in Hovering Animals, Including Novel Mechanisms for Lift Production. *J. Exp. Biol.* **59**, 169-230.
Williamson, C. H. K. and Roshko, A. (1988). Vortex formation in the wake of an oscillating cylinder. *J. Fluid Struc.* **2**, 355-381.

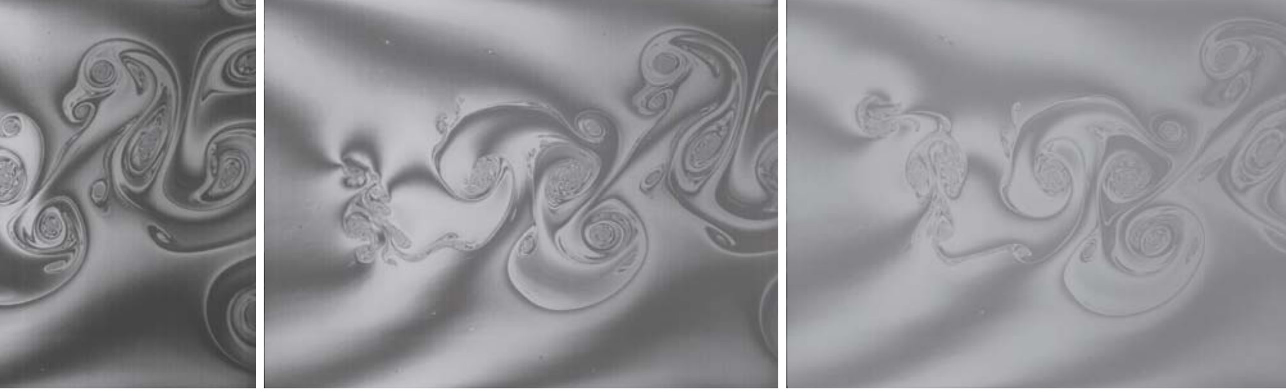

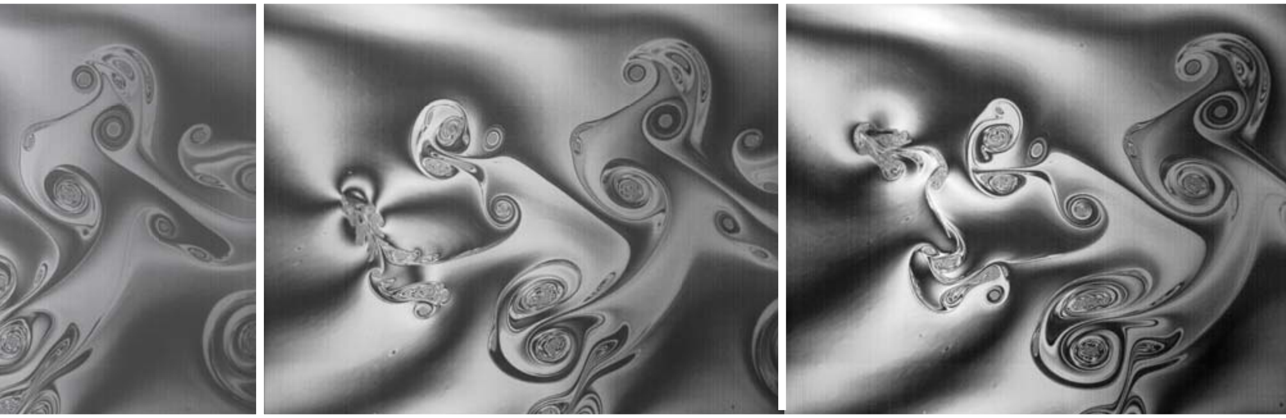

3 A journey through flatland

3.1

Vortex-wake interactions of a flapping foil that models animal swimming and flight

David Lentink*, Florian T. Muijres, Frits J. Donker-Duyvis and Johan L. van Leeuwen

Summary

The fluid dynamics of many swimming and flying animals involves the generation and shedding of vortices into the wake. Here we study the dynamics of similar vortices shed by a simple two-dimensional flapping foil in a soap film tunnel. The flapping foil models an animal wing, fin or tail in forward locomotion. The vortical flow induced by the foil is correlated to (the resulting) thickness variations in the soap film. We visualized these thickness variations through light diffraction and recorded it with a digital high speed camera. This setup enables us to study the influence of foil kinematics on vortex wake interactions. We varied the dimensionless wavelength of the foil ($\lambda^* = 4$-24) at a constant dimensionless flapping amplitude ($A^* = 1.5$) and geometric angle of attack amplitude ($A_{\alpha,\mathrm{geo}} = 15^0$). The corresponding Reynolds number is of order 1000. Such values are relevant for animal swimming and flight.

We found that a significant leading edge vortex (LEV) was generated by the foil at low dimensionless wavelengths ($\lambda^* < 10$). The LEV separates from the foil for all dimensionless wavelengths. The relative time (compared to the flapping period) that the unstable LEV stays above the flapping foil increases for decreasing dimensionless wavelengths. As the dimensionless wavelength decreases the wake dynamics evolves from a wavy von Kármán like vortex wake shed along the sinusoidal path of the foil into a wake densely packed with large interacting vortices. We found that strongly interacting vortices can change the wake topology abruptly. This occurs when vortices are close enough to merge or tear each other apart. Our experiments show that relatively small changes in the kinematics of a flapping foil can alter the topology of the vortex wake drastically.

Introduction

The complex fluid mechanics of many animals that swim or fly is governed by the non-linear formation, shedding and dynamics of vortices (e.g. Dickinson *et al.*, 2000). These vortices can potentially affect performance through their interactions with wings, fins or tails (e.g. Birch and Dickinson, 2003). The nature of the interactions is related to the kinematics of the wing, fin or tail, though the precise relation is not yet known. This relation is better understood for vibrating cylinders. Williamson and Roshko (1988) report in their inspirational paper how the vortex wake topology of a vibrating cylinder depends on both the dimensionless amplitude, (A^*, Eqn. 2.) and dimensionless wavelength (λ^*, Eqn.1) which is analogous to the dimensionless stride length and the inverse of the reduced frequency. Williamson and Roshko showed that synchronization

J. Exp. Biology. **211**, 267 – 273 (2008).

(lock-in) can occur between the driving frequency of a vibrating cylinder and multiples (*n*) of the natural von Kármán (eigen-) frequency of the vortical flow. Synchronization resulted in periodic vortex wakes shed by the vibrating cylinder. The synchronization region consists of two bands of periodic wakes, in between the wake is mostly aperiodic. Both synchronization bands are approximately elliptic in the parametric space spanned by A^* and λ^*: $A^* = 1/4\sqrt{n \cdot \lambda_0^* - \lambda^{*2}}$ in which λ_0^* is the dimensionless wavelength based on von Kármán frequency (independently found by Lentink (2003) and Ponta and Aref (2005)). The first band is related to the von Kármán frequency itself ($\lambda_0^* \approx 5$; $A^* = 0$), the second to a third of that frequency ($\lambda_0^* \approx 15$; $A^* = 0$). Similar computational fluid dynamic studies of two-dimensional plunging foils (Lewin and Haj-Hariri, 2003; Lentink and Gerritsma, 2003) showed that the wake and fluid forces that act on a foil can either be periodic or aperiodic. Lentink and Gerritsma (2003) found evidence for the existence of chaotic modes. The actual mode depends on the dimensionless wavelength and amplitude of the foil. The simulations show that the near-wake dynamics (wake mode) of the foil directly affect the character of the fluid forces (periodic versus aperiodic) that act on the foil. Hence these results suggest that kinematics potentially have a significant influence on the periodicity of the wake of a flapping foil and its corresponding propulsive and lifting forces.

Here we study the possible significance of vortex dynamics as a physical constraint to animal locomotion in fluids. A two dimensional flapping foil is a simplified model of animal wings, fins or tails. We aim to visualize and quantify the vortex wake interactions of such a two-dimensional flapping foil as a function of its kinematics. To this end we decided to flap our foil in a soap film tunnel: A thin layer of water between two molecular layers of soap molecules, driven by gravity (Rutgers *et al.*, 2001). Gharib and Derango (1989) have demonstrated that a soap tunnel is effective for studying a wide range of two-dimensional flow phenomena. To our knowledge Couder *et al.* (1989) were the first to actively drive an object similar to a flapping foil in a soap film. In their pioneering work they studied the vortical flow generated by a vibrating cylinder that moved trough a static soap film. To our knowledge the present study is the first to consider a flapping foil in a soap tunnel.

Earlier flapping foil studies have demonstrated both the value and effectiveness of a two-dimensional approach for gaining new insight into animal locomotion (Triantafyllou *et al.*, 1993; Dickinson, 1994; Wang, 2000a, 2000b; Miller and Peskin, 2004). We foresee, nevertheless, that a full study of vortex dynamics as a physical constraint to animal locomotion requires an extension to three dimensions. In three dimensions the vortex dynamic complexity is further increased (e.g. Buchholz and Smits, 2006; Ellenrieder *et al.*, 2003) by processes like vortex stretching (Guyon *et al.*, 2001**).** High Reynolds numbers also facilitate three-dimensional instabilities that can result; for example, in coherent vortices with a turbulent structure (e.g. Van Dyke, 1982). Note, however, that two-dimensional vortex dynamic mechanisms are a sub-set of three-dimensional vortex dynamics. This makes two-dimensional flapping foil studies intrinsically valuable for our understanding of how vortices generated by animals that swim or fly interact with each other and the animal.

Here we focus on the two-dimensional dynamics of vortices shed by a flapping foil in forward motion as a function of dimensionless wave length. It enables us to gain more insight in the generation and dynamics of leading edge vortices and vortex-wake interactions.

Materials and methods

Parameterization of the flapping foil

Similar to others (Triantafyllou *et al.*, 1993; Dickinson, 1994; Wang, 2000a, 2000b; Miller and Peskin, 2004), we model the kinematics of wings, fins and tails with a two-dimensional sine shaped excursion and rotation of the foil with a phase difference of 90°. The five main scaling variables of such a foil are: (1) The flapping frequency f of the excursion and rotation, which are equal to the animal's flapping frequency; (2) The excursion amplitude A, typically taken at the radius of gyration or 75% of an animal's wing, fin or tail semi-span; (3) The geometric angle of attack amplitude $A_{\alpha,\mathrm{geo}}$, taken at the same span-wise position as the excursion amplitude A. (4) The (average) forward speed of the foil U_∞, which is equivalent to the animals forward speed; (5) the chord length of the foil l, which represents the average chord length of an animal wing, fin or tail (we will describe foil shape in the next section).

Non-dimensionalization allows us to objectively quantify the scale effects (Guyon *et al.*, 2001) of a flapping foil. We follow an approach described in Lentink and Gerritsma (2003) that is consistent from hovering fight, with zero dimensionless wavelength, to fast forward flight for which the dimensionless wavelength approaches infinity. The resulting non-dimensionalization is defined below and illustrated in Fig. 1. The dimensionless wavelength (λ^*) represents the number of foil lengths traveled forward during one stroke:

$$\lambda^* = \frac{U_\infty}{f \cdot l}, \tag{1}$$

in which, U_∞ is the free stream velocity, f the flapping frequency and, l the foil length. The non-dimensional amplitude A^* represents the amplitude of the foil excursion A with respect to the foil length l:

$$A^* = \frac{A}{l}. \tag{2}$$

The amplitude based Strouhal number St_A is equal to the ratio of dimensionless amplitude (A^*) and dimensionless wavelength (λ^*) and scales with the maximum induced angle of attack at mid-stroke (see Fig. 1 and equation 4):

$$St_\mathrm{A} = \frac{A^*}{\lambda^*}. \tag{3}$$

The effective angle of attack amplitude $A_{\alpha.\mathrm{eff}}$ is equal to the angle of attack amplitude induced by the flapping foil minus the geometric angle of attack amplitude, $A_{\alpha,\mathrm{geo}}$:

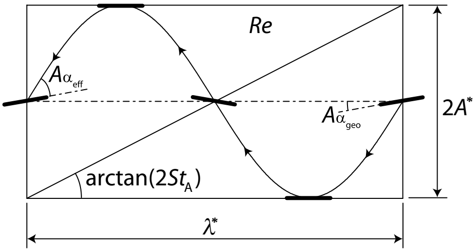

Fig. 1 | A graphical representation of the non-dimensional parameters of a sinusoidally flapping foil: Dimensionless wavelength λ^*, amplitude ratio A^*, amplitude based Strouhal number St_A, geometric angle of attack amplitude $A_{\alpha,\mathrm{geo}}$, effective angle of attack amplitude $A_{\alpha,\mathrm{eff}}$, and the stroke averaged Reynolds number *Re*.

$$A_{\alpha,eff} = \arctan(2\pi \cdot St_A) - A_{\alpha,geo}. \tag{4}$$

The time averaged velocity U_{ave} of the flapping foil can be approximated as follows (Lentink and Gerritsma, 2003):

$$U_{ave} \approx \sqrt{U_\infty^{\ 2} + (4Af)^2}\ . \tag{5}$$

Based on this average velocity we define the time averaged Reynolds number, *Re* that represents the relative importance of inertia vs. viscosity:

$$Re = Re_\infty \cdot \sqrt{1 + (4 \cdot St_A)^2}\text{, in which } Re_\infty = \frac{U_\infty \cdot l}{\nu}, \tag{6}$$

where ν is the kinematic viscosity. In our model we choose the dimensionless wavelength (λ^*) and amplitude ratio (A^*) as independent variables following Williamson and Roshko (1988), to which we need to add the angle of attack amplitude. The other parameters (St_A and *Re*) can therefore be expressed as a function of λ^*, A^* and Re_∞ (Eqn. 3-6).

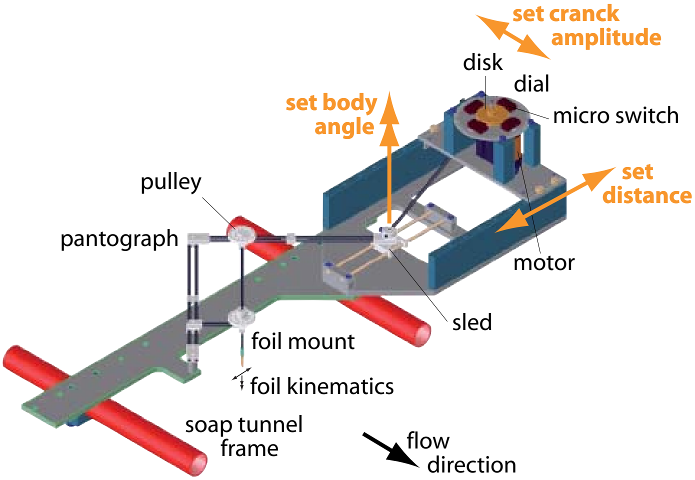

Fig. 2 | Flapping mechanism as mounted on the soap tunnel framework (further illustrated in Fig. 4). The flapping mechanism consists of a crank mechanism that generates both a stroke and angle of attack amplitude that are 90 degrees out of phase with respect to each other. The angle of attack amplitude is reduced with a series of pulleys. The stroke amplitude is reduced with the aid of a pantograph. The flapper is driven by a DC motor. We mounted a special dial-plate with one micro-switch (four are drawn) on the motor housing. This switch is pressed by a disk with a small knob in a phase we predetermined with the dial, in this way the camera can be triggered in a specific phase of the stroke. The angle of attack and stroke amplitude can be varied independently by changing the distance between the motor and the sled, indicated with “set distance”, and the arm length of the crankshaft “set crank amplitude”, which is hidden under the motor house in its current position. Finally the angle of the stroke plane of the foil can be set with respect to the free stream direction by rotating the whole crank mechanism which is indicated with “set body angle”, in this study it is zero (as drawn).

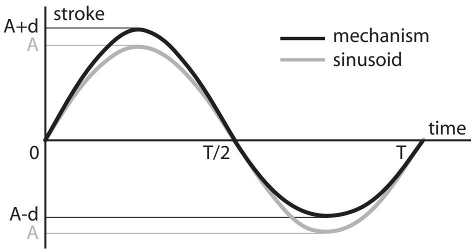

Fig. 3 | Stroke kinematics generated with our flapping mechanism. The stroke kinematics deviates with magnitude +/- *d* from a sine with amplitude *A*.

Foil shape and flapping mechanism

The foil is a flat plate and its kinematics is generated with a crank-shaft mechanism. The foil has a thickness *t* of 0.3 mm and length *l* of 3 mm; hence it has a relative thickness of 10%. It is made out of a thin piano-steel wire bend into an “L” shape. The horizontal part of the “L” functions as the foil in the soap film while the vertical part is mounted to the mechanism. The foil is mounted such that its axis of rotation is located at approximately ¼ foil length (with respect to the leading edge). The leading edge of the foil is naturally rounded as a result of bending the wire, while the trailing edge is more or less blunt (flat) as a result of cutting the wire.

Our custom-build flapping mechanism is illustrated and described in Fig. 2. It consists of a crank-shaft that generates both the stroke amplitude and a 90° out of phase angle of attack amplitude. The stroke amplitude is reduced with a pantograph and the angle of attack amplitude is reduced with a series of pulleys. A crank-shaft mechanism cannot generate pure sinusoidal stroke amplitudes (Fig. 3). The angle of attack amplitude is, however, very close to being sinusoidal. In our experiments we applied $A_{\alpha,geo} = 15°$. All deviations from purely sinusoidal kinematics are therefore as follows: The root mean square (rms) deviation of the excursion is 9.4% of A^*, and the rms deviation of $A_{\alpha,\mathrm{geo}}$ is 0.4%. Note that the resulting stroke kinematics is not fully symmetric (Fig. 3).

Soap-film tunnel set-up

The present soap-film tunnel design (Fig. 4) is based on a gravity driven, constant flow design by Rutgers *et al.* (2001). The ratio of the soap-film width to thickness is of order 10,000 (Rutgers *et al.*, 2001). The vortices generated in a soap film are therefore roughly 1000 times wider than thick, indicating that the flow field is essentially two-dimensional. As a result, a soap film is ideally suited for studying the two-dimensional vortical field behind a flapping foil. The corresponding vorticity field is directly correlated to minute thickness variations in the soap film (Chomaz and Costa, 1998; Rivera *et al.*, 1998; Chomaz, 2001). These thickness variations can be visualized as they diffract light transmitted by a mono-chromatic lamp (Rutgers *et al.*, 2001). We used a high-frequency, low pressure, SOX lamp (Philips) as light source. The resulting diffraction patterns were recorded time-resolved with a Redlake® (Redlake MotionPro, San Diego, CA, USA) high speed camera system at 800 fps and a shutter time of 1/1600 s. This visualization and capturing technique enables us to time-resolve the dynamics of the vorticity field effectively: Little experimental and computational time is required for generating and interpreting the flow field of a soap tunnel in order to study complex vortex dynamic flows as a function of foil kinematics. Additionally the flow visualizations have a certain artistic appeal.

The most important physical variables of the soap-film in our experimental setup are its

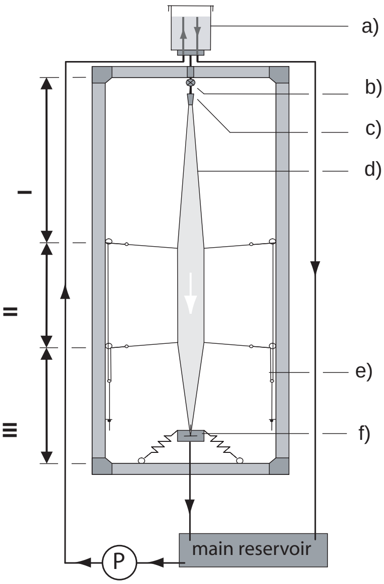

Fig. 4 | The soap-film tunnel is mounted in an inclined frame and driven by gravity. It consists out of three sections: a divergent section (I), the constant width (60 mm) test section in which the foil flaps (II) and a convergent section (III). The soap reservoir (a) produces a constant head by using an overflow. The soap flows from the reservoir (a) through a tuning valve (b) and an oval nozzle made out of a plastic pipette (c). At the pipette (c) the soap film starts: it runs down, driven by gravity, between two 1mm thick Nylon wires (d) into tunnel sections (I-III). The Nylon wires are pulled apart with 0.2 mm Dynema fishing lines (e). Finally the soap is collected in a reservoir (f) and is drained into the main soap reservoir and pumped (P) again to reservoir (a).

flow velocity, U_∞, and kinematic viscosity, υ. The viscosity of a soap-film is not exactly known. However, accurate measurements by Martin and Wu (1995) show that the viscosity, for a solution similar to ours, is approximately $1\cdot10^{-6}\,m^2/s$ (4% Dawn dishwashing detergent). We will adopt this value for our solution of approximately 2% Dawn dishwashing detergent (Procter & Gamble, professional line). The soap-film velocity varies over the width of the film from zero at the walls (due to the no-slip condition) to a maximum velocity in the middle. In air the resulting velocity profile obtained in a soap tunnel corresponds to a plug-like profile (Rutgers *et al.*, 2001). We determined the variation of the flow velocity over the amplitude range of the flapping foil with particle tracking velocimetry (PTV) of small pollutants in the soap-film. The flow velocity was determined at three locations; at the start, middle and end of the stroke, of which the maximum standard deviation is 12%. The accuracy of the frequency measurement is better than 3% while the length of the foil is measured with an accuracy of approx. 5%.

Applied foil kinematics and soap tunnel settings

We chose to study the influence of dimensionless wavelength on vortex wake interactions inspired by a two-dimensional numerical study of insect flight (Lentink and Gerritsma, 2003). In this study of a plunging foil, a chaotic mode was found for $\lambda^*=4$ at $Re=150$. Similar simulations for $\lambda^*=6$ (unpublished) revealed a periodic mode. A plunging foil is, however, a limited model of insect flight and animal locomotion in general. The main reason being that thrust generation is minimal for zero geometric angle of attack amplitude. This is due to a minimal frontal surface area for the pressure-difference to act on in forward direction (Lentink and Gerritsma, 2003). Therefore we chose to fix the angle of attack amplitude in this study to a more realistic value, $A_{\alpha,geo}=15°$. This value facilitates the generation of significant thrust (note that the corresponding time average lift is approximately zero if the near flow field is symmetric). The stroke amplitude of the foil was adopted from the numerical study; $A^*=1.5$. Such amplitude has relevance for insects and bird wings and fish fins and tails, but is not related to a specific animal (because time average lift is approximately zero, the present study relates best to forward swimming and climbing flight, e.g. during vertical take-off). Intrigued by the numerically found dependence of wake mode on dimensionless wavelength, we decided to study the wake patterns and the leading edge vortex (LEV) as a function of dimensionless wavelength for $4 \leq \lambda^* \leq 24$. We fixed the soap film speed to approximately $U_\infty = 0.20$ m/s. As a result the time-averaged Reynolds number ranges between 600 and 900, the lowest obtainable range in our facility. These Reynolds numbers are 4-6 times higher than in the numerical study (Lentink and Gerritsma, 2003).

Results

We have visualized and subsequently classified the vortical wakes of our flapping foil as a function of dimensionless wavelength inspired by the nomenclature developed by Williamson and Roshko (1988) for vibrating cylinders. In this approach, the number of single vortices (S) and vortex pairs (P) are identified per stroke (period). However, such a classification is almost never fully objective. The shedding of tiny vortices, which usually merge immediately with larger vortices, can make the flow analysis tedious. Williamson and Roshko, for example, had to work around the coalesce of many small and large of vortices in some cases. This approach is nevertheless suitable for describing and sorting out the relation between the shedding of leading and trailing vortices (LEVs and TEVs) and the subsequent formation of the wake as a function of dimensionless wavelength.

For all experiments we started at zero flapping frequency which we subsequently increased monotonically to obtain the desired dimensionless wavelength. In this way we avoided hysteresis loops. Similar to earlier findings for hovering insect flight (Dickinson, 1994), we found that the LEV is unstable at all dimensionless wavelength in two-dimensions. We define a LEV as unstable when it moves from the leading edge towards the trailing edge during the stroke. We restrict ourselves to scoring if the LEV is generated and if its center passes the trailing edge before stroke reversal. If a LEV does not pass the trailing edge we refer to it as “attached”. We further describe the wake structure as a function of vortices shed at the leading and trailing edge of the foil. We loosely refer to a ‘bifurcation’ when the wake switches between two seemingly co-existing wake patterns at a constant wavelength (an introduction to bifurcations can be found in Addison, 1997). We found an array of wake patterns and vortex interactions, which we will illustrate starting at $\lambda^* = 24$ and ending at $\lambda^* = 4$:

Vortex wake for $\lambda^* = 12$-24, Fig. 5A

The effective angle of attack amplitude is low at these high dimensionless wavelength, $A_\alpha = 7°$-$23°$, hence no LEVs or TEVs are formed during a stroke. Although a minute LEV starts to become visible at $\lambda^* = 12$, it remains negligible compared with the ones found for lower dimensionless wavelengths. The basic wake pattern emerges from a wake instability that results in the roll-up of the shear layer behind the foil into an alternating row of vortices. This wake shed along the sinusoidal path of the flapping foil is similar to the von Kármán vortex street shed by a cylinder; hence our name wavy von Kármán wake: WK. The Reynolds number is close to 600 and the specific parameters in Fig. 5A are: [$\lambda^* = 24$, $A^* = 1.5$, $A_\alpha = 7°$ and $Re = 600$].

Fig. 5 | Visualization of the evolution of vortex wake topology and the attachment of the LEV for decreasing dimensionless wavelength λ^*: The wake dynamics evolves from a wavy von Kármán wake (WK) into an aperiodic wake densely packed with large interacting vortices (Fig. A-G, left: overview wake, right: zoom in on LEV). The soap film flows from left to right and all images have been taken mid-stroke during the down-stroke. The leading edge vortex is indicated with *LEV*, a vortex pair with P, a single vortex with S, vortex tearing with *t*, and vortex merging with *m*. Note that the naming of the wakes is simplified and should be taken as a guide-line: We have neglected a few tiny vortices that are shed at some advance ratios for simplicity.
Note;

$\lambda^*_{Fig,A} = 24$,
$\lambda^*_{Fig,B} = 10$,
$\lambda^*_{Fig,C} = 7.9$,
$\lambda^*_{Fig,D} = 6.8$,
$\lambda^*_{Fig,E} = 6.3$,
$\lambda^*_{Fig,F} = 4.5$,
$\lambda^*_{Fig,G} = 4.0$.

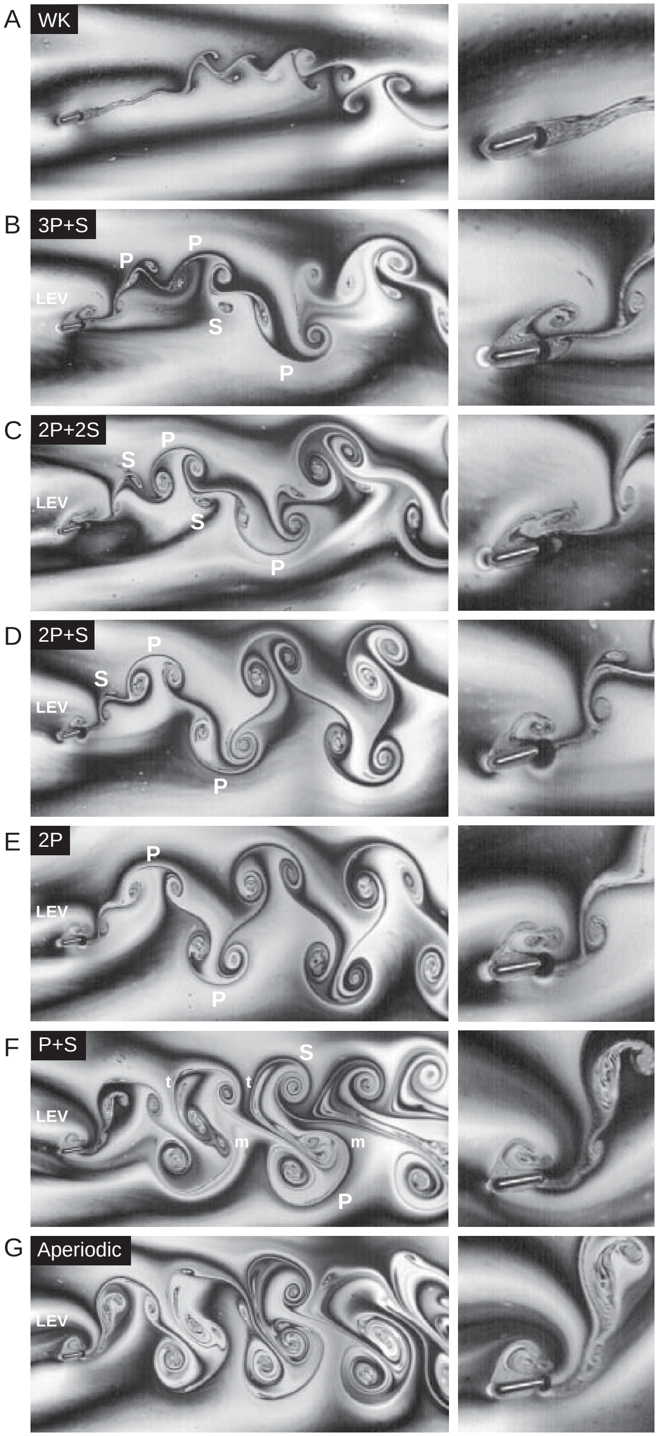

Vortex wake for λ^* *= 8.6-10, Fig. 5B.*

At these dimensionless wavelengths, A_α ranges from 29° to 33° and as a result LEVs and TEVs are generated, which form in most cases a pair when shed. Due to the high dimensionless wavelengths, however, the initial vortices shed long before the end of the stroke, enabling the flow to generate and shed a secondary LEV and / or TEV within the same stroke**.** During the upstroke 2 LEVs and 2 TEVs are formed, which form two vortex pairs (2P), in contrast to the down-strok when 1 LEV and 2 TEVs are generated, which form a single vortex (S) and a vortex pair (P). The net result is a **3P+S** vortex wake that evolved out of the vortices (3LEVs+4TEVs) shed during a flap period. At $\lambda^* = 8.6$ a bifurcation is observed: The vortex wake switches between the current 3P+S and a 2P+2S mode (Fig. 6, bifurcation 1). LEVs are in all cases shed before the end of the stroke. The Reynolds number for this range of λ^* is again close to 600 while the parameters of Fig. 5B are: [$\lambda^* = 10$, $A^* = 1.5$, $A_\alpha = 29°$ and $Re = 600$].

Vortex wake for λ^* *= 6.8-8.6, Fig. 5C.*

For these dimensionless wavelengths A_α ranges from 33° to 39°, the vortices become increasingly larger due to the higher effective angle of attack. We find that 1 LEV and 2 TEVs are formed and shed during both the up and down stroke. These vortices (2LEV+4TEV) organize into a **2P+2S** wake. For lower dimensionless wavelengths the wake evolves from a 2P+2S into a 2P+S mode. The dimensionless wavelengths at which this happens has, however, not been determined. LEVs are in all cases shed before the end of the stroke. The Reynolds number range is 600-700 while the parameters resulting in Fig. 5C are: [$\lambda^* = 7.9$, $A^* = 1.5$, $A_\alpha = 29°$ and $Re = 600$].

Vortex wake for λ^* *= 6.3-6.8, Fig. 5D.*

The effective angle of attack amplitude starts at 39° and ends at 41° for this range of λ^*. During the up-stroke 1 LEV and 2 TEVs are shed which form a P+S. During the down stroke 1 LEV and 1 TEV are shed which form a P. The final result is a **2P+S** wake pattern. LEVs are again shed before stroke reversal. The single vortex is subsequently merged with a vortex pair down stream. We observed a bifurcation between the 2P+S and 2P mode at $\lambda^* = 6.3$ (Fig. 6, bifurcation 2). The Reynolds number for this range of λ^* is close to 700 while the parameters of Fig. 5D are: [$\lambda^* = 6.8$, $A^* = 1.5$, $A_\alpha = 39°$ and $Re = 700$].

Vortex wake for λ^* *= 5.4-6.3, Fig. 5E.*

The effective angle of attack amplitude ranges from 41° to 45°. During each flapping period 2 LEVs and 2 TEVs are shed, that evolve into a **2P** wake pattern. At these low dimensionless wavelengths the LEVs and TEVs stay long enough attached to the wing to prevent the development of secondary vortices during a stroke. We did not identify a bifurcation between the current and next mode found at lower dimensionless wavelengths. The LEVs stay attached to the wing until stroke reversal while the Reynolds number ranges from 700 to 800. The parameters that result in Fig. 5E are: [$\lambda^* = 6.3$, $A^* = 1.5$, $A_\alpha = 41°$ and $Re = 700$].

Vortex wake for λ^* *= 3.9-4.6, Fig. 5F,G.*

As A_α further decreases from 49° to 53° we encounter the strongest vortex wake interactions. At the beginning of the down-stroke, the LEV created during the upstroke is still attached to the foil. This LEV interacts with the new developing TEV and finally these vortices are either merged or torn apart when they come within critical distance. This merging *m* and tearing *t* has a significant influence on the wake formation and results in a strongly asymmetric **P+S** wake mode. In the same wake some tiny vortices are shed that are either merged or torn apart due to mutual interactions. The parameters of Fig. 5F are [$\lambda^*=4.5$, $A^*=1.5$, $A_\alpha=49°$ and $Re=800$].

Within this range of dimensionless wavelengths we found two co-existing wake modes that are sensitive to small disturbances resulting in bifurcations (Fig. 6, bifurcation 3). The second wake mode is an aperiodic variant of the first, which is illustrated in Fig. 5G [$\lambda^*=4.0$, $A^*=1.5$, $A_\alpha=52°$ and $Re=900$]. The overlap of both modes is most likely due to a combination of experimental challenges, as they occur at the highest frequencies obtainable, and dynamical complexity. The LEV is 'attached' for all these dimensionless wavelengths, while the Reynolds number ranges from 800-900.

Discussion

We summarized the 'attachment' of the LEV, the number of shed LEVs and TEVs and the resulting wake patterns and bifurcations of the flapping foil as a function of dimensionless wavelength in Fig. 6.

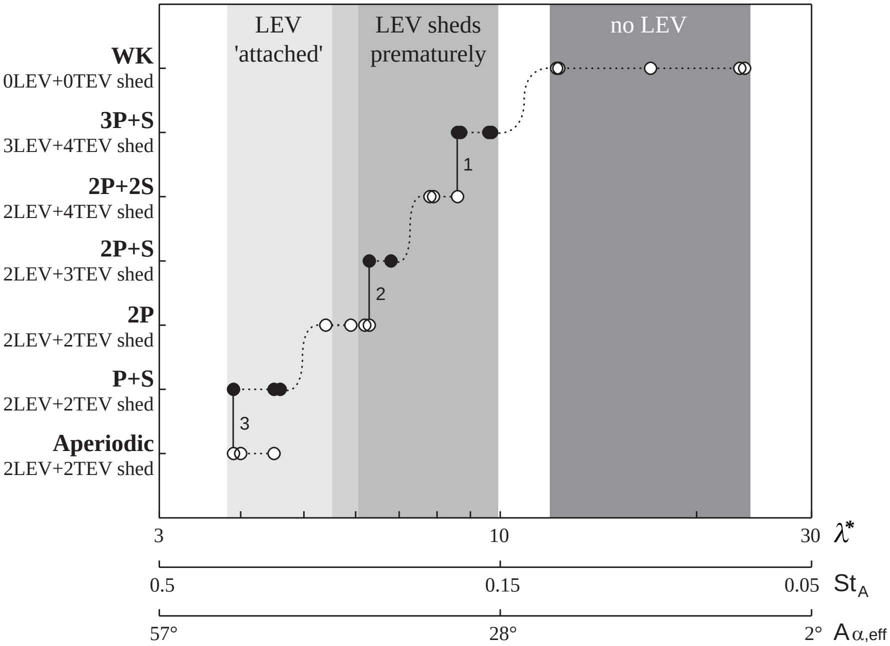

Fig. 6 | Summary of vortex wake topologies: The attachment of the LEV and the number of shed leading and trailing edge vortices (LEVs and TEVs) as a function of dimensionless wavelength λ^*. Note that the effective angle of attack amplitude A_α strongly increases with decreasing λ^*, which in part explains the increasing vortex size. The more densely packed wake at low λ^* is a direct result from the smaller distances between shed vortices. Solid lines (1-3) indicate bifurcations found in one movie sequence. Black and white filling of the circles is for easy distinction between modes only.

Attachment of the LEV

The two-dimensional LEVs generated by our flapping foil are unstable at all dimensionless wavelengths. The LEVs grow stronger due to the higher effective angle of attack amplitudes at low λ^*. For such λ^* we *define* the LEV as 'attached', because its center has not yet traveled past the trailing edge at stroke reversal (Fig. 6). 'Attachment' of LEVs at low λ^* is beneficial for both lift and thrust generation because the low pressure core of the LEV can act on the wing during the full stroke (Dickinson, 1994; Ellington *et al.*, 1996). Note that the position of such LEVs are stable with respect to the leading edge in three-dimensional models of hovering insects due to three dimensional flow effects such as spanwise flow (Ellington *et al.*, 1996; Lentink and Dickinson, 2005).

Vortex wake formation and interactions

Our experimental analysis shows that the wake topology depends in part on the number of leading and trailing edge vortices (LEVs and TEVs) shed in the wake (Fig. 6). The vortex modes were found to bifurcate between subsequent modes in three instances. These bifurcations influenced only small (single) vortices at high dimensionless wavelengths (Fig. 6, bifurcation 1, 2). Hence we consider these bifurcations weak. At low dimensionless wavelengths it involved, however, vortex merging and tearing which alter the vortex wake topology drastically (Fig. 6, bifurcation 3). We consider such bifurcations and the corresponding vortex interactions strong. Compared with weak bifurcations, strong bifurcations appear more sensitive to disturbances and the wake modes switch more abruptly.

The number of shed vortices (LEVs and TEVs) decreases with dimensionless wavelength because they have relatively less time to develop and shed from the foil. At very low dimensionless wavelengths, the barely shed LEVs will be hit by the foil during stroke reversal, resulting in strong foil-vortex interactions. The similarly strong vortex merging (Cerretelli and Williamson, 2003; Leweke *et al.*, 2001) and tearing interactions depend critically on the timing of vortex shedding, because it determines the spacing of the vortices in the wake.

Asymmetric and aperiodic vortex wakes

We expect that both wake asymmetry and wake aperiodicity could be relevant to animal locomotion. The presented wakes result from slightly asymmetric stroke kinematics. This makes it difficult to rigorously determine the influence of vortex-interactions on the asymmetry of a wake. Numerical studies (e.g. Lewin and Haj-Hariri, 2003; Lentink and Gerritsma, 2003) show, however, convincingly that asymmetric wakes can arise from symmetric foil kinematics. The orientation of the asymmetric wakes (e.g. in Fig. 5F; with respect to the horizontal axis) depends on the start-up condition and is sensitive to large disturbances. For λ^*= 3.9-4.6 we find strong vortex wake interactions that result in an aperiodic mode. This corresponds with the chaotic mode found numerically for a roughly similar plunging foil by Lentink and Gerritsma (2003). Using the current setup we were, however, unable to determine if the aperiodic mode is chaotic (Addison, 1997).

Vortex wake synchronization?

We found almost exclusively periodic vortex wakes in this study. We did not find a (confined) synchronization 'band' for our flapping foil similar to those found for cylinders (Williamson and Roshko, 1988). We think this could be due to two reasons. First the lower number of experiments we were able to perform with our setup in the parameter space of the flapping foil (λ^*; A^*; $A_{\alpha,\text{geo}}$).

Second such ‘bands’, or regions, might well be very complex shaped for a flapping foil, because a translating (non-flapping) foil has a range of natural vortex shedding frequencies as a function of angle of attack (α) (e.g. Katz, 1981; Dickinson and Götz, 1993) instead of a single shedding frequency (like cylinders have). We conclude that the role of vortex-wake synchronization in the wake of a flapping foil remains to be determined, both in 2D and 3D, for a wide range of flapping kinematic parameters and more realistic wing, fin and tail morphologies.

Finally, we observed in our two-dimensional experimental setup that relatively small changes in the kinematics of a flapping foil can alter the topology of its vortex wake drastically. Numerical simulations have shown that the corresponding fluid mechanic forces can change drastic too (e.g. Lewin and Haj-Hariri, 2003; Lentink and Gerritsma, 2003). The possible relevance of similar vortex wake bifurcations for animals that swim or fly could be studied, inside and outside of the behavioral envelope of the animal, with realistic three-dimensional robotic animal models (e.g. Ellington, 1996). We hypothesize that such a study might provide new insight into the influence of vortex wake dynamics on the swimming and flight behaviour of animals.

Acknowledgements

We would like to thank Jos van den Boogaard for helping us with the construction and design of the soap tunnel, Maarten Rutgers for advise and good soap, Bas van Oudheusden for co-supervising FTM at the TU Delft, and the Delft Aerospace Engineering workshop for building the flapping mechanism. Finally we would like to thank Andrew Biewener, Geoff Spedding and Ulrike Müller for valuable comments.

Symbols

λ^*	dimensionless wavelength
λ_0^*	dimensionless wavelength based on von Kármán frequency
A	flapping amplitude
A^*	dimensionless flapping amplitude
$A_{\alpha.\mathrm{eff}}$	effective angle of attack amplitude
$A_{\alpha,\mathrm{geo}}$	geometric angle of attack amplitude
d	amplitude deviation from sinusoidal kinematics
f	flapping frequency
l	foil length
n	multiple (of the natural von Kármán frequency)
Re	Time averaged Reynolds number of a flapping foil
Re_∞	Reynolds number of a flapping foil based on U_∞
St_A	amplitude based Strouhal number
t	thickness foil
U_{ave}	Time averaged velocity of the flapping foil
U_∞	forward velocity of flapping foil; equavalent to free stream velocity

References

Addison P. S. (1997), *Fractals and chaos, an illustrated course*, IoP publishing.

Birch, J. M. and Dickinson, M. H. (2003). The influence of wing-wake interactions on the production of aerodynamic forces in flapping flight. *J. Exp. Biol.* **206**, 2257-2272.

Buchholz, J. and Smits, A. J. (2006). On the evolution of the wake structure produced by a low aspect ratio pitching panel. *J. Fluid Mech.* **546**, 433-443.

Cerretelli, C. and Williamson, C. H. K. (2003). The physical mechanism for vortex merging *J. Fluid Mech.* **475**, 41-77.

Chomaz, J. M. and Costa, M. (1998). Thin film dynamics. In '*Free Surface Flows*' (ed. Kuhlmann, H.C. and Rath, H.J.), *CISM Courses & Lectures* **391**, 44-99.

Chomaz, J. M. (2001). The dynamics of a viscous soap film with soluble surfactant, *Journal of Fluid Mechanics* **442**, 387-409.

Couder, Y., Chomaz, J. M. and Rabaud, M. (1989). On the hydrodynamics of soap films. *Physica D* **37**, 384-405.

Dickinson, M. H. and Götz, K. G. (1993). Unsteady aerodynamic performance of model wings at low Reynolds numbers. *J. Exp. Biol.* **174**, 45-64.

Dickinson, M. H. (1994). The effects of wing rotation on unsteady aerodynamic performance at low Reynolds numbers. *J. Exp. Biol.* **192**, 179-206.

Dickinson, M. H., Farley, C. T., Full, R. J., Koehl, M. A. R., Kran, R. and Lehman, S. (2000). How animals move: An integrative view. *Science* **288**, 100-106.

Ellington, C. P., Van den Berg, C., Willmott, A. P. and Thomas, A. L. R. (1996). Leading-edge vortices in insect flight. *Nature* **384**, 626-630.

Gharib, M. and Derango. P. (1989). A liquid film (soap film) tunnel to study two-dimensional laminar and turbulent flows. *Physica D* **37**, 406-416.

Guyon, E., Hulin, J. P., Petit, L. and Mitescu C. D. (2001). *Physical hydrodynamics.* Oxford University Press.

Katz, J. (1981). A discrete vortex method for non-steady separated flow over an airfoil. *J. Fluid. Mech.* **102**, 315-328.

Lentink, D. (2003). Influence of airfoil shape on performance in insect flight. MSc. Thesis, *Delft University of Technology* (fac. AE), 187.

Lentink, D. and Gerritsma, M.I. (2003). Influence of airfoil shape on performance in insect flight. *AIAA* 2003-3447.

Lentink, D. and Dickinson, M.H. (2005). Structure, stability and strength of leading edge vortices in insect flight. *Comp. Biochem. Phys.* A141 3/suppl., S139.

Leweke, T., Meunier, P., Laporte, F., Darracq, D. (2001). Controlled interaction of co-rotating vortices. *ONERA-DLR Symposium*, ODAS.

Lewin, G. C. and Haj-Hariri, H. (2003). Modelling thrust generation of a two-dimensional heaving airfoil in a viscous flow. *J. Fluid Mech.* **492**, 339-362.

Martin, B. and Wu, X. L. (1995). Shear flow in a two-dimensional couette cell: a technique for measuring the viscosity of free-standing liquid films. *Rev. Sc. Instr.* **66**, 5603-5608.

Miller, L. A. and Peskin, C. S. (2004). When vortices stick: An aerodynamic transition in tiny insect flight. *J. Exp. Biol.* **207**, 3073 -3088.

Ponta, F. L. and Aref, H. (2005). Vortex synchronization regions in shedding from an oscillating cylinder. *Phys. of Fluids* **17**, 011703.

Rivera, M., Vorobieff, P. and Ecke, R. E. (1998). Turbulence in flowing soap films: Velocity, vorticity, and thickness fields. *Phys. Rev. Lett.* **81**, 1417-1420.

Rutgers, M. A., Wu, X. L. and Daniel, W. B. (2001). Conducting fluid dynamics experiments with vertically falling soap films. *Rev. Sc. Instr*. **72**, 3025-3037.

Triantafyllou, G. S., Triantafyllou, M. S. and Grosenbaugh, M. A. (1993). Optimal thrust development in oscillating foils with application to fish propulsion. *J. Fluid Struc.* **7**, 205-224.

Van Dyke, M. (1982). *An album of fluid motion*. Stanford: The Parabolic Press.

von Ellenrieder, K. D., Parker, K. and Soria, J. (2003). Flow structures behind a heaving and pitching finite-span wing. *J. Fluid Mech.* **490**, 129 -138.

Wang, Z. J. (2000a). Two dimensional mechanism for insect hovering. *Phys. Rev. Lett.* **85**, 2216 -2218.

Wang, Z. J. (2000b). Shedding and frequency selection in flapping flight. *J. Fluid. Mech.* **410**, 323 -341.

Williamson, C. H. K. and Roshko, A. (1988). Vortex formation in the wake of an oscillating cylinder. *J. Fluid Struc.* **2**, 355-381.

3.2

WAKE VISUALIZATION OF A HEAVING AND PITCHING FOIL IN A SOAP FILM

Florian T. Muijres and David Lentink*

Summary

Many fish depend primarily on their tail beat for propulsion. Such a tail is commonly modeled as a two-dimensional flapping foil. Here we demonstrate a novel experimental setup of such a foil that heaves and pitches in a soap film. The vertical flow field generated by the foil correlates with thickness variations in the soap film, which appear as interference fringes when the film is illuminated with a monochromatic light source (we used a high-frequency SOX lamp). These interference fringes are subsequently captured with high-speed video (500 Hz) and this allows us to study the unsteady vortical field of a flapping foil. The main advantage of our approach is that the flow fields are time and space resolved and can be obtained time-efficiently.

The foil is driven by a flapping mechanism that is optimized for studying both fish swimming and insect flight inside and outside the behavioral envelope. The mechanism generates sinusoidal heave and pitch kinematics, pre-described by the non-dimensional heave amplitude (0-6), the pitch amplitude (0°-90°), the phase difference between pitch and heave (0°-360°), and the dimensionless wavelength of the foil (3-18). We obtained this wide range of stride lengths for a foil 4 mm long by minimizing the soap film speed (0.25 ms^{-1}) and maximizing the flapping frequency range (4-25 Hz). The Reynolds number of the foil is of order 1000 throughout this range.

The resulting setup enables an effective assessment of vortex wake topology as a function of flapping kinematics. The efficiency of the method is further improved by carefully eliminating background noise in the visualization (e.g. reflections of the mechanism). This is done by placing mirrors at an angle behind the translucent film such that the camera views the much more distant and out-of-focus reflections of the black laboratory wall. The resulting high-quality flow visualizations require minimal image processing for flow interpretation. Finally, we demonstrate the effectiveness of our setup by visualizing the vortex dynamics of the flapping foil as a function of pitch amplitude by assessing the symmetry of the vortical wake.

Introduction

Marine fish that live and hunt in the water column (pelagic piscivorous fish) are both fast and efficient swimmers. Many of such fish, like tuna, have slender tails (caudal fins) and propel themselves primarily with their tail beat; hence they are referred to as thunniform swimmers (e.g. Sfakiotakis *et al.* 1999). Thunniform swimmers operate at a Reynolds number of 1000 and up

Exp. Fluids **43**, 665 – 673 (2007).

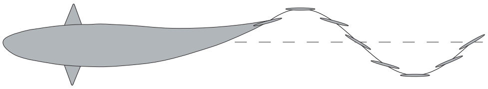

Figure 1 | The tail (caudal fin) of a thunniform swimmer (e.g. tuna and many sharks) forms the main source of propulsion. The tail can be effectively approximated as a heaving and pitching foil.

(Webb and Weihs 1986). The fluid mechanics of the heaving and pitching tails is governed by the generation and shedding of vortices (e.g. Triantafyllou *et al.* 1993**;** Sfakiotakis *et al.* 1999). These vortices influence swimming performance through their interactions with the tail. The nature of these vortex interactions depend on the foils kinematics and are not fully understood (Lentink *et al.* 2007). To better understand the vortex dynamics of thunniform swimmers, scientists often model the tail with a simple, non-flexible, pitching and heaving foil (Fig. 1) (Triantafyllou *et al.* 1993). Studying such simple foil geometry, kinematics and dynamics is a fair first approximation of thunniform swimmers.

Here we present a novel experimental setup for studying such a flapping foil in a soap film tunnel. Soap films provide an important advantage compared with conventional setups using digital particle image velocimetry (DPIV): the vortical flow can be visualized and filmed time and space resolved without image correlation. Gharib and Derango (1989) illustrated the effectiveness of such setups for studying many types of two-dimensional flows. Rutgers *et al.*, 2001 developed a simple and high quality soap tunnel (driven by gravity) that has eliminated many of the challenges of earlier designs (e.g. Gharib and Derango 1989; Couder *et al.* 1989). Georgiev and Vorobieff (2001) improved this setup for low flow speeds. Couder *et al.* (1989) studied vibrating cylinders in a static soap film, they were probably the first to actively drive an object similar to a flapping foil in a soap film. Zhang *et al.* (2000) studied freely flapping flags in a soap film tunnel, such fluid-structure interactions are also relevant for understanding anguilliform swimming of fish larvae, eels and swimming snakes. To our knowledge we were the first to actively flap a foil in a soap film tunnel (Lentink *et al.* 2007).

A soap film consists of a thin sheet of water stabilized by soap molecules on the surfaces. The soap molecules give the film elasticity, which mediates the propagation of disturbances through the film in the form of elastic Marangoni waves (Couder *et al.* 1989). Couder *et al.* (1989) and Chomaz and Costa (1998) showed that the in-plane dynamics of thin soap-films dominate the out-off-plane dynamics if the film speed is significantly slower than the Marangoni wave speed (elastic Mach number significantly smaller than 1). Hence “sub-sonic” soap-films can be regarded as 2D fluids. Chomaz and Costa (1998) further showed that a soap film obeys the 2D incompressible Navier-Stokes equations provided that the elastic Mach number is significantly lower than one and the initial film thickness variations are small. In the same paper Chomaz and Costa show that the vorticity field in the film is correlated to thickness variations of the soap-film. Rivera *et al.* (1998) showed that the correlation between the thickness and vorticity field in the wake of a grid of cylinders, generating 2D turbulence, remains strong well beyond 19 cylinder diameters downstream (region of interest: 50 mm downstream; cylinder diameter: 2.7 mm). Here we will study the vortical flow generated by a flapping foil less than 10 chord lengths downstream. Hence we may expect a particular strong correlation between vorticity and thickness field. Thickness variations in a soap film can be visualized by illuminating the soap film with monochrome light, which results in interference fringes (Rutgers *et al.* 2001). Filming

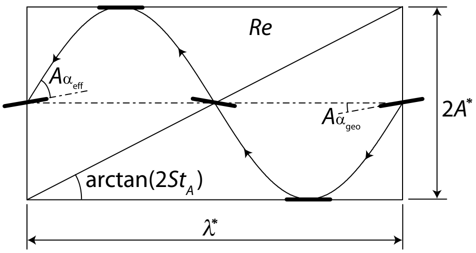

Figure 2 | A graphical representation of the non-dimensional parameters of a sinusoidally flapping foil: dimensionless wavelength, λ^*, dimensionless heave amplitude, A^*, amplitude-based Strouhal number, St_{A}, geometrical angle of attack amplitude, $A_{\alpha,\mathrm{geo}}$, effective angle of attack amplitude, $A_{\alpha,\mathrm{eff}}$, and the stroke-averaged Reynolds number, *Re*. (adapted from Lentink *et al.* 2007).

these fringes time and space resolved enables the quantitatively study of vortex dynamics in soap films. This makes slow and uniform soap-films ideally suited for studying two-dimensional vortex dynamics at sub-sonic speeds.

Here we quantitatively describe our set-up and illustrate its effectiveness for studying the topology of the vortical wake of a harmonically flapping foil. We chose a dimensionless wavelength and flapping amplitude of the foil that is relevant for thunniform swimmers. Subsequently we qualitatively study the symmetry of the vortical wake of the flapping foil as a function of pitch amplitude.

Materials and methods

Dimensionless parameterization of a flapping foil

The kinematics of a two dimensional foil can be described using different dimensionless variables; we chose an approach inspired by the work of Williamson and Roshko (1988). We have published this approach (Fig. 2) elsewhere (Lentink *et al.* 2007). We describe the harmonic kinematics of a heaving and pitching foil with an dimensionless wavelength λ^*, dimensionless amplitude A^*, geometric angle of attack amplitude (or pitch angle) $A_{\alpha,\mathrm{geo}}$ and Reynolds number *Re*. The dimensionless wavelength λ^* represents the number of chord lengths travelled forward during one full flap period of the foil:

$$\lambda^* = \frac{U_\infty}{f \cdot l}, \tag{1}$$

in which, U_∞ is the free stream velocity, f the flapping frequency and, l the foil length. The non-dimensional amplitude A^* represents the amplitude of the foil excursion A with respect to the foil length l:

$$A^* = \frac{A}{l}. \tag{2}$$

The amplitude-based Strouhal number St_{A} is equal to the ratio of dimensionless amplitude A^* and dimensionless wavelength λ^*, and scales with the maximum induced angle of attack at mid-stroke (see Fig. 2 and equation 4):

$$St_A = \frac{A^*}{\lambda^*}. \tag{3}$$

The effective angle of attack amplitude $A_{\alpha,\text{eff}}$ is equal to the angle of attack amplitude induced by the flapping foil minus the geometric angle of attack amplitude, $A_{\alpha,\text{geo}}$ (the pitch amplitude):

$$A_{\alpha,\mathit{eff}} = \arctan(2\pi \cdot St_A) - A_{\alpha,\mathit{geo}} \ . \tag{4}$$

The time-averaged velocity U_{ave} of the flapping foil can be approximated as follows (Lentink and Gerritsma 2003):

$$U_{\text{ave}} \approx \sqrt{U_\infty{}^2 + (4Af)^2} \, . \tag{5}$$

Based on this average velocity we define the time-averaged Reynolds number, *Re* that represents the relative importance of inertia *vs*. viscosity in the flow:

$$Re = Re_\infty \cdot \sqrt{1 + (4 \cdot St_A)^2} \, , \text{ in which } Re_\infty = \frac{U_\infty \cdot l}{\nu}, \tag{6}$$

note that ν is the kinematic viscosity.

Flapping foil mechanism

The foil is a flat plate and its kinematics is generated with a mechanism that can generate nearly perfect sinusoidal heave and pitch kinematics. Our first mechanism generated kinematics with a small asymmetry because the design is based on a crank-shaft mechanism (Lentink *et al.* 2007). Here we present and describe an improved flapping mechanism that can generate symmetric sinusoidal kinematics.

The foil has a thickness *t* of 0.2 mm and length *l* of 4 mm (relative thickness 5%). It is made out of a thin piano-steel wire bend into an “L” shape. The horizontal part of the “L” functions as the foil (in the soap film), while the vertical part is mounted to the flapping mechanism (Fig. 4b). The foil is mounted such that its axis of rotation is located at approximately ¼ foil length behind the leading edge. The leading edge of the foil is naturally rounded as a result of bending the wire, while the trailing edge is more or less blunt (flat) as a result of cutting the

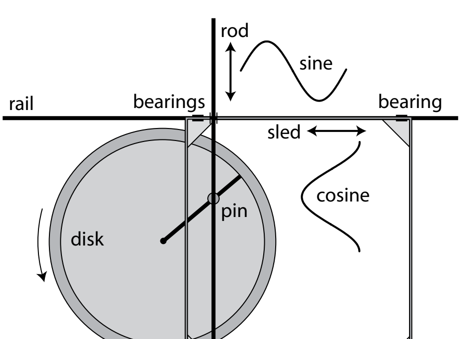

Figure 3 | Working principle of our flapping mechanism. The spinning disk (constant RPM) is connected to the rod (by a pin fixed with bearings), and the rod is connected to the sled that slides over two (horizontal) rails. The rod moves up and down with a sine, while the sled moves left and right with a cosine. The cosine of the sled is used to drive the heave of the foil while the sine of the rod drives the pitch of the foil. We use one such mechanism to generate the heave kinematics (using the sleds cosine) and another one to generate the pitch kinematics (using the rods sine). We coupled the disks of both mechanisms such that they operate at the same frequency, phase locked (Fig. 4).

wire.

The harmonic heave and pitch kinematics of the foil are generated by two coupled mechanisms. A single mechanism consists of a high-inertia constant-RPM spinning disk (aluminum) that drives a lightweight sled (aluminum) of which a schematic is shown in Fig. 3. The disk is connected with a pin (brass) to a rod (carbon fiber tube) that is connected to the sled. Simple Nylon and Brass bearings and proper lubrication resulted in a smoothly running mechanism that can generate both a sine (translation of rod) and cosine (translation of sled). The frequency of these harmonics is determined by the disk's RPM, while the *radius* at which the pin connects the disk to the rod (and hence the sled) determines the *amplitude* of the harmonic. Both the heave and pitch amplitude can be varied independently (at the same frequency), because we used two coupled disk-sled mechanisms to generate both the heave and pitch kinematics, which we further explain in Fig. 4.

The mechanism allows presetting the heave amplitude (0-6 chord lengths), the geometrical pitch amplitude (0°-90°) and the phase difference between pitch and heave (0°-360°). The mechanism is driven by a reduced electric motor (water cooled) that spins at moderate frequencies (4-25 Hz). Additionally we can also preset the stroke plane angle of the flapping foil with respect to the free-flow velocity of the soap-film, which is relevant for flapping flight, e.g. insects (David 1978).

We determined how accurate the mechanism can generate harmonic kinematics by tracking the foil in the soap film tunnel with our high speed video. For our error analysis we considered three flap periods to determine the error in heave amplitude (ε_A), pitch amplitude ($\varepsilon_{A\alpha}$), heave-pitch phase-difference (ε_φ) and frequency (ε_f) (Fig. 5). We determined the error using a best fit

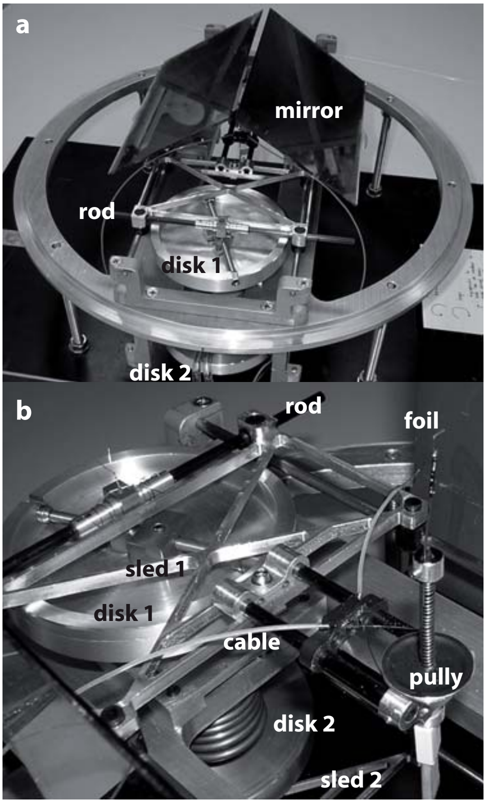

Figure 4 | Overview of flapping mechanism (a) and detailed photo (b). The upper part of the mechanism is indicated with "1", the lower part with "2". The flap mechanism consists of two rotating disks driven by an electric motor (water cooled). The upper disk (see b) is connected to a sled such that it generates the harmonic stroke kinematics (Fig. 3). We mounted the foil on the upper sled. The lower disk is connected to the lower sled with a rod that drives the harmonic pitch kinematics of the foil. The pitch kinematics is transferred by 0.2 mm piano steel wires, which slide through a flexible Teflon tube, to the upper sled were they connect to a pulley on which the foil is mounted. The whole mechanism is shielded by two mirrors set at an approximate angle of 45°.

Figure 5 | Measured pitch and heave kinematics fitted with sine and cosine functions to determine the accuracy of our mechanism. Note that we made the kinematics dimensionless with respect to the frequency (here 23 Hz), amplitude (here 1*l*) and geometric angle of attack amplitude (here 60°) in Table 1. The subsequent error indicators are the heave amplitude error ε_A, the pitch amplitude error, $\varepsilon_{A\alpha}$ the phase error, ε_φ and the frequency error ε_f.

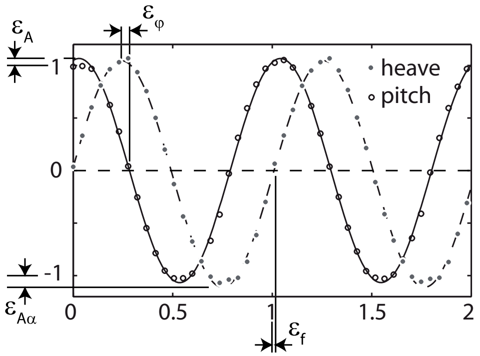

method (cftool Matlab 7, method: least squares, algorithm: trust-region) for kinematics generated at different heave amplitudes (1 and 4 chord lengths), pitch amplitudes (0°, 45°, 60°) and frequencies (4-21Hz), see Table 1. The heave-pitch phase-shift is set to 90° (Read *et al.* (2002) showed that a flapping foil produces maximal thrust for such a phase shift). We normalized the data with respect to these input variables in our error analysis. The variable range considered (Table 1) comprises the most extreme cases that we can obtain with our setup. Hence our error analysis can be considered a worst case analysis. We found that the mechanism accurately produces harmonic (sinusoidal) pitch and heave kinematics (Fig. 5). The maximum (local) deviation from ideal sinusoidal kinematics occurs at maximum excursion and is less than 5%, but this an extreme value, it is typically less than 2%. Hence our new mechanism does not produce perfectly symmetric kinematics (as any other mechanism would) but it does generate much more symmetric kinematics than our earlier design (Lentink *et al.* 2007).

Table 1 | Variables used in error analysis.

f [s^{-1}]	**A [mm]**	**A$_{\alpha,geo}$ [°]**	**symbol**
20.0	4	60°	□
23.0	4	60°	░
20.4	16	0°	▒
20.6	16	45°	▓
4.5	16	60°	■

Figure 6 | Error analysis of the kinematics generated by mechanism compared with ideal harmonic kinematics. Black lines indicate average; filled circles indicate individual measurements and correspond to Table 1; triangle not part of average (measured at 4.5 Hz). Left, RMSE for both heave and pitch kinematics, showing that the kinematics are indeed harmonic. Right, mean relative errors in heave amplitude ε_A, pitch amplitude $\varepsilon_{A\alpha}$, phase ε_φ (with respect to the max. phase error; 360°) and frequency ε_f. All errors are of order 0.05 (5%) or less. At low frequency (4.5 Hz) we found that the amplitude error (but not the other errors) is significantly lower than at high frequency (~20 Hz). We expect that this is due to the inertial loading on the mechanism.

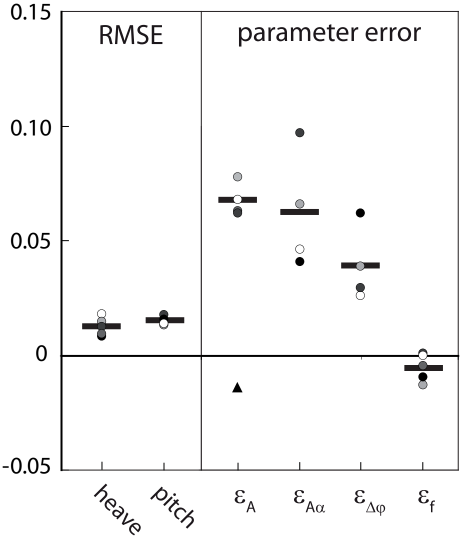

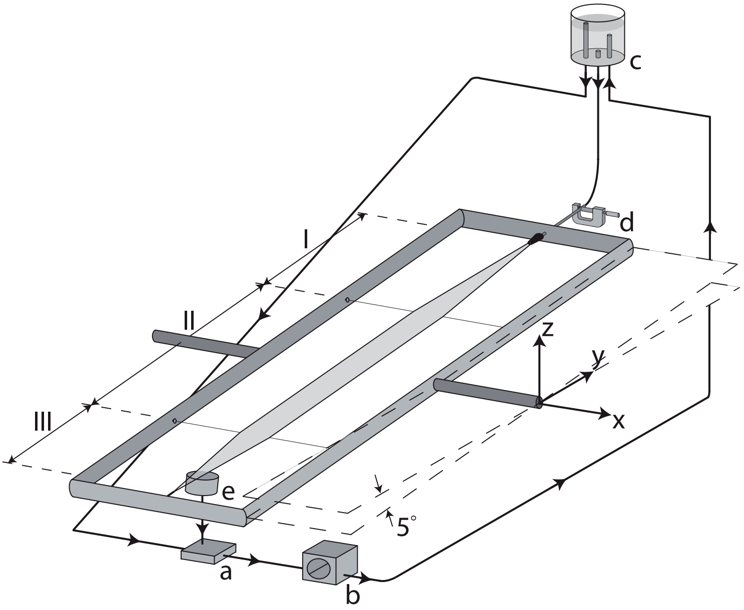

Figure 7 | The soap film tunnel consists of a frame that spans two Nylon tunnel "walls". The frame is set at an inclination of 5°. The tunnel has a diverging section (I), a test section (II) in which the foil is placed in the film, and a convergent section (III). The main components of the soap tunnel are: the main reservoir (a), a medical pump (b), a constant-height reservoir (c), a valve (a micrometer that constricts the tubing) (d) and a drain (e).

The average root mean square error (RMSE) of the present mechanism is small for both the pitch and heave kinematics (<0.02), Fig. 6. The results of the error analysis for the four flap variables are given in Fig. 6, they represent simply the difference between the intended value and the observed value of the flap parameters. Within one image sequence of three periods (part of a run of orders of magnitude more periods) we did not find significant fluctuations. Hence, the errors in Fig. 6 represent the resolution at which we can predetermine the parameters of the mechanism that define the flap kinematics. From this analysis we conclude that the harmonics generated with our mechanism can be preset reasonably accurately (under worst case conditions) with errors close to 0.05. Note that the frequency error is particular low, less than 0.01. Further note that phase shifts (errors) do not influence the symmetry of the foils kinematics provided that this shift is constant, as found for our mechanism. We found that such phase shifts are due to a misalignment of the top and bottom disk in the mechanism (Fig. 4).

Soap film tunnel

Our soap film tunnel generates a constant velocity soap film that runs between two wires, driven by gravity. We based our design (Fig. 7) on the simple and effective soap tunnel designed by Rutgers *et al.* (2001) and Georgiev and Vorobieff (2001). The frame of the current design is made out of cast iron and steel and is therefore more rigid than our first light weight soap tunnel build out of glass fiber tubes (Lentink *et al.* 2007). Our soap solution consists of tap water and 3% Dawn dishwasher detergent (Dawn "Manual pot and pan detergent", Professional line, USA). In

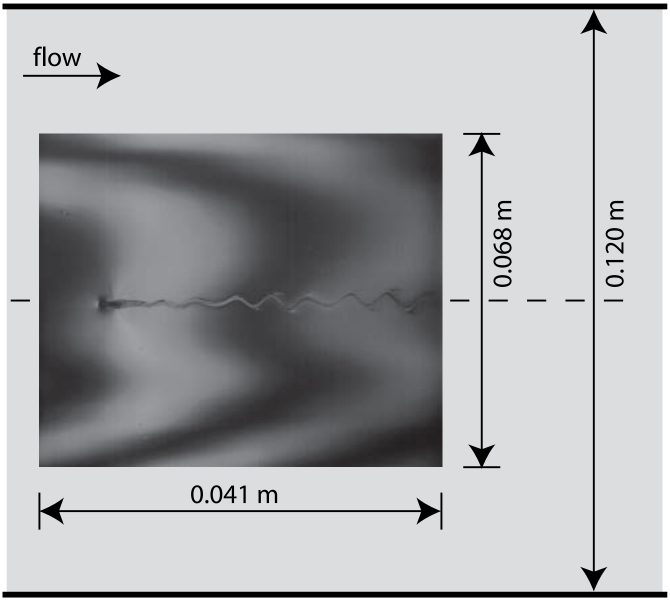

Figure 8 | Foil in the test section of the soap film tunnel (34 × 41 mm). The non-flapping foil generates small vortices downstream. Nylon wires (1 mm thick) that bound the test section are indicated with thick horizontal lines.

the current literature there is still considerable controversy with respect to the exact viscosity of soap-films (Rutgers *el al*, 1996). One of the most extensive studies to date has been performed by Martin and Wu (1995), they determined that the kinematic viscosity of a soap-film consisting of a 4% Dawn soap solution (Dawn “Manual pot and pan detergent”, Professional line, USA) is in the order of $10^{-6}\,m^2s^{-1}$, we adapt this value in our study. We stored the soap solution in a one-liter reservoir (Fig. 7: a) and pumped it with a peristaltic pump (1000 Mity Flex) into a two meter high, constant height, ‘overflow’ reservoir (Fig. 7: b). The soap solution then flows from the reservoir through tubing into a valve (Fig. 7: c) that regulates the mass flow. From the valve the soap solution flows to two parallel 1mm thick nylon wires that gradually diverge (Fig. 7: section I), which results in a stable flowing soap-film. The two Nylon wires run parallel (separation: 0.12 m) along the test section (Fig. 7: section II), in which the flow velocity is approximately constant in flow direction. The flapping foil is inserted in this test section. The soap film continues flowing from the test section along two converging wires (Fig. 7: section III) into the drain (Fig. 7: d) from where the film flows into the main reservoir, which completes the cycle.

The soap film speed and thickness can be controlled by two parameters once the Nylon wires are fixed to the frame: First, the valve (control of mass flow) and second, the tilt angle of the film with respect to the horizon (preset of gravitational component in flow direction). Reducing the flow at the valve results in slower and *thinner* films, while reducing the tilt angle results in slower and *thicker* films. Super-critical film speeds, at elastic Mach numbers (ratio of film speed over elastic wave speed) of order one, can be obtained at large tilt angles (up to 90°) when the valve is wide open (Rutgers 1999). Under “supersonic” conditions, at flow speeds up to $4\,ms^{-1}$ and higher, “shockwaves” can occur in the film (Rutgers 1999; Wen *et al.* 2003). Such flows are not relevant for fish and should be avoided, also because flows at high elastic Mach numbers do not correlate with transonic and supersonic fluid dynamics in air or water (Wen and Lai 2003). For studying subsonic flows, our goal, tilt angles need to be low. For a tilt angle of 5° (at low

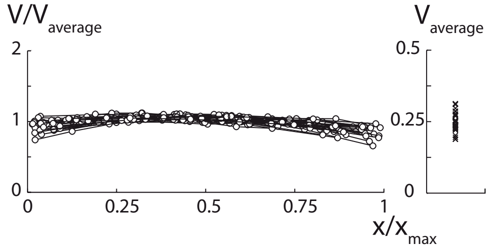

Figure 9 | The normalized (plug-like) velocity profiles as measured in the soap tunnel. We chose velocities at which no flow separation would occur in the test section; on average we obtained our slowest films without separation at 0.25 ms^{-1}.

mass flow, not measured) we obtained a thick film (not measured) with an average speed of 0.25 ms^{-1}, which is 50% slower than "The slowest soap-film tunnel in the Southwest" (Georgiev and Vorobieff 2002). At lower speeds, typically lower than 0.15 ms^{-1}, flow separation starts to occur at the end of the test section near the Nylon wires. For every run we tuned our valve to obtain the lowest possible speed without flow separation. Our optimally tuned soap films produced nice plug-like velocity profiles in the test section (Fig. 8). Note that we measured the velocity profile over a width of 34 mm, compared with the 60 mm width of the test section (Fig. 8, 9). These profiles were obtained by tracking small pollutants in the soap film, which we filmed with a RedLake ® MotionPro digital high speed video. Pollutant tracking was performed manually with a dedicated Matlab program. We tracked pollutants (diameter of order 10 pixels) over the full width of the camera image (of order 1000 pixels), which resulted in good tracking accuracy (better than 1%). The measured velocity profiles in the area of investigation in the test section are shown in Fig. 9. The velocity profiles are reasonably flat, while the average film speed is non-constant over a time period of several hours. Hence we measured the velocity profile several times during a measurement cycle to account for these slow fluctuations in our experiments. We always determined the average velocity over the whole heave excursion (twice the amplitude) in order to obtain good average velocities for the non-dimensional variables that depend on this velocity (dimensionless wavelength and Reynolds number).

Visualization setup

The flapping foil in the soap film generates shear layers that roll up into vortices. The resulting vorticity field correlates strongly with thickness variations in the soap-film (Rivera *et al.* 1998). We visualize the thickness variations by illuminating the film with monochromatic light of a sodium lamp (SOX, wavelength 590 nm,) and film the reflected interference fringes at high speed (Fig.10). The intensity of the reflected light changes from light to dark and vise versa for thickness variations that approach a quarter of the wavelength of the light source (Fig. 10). To acquire both a high spatial and temporal resolution a RedLake ® high speed digital camera is used to record the interference fringes in the soap film. The camera settings are: resolution of 1280 by 1024 pixels at 500 frames per second. To eliminate intensity fluctuations in the recordings we used a special 30 kHz SOX lamp (Philips) (Palmer and Beach 1995). We further improved the image quality by reducing the background reflections (noise) viewed by the camera through the translucent soap film. The light reflected by the mechanism formed the main source of noise in the images. After trying several alternative solutions (e.g. spray painting the mechanism black, shielding it with black paper, etc.) we found that putting mirrors (at an angle of approx. 45°) between the mechanism and film worked best (Fig. 4). These mirrors reflect the little light from the distant, out of focus, black laboratory wall into the camera, which resulted in negligible image noise.

Results

Vortex wake symmetry of a flapping foil

The heave and pitch variables of our flapping foil setup can be set as follows; $A^* = 0\text{-}6$, $A_{\alpha,geo} = 0°\text{-}90°$, $\lambda^* = 3\text{-}18$ and the phase difference between heave and pitch can be set between 0°-360°. The Reynolds number of the foil in our soap tunnel is of order thousand. The ranges of these parameters are representative for thunniform swimmers (including the Reynolds number; Webb and Weihs 1986). The caudal fin and its beat are approximated with a flat plate and harmonic kinematics. We focus our experimental study on how foil kinematics affects vortex wake symmetry. Several CFD studies have shown that the vortex wake and the corresponding forces generated by a symmetrically flapping foil can be asymmetric (e.g. Lewin and Haj-Hariri 2003; Lentink and Gerritsma 2003). Symmetry is relevant for thunniform swimmers because force asymmetries can result in net turning moments, which complicate straight swimming in fish. Here we show how a soap tunnel could potentially be used to effectively explore the parametric space of a flapping foil to identify asymmetric vortical wakes. For this study we focus on the influence of pitch amplitude on wake symmetry for a fixed amplitude $A^* = 3$ and dimensionless wavelength $\lambda^* = 11$ at a Reynolds number of order 1000 while varying the geometric angle of attack $A_{\alpha,geo} = [0°,15°,25°,45°]$. Recently we have made a much broader parametric study with our soap tunnel that will be published elsewhere.

We assess the wake symmetry by making series of 99 triggered photos at a fixed flap phase. We then high-pass filter the individual images and subsequently calculate the average filtered image (Fig. 11) for four phases; 0°, 90°, 180° and 270°. If the vortex wake is symmetric, then the vortical fields must be anti-symmetric for 180°-out-of-phase triggered images (Fig. 11). We developed a simple procedure that enables a graphical check for wake symmetry: we add two 180°-out-of-phase locked images using different RGB channels. The first phase is represented by an orange image and the second by a *mirrored* pink image. If the two wakes overlap they produce a red image (Fig. 11) and one can assess wake symmetry by eye. We did this for all four pitch angles and found that wake symmetry strongly depends on pitch angle for the heave amplitude and dimensionless wave lengthconsidered (Fig. 11).

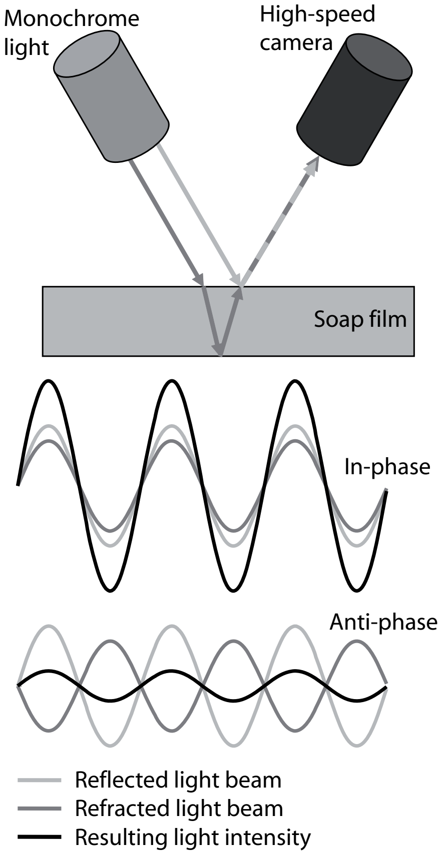

Figure 10 | Interference fringes reflected by a soap film that is illuminated with a monochromatic light source. We capture these fringes with digital high speed video.

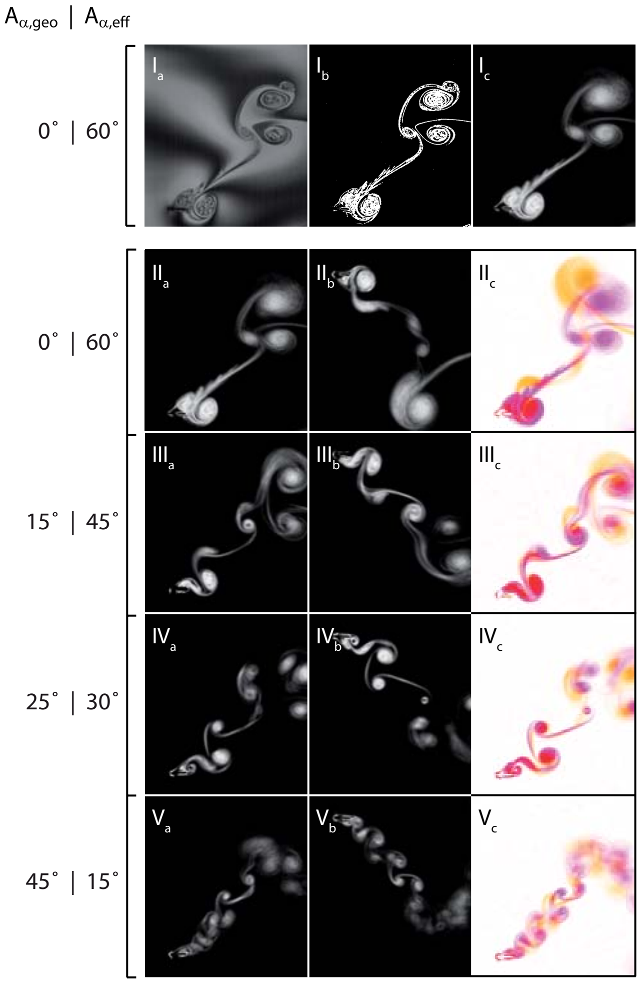

Figure 11 | Wake visualization of a flapping foil in a soap film. We first filter the raw images (Ia) using the Matlab 7.0 gradient and median (3×3) filter (Ib) and than average 99 subsequent filtered frames (Ic), these 99 images were all shot at the same flapping phase. We then assess the symmetry of the wake as a function of the geometric angle of attack ($A_{\alpha,geo}$); note that the resulting effective angle of attack is also indicated ($A_{\alpha,eff}$): II-V. The symmetry of the wake can be assessed qualitatively by comparing the average images at the start of the up- and down stroke (indicated with a, b). We subsequently reflect the upstroke wake "b" with respect to the horizontal centerline, in orange, and add it to the downstroke wake "a" in pink. Hence the overlapping parts of the wake become red (c).

Our experiments show that high effective angles of attack result in large vortices and wakes. When the effective angle of attack becomes small, an array of small vortices are generated along the foils path, similar to (but larger than) the wake shed by the non flapping foil at the same speed (Fig. 8). The vortex wake asymmetry is most likely due to non-linear near-vortex-wake interactions, as found by Williamson and Roshko (1988) for vibrating cylinders. How the vortex interactions in the wake and the interactions with the foil induce the wake asymmetry is largely unclear. In some cases the asymmetry is due to vortex merging or tearing (Lentink *et al.* 2007), but not for the foil kinematics considered here as we did not observe such vortex interactions. There are two sources of imperfections in the experimental setup that could potentially result in wake asymmetry: First flow asymmetry, because our plug like velocity profiles are slightly asymmetric. We do not expect this to result in the wake asymmetry, because wake asymmetry also occurs in close to perfectly symmetrical CFD simulations (e.g. Lewin and Haj-Hariri 2003). The influence of flow asymmetry could, however, be tested in future CFD studies. Second asymmetries in the kinematics generated by the mechanism, these are however small, we again note that wake asymmetry also occurs for close to perfectly symmetrical kinematics in CFD simulations (e.g. Lewin and Haj-Hariri 2003). Note, however, that the symmetry of the tail beat kinematics of fish and the background flow in which they swim in their habitat is not perfectly symmetric either (a detailed study of the level of symmetry of both swimming kinematics and background flow does not exist to our knowledge). Finally despite small asymmetries in our setup we found both symmetric and asymmetric wake patters while varying the geometric angle of attack amplitude in our experiment. Hence we conclude that we found experimental evidence for vortex wake asymmetry generated by a (to good approximation) symmetrically flapping foil in a soap tunnel. This finding is similar to findings by others in three-dimensional water tunnels (e.g. Jones *et al.* 1996) and two-dimensional CFD simulations (e.g. Lewin and Haj-Hariri 2003).

Discussion

We presented a novel soap tunnel setup to effectively study the vortex dynamics of a pitching and heaving foil. The visualization of the vortex dynamics is based on the strong correlation between the vorticity field and thickness variations in the soap film. A high-frequency monochromatic SOX lamp enabled us to film the resulting interference fringes (due to thickness variations) of the soap film at high speed — time and space resolved.

The soap film can flow as slow as 0.25 ms^{-1} in our setup, 50% slower than previously published setups (Georgiev and Vorobieff 2002), which is essential for operating at both high *and* low stride lengths. Low stride lengths are obtained when the mechanism flaps at maximum frequency. The mechanism itself generates accurate and *symmetric* harmonic kinematics at all frequencies. We can preset the parameters of the harmonics (the heave amplitude, pitch amplitude, phase difference and flap frequency) with an error close to 5% or less.

To analyze the flow, we filtered and subsequently averaged a large series of images ($n = 99$). We then compared the average filtered images shot at a constant-phase with similar images shot at a 180°-phase-difference. We demonstrated the usefulness of such an approach for assessing the wake symmetry qualitatively. We could not find any reliable numerical method to assess the wakes asymmetry quantitatively; to our knowledge this is an open question.

The main advantage of our setup is that it facilitates a detailed and efficient study of the vortex wakes generated by flapping foils. The experiments are time-efficient — they only take 10 minutes per run, which is much faster than numerical simulations of similar flows on a high-end PC, which can take up to 30 days. Hence our experimental approach is ideally suited for a time-efficient study of the different vortex wake modes in the large parametric space of a flapping foil.

The main restrictions of our method are: it is limited to low Reynolds numbers, has a simplistic foil geometry and a fixed kinematics pattern (harmonic, two-dimensional), and the flow fields in the soap film are intrinsically two-dimensional. Within these constraints one can, however, use the results obtained with our setup as an efficient first order approximation of the more complicated three-dimensional flows generated by swimming animals such as thunniform swimmers. Interestingly we found, like others, asymmetric wakes for symmetric foil kinematics. The question emerges if thunniform swimmers encounter such wake modes during straight swimming.

Acknowledgements

We thank Johan van Leeuwen for supporting both D.L. and F.T.M.; Mees Muller and Ulrike Müller for their help; Jos van den Boogaard, Eric Karruppannan, Evert Janssen and Henk Schipper for helping us with the design and construction of the soap tunnel and flapping mechanism; Bas van Oudheusden for co-supervising F.T.M. at the TU Delft. We thank Marc van Geest for help with some of the preliminary experiments. Finally we would like to thank Maarten Rutgers for advice and great soap (Dawn from the USA rocks).

References

Chomaz J.M., Costa, M. (1998) Thin film dynamics. In 'Free surface flows' (ed. Kuhlmann, H.C. and Rath, H.J.). CISM courses & lectures 391:44–99

Couder Y., Chomaz J.M., Rabaud M. (1989) On the hydrodynamics of soap films. Physica D 37:384–405

David, C.T. (1978) The relationship between body angle and flight speed in free-flying Drosophila. Physiological Entomological 3:191–195

Georgiev D., Vorobieff P. (2002) The slowest soap-film tunnel in the Southwest. Rev. of Scientific Instruments 73:1177–1184

Gharib M., Derango. P. (1989) A liquid film (soap film) tunnel to study two-dimensional laminar and turbulent flows. Physica D 37:406–416.

Jones K.D., Dohring C.M., Platzer M.F. (1996) Wake structures behind plunging airfoils: A comparison of numerical and experimental results. AIAA 1996–0078:1–9

Lentink D., Gerritsma M. (2003) Influence of Airfoil Shape on Performance in Insect Flight. AIAA 2003–3447:1–17

Lentink D., Muijres F.T., Donker-Duyvis F.J., van Leeuwen J.L. (2007) Vortex-wake interactions of a flapping foil that models animal swimming and flight. J Exp Biol (submitted)

Lewin G.C. and Haj-Hariri H. (2003) Modelling thrust generation of a two-dimensional heaving airfoil in a viscous flow. J. Fluid Mech 492:339–362

Martin B., Wu X.L. (1995) Shear flow in a two-dimensional couette cell: a technique for measuring the viscosity of free-standing liquid films. Rev Sc Instr 66:5603–5608

Palmer G.T., Beach A.D. (1995) Sodium vapour discharge lamps with high-frequency electronic ballast for machine vision systems illumination. Meas Sci Technol 6:1634–1635

Read D.A., Hover F.S., Triantafyllou M.S. (2003) Forces on oscillating foils for propulsion and maneuvering. J Fluid Struct 17:163–183

Rivera M., Vorobieff P., Ecke R.E. (1998) Turbulence in flowing soap films: Velocity, vorticity, and thickness fields. Phys Rev Lett 81: 1417–1420

Rutgers M.A., Wu X-I., Bhagavatula R., Petersen A.A., Goldburg W.I. (1996). Two-dimensional velocity profiles and laminar boundary layers in flowing soap films. Phys Fluids 8: 2847–2854

Rutgers M. A. (1999) Flowing soap films: a platform for 2D non-linear dynamics experiments, Department of Physics, The Ohio State University, Columbus.

Rutgers M.A., Wu X.L., Daniel, W.B. (2001) Conducting fluid dynamics experiments with vertically falling soap films. Rev Sc Instr 72:3025–3037

Sfakiotakis M, Lane D.M., Davies J.B.C. (1999) Review of fish swimming modes for aquatic locomotion. J of Oceanic Engin 24:237–252

Triantafyllou G.S., Triantafyllou M.S., Grosenbaugh M.A. (1993) Optimal thrust development in oscillating foils with application to fish propulsion. J Fluids and Structures 7:205–224

Webb P.W, Weihs D. (1986) Functional locomotor morphology of early-life-history stages of fishes. Trans Am Fisher Soc 115: 115–127

Wen C.Y., Lai J.Y. (2003) Analogy between soap film and gas dynamics. I Equations and shock jump conditions. Exp in Fluids 34:107–114

Wen C.Y., Chang-Jian S.K., Chuang M.C. (2003) Analogy between soap film and gas dynamics. II Experiments on one-dimensional motion of shock waves in soap films. Exp in Fluids 34:173–180

Williamson C.H.K., Roshko A. (1988) Vortex formation in the wake of an oscillating cylinder. J Fluid Struc 2:355–381

Zhang J., Childress S., Libchaber A., Shelley M. (2000) Flexible laments in a flowing soap film as a model for one-dimensional flags in a two-dimensional wind. Nature 408:835–839.

3.3

SYMMETRICALLY AND PERIODICALLY FLAPPING FOILS MEDIATE CHAOTIC VORTEX-WAKE INTERACTIONS

David Lentink*, GertJan F. van Heijst, Florian T. Muijres and Johan L. van Leeuwen

We found abundant chaotic vortex-wake interactions mediated by a symmetrically and periodically pitching and heaving foil in a two-dimensional soap film tunnel. The phase-locked movie sequences reveal that chaotic vortex-wake interactions occur at high Strouhal numbers. These numbers are representative for the fins and wings of near-hovering animals. The chaotic wake limits the forecast horizon of the corresponding force and moment integrals. We find periodic vortex wakes with an unlimited forecast horizon for lower Strouhal numbers (0.2 – 0.4) at which animals cruise. Our two-dimensional model predicts that animals cope with chaos when they transition between cruising and hovering.

Many swimming and flying animals create large vortices with their fins and wings. These vortices are shed, and together they form the footprint of the animal in the fluid: the wake. In the wake vortices arrange in shapes and patterns that not only reflect the motion of animals, but also reflect the dynamics of vortex-vortex and vortex-animal interactions. Two well known examples of intense vortex-vortex interactions are vortex merging (Cerretelli and Williamson, 2003) and tearing (Legras and Dritschel, 1993; Trieling *et al.*, 1998). In some cases vortex-animal interactions are known to be beneficial to an animal's locomotory performance. Insects, for example, can recapture their vortex wake and thus generate extra lift (Dickinson *et al.*, 1999) while birds fly in formation to capture energy from each other's wake (Lissaman and Schollenberg, 1970). The dynamics of wake vortices might, however, not always be as easy to tune into.

Vortex wakes of animals are typically interpreted and drawn as a periodic row of alternating vortices. This is contrasted by several computational fluid dynamic studies of two-dimensional pitching and heaving (flapping) foils that model swimming and flight. Lewin and Haj-Hariri (2003) found aperiodic vortex flows generated by a heaving foil at low amplitude. At a higher heave amplitude representative of forward insect flight, Lentink and Gerritsma (2003) found chaotic vortex wake-interactions. The corresponding strange attractor in the phase plot of fluid lift and thrust is accompanied by a broad frequency spectrum and sensitivity to initial conditions. This finding has been confirmed for hovering insect flight by similar simulations in which the foil also pitched (Blondeaux *et al.*, 2005). In a more realistic simulation, in which the forward motion of the heaving foil results from the thrust generated by the heaving foil, also chaotic forward motion was found in a few cases (Alben and Chelley, 2005). For an even more realistic simulation in which the foil also pitched, Iima (2007) found a chaotic mode for free vertical motion, which corresponds to near-hovering flight. Chaos significantly limits the forecast horizon of the vortex dynamics and corresponding fluid forces (Lorenz, 1963). If animals actually need to cope with chaotic vortices and forces, it might well constrain their neural control of body motion. There exists, however, no experimental confirmation of chaotic vortex wake interactions generated by pitching and heaving foils.

Submitted

We experimentally determined to what extent chaotic vortex-wake interactions are mediated by a two-dimensional foil as a function of its kinematics. Our foil pitches and heaves periodically and symmetrically, 90° out of phase, in a nearly horizontal, gravity driven, soap film tunnel that flows at approximately 0.25 m / s, Fig. 1(a). We explicitly chose symmetric and periodic foil kinematics to ensure that measured asymmetric and aperiodic vortex-wake interactions can be linked explicitly to vortex dynamics. The foil is made out of a thin 4 mm long and 0.2 mm thick steel wire. It is attached to a custom designed and built flapping mechanism that accurately produces sinusoidal pitch and heave kinematics. Through pilot experiments we found that the stability of the soap film is unaffected by high flap frequencies of the foil (Lentink *et al.*, 2008), as found for vibrating cylinders (Couder *et al.*, 1989). We flapped the foil at 4-25 Hz and filmed its quasi two-dimensional vortex wake time- (500 Hz) and space- (1024×1280 pixels) resolved. For this we made use of the strong correlation between the vorticity field and minute thickness variations in the soap film (Rivera *et al.*, 1998). These thickness variations were visualized by illuminating the film with a monochromatic SOX lamp, which results in interference fringes that reveal the vortex wake (Rutgers *et al.*, 2001). A full description of the setup can be found in Muijres and Lentink (2007).

The vortex wake of vibrating cylinders is known (Williamson and Roshko, 1988) to synchronize with the cylinder when it vibrates with a wavelength λ close to multiples of the natural, von Kármán, vortex shedding wavelength λ_0. For vibrating cylinders two synchronization bands, starting at λ_0 and $3\lambda_0$, have been found. These two bands consist of periodic wakes and are separated by a region of aperiodic wakes. To determine if the vortex wake generated by the flapping foil synchronizes with flapping frequency, we first measured the dimensionless natural wavelength $\lambda_0^* = \lambda_0 / c$ of the wake behind the foil, in which c is chord length. We made peak to peak measurements and averaged them over 5 periods for effective angles of attack $\alpha_{eff} = 0°, 2.5°, \ldots, 90°$, Fig. 1(b). Like others (Katz, 1981; Dickinson and Gotz, 1993) we find that λ_0^* is constant for a foil when calculated using the vertical projection of chord length, i.e. $c \cdot \sin(\alpha_{eff})$, for $\alpha_{eff} \geq 45°$. On average we find $\lambda_0^* \cdot \sin(\alpha_{eff}) = 5.5$ with $std = 0.2$.

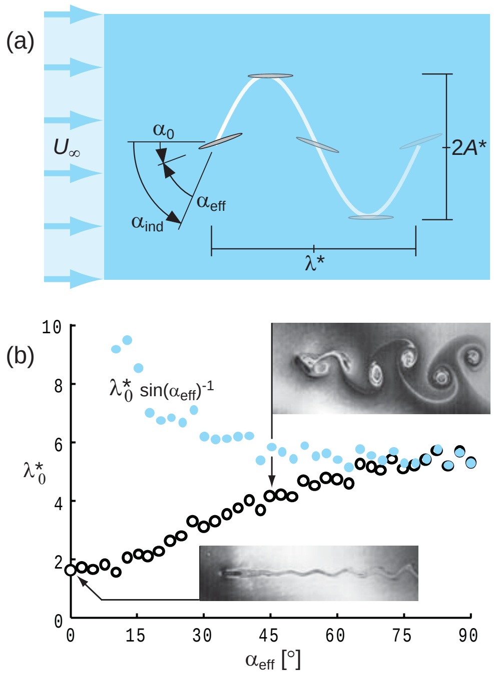

Fig. 1 | Foil kinematics and vortex shedding. (a) Definition of flapping kinematics of the foil (see text). The four heave phases for which we filmed the vortex wake are indicated with 'convected' foils along the foils path in the soap film. (b) Natural wavelength λ_0^* band of a foil as function of its angle of attack α_{eff}, indicated with black dots. At low angles we find a wavy shear layer in the wake, at high angles a von Kármán vortex wake shed by the foil. The blue dots indicate λ_0^* divided by $\sin(\alpha_{eff})$, which is approximately

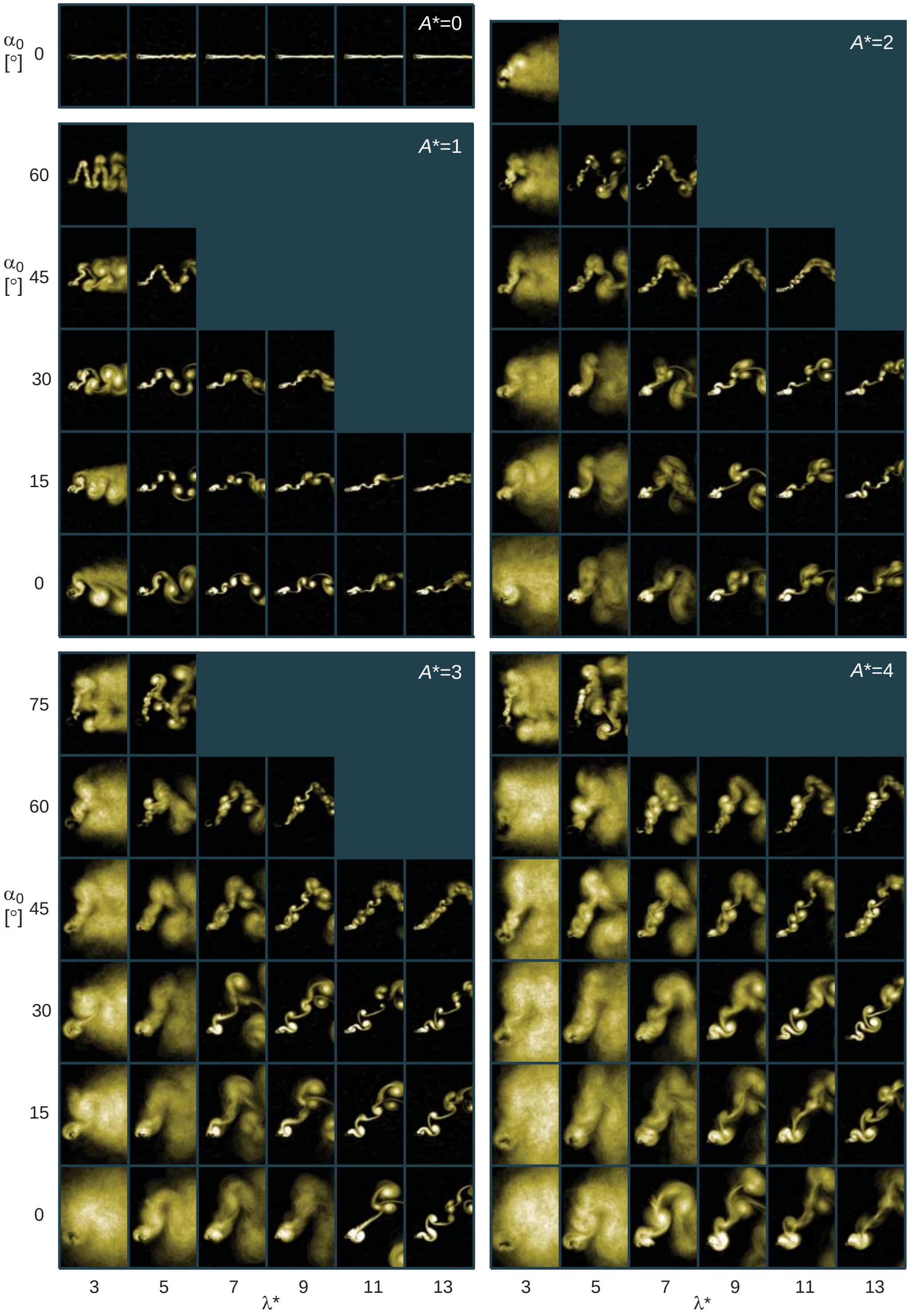
A*=0
A*=1
A*=2
A*=3
A*=4
α0 [°]
0
60
45
30
15
0
75
60
45
30
15
0
3
5
7
9
11
13
λ*
3
5
7
9
11
13
λ*

The flapping foil in our soap tunnel can generate thrust when the angle of attack amplitude induced by the foil's sinusoidal motion α_{ind} is larger than the pitch amplitude α_0, such that the effective angle of attack amplitude $\alpha_{eff} = \alpha_{ind} - \alpha_0 > 0°$, Fig. 1(a). The induced angle of attack amplitude is calculated as $\alpha_{ind} = \arctan\,(2\pi \cdot A^*/\lambda^*)$, in which $A^* = A/c$ is the dimensionless heave amplitude and $\lambda^* = U_\infty/fc$ is the dimensionless heave length, where A is the heave amplitude, U_∞ the free stream velocity and f the flap frequency (Lentink *et al.*, 2008), Fig. 1(a). The combinations of $(A^*, \lambda^*, \alpha_0)$ of the foil studied here are all combinations of ($A^* = 0, 1, ..., 4$; $\lambda^* = 3, 5, ..., 13$; $\alpha_0 = 0°, 15°, ..., 90°$) resulting in $\alpha_{eff} \geq 0°$, such that thrust is positive. These values of $(A^*, \lambda^*, \alpha_0)$ are most relevant for slender flapping wings and caudal fins of animals. The average Reynolds number Re of the flapping foil in our soap tunnel is $Re \approx Re_\infty \cdot \sqrt{1+(4A^*/\lambda^*)^2}$, in which $Re_\infty = U_\infty \cdot c/\nu \approx 1000$ is the free stream Reynolds number (Lentink *et al.*, 2008), with kinematic viscosity $\nu \approx 1 \cdot 10^{-6}\,m^2/s$ (Martin and Wu, 1995; Muijres and Lentink, 2007). We filmed the vortices shed by the flapping foil as a function of $(A^*, \lambda^*, \alpha_0)$ phase locked over 99 periods; at stroke reversal and midstroke, Fig. 1(a). Of every single image we first calculated the absolute gradient field and median filtered it (Matlab 2007; medfilt2, 5 × 5 pixels) to eliminate background fringes (Muijres and Lentink, 2007). Next small pollutants where automatically removed (Matlab; bwareaopen), after which we normalized and averaged all 99 image intensity fields. For periodic flows the average vortex wake at a constant phase is identical to the vortex wake of all individual images. For chaotic flow, the vortex wake at constant phase is erratic over the 99 frames and the average image is therefore blurred or even unrecognizable, Fig. 2. We enhanced the dynamic range of all average images and colored them using identical Photoshop image adjustments (auto levels, shadow / highlight, tri-tone coloring). Several standard periodic wake types can be found at $A^* = 1$, such as 'two vortex pairs' at ($\lambda^* = 5$, $\alpha_0 = 15°, 30°$) and 'two single vortices' at ($\lambda^* = 5$, $\alpha_0 = 0°$) per flap period. These periodic vortex configurations are typical for vortex-wake synchronization and have been found earlier for flapping foils and vibrating cylinders (Williamson and Roshko, 1988). Additionally we find, however, many other topologically more complicated patterns. By visual inspection of Fig. 2, it can be seen that many vortex wakes are chaotic, ranging from partially chaotic in the far-field e.g. ($A^* = 4$, $\lambda^* = 11$, $\alpha_0 = 30°$) to fully chaotic e.g. ($A^* = 4$, $\lambda^* = 3$, $\alpha_0 = 0°$). In an earlier study we described the detailed transition from a periodic to an aperiodic vortex wake as a function of leading and trailing edge vortices shed, and vortex merging and tearing in the wake (Lentink *et al.*, 2008). Here we also find that vortex wake interactions such as merging and tearing can alter wake topology. At higher Reynolds numbers we also observe that the shear layer rolling up at the leading edge can become unstable, such that the leading edge vortex consists of a number of smaller vortices (Wang *et al.*, 1999), especially at high α_{eff}. At high α_{ind} we also find that the foil flaps through its previously shed vortices, which it shears and tears. Through visual inspection of the movie sequences, both phase locked over 99 flap periods and continuously over three periods, we observed that the vortex wakes are more chaotic for more intense vortex-wake interactions.

To quantify the significance of chaotic vortex wakes we calculated the standard deviation of the moment of area integrals of the 99 normalized image intensity fields we filmed phase

Fig. 2 | Abundant chaotic vortex-wake interactions in the parametric space of flapping foil kinematics; dimensionless heave amplitude A* and wave length λ^*, and pitch amplitude α_0. Shown are phase locked averages of 99 filtered wake images. The more blurry an average image is the more chaotic the vortex wake, white bright areas are periodic. The dark grey areas correspond with $\alpha_{eff} < 0$, negative thrust, for which we made no measurements.

locked. Before integrating the intensity fields I we simplified every image into a black and white image with an intensity of 1 where we visualized vortices and 0 elsewhere (cut-off value 0.17) (Muijres and Lentink, 2007). We next determined the first three polar moments of area of these image intensity fields: area, $I_0 = \iint Idxdy$; first polar moment, $I_{1,r} = \left(\iint xIdxdy^2 + \iint yIdxdy^2\right)^{1/2}$; and second polar moment $I_{2,r} = \iint (x^2 + y^2) Idxdy$. A theoretical analysis of Wu (1981) shows that if we would calculate these moments of area for the vorticity field instead of the filtered image intensity field, I_0 would represent circulation, whereas $I_{1,r}$ and I_{2r}would be part of the integrals for calculating net force and moment, respectively (Wu, 1981). Here we assume that if the image intensity integrals of the vortex wake are chaotic that the corresponding integrals for calculating circulation, force and moment will be chaotic too. Hence we calculate the three intensity moments of area sequences for the 99 images of all four flap phases (area of integration starts $c/4$ behind the foil with width 8*c* and height 16*c*). Because we are primarily interested in short term variation, we subtract the period-16 Butterworth filtered moment of area sequence from the original sequence per phase (Matlab, 4th order butter). We next determine the standard deviation, which we average over all four flap phases. These standard deviations are plotted for I_0, I_{1r} and I_{2r} as a function of foil kinematics and we find their relative magnitude to correlate well; when standard deviation of one moment of area is high, others are too, Fig. 3(a). The standard deviation peaks for maximal heave amplitude, minimal heave wavelength and zero pitch amplitude. Further, the standard deviation of all three moments of area correlates well with the blurriness of the average wake images in Fig. 2. A gradual boundary exists between the periodic and chaotic vortex wakes. This boundary appears not to be connected through a 'synchronization band' with the λ_0^* band of Fig. 1(b) for $A^* = 0$, which we indicated in yellow in Fig. 3(a). The wake amplitude, however, increases as λ^* approaches the λ_0^* band for ($A^* = 0$, $\lambda^* = 3\text{-}13$, $\alpha_0 = 0°$); see panel $A^* = 0$ in Fig. 2. Both this amplified wave and the many periodic vortex wakes suggest that synchronization phenomena do occur. The synchronization between the vortex wake and a flapping foil is probably more complex due to the band width of λ_0^* of a foil, compared to the single valued λ_0^* of a cylinder (Lentink *et al.*, 2008). And perhaps more importantly, a finer resolution in the (A^*, λ^*, α_0) space is needed to clearly distinguish synchronization bands.

By plotting the standard deviation of the moment of area integrals as a function of the induced and effective angle of attack we find that the standard deviation is maximal at high angles, corresponding with the area delineated by the dashed line in Fig. 3(b). In this graph we observe a gradient between two different regimes; a periodic regime at low α_{ind} and a chaotic regime at high α_{ind}. The most-chaotic wakes occur at high α_{ind} along the line $\alpha_{eff} = \alpha_{ind}$, which corresponds with plunging motion. Plunging foils have zero pitch amplitude, and therefore minimal thrust, which makes them inefficient (Lentink and Gerritsma, 2003). Triantafyllou *et al.* (1993) found that pitching and heaving foils are most efficient for Strouhal numbers $St = \tan(\alpha_{ind}) / \pi$ in the range 0.2–0.4. Many swimming and flying animals actually cruise in this *St* range (Triantafyllou *et al.*, 1993, Taylor *et al.*, 2003), for which we find solely periodic vortex-wake interactions, Fig. 3(b). When animals transition from cruising to hovering their *St* increases and, approaches infinity as α_{ind} approaches 90°. For such high *St*–values we find abundant chaotic vortex-wake interactions, suggesting therefore that animals cope with chaos at high *St*-values.

Our measured standard deviations of the moment of area integrals of the non-zero vorticity field are high for high *St*-values, for which we find chaotic vortex-wake interactions. Existing numerical simulations confirm that the net forces and moments can indeed become chaotic in two dimensions (Lewin and Haj-Hariri, 2003; Lentink and Gerritsma, 2003; Blondeaux *et al.*,

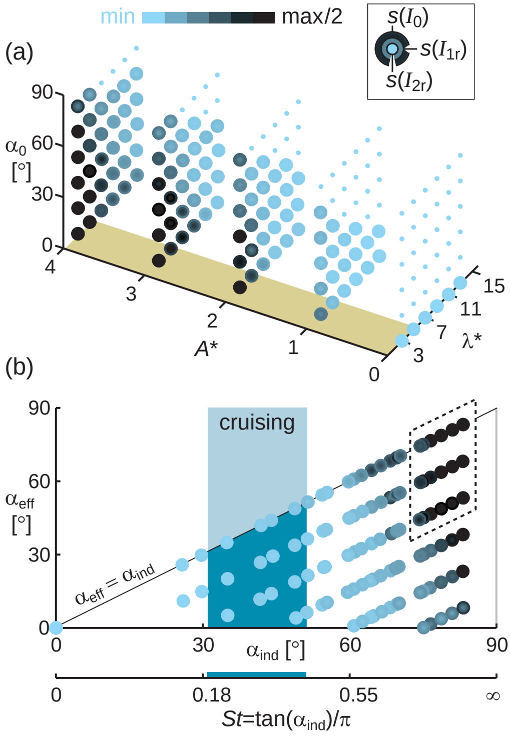

Fig. 3 | Standard deviation of the moment of area integrals. (a) Standard deviation of the moment of area integrals plotted as a function of foil kinematics. We plotted three filled circles with different radii on top of each other, of which the color corresponds with the standard deviation of I_0 (outer circle), I_{1r} (middle circle), and I_{2r} (inner circle); see the illustration in the boxed area. (Note that all flat circles are plotted such that they face the page.) The magnitude of the standard deviation of the moments of area $(0.4c)^2 \leq s(I_0) \leq (2.6c)^2$; $(1.2c)^3 \leq s(I_{1r}) \leq (4.1c)^3$; $(2.1c)^4 \leq s(I_{2r}) \leq (5.6c)^4$ are color coded from min. to max./2; We find no compelling evidence for synchronization bands that start at λ^* values that are multiples of the λ_0^* band. Small blue dots indicate points for which $\alpha_{eff} < 0$. (b) Same data as shown in (a), now plotted as function of α_{eff} and α_{ind}, standard deviation peaks in the area delineated by the dashed line. Animals preferably cruise at low Strouhal numbers *St,* in the range 0.2 to 0.4, for which we find solely periodic vortex-wake interactions. Chaos occurs at the higher Strouhal numbers of near-hovering motion when α_{ind} approaches 90°.

2005). Simulations in which forward or upward motion is unconstrained show that chaotic forces result in erratic motion due to chaotic vortex-body interactions (Alben and Chelley, 2005; Iima, 2007). A free flight model of a butterfly, based on potential vortex flow, further shows that there is also a tight coupling between vortex-wake dynamics and flight path in three dimensions (Senda *et al.*, 2008). In fact, it has been found that relatively subtle changes in the wing kinematics of red admirals can radically changes the aerodynamic mechanism they use to fly, which includes vortex-wake capture (Srygley and Thomas, 2002). Many insects, in particular butterflies and moths, are known to fly erratically to presumably confound predators (Dudley, 2000). How insects generate these erratic flight paths is unknown. Insects could simply flap erratically, but this is contrasted by the relatively subtle kinematic changes found in butterflies (Srygley and Thomas, 2002). An alternative explanation could be that these insects exploit the chaotic vortex-wake interactions similar to the ones we found for a two-dimensional symmetrically and periodically flapping foil. Perhaps butterflies tune into such chaotic vortex-wake interactions to exploit the 'butterfly effect' themselves and limit the forecast horizon of their flight path, making them hard to catch. This could be tested using three-dimensional fluid dynamic simulations or robot models to determine to which extent three-dimensional flapping wings mediate chaotic vortex-wake interactions.

References

Alben, S. and Shelley, M. (2005). Coherent locomotion as an attracting state for a free flapping body, *PNAS* **102**, 11163-11166.

Blondeaux, P., Guglielmini, L. and Triantafyllou, M. S. (2005). Chaotic flow generated by an oscillating foil. *AIAA J.* **43**, 918-922.

Cerretelli, C. and Williamson, C. H. K. (2003). The physical mechanism for vortex merging *J. Fluid Mech.* **475**, 41-77.

Couder, Y., Chomaz, J. M. and Rabaud, M. (1989). On the hydrodynamics of soap films. *Physica D* **37**, 384-405.

Dickinson, M. H. and Götz, K. G. (1993). Unsteady aerodynamic performance of model wings at low Reynolds numbers. *J. Exp. Biol.* **174**, 45-64.

Dickinson, M. H., Lehmann, F. O. and Sane, S. P. (1999). Wing rotation and the aerodynamic basis of insect flight. *Science* **284**, 1954-1960.

Dudley, R. (2000). *The biomechanics of insect flight*. Princeton University Press.

Iima, M. (2007). A two-dimensional aerodynamic model of freely flying insects. *J. Theor. Biol.* **247**, 657-671.

Katz, J. (1981). A discrete vortex method for non-steady separated flow over an airfoil. *J. Fluid Mech.* **102**, 315–328.

Lentink, D. and Gerritsma, M. I. (2003). Influence of airfoil shape on performance in insect flight. *AIAA* 2003-3447.

Lentink D., Muijres, F. T., Donker-Duyvis, F. J. and van Leeuwen J. L. (2008). Vortex-wake interactions of a flapping foil that models animal swimming and flight. *J. Exp. Biol.* **211**, 267-273.

Lewin, G. C. and Haj-Hariri, H. (2003). Modelling thrust generation of a two-dimensional heaving airfoil in a viscous flow. *J. Fluid Mech.* **492**, 339-362.

Legras B. and Dritschel D. (1993). Vortex stripping and the generation of high vorticity gradients in two-dimensional flows. *Appl. Sci. Res.* **51**, 445-455.

Lissaman, P. B. S. and Schollenberg, C. A. (1970). Formation flight of birds. *Science* **168**, 1003-1005.

Lorenz, E. N. (1963). Deterministic nonperiodic flow. *J. Atmos. Sci.* **20**, 130-141.

Martin B. and Wu X. L. (1995) Shear flow in a two-dimensional Couette cell: a technique for measuring the viscosity of free-standing liquid films. *Rev. Sc. Instr.* **66**, 5603-5608.

Muijres, F. T. and Lentink, D. (2007). Wake visualization of a heaving and pitching foil in a soap film. *Exp. Fluids* **43**, 665-673.

Rivera, M., Vorobieff, P. and Ecke, R. E. (1998) Turbulence in flowing soap films: Velocity, vorticity, and thickness fields. *Phys. Rev. Lett.* **81**, 1417.

Rutgers, M. A., Wu, X. L. and Daniel, W. B. (2001). Conducting fluid dynamics experiments with vertically falling soap films. *Rev. Sc. Instr.* **72**, 3025-3037.

Senda, Sawamoto, K. M., Kitamura, M. and Tanaka, T. (2008). Stabilization of flapping-of-wings flight of a butterfly, considering wakes. In: *Bio-mechanisms of Swimming and Flying*. Ed. Naomi Kato and Shinji Kamimura, Springer books.

Taylor, G. K., Nudds, R. L. and Thomas, A. L. R. (2003). Flying and swimming animals cruise at a Strouhal number tuned for high power efficiency. *Nature* **425**, 707-711.

Triantafyllou, G. S., Triantafyllou, M. S. and Grosenbaugh, M. A. (1993). Optimal thrust development in oscillating foils with application to fish propulsion. *J. Fluid Struc.* **7**, 205-224.

Trieling, R. R., Linssen, A. H. and van Heijst, G. J. F. (1998). Monopolar vortices in an irrotational annular shear flow. *J. Fluid Mech.* **360**, 273-294.

Wang, Z. J., Liu, J. G. and Childress, S. (1999). Connection between corner vortices and shear layer instability in flow past an ellipse *Phys. Fluids* **11**, 2446-2448.

Williamson C. H. K. and Roshko A. (1988). Vortex formation in the wake of an oscillating cylinder. *J. Fluid Struc.* **2**, 355-381.

Wu, J. C. (1980). Theory for aerodynamic force and moment in viscous flow. *AIAA J.* **19**, 432-441.

4 Take-off into the third dimension

4.1

ROTATIONAL ACCELERATIONS STABILIZE LEADING EDGE VORTICES ON REVOLVING FLY WINGS

David Lentink* and Michael H. Dickinson

Summary

The aerodynamic performance of hovering insects is largely explained by the presence of a stably attached leading edge vortex (LEV) on top of their wings. Although LEVs have been visualized on real, physically-modelled, and simulated insects, the physical mechanisms responsible for their stability are poorly understood. To gain fundamental insight into LEV stability on flapping fly wings we express the Navier-Stokes equations in a rotating frame of reference attached to the wing's surface. Using these equations we show that LEV dynamics on flapping wings are governed by three terms: angular, centripetal, and Coriolis acceleration. Our analysis for hovering conditions shows that angular acceleration is proportional to the inverse of dimensionless stroke amplitude, whereas Coriolis and centripetal acceleration are proportional to the inverse of the Rossby number. Using a dynamically-scaled robot-model of a flapping fruit fly wing to systematically vary these dimensionless numbers, we determine which of the three accelerations mediate LEV stability.

Our force measurements and flow visualizations indicate that the LEV is stabilized by the 'quasi-steady' centripetal and Coriolis accelerations that are present at low Rossby number and result from the propeller-like sweep of the wing. In contrast, the unsteady angular acceleration that results from the back and forth motion of a flapping wing does not appear to play a role in the stable attachment of the LEV. Angular acceleration is, however, critical for LEV integrity as we found it can mediate LEV spiral bursting, a high Reynolds number effect.

Our analysis and experiments further suggest that the mechanism responsible for LEV stability is not dependent on Reynolds number, at least over the range most relevant for insect flight ($100 < Re < 14{,}000$). LEVs are stable and continue to augment force even when they burst. These and similar findings for propellers and wind turbines at much higher Reynolds numbers suggest that even large flying animals could potentially exploit LEV-based force augmentation during slow hovering flight, take-offs, or landing. We calculated the Rossby number from single-wing aspect ratios of over 300 insects, birds, bats, autorotating seeds, and pectoral fins of fish. We found that, on average, wings and fins have a Rossby number close to that of flies ($Ro = 3$). Theoretically, many of these animals should therefore be able to generate a stable LEV, a prediction that is supported by recent findings for several insects, one bat, one bird, and one fish. This suggests that force augmentation through stably attached (leading edge) vortices could represent a convergent solution for the generation of high fluid forces over a quite large range in size.

Submitted

Introduction

The presence of a stable leading edge vortex (LEV) is a key feature in the unexpectedly high performance of insect wings during hovering flight (Maxworthy, 1979; Ellington *et al.*, 1996; Dickinson *et al.* 1999; Srygley and Thomas, 2002). Whereas a LEV is shed after a few chord lengths of travel on a translating 2D model of an insect wing (Dickinson and Götz, 1993; Dickinson,1994; Miller and Peskin 2004; Lentink *et al.* 2008), it remains stably attached on a 3D model wing that revolves about its base (Dickinson *et al.*, 1999; Usherwood and Ellington, 2002; Birch *et al.*, 2004). Van Den Berg and Ellington (1997) note that the spiral LEV generated by their mechanical model of a hawkmoth wing is remarkably similar to the spiral LEV generated by delta and swept wings (Ellington *et al.*, 1996; Van Den Berg and Ellington, 1997). The spiral LEVs on such swept wings are stabilized by spanwise flow induced by wing sweep, suggesting that spanwise flow is similarly cridigtical to the stability of LEVs on insect wings (Ellington *et al.*, 1996; Van Den Berg and Ellington, 1997). Specifically, the growth of the LEV on insect wings might be stabilized by spanwise flow in the core of the LEV, driven either by the dynamic pressure gradient associated with the velocity gradient along the flapping wing, by 'centrifugal' acceleration in the boundary layer, or by the induced velocity field of the spiral vortex lines (Ellington *et al.*, 1996). An additional hypothesis is that the flow induced by the strong tip vortices of low aspect ratio insect wings stabilizes the LEV by greatly lowering the effective angle of attack (Birch and Dickinson, 2001). An attempt to block spanwise flow using a variety of baffle found little or no effect on LEV strength or stability (Birch and Dickinson, 2001), but these experiments do not clearly identify a unique explanation for LEV stability.

We start with showing experimentally that neither the swept-wing analogy or induced flow due to the tip vortex can fully explain LEV stability on fly wings. Based on the notion that revolving insect wings also stabilize LEVs (Dickinson *et al.*, 1999; Usherwood and Ellington, 2002; Birch *et al.*, 2004) we then derive the Navier-Stokes equations for flapping wings using a coordinate transformation that attaches the frame of reference to the surface of the flapping wing (Lentink and Dickinson, 2008). This analysis shows how wing kinematics can potentially stabilize the LEV on a revolving wing. Based on the two governing dimensionless numbers, Rossby number (*Ro*) and dimensionless stroke amplitude (A^*), we then carry out a set of experiments to determine whether any of these dimensionless numbers mediate LEV stability through their corresponding accelerations. Using both flow visualization and force measurements we show that *Ro*, and not A^*, appears to explain LEV stability. We then compare our theoretical and experimental findings to literature on other wings and fins in nature and technology.

Materials and Methods

The basic methods used for dynamically scaling an insect wing have been described previously (Dickson and Dickinson, 2004). We constructed a model *Drosophila melanogaster* wing from 2.0-mm thick clear acrylic plate with a (single) wingspan b_s of 0.187 m and surface area S of 0.0167 m^2 . Mean chord width c is defined as S/b_s. Here and elsewhere our wing parameters (b_s, S, and c) refer to single wings, not a bilateral wing pair. The force sensor connects the robot arm with the wing base which results in a wingtip radius R of 0.254 m. The wing was attached to a force transducer in series with a 3 degree of freedom actuator which was connected to a translating robot arm immersed in a 1x1x2 m tank filled with either oil or water. The Reynolds number was calculated as $Re = cU_g/\nu$ in which c is average chord length, U_g the average velocity at the radius of gyration R_g (Ellington, 1984) and ν the kinematic viscosity. The tank was filled with thick mineral oil (density $\rho = 840\,\mathrm{kg\,m^{-3}}$; $\nu = 140 \cdot 10^{-6}\,\mathrm{m^2\,s^{-1}}$) to obtain $Re = 110$, thin mineral oil ($\rho = 830\,\mathrm{kg\,m^{-3}}$; $\nu = 11.0 \cdot 10^{-6}\,\mathrm{m^2\,s^{-1}}$) to obtain $Re = 1400$ and water ($\rho = 998\,\mathrm{kg\,m^{-3}}$; $\nu = 1.004 \cdot 10^{-6}\,\mathrm{m^2\,s^{-1}}$) to obtain $Re = 14{,}000$.

In our experiments we use the following kinematic patterns for flapping: sinusoidal motion for stroke position and smoothed trapezoidal for angle of attack motion (Dickinson *et al.*, 1999). We based the stroke amplitude of 70° in our experiments on the free flight kinematics of six slowly hovering fruit flies (Fry *et al.*, 2003). Note that we use amplitude in the mathematical sense, which is equal to half the total wing amplitude as defined by Ellington (1984). In each flapping trial, the robot flapped for six complete periods. The geometric angle of attack amplitude α_0 was varied from 0° to 90° with steps of 4.5° (for definitions of flapping kinematics see Sane and Dickinson, 2001; Lentink and Dickinson, 2008). The unidirectional revolving and translating wing kinematics consisted of a constant velocity stroke with constant acceleration and deceleration to begin and end the stroke. The duration of the acceleration was 10% of the stroke for both revolving and translating wings. As with flapping trials, α_0 was varied from 0° to 90° in steps of 4.5°. The revolving wing swept over an arc of 320°; the travel distance of the translating wing was calculated such that it moved over a similar distance as the revolving wing at its radius of gyration.

We generated a range of Rossby numbers (*Ro*) for a particular Reynolds number ($Re = 1400$) by elongating the robot arm by factors of 1.27 and 1.53, which increased *Ro* at the radius of gyration to 3.6 and 4.4, respectively. The unidirectionally- and reciprocally-translating wing kinematics ($Ro = \infty$) were obtained by setting the stroke amplitude of the robot arm to zero and translating the stage to which it was fixed. The stroke amplitudes for the $Ro = 3.6$, 4.4, and ∞ cases were calculated under the condition that the actuator disk area (Stepniewski and Keys, 1984), swept by the wing during the stroke was identical to within a precision of $< 0.1\%$. The average Reynolds number at R_g varies $< 0.5\%$ for unidirectional and $< 5\%$ reciprocating kinematics.

Flow visualization using air bubbles.

We released small air bubbles at the leading edge (~25 mm apart) and trailing edge (~30 mm apart) of the wing into the oil (at $Re = 110$ and 1400). Air was transported to the leading and trailing edges using a 2 mm thin tube glued flush to the edge of the 2 mm thick wing such that the flow was minimally disturbed by the tube. We made holes in the tube, marked with a white dot of paint, using insect pins. The air bubbles released through these holes rise upward because they are not neutrally buoyant and thus do not form perfect streak lines. This method is, however, particularly suited for LEV visualization because the bubbles will be drawn into strong vortices with low pressure cores resulting in tight spirals while weaker and wider vortices will result in wider spirals of bubbles. In addition, the bubbles will be driven preferentially inward (from wingtip to base) under centrifugal loading, because of their low density. Thus, bubbles that flow outward reliably indicate outward flow.

We visualized the flow around translating and revolving wings with either unidirectional or reciprocating stroke kinematics for $\alpha_0 = 0°$, 18°, 36°, 45°, 54°, 72° and 90°. For image recording we used a digital monochrome Basler camera: 656 x 491, sampling at 100 frames per second.

For flapping wings we obtained visualizations for 6 flap periods. We excluded the first cycle and determined the time of bursting for the subsequent 5 periods at $Re = 1400$. The images have been enhanced with the Auto Contrast function of Photoshop (8.0, Adobe) and the online movies are compressed with VirtualDub (1.5.10, www.cole2k.net).

Lift and drag measurements

The lift and drag forces acting on the wing were measured with a custom-built force sensor as previously described (Dickinson *et al.*, 1999; Birch and Dickinson, 2001; Birch *et al.*, 2004; Dickson and Dickinson, 2004). For post processing we down-sampled the measurements at 300Hz, which is still approximately 1400 times the flapping frequency. The force signals were filtered offline using a zero phase delay low-pass 4-pole digital Butterworth filter. The cut-off frequency was determined such that it corresponded with an average distance travelled of 0.3 chord lengths at R_g. This distance is at least ten times lower than the distance over which an LEV is known to shed (Dickinson, 1994; Dickinson and Götz, 1993). The forces of the wing with reciprocating kinematics (6 flaps) were averaged over 4 cycles (2^{nd}-5^{th}) whereas they were averaged between 70% and 90% of the stroke period for wings with unidirectional kinematics (to exclude the start and stop transient). The final values were obtained as an average of 3 trials, except for the unidirectionally-translating case at $Re = 110$ and the swept wing polars for which $n = 1$.

For a fair comparison among experiments we calculated how effective a wing generates force for equal dynamic pressures, which is the standard approach in engineering and animal flight literature. These force coefficients were calculated based on the mean dynamic pressure $1/2\,\rho\overline{V_g^2}$ which we calculated using a blade element method (Ellington, 1984; Dickinson *et al.*, 1999; Sane and Dickinson, 2001; Dickson and Dickinson, 2004). The lift coefficient was calculated as $C_L = 2\overline{L}\big/\rho S\overline{V_g^2}$ whereas the drag coefficient was calculated as $C_D = 2\overline{DV_g}\big/\rho S\overline{V_g^2}^{3/2}$ in which V_g is the velocity at the radius of gyration, ρ the density, and S the wing surface area. According to this definition,

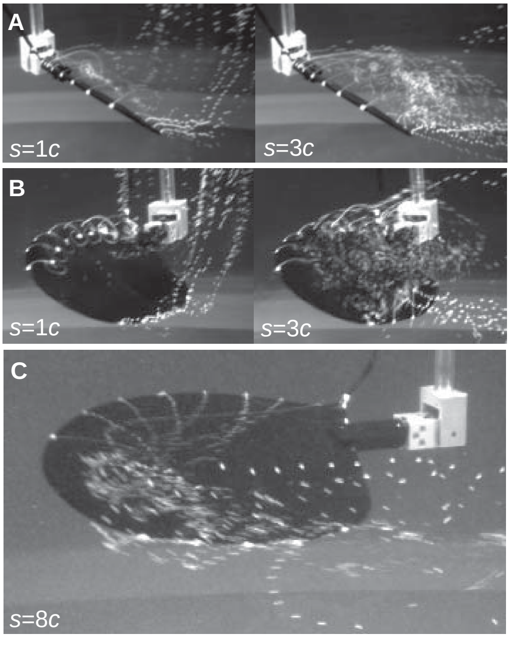

Fig. 1 | The leading edge vortex (LEV) sheds from a translating model insect wing, regardless of its sweep angle, whereas it remains stably attached when the wing revolves. The LEV is visualized at $Re = 110$ and 1400 with small air bubbles released at the leading and trailing edges of the wing. The distance traveled by the wing s is given in chord lengths c at the radius of gyration R_g. (A) LEVs are unstable on swept wings, shown for 40° sweep at $\alpha = 36°$ and $Re = 1400$. (B) The LEV is also unstable on the same wing without sweep. (C) Revolving the same wing results in a LEV that remains stably attached, shown for clarity at $Re = 110$ and $s = 8c$.

C_D reduces to the classic drag coefficient for the translational kinematics. For revolving wing kinematics, C_D is the mean drag coefficient, which is equal to the power coefficient in the case that the local drag coefficient does not change along the wing's radius.

Results

Test of existing hypotheses

Using the dynamically-scaled fly wing (*Drosophila melanogaster*) (Dickson *et al.*, 1999; Dickson and Dickinson, 2004) to measure forces and visualize flows, we first tested whether wing sweep and tip effects alone could stabilize a LEV on a fly wing that was translating (but not revolving) at fixed velocity. We systematically varied sweep angle from 0° to 60° over a large range of angles of attack (0° and 90°). The results, performed at *Re* = 110 and 1400, show that wing sweep cannot stabilize the LEV (Fig. 1A, supplementary movie 1). Further, the results at zero sweep angle indicate that the presence of a tip vortex is also insufficient to stabilize the LEV (Fig. 1B, supplementary movie 2). It is important to note that the same wing generates a stable LEV and elevated forces when revolved at constant angular velocity around its base (Fig. 1C and supplementary movie 3), as found by others (Dickinson *et al.*, 1999; Usherwood and Ellington, 2002; Birch *et al.*, 2004). The translating swept fly wing did not only rapidly shed its LEV it actually generates less lift than the unswept wings at Reynolds numbers of 110 and 1400 (Fig. 2). Thus, a strict analogy of the mechanisms that operates to stabilize LEVs on swept wing aircraft does not appear to hold for insect wings.

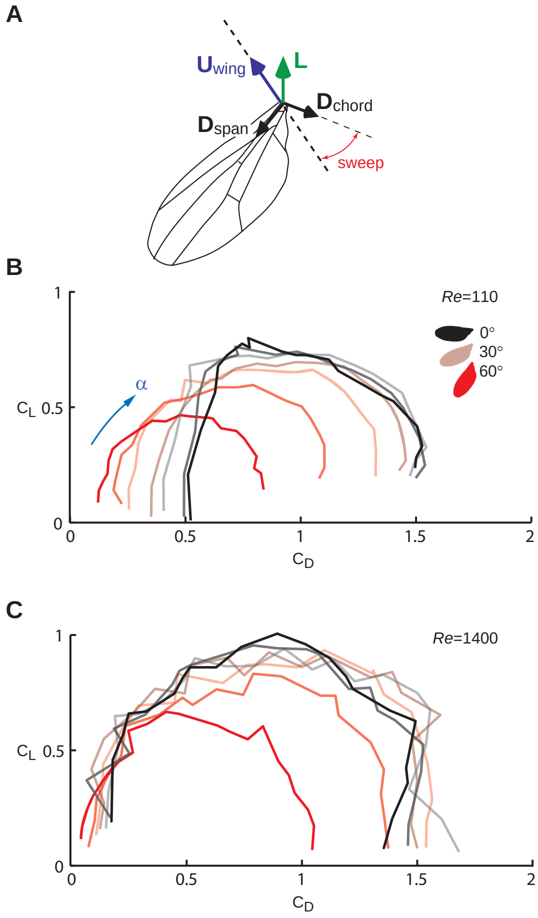

Fig. 2 | Sweep does not increase the lift created by a translating fruit fly wing at *Re* = 110 and 1400. (A) The lift (C_L) – drag (C_D) polar shown for *Re* = 110 (B) and *Re* = 1400 (C), represents the dimensionless lift (**L**) and chordwise drag (**D**$_{\text{chord}}$) forces obtained by varying the angle of attack from 0°-90° in steps of 4.5°. We tested this for wing sweeps from 0°; indicated with black, to 60°; indicated with red, in increments of 10° sweep.

In addition, the shed LEV and low performance of an unswept, translating wing indicates that tip effects alone cannot generate a stable LEV, at least not at the aspect ratio of our model fly wing. Tip effects, however, do appear to explain LEV stability on wings with very low aspect ratios close to one and less (Winter, 1936; Ringuette, 2007).

These preliminary experiments motivated us to explicitly examine the role of revolving, propeller-like, motion in LEV stability. When hovering, most insects flap their wings back and forth in a roughly horizontal stroke plane. At each stroke reversal, the wings rapidly flip over and change direction, during which time the forces and flows are highly unsteady. The LEV created at the start of one stroke sheds, and a new counter-rotating LEV forms as the wing flips over and reverses direction (Poelma, *et al.*, 2006). However, during each half-stroke (i.e the upstroke and the downstroke), the motion is 'propeller-like' in that the wing revolves around its base at roughly constant angle of attack (UsherwoodandEllington, 2002). Our working hypothesis is that some feature of the fluid dynamics intrinsic to this revolving, propeller-like motion is responsible for the stability of the LEV. We explore this hypothesis by first identifying a complete list of rotation-based fluid accelerations that theoretically could be responsible for LEV stability, which we then test experimentally.

Navier-Stokes equations for flow near a flapping wing

We developed a simple theoretical framework to identify the dimensionless numbers that might influence flow near wings undergoing both unidirectional (propeller-like) and reciprocating (insect-like) motion during hovering conditions. A key feature of our analysis is that it accommodates a continuous range of stroke kinematics from pure revolving to pure translational motion. The analysis is continuous because translation represents the limiting case of a wing revolving over an infinitesimal angle about an infinite radius (Fig. 3A), in this sense a translating wing performs hovering flight around an infinite turning radius. For a consistent comparison among experiments, three key conditions are met with good approximation. First, the area swept by the

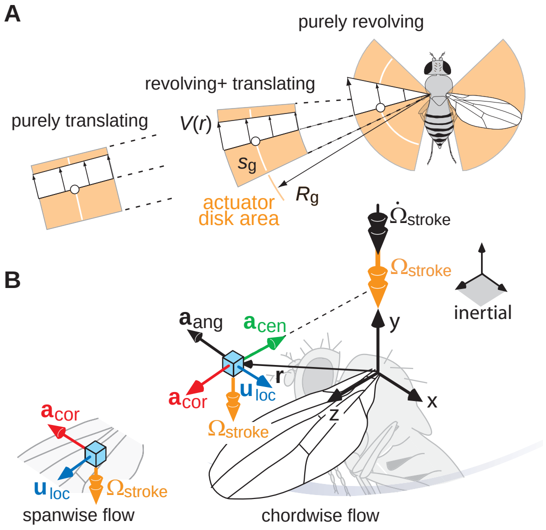

Fig. 3 | Theoretical and experimental approach. (A) Framework used to analyze fluid accelerations on translating and revolving wings. The area of the actuator disk is constant within the model. R_g is the radius of gyration, s_g the number of chord lengths traveled at R_g during a full stroke, and $V(r)$ is the velocity distribution along the wings radius r. (B) In the wing-bound frame, the fluid close to the wing experiences three accelerations due to the wing's stroke kinematics: an angular acceleration $\mathbf{a}_{ang}$ a centripetal acceleration $\mathbf{a}_{cen}$ and a Coriolis acceleration $\mathbf{a}_{cor}$. Note that $\mathbf{u}_{loc}$ is the local velocity in the wing-bound frame, $\mathbf{\Omega}_{stroke}$ is the angular velocity due to stroke, and $\dot{\mathbf{\Omega}}_{stroke}$ is the angular acceleration due to stroke.

revolving wing is kept constant, thereby maintaining constant Froude efficiency (Stepniewski and Keys, 1984). Second, the dimensionless stroke amplitude (A^*) at the radius of gyration (Ellington, 1984) is kept constant to ensure that wing-wake interactions (Birch and Dickinson, 2003) are similar. Finally, *Re* at the radius of gyration is kept constant as well (Fig. 3A). The most convenient theoretical framework for such an analysis is a dimensionless form of the Navier-Stokes equations, expressed in a non-inertial frame of reference fixed to the revolving wing in *hovering* flight (for derivation see Lentink and Dickinson, 2008, see also Vanyo, 1993; Greitzer *et al.*, 2004). The dimensionless fluid acceleration due to net viscous and pressure forces acting on a fluid 'particle' in an inertial frame $\mathbf{a}_{\mathrm{inert}}$ is related to that in the rotating frame $\mathbf{a}_{\mathrm{loc}}$ by (Baruh, 1999):

$$\mathbf{a}_{\mathrm{inert}} = \mathbf{a}_{\mathrm{loc}} + [\mathbf{a}_{\mathrm{ang}} + \mathbf{a}_{\mathrm{cen}} + \mathbf{a}_{\mathrm{Cor}}], \text{ where} \tag{1}$$

$$\mathbf{a}_{\mathrm{ang}} = 1/A^* \cdot \dot{\mathbf{\Omega}} \times \mathbf{r}, \tag{2}$$

$$\mathbf{a}_{\mathrm{cen}} = 1/Ro \cdot \mathbf{\Omega} \times (\mathbf{\Omega} \times \mathbf{r}), \text{ and} \tag{3}$$

$$\mathbf{a}_{\mathrm{cor}} = 1/Ro \cdot 2\mathbf{\Omega} \times \mathbf{u}_{\mathrm{loc}}. \tag{4}$$

Here, $\mathbf{\Omega}$ is the angular velocity and $\dot{\mathbf{\Omega}}$ is the angular acceleration of the rotating frame, and $\mathbf{r}$ and $\mathbf{u}_{\mathrm{loc}}$ are the position and velocity of a fluid volume in the rotating frame, respectively (Fig. 3B). The angular acceleration is inversely proportional to A^*, which is a measure of dimensionless stroke amplitude:

$$A^* = \Phi_0 R/c, \tag{5}$$

where Φ_0 is the stroke amplitude in radians, R is wing length, and c is the average chord. This term expresses the amplitude as the number of chord lengths traveled.

The three terms enclosed in brackets in Eqn. 1 are the angular ($\mathbf{a}_{\mathrm{ang}}$), centripetal ($\mathbf{a}_{\mathrm{cen}}$) and Coriolis ($\mathbf{a}_{\mathrm{cor}}$) accelerations. Physically, these three accelerations result from the wing's kinematics and are enforced on the air close to the wing's surface, which can neither flow though, nor slip with respect to the wing at its surface (Vanyo, 1993; Greitzer *et al.*, 2004). We illustrate the three rotational accelerations that result from the dominant angular velocity due to stroke (Lentink and Dickinson, 2008) in Fig. 3B. The first component $\mathbf{a}_{\mathrm{ang},}$ is the manifestation of the angular acceleration of the wing around its base, which results locally in a chord-wise acceleration (Fig. 2B). This term is absent on a wing that revolves unidirectionally at constant angular speed, but will be present if the angular velocity changes, as with reciprocating back and forth motion (Fig. 2A). The second term $\mathbf{a}_{\mathrm{cen}}$ represents the centripetal acceleration, which is directed spanwise towards the wing's base (Fig. 2B). The third term $\mathbf{a}_{\mathrm{cor}}$ represents the Coriolis acceleration, its direction depends on the direction of local fluid velocity $\mathbf{u}_{\mathrm{loc}}$ (Fig. 2B). Both the centripetal and Coriolis accelerations ($\mathbf{a}_{\mathrm{cen}}$ and $\mathbf{a}_{\mathrm{cor}}$) are 'quasi-steady' in that they depend on the instantaneous value of the angular velocity $\mathbf{\Omega}$, of the wing. This is in contrast to the angular acceleration ($\mathbf{a}_{\mathrm{ang}}$), which depends on changes in angular velocity; $\dot{\mathbf{\Omega}}$. Note that we consider accelerations (Eqns. 2-4, Fig. 2B) instead of the analogous "fictitious forces", which point in the opposite direction (Vanyo, 1993; Greitzer *et al.*, 2004).

The magnitude of the three acceleration terms $\mathbf{a}_{\mathrm{ang}}$, $\mathbf{a}_{\mathrm{cen}}$ and $\mathbf{a}_{\mathrm{cor}}$ are scaled with respect to the fluid's convective acceleration (in the local frame), which results in the three independent dimensionless numbers in Eqns. 2-4. In the special case of hovering flight, both the centripetal and Coriolis accelerations are inversely proportional to the Rossby number Ro (Rossby, 1936) (Lentink and Dickinson, 2008). From now on we will use the dimensionless length scales A^* and Ro to quantify the angular centripetal, and Coriolis accelerations. For a revolving wing, Ro is equal to R_g/c, the ratio of the radius of gyration divided by the mean chord length. Ro is infinite for wings that translate, because the radius of gyration is infinitely large (Fig. 3A). It is convenient to calculate the Rossby number with respect to wingtip radius, R, rather than radius of gyration:

$$Ro = R/c, \tag{6}$$

because this value is equivalent to the aspect ratio of a single wing AR_s and is easily extracted from the biological literature (details in Lentink and Dickinson, 2008). Typical values of Ro (based on wingtip radius) for insect wings cluster near 3 (Fig. 12C), which immediately suggests that rotational accelerations may be significant (note $R_g/c \approx 1.5$ because $R_g \approx 0.5R$ for insects). For a reciprocating wing, A^* is equal to A/c; the ratio of stroke amplitude A to mean chord length c. Again, we consider the stroke amplitude at the wing's tip instead of the radius of gyration, for simplicity. Note that for a unidirectional revolving wing A, and therefore A^*, is infinite.

What is the relative importance of $\mathbf{a}_{\mathrm{ang}}$, $\mathbf{a}_{\mathrm{cen}}$ and $\mathbf{a}_{\mathrm{cor}}$ for insect wings? In hovering flight, the ratio of A^* to Ro (the quotient of Eqs. 5 and 6) is Φ_0, where Φ_0 is the amplitude (in radians) of the harmonic function that defines the reciprocating motion of the wing (see definitions A^* and Ro in Eqn. 5, 6) Φ_0 ranges from about 0.6 to 1.5 for insects (Ellington, 1984). Therefore A^* is of the same order of magnitude as Ro across insects, order one, which suggests that the $\mathbf{a}_{\mathrm{ang}}$, $\mathbf{a}_{\mathrm{cen}}$ and $\mathbf{a}_{\mathrm{cor}}$ have similar magnitudes as well. This holds true not just for insects, but also larger animals under continuous or transient hovering conditions. Further insight can be gained by coarsely evaluating the rotational accelerations at the start, middle, and end of each stroke assuming that the back and forth motion is roughly harmonic, a reasonable assumption for many insects (Ellington, 1984). At the end and start of the stroke both $\mathbf{a}_{\mathrm{cen}}$ and $\mathbf{a}_{\mathrm{cor}}$ are minimal because $\mathbf{\Omega}$ is zero, whereas $\dot{\mathbf{\Omega}}$ and thus $\mathbf{a}_{\mathrm{ang}}$ is maximal and scaled by $1/A^*$. However, these conditions are probably of little importance in LEV stability, because the LEV sheds and reforms (with opposite sense) during stroke reversal (e.g. see Poelma *et al.,* 2006). At midstroke, when LEV stability is at issue, $\mathbf{a}_{\mathrm{cen}}$ and $\mathbf{a}_{\mathrm{cor}}$ are maximal and scaled by $1/Ro$, whereas $\mathbf{a}_{\mathrm{ang}}$ is near zero. This simple analysis suggests that LEV stability might be mediated by the rotational accelerations $\mathbf{a}_{\mathrm{cen}}$ and $\mathbf{a}_{\mathrm{cor}}$ and not by the unsteady acceleration $\mathbf{a}_{\mathrm{ang}}$. The primary goal of the following experimental analysis is to explicitly test this theoretical prediction.

Dependence of LEV dynamics on dimensionless numbers

We performed a series of flow visualizations and force measurements on revolving ($Ro = 2.9$) and translating ($Ro = \infty$) fly wings undergoing unidirectional ($A^* = \infty$) and reciprocating ($A^* = 3.5$) motion for angles of attack amplitudes between 0° and 90°. The finite values of Ro and A^* are representative of slowly hovering fruit flies in free flight (Fry *et al.*, 2003) and are close to the mean value found for many insects. (Note that $Ro = \infty$ corresponds with $1/Ro = 0$, i.e. Coriolis and centripetal accelerations are zero. Similarly, $A^* = \infty$ indicates zero angular acceleration).

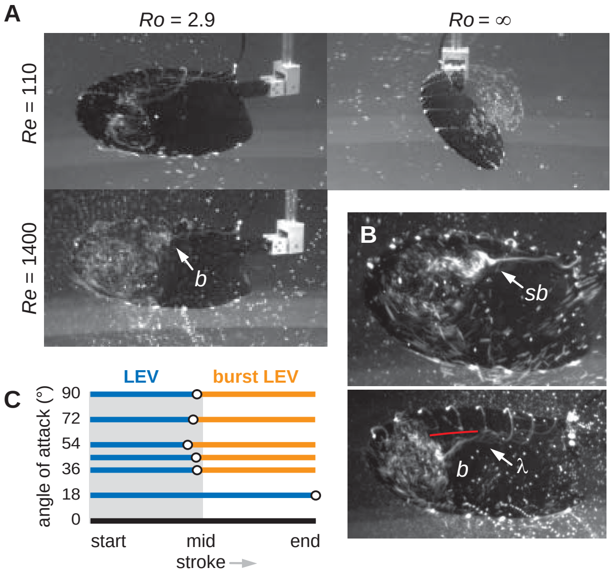

Fig. 4 | Influence of *Ro* on LEV stability. (A) LEV visualized on wing undergoing revolving reciprocating motion ($Ro = 2.9$, $A^* = 3.5$) or translational reciprocal motion ($Ro = \infty$) at $\alpha = 36°$. The visualizations were made at $s = 4c$ at the radius of gyration, near the end of the stroke ($4.4c$). At $Re = 1400$ and $Ro = 2.9$, the LEV bursts (*b*) halfway along the wing, but remains stably attached. (B) Top panel: close up of a LEV exhibiting spiral bursting (*sb*) at $Re = 1400$ midway through the stroke at $\alpha = 45°$. Bottom-panel: at the end of the stroke for $\alpha = 18°$ at midstroke we observed that the burst LEV was λ-shaped; it splitted up into two 'dual vortices' near the tip, of which the bottom one, below the red line, burst spiral-like (b). (C) Observations of the occurrence of a stable LEV and the onset of spiral bursting within a stroke of a reciprocally-revolving wing ($Ro = 2.9$) at $Re = 1400$. The LEVs are stable for all angles of attack and exhibit spiral bursting midstroke for $\alpha > 18°$, of which the start is indicated with a circle (diameter is larger than the S.D. calculated over 5 strokes).

The LEV is stable on an unidirectionally revolving wing ($Ro = 2.9$, $A^* = \infty$; Fig. 1C and supplementary movie 3), as found in prior studies (Dickinson *et al.*, 1999; Usherwood and Ellington, 2002; Birch *et al.*, 2004), but not on a unidirectionally-translating wing ($Ro = \infty$, $A^* = \infty$; Fig. 1B and supplementary movie 2). The LEV is also stable on a reciprocally-revolving wing ($Ro = 2.9$; $A^* = 3.5$), but not on a reciprocally translating wing ($Ro = \infty$; $A^* = 3.5$) (Fig. 4A and the supplementary movie 4, 5). These results are similar at *Re* 110 (fruit fly scale) and 1400 (house fly or bee scale). In summary, reciprocating motion (finite A^*) is not sufficient to stabilize a LEV. Rather, LEV stability appears only to require the low *Ro* resulting from revolving propeller-like motion.

Although we observed a stable LEV at both *Re* 110 and 1400 on both unidirectionally- and reciprocally-revolving wings, the flow structure was not identical for these *Re* numbers, as found previously (Birch *et al.*, 2004). In particular, the LEVs generated in experiments at *Re* 1400 exhibited spiral bursting under both unidirectional and reciprocating motion (Fig. 3B). The 'bursting' of a spiral vortex is a phenomenon that is thought to be initiated by deceleration of the core flow (Greenwell, 2002) and has been described for delta wings operating above a *Re* of about 1000. For a unidirectional revolving wing, the LEV bursts immediately after startup at angles of attack above 18°, whereas for the reciprocating case the LEV bursts after the wing almost reached the mid-stroke position when the wing starts to decelerate (Fig. 4C). On our model insect wing, the LEV remained coherent after it bursts, resulting in a 'turbulent' volume of rotating fluid whose position remained stable with respect to the wing. Examples of spiral bursting are shown in Fig. 3A for the end of a stroke at an angle of attack $\alpha = 36°$ at midstroke and in Fig. 4B for midstroke at $\alpha = 45°$ (note $\alpha = 90° - \alpha_0$ for flapping wings; Sane and Dickinson, 2001). Similar

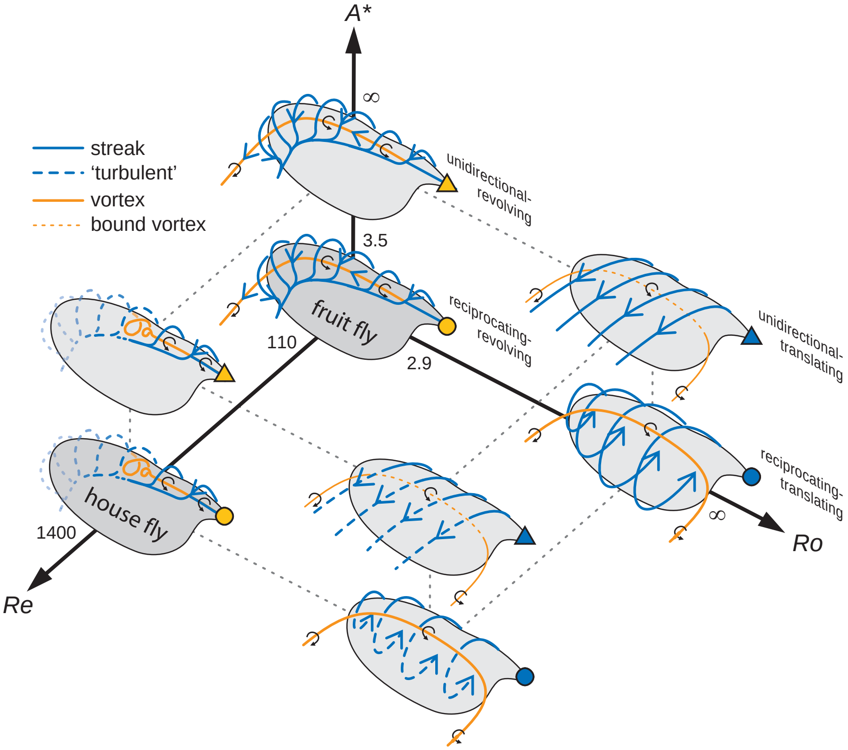

Fig. 5 | Flow cartoons that summarize our flow visualization experiments as a function of *Re*, *Ro* and A^*. Low *Ro* (2.9) results in stable LEVs, A^* $(3.5, \infty)$ does not modify this and higher *Re* (110 →1400) induces vortex bursting, but does not affect the stable attachment of the LEV with respect to the wing. $Re = 110$ represents fruit flies and $Re = 1400$ house flies. Triangles represent unidirectional stroke kinematics, circles represent reciprocating stroke kinematics. *Ro* is indicated by color: yellow ($Ro = 2.9$), blue ($Ro = \infty$), as used in Fig. 6.

to Lu *et al.* (2006), we observed in a few cases a double leading edge vortex structure with a small LEV in front of a larger burst LEV (Fig. 4B).

We summarize our flow visualizations in Fig. 5 using cartoons to indicate the basic flow structure at different values of A^* , *Ro*, and *Re*. It shows that revolving wings ($Ro = 2.9$) mediate compact and stable spiral LEVs, whereas the LEV is unstable for translating wings ($Ro = \infty$). Reciprocating motion (A^*) does not modify LEV stability, but does at small stroke amplitudes, however, keep the LEV close to the wing as it sheds the unstable LEV in time and forms a new one (with opposite sense) during every stroke reversal ($A^* = 3.5$). For higher stroke amplitudes this does not work because the LEV sheds before stroke reversal; unidirectional translational motion being the limiting case ($A^* = \infty$). Reynolds number does not seem to affect LEV stability within the range examined. An increasing Reynolds number does, however, modify LEV integrity as it induces vortex bursting on revolving wings. On translating wings we did not observe vortex bursting but the flow did become more erratic after a tight vortex was formed and started to separate from the wing, suggesting a transition to turbulent flow.

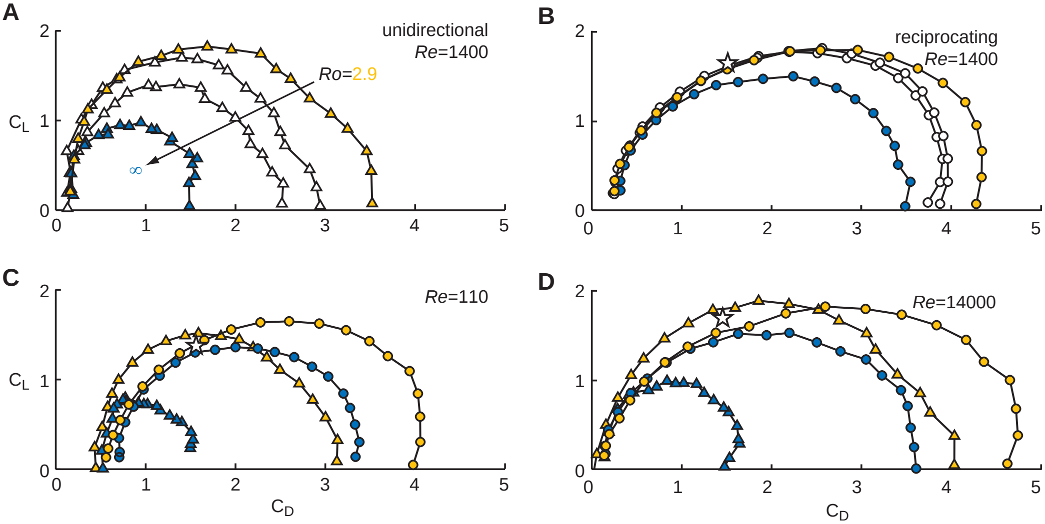

Fig. 6 | The lift and drag coefficients of revolving wings (low *Ro*) are larger than that generated by translating wings (high *Ro*) at *Re* 110, 1400 and 14,000. The lift (C_L) – drag (C_D) polar shown are obtained by varying the angle of attack from 0°-90° in steps of 4.5°. Triangles represent unidirectional stroke kinematics, circles represent reciprocating stroke kinematics. *Ro* is indicated by color: yellow ($Ro = 2.9$), blue ($Ro = \infty$), white ($Ro = 3.6$ and $Ro = 4.4$). (A, B) At $Re = 1400$, the lift and drag coefficients depend directly on *Ro* both for unidirectional and reciprocating stroke kinematics. The force augmentation of the unstable LEV on the translating reciprocating wing in (B) is still substantial compared to the performance of a unidirectional translating wing (A). (C, D) Force augmentation at low *Ro* is found from *Re* 110 to 14,000.

Dependence force coefficients on dimensionless numbers

One critical question in assessing efficacy of LEVs at different *Re* is whether a burst LEV still augments the force generated by the wing. To address this, we measured the forces generated by the model fly wing under different kinematics conditions. Comparing the lift and drag coefficients (C_D and C_L) generated at $Re = 110$ and 1400 under the four kinematic conditions discussed above (the four combinations of *Ro* and A^* in Fig. 5) indicates that bursting does not result in a loss of force augmentation (Fig. 6A-C and Fig. 7). To the contrary, force coefficients are actually elevated at higher *Re*, as has been reported previously (Birch *et al.*, 2004). The presence of a stably attached LEV at low *Ro* (revolving motion) was in all cases accompanied by an increase of the lift and drag coefficients relative to the $Ro = \infty$ case (translational motion).

To test if LEV stability and force augmentation depend directly on *Ro*, we varied *Ro* for both a unidirectionally- and reciprocally-revolving wing. This was achieved experimentally by extending the wing away from its rotational axis to create *Ro* values of 3.6 and 4.4 ($Re = 1400$). Force augmentation decreased with increasing *Ro* (Fig. 6A,B), consistent with the general prediction that the LEV is stabilized at low *Ro*. However, we saw no evidence for LEV shedding in our force or video records under these conditions. We speculate that within the permissive range of low *Ro* the precise magnitude of rotational accelerations may influence equilibrium conditions and determine the strength and efficacy of the LEV.

The observation that the LEV was stable even after it bursts encouraged us to test whether

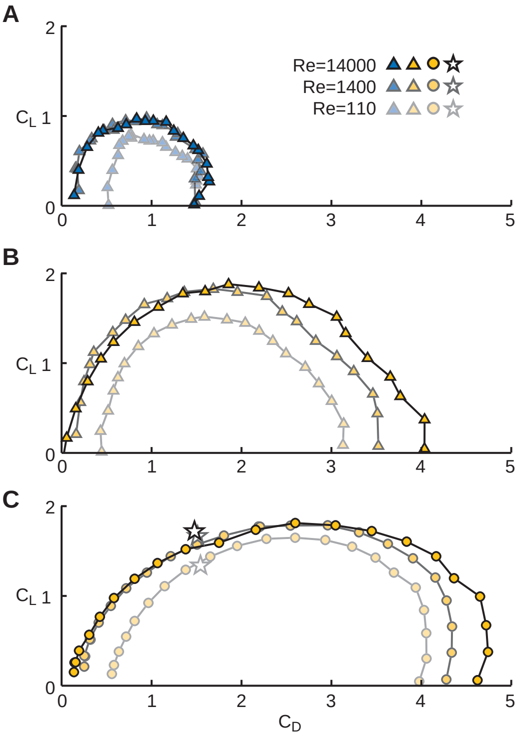

Fig. 7 | Lift and drag augmentation of the LEV varies little with Reynolds number. (A) Unidirectionally-translating wing. (B) Unidirectionally-revolving wing. (C) reciprocally-revolving wing, star represents fruit fly kinematics. The force polars at Reynolds 1,400 and 14,000 overlap for angle of attacks lower than 45 degrees. The main effect of a low Reynolds number (110) is that it damps both lift and drag force.

LEV force augmentation might extend to even higher *Re*. At *Re* 14,000 (hummingbird scale) we continued to find force augmentation (Fig. 6D). In Fig. 7 it can be seen that aerodynamic force polars of flapping, spinning and translating wings depend only weekly on *Re*. Important *Re* effects do, however, still exist as the minimum drag coefficient at zero lift, C_{D0}, decreases with increasing Reynolds number.

Efficacy of flapping, spinning and translating fly wings

In the past, performance analyses of insect wings were focused primarily on maximum lift production, which is augmented by the LEV, but how efficient is this high-lift mechanism? To assess one measure of aerodynamic efficacy, we constructed 'performance polars' using two relevant indices: glide number, C_L/C_D, and power factor, $C_L^{3/2}/C_D$ (e.g. Ruijgrok, 1994; Wang, 2008). The required power for a certain amount of lift decreases with increasing power factor. Figure 8 shows how both force and performance polars are related. We further illustrate the effect of decreasing C_{D0},

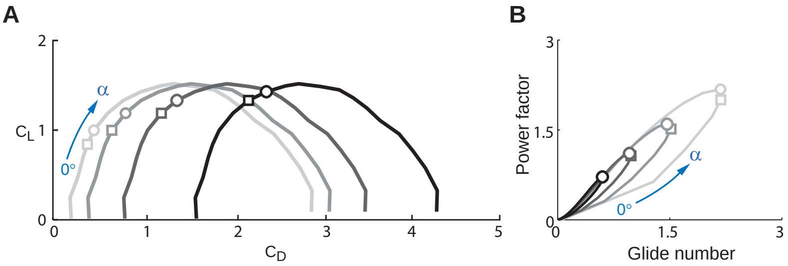

Fig. 8 | Illustration of how the lift-drag polar is related to the performance polar. Decreasing minimum drag coefficient, which occurs for increasing Reynolds number, increases performance (starting with black and ending with gray we plot polars for $C_{D0} = 1.6; 0.8; 0.4; 0.2; 0.1$). A circle indicates maximum power factor and a square maximum glide number.

which increases performance, the corresponding performance maxima occur at lower angles of attack for lower C_{D0}. The power factor is maximal (circle) at an angle of attack that is slightly higher than the one for which the glide number is maximal (square) (Ruijgrok, 1994).

Insects use reciprocally-revolving wings to generate lift, whereas helicopters use spinning blades and airplanes simply translate their wings through air. Based on Fig. 7 we can readily infer that flapping and spinning fly wings generate easily up to twice as much lift and drag force compared to translating fly wings for $110 < Re < 14{,}000$. But which kinematics generates lift most efficiently? For $Re = 110\text{-}14{,}000$ we find that the spinning fly wings perform up to 100% better than flapping fly wings and up to 50% better than translating fly wings, as measured by power factor (Fig. 9). Further, for $1{,}400 < Re < 14{,}000$ we find that translating wings also outperform flapping wings, whereas flapping fly wings slightly outperform translating wings at $Re = 110$ (fruit fly scale). Our measurements show that fruit flies actually flap their wings with kinematics that are near optimal with respect to power factor; their wing kinematics results in a hovering performance that matches well the peak performance for our simplified robot kinematics at $Re = 110$ (Fig. 9). As Reynolds number increases, the angle of attack corresponding with minimum power decreases, indicating that less prominent LEVs result in maximal hover efficiency. This analysis, however, assumes that power factor is the most appropriate measure of general performance. If maximum lift were limiting,

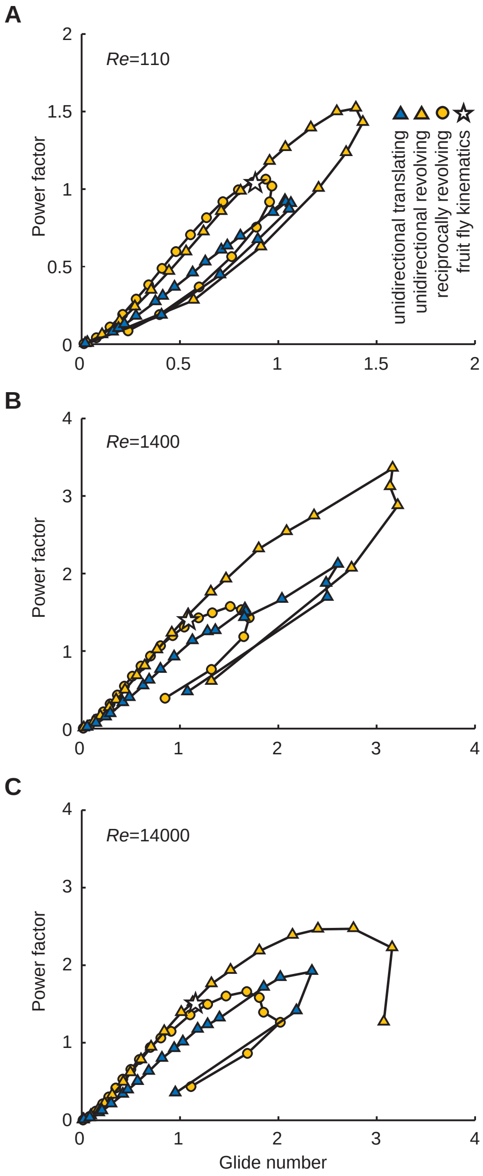

Fig. 9 | Spinning fly wings outperform translating and flapping fly wings at $110 < Re < 14{,}000$; (A), (B) and (C). The same symbols are used as in Fig. 6. and 7. Maximal power factor represents the minimum aerodynamic power required to hover. Fruit fly kinematics is indicated with a star, note that this corresponds approximately to minimal power required to hover (maximal power factor) at $Re = 110$; at which they operate. At higher Re, fruit fly kinematics also do well for hovering at minimal power, although the power factor is slightly below optimal (B, C).

one would reach quite different conclusions as maximum lift occurs at roughly $\alpha = 45°$, quite independent of *Re*.

Discussion

Using a dynamically scaled robot fly wing we visualized the flow and measured the corresponding lift and drag forces that result from a range of wing kinematics at Reynolds $110 < Re < 1400$. We tested swept wings and revolving and translating wings undergoing unidirectional and reciprocating motion. This allowed us to determine which kinematics results in stable LEVs, maximum lift augmentation, and maximum aerodynamic performance. Ultimately this test allowed us to determine which dimensionless number and corresponding rotational accelerations best predict LEV stability.

Rossby numbers of order one mediate stabile LEVs

Our results suggest that the centripetal $\mathbf{a}_{\mathrm{cen}}$ and Coriolis $\mathbf{a}_{\mathrm{cor}}$ accelerations mediate the stability of a LEV on a unidirectional and reciprocally revolving insect wing (Fig. 5), and that these rotational accelerations are inversely proportional to Rossby number (*Ro*). The decrease in force augmentation from $Ro = 2.9$, 3.6 to 4.4 (Fig. 6A,B) suggests that LEV stability is confined to *Ro* of order 1 or lower. However, high aspect ratio revolving wings still experience significant rotational accelerations near the root were the radial position r is small compared to chord length c and thus could locally support a stable LEV. This effect is likely responsible for the higher than expected forces found near the hub of high aspect ratio wind turbine blades where local $Ro = r/c$ is less than 3 (Tangler, 2004), a phenomenon that has been confirmed by computational fluid dynamic (CFD) simulations (Beom-Seok *et al.*, 2002). The LEV visualizations of Lu *et al.* (2006) on flapping high aspect ratio wings ($Ro = 1.3$-10) suggest that the most prominent LEV (they find dual vortices for $Re > 640$) is indeed confined to the base-region where local *Ro* is approximately lower than 3.

Our theoretical prediction and experimental confirmation suggest that rotational accelerations mediate LEV stability, but how are $\mathbf{a}_{\mathrm{cen}}$ and $\mathbf{a}_{\mathrm{cor}}$ physically involved? On wind turbines, operating at *Re* of order 10^6, $\mathbf{a}_{\mathrm{cen}}$ has been attributed to centrifugal pumping (e.g. Lindenburg, 2004; Vanyo, 1993; Greitzer *et al.*, 2004), which results in an outward spanwise flow near the hub. At the hub the blade undergoes so-called '3D stall' and generates elevated lift forces resulting in local lift coefficients well above 2 (Tangler, 2004). The flow pattern in the hub region of a wind turbine, where local *Ro* is similar to that of insect wings, is distinct from the pattern more distally, where the slender blades are said to undergo '2D stall' (Beom-Seok *et al.*, 2002; Tangler, 2004; Lindenburg, 2004).

For simple rotating disks, the outward radial fluid flow mediated by centripetal acceleration of the disk is well known (e.g. Vanyo, 1993). The radial flow is limited to a boundary region known as the Ekman layer (Fig 10). The corresponding Ekman number, $Ek = \nu/\Omega c^2$, is a measure of the ratio of viscous forces to Coriolis accelerations in this boundary layer. In the case of revolving disks and wings, *Ek* is equal to Ro/Re, hence one can independently choose any pairwise combination of *Ek*, *Ro*, and *Re* as the set of characteristic dimensionless numbers (Vanyo, 1993; Greitzer *et al.*, 2004). The first set, *Re* and *Ro*, is preferable for analyses of biological flight, because *Re* is more widely reported in the literature. In the Ekman layer, the fluid at the surface

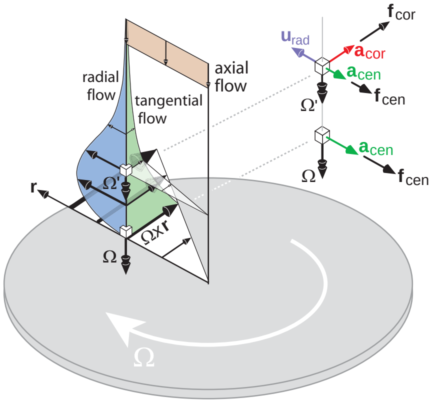

Fig. 10 | Boundary layer on a spinning disk (after Vanyo, 1993). A rotating boundary layer is commonly referred to as the Ekman layer and the axial flow towards the wing, needed to balance the radial flow is referred to as Ekman pumping. The boundary layer velocity profile is self-similar in that it scales with angular velocity times radial distance. Therefore, the velocity profiles shown depict the whole velocity field. The pressure field is rotationally symmetric and does not vary with radius; it only varies with the axial distance from the disk. The forces needed to support Coriolis and centrifugal accelerations are therefore solely due to friction, which is proportional to velocity gradient. Whereas solving the NS-equations on revolving wings is practically impossible in the inertial (lab) reference frame, because of the surface tracking needed, in the special case of spinning disks it is easiest to solve the equations in the inertial (lab) frame. The reason being that the disks surface fills an infinite plane and does not need to be tracked, which simplifies the math dramatically. Note that $\mathbf{\Omega}$ is the angular velocity of the disk and the fluid particle that sticks to it, $\mathbf{\Omega}' < \mathbf{\Omega}$; **r,** radial vector; $\mathbf{u}_{\mathrm{rad}}$, radial velocity; $\mathbf{a}_{\mathrm{cen}}$, centripetal acceleration; $\mathbf{a}_{\mathrm{cor}}$, Coriolis acceleration; $\mathbf{f}_{\mathrm{cor}}$, normalized coriolis force; $\mathbf{f}_{\mathrm{cen}}$, normalized centripetal force.

of the spinning disk has the same angular velocity as the disk (due to the no-slip condition at the surface) and therefore undergoes a centripetal acceleration $\mathbf{a}_{\mathrm{cen}}$ equal to that of the spinning disk, supported by a radial friction force $\mathbf{f}_{\mathrm{cen}}$. A bit higher above the surface of the disk, the fluid is pulled along in a tangential direction due to friction, but at the same time it slips outward radially. It slips because there is not a large enough friction force (from the gradient of radial velocity) to support the full centripetal acceleration acquired by the fluid at the disk's surface. While slipping radially outward the fluid particle undergoes Coriolis acceleration $\mathbf{a}_{\mathrm{cor}}$ in tangential direction, because it speeds up to match the higher tangential velocity outward *and* changes direction (it rotates while pulled along by the disk). This Coriolis acceleration is supported by a tangential friction force $\mathbf{f}_{\mathrm{cor}}$ that results from the tangential flow gradient in axial direction. Even higher above the disk's surface the boundary layer seizes to exist. Because mass is conserved, the outward radial flow of fluid must be supplied with 'fresh' fluid that flows towards the disk in axial direction. This process is called Ekman pumping.

The region of outward radial flow on top of a spinning disk is also a conspicuous feature found on top of insect wings (Maxworthy, 1979; Ellington *et al.*, 1996; Birch and Dickinson, 2001; Birch *et al.*, 2004; Poelma *et al.*, 2006) and near the hub of both propellers (Himmelskamp, 1947) and wind turbines (Tangler, 2004; Lindenburg, 2004) were *Ro* is low locally. In fact, Ekman-like boundary layer profiles have been calculated for wind turbine blades (Dumitrescu and Cardos, 2003). Important historic evidence for spanwise flow on a propeller at low *Ro* can be found in Himmelskamp (1947), a classic reference in wind turbine literature. In Fig. 11, we reproduce his visualizations of spanwise flow on a low-aspect ratio propeller. Early spanwise flow visualizations and measurements on insect wings suggested that spanwise flow is confined primarily to the fluid region occupied by the core of the LEV (Maxworthy, 1979; Ellington *et al.*, 1996). Later Digital Particle Image Velocimetry (DPIV) measurements of unidirectional and

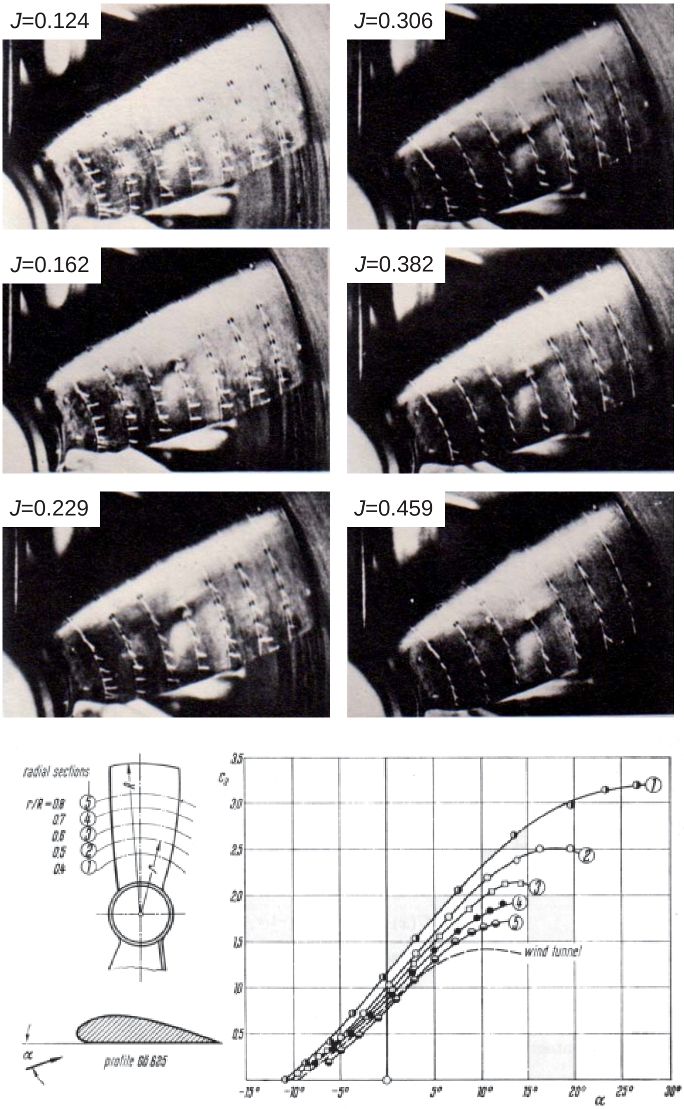

Fig. 11 | Elevated forces and spanwise flow on a stubby propeller operating at *Ro*≈2 and *Re*=280.000. (A) These unique tuft-based flow visualizations made by Himmelskamp (1947) have never been published in a journal and are therefore reproduced here. The advance ratio *J* of the propeller is calculated as the ratio of forward speed and wing tip speed, it varies from 0.124, almost hovering conditions, to 0.459, forward flight conditions. The tufts indicate increasingly strong spanwise flow at low advance ratios approaching hover conditions. This spanwise flow corresponds with elevated lift. (B) For completeness we also reproduced a sketch of the propeller and the measured section lift coefficients, based on pressure measurements at radial stations, published in Schlichting (1979). Note that *R* is the wing tip radius, *r* the local radius, α the angle of attack, and C_a is the section lift coefficient. The maximum section lift coefficient of 3 is well above maximum lift coefficient generated by the same airfoil in a wind tunnel (dashed line). Inboard sections, where *Ro* is lowest, correspond with maximum lift, which is also due to the twist in the propeller blade.

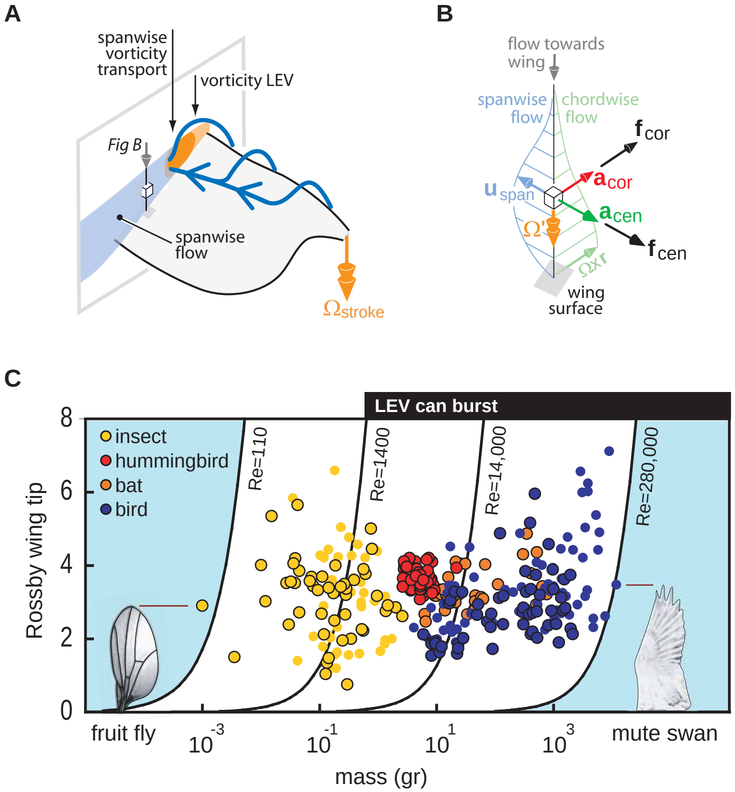

Fig. 12 | Proposed 3D flow structure of a stable LEV and feasibility of its general use by flying animals. (A) Sketch of the local flow field on a revolving fruit fly wing at *Re* 110 and 1400 based on previously published PIV data (Birch *et al.*, 2004) and Fig. 1, 4 and 5. Spanwise flow is present in the whole region on top of the wing and convects the accumulating vorticity in the LEV towards the tip vortex. (B) The large spanwise flow region of the wing is mediated by the rotational accelerations, $\mathbf{a}_{cen}$ and $\mathbf{a}_{cor}$, which results in an Ekman-like boundary layer, similar to that on spinning disks and wind turbine blades. The accelerations are balanced by the corresponding normalized centripetal ($\mathbf{f}_{cen}$) and Coriolis ($\mathbf{f}_{Cor}$) forces in the flow that can be composed out pressure and friction forces. (C) Rossby number of animal wings assuming zero advance ratio as a function of body mass ($n = 319$ in total). The average values are close to those found for fruit flies (2.9): insects $Ro = 3.1$ (*std* 1.1, $n = 98$), hummingbirds $Ro = 3.7$ (*std* 0.3, $n = 65$), bats $Ro = 3.3$ (*std* 0.4, $n = 39$) and birds $Ro = 3.2$ (*std* 1.18, $n = 117$). The circles with a black outline represent values that are directly based on the aspect ratio of one wing. Circles without a black outline represent values for which we corrected the aspect ratio of the tip-to-tip distance between paired wings and total wing surface such that we obtained the single-wing aspect ratio comparable to the calculation of the wingtip Rossby number. This amounted to subtracting the distance contributed by the body width between the wing bases. Information on this and all the insect, bat, hummingbird and bat wing morphology references can be found in Appendix I. The constant-Reynolds number lines are calculated assuming an average C_L of 1.5 and represent the Reynolds numbers of our experiments and the one of Himmelskamp (1947), details are given in Appendix II.

reciprocating revolving model fruit fly wings have show that spanwise flow is not primarily confined to the LEV, but extends all the way to the trailing edge (Birch and Dickinson, 2001; Birch *et al.*, 2004; Poelma *et al.*, 2006). Concurrently to the spanwise flow there is significant flow in an orthogonal direction, parallel to the axis of rotation, which suggests Ekman-like pumping This flow is even visible quite far from the wing's surface (Birch *et al.*, 2004; Poelma *et al.*, 2006). The region of radial flow and the orthogonal flow towards the 'hub' of the wing on inclined reciprocating and unidirectional revolving insect wings indicate the presence of an Ekman-like boundary layer, although due to 'flow separation' its spatial extent is much larger, Fig. 12A (Vanyo, 1993).

Our measurements and the observations for spinning disks, wind turbines and a propeller suggest that the spanwise flow results from 'centrifugal pumping' as the fluid near the wing's surface slips radially outward. The fluid slips, because there is not enough friction to support the full centrifugal acceleration $\mathbf{a}_{\text{cen}}$ that the fluid requires at the wing's surface, (Fig. 12 A, B). In these cases, the centripetal acceleration also results from a net specific force directed towards the wing base ($\mathbf{f}_{\text{cen}}$ in Fig. 12B) that is presumably composed of both a pressure component as well as the friction component that would be present on a spinning disk, (Fig. 10). All these findings strongly suggests that centrifugal pumping due to wing rotation at low *Ro* can be found for both low and high *Re* - from insect wings to wind turbine blades.

The observation that the region of separated spanwise flow (which includes the LEV, Fig. 5) stays stably attached to a revolving wing implies that it is not only subject to a centripetal acceleration $\mathbf{a}_{\text{cen}}$ but also to a continuous acceleration in the chord wise direction. The required acceleration for this kinematic condition is precisely the Coriolis term $\mathbf{a}_{\text{cor}}$ (similar to the flow on spinning disks). This implies that the spanwise flow driven by $\mathbf{a}_{\text{cen}}$ is stabilized with respect to the wing through $\mathbf{a}_{\text{cor}}$, which must be supplied by a net specific chordwise force that points in the direction of travel ($\mathbf{f}_{\text{cor}}$ in Fig. 12B). Lindenburg (2004) showed that if $\mathbf{a}_{\text{cor}}$ is supported by a *fore-aft* pressure gradient acting across the region of spanwise flow it could account for the elevated forces generated close to the hub of a wind turbine. Whether this force augmentation model works quantitatively for flapping insect wings is unknown, but could be examined in future research.

Our qualitative analysis of centripetal and Coriolis acceleration holds globally for the whole region of spanwise flow, but perhaps not in detail. For calculating the detailed acceleration distribution, and corresponding local directions, the velocity field is needed. Sun and Wu (Sun and Wu, 2004) calculated this velocity field around an unidirectional revolving insect wing at $Re = 480$ using CFD. Based on the velocity field they computed the "fictitious forces", which point in the opposite direction of the corresponding rotational accelerations (Vanyo, 1993; Greitzer *et al.*, 2004). Their computation of the spanwise components of the 'Coriolis force' and 'Centrifugal force' in the boundary layer flow for an angle of attack of 40° confirms that Coriolis and centrifugal accelerations are indeed significant. They further found that the radial pressure gradient force, due to the linear spanwise velocity distribution, is even larger and concentrated in the LEV, which can therefore explain spanwise flow in the whole LEV at $Re = 480$. But the pressure-gradient force is also significant in other regions where there is no spanwise flow. In light of this, we note that the DPIV measurements of (Birch *et al.*, 2004) at $Re = 110$ and 1400, show significant chordwise velocity in extended regions below, in front, and above a fly wing, without spanwise flow. This is significant, because in this region viscous effects from the wing's surface are negligible, so the viscous 'centrifugal pumping' mechanism cannot work. The pressure-gradient force in this region is, however, non-zero because chordwise flow varies radially from wing root to tip, which again should drive a spanwise flow if such gradients were effective, but this does not seem to be the case. Thus, there appears to be no one-to-one link between spanwise flow and pressure gradient force throughout the flow field around a fly wing at both low and high *Re*. Most likely spanwise flow due to pressure gradient is primarily confined to the core of the LEV. Aono and co-workers (Aono *et al.*, 2008) further show that little spanwise flow and pressure-gradient exists in the LEV of a fruit fly at $Re = 134$, while they do find significant spanwise flow behind the LEV. For a Hawkmoth at $Re = 6300$ they did find strong spanwise flow and pressure-gradient in the LEV. These findings of spanwise flow agree with our findings as well as those of Birch *et al.* (Birch *et al.*, 2004). Aono and co-workers further suggest that Coriolis and centripetal accelerations are the likely candidates for explaining the spanwise flow they found behind the LEV on fruit fly wings.

Integrating all these observations, including our theoretical predictions and experimental confirmation we conclude that: 1) the spanwise flow in the core of the LEV of an insect, when present, is most likely to be driven by the spanwise pressure gradient; 2) the spanwise flow in the extended viscous flow region behind the LEV can be explained best by centrifugal pumping, directly analogous to that found on spinning disks, propeller blades, and wind turbine blades.

LEV integrity is mediated by Re and A^*

Similar to findings of vortex-breakdown by van den Berg and Ellington (1997) and Lu *et al.* (2006) we found that the LEV on a fly wing exhibits spiral bursting at *Re* 1400. Spiral bursting is a phenomenon that has been described for delta wings operating above a critical *Re* of about 1000, and is thought to be initiated by core flow deceleration (Greenwell, 2002). If we assume that the flow around an insect wing, including the core of the LEV, accelerates when the wing accelerates, we can qualitatively understand why the LEV starts to bursts near mid-stroke when the wing, and therefore the LEV's core, starts to decelerate. This shows that, although A^* does not affect LEV stability, the corresponding angular acceleration can mediate LEV integrity. Vortex bursting may explain the erratic velocity vectors in the LEV found during previous quantitative flow measurements under similar conditions (Birch *et al.*, 2004). Finally, our measurements show that the force coefficients do not decrease as a result from vortex bursting, Fig. 5 and 6. This suggest that LEV based force augmentation is robust to high *Re* number effects.

Comparing old and new LEV stability hypotheses

How do our findings relate to the previous ones that resulted in the swept wing analogy and tip vortex hypothesis? We found that LEV stability induced by the tip-vortex does not seem to work for fly wings at $Re = 110$ and 1400 (Fig. 1, 2), although there is evidence for higher Reynolds numbers that translating stubbier wings with an aspect ratio of roughly one (and less) do generate stable LEVs (Winter, 1936; Ringuette, 2007). Ellington and co-workers (Ellington, *et al.*, 1996) suggested that three mechanisms could potentially explain how spanwise flow could be generated. Our theoretical analysis, experimental test and literature survey show that 'centrifugal' acceleration in the boundary layer is the likely mechanism at the low *Re* of fruit flies. At high *Re*, the pressure gradient force can explain spanwise flow in the LEV core, whereas centrifugal pumping can explain spanwise flow behind the LEV. The region of spanwise flow is clearly not confined to the LEV core alone, at low and high Reynolds numbers, and its spatial distribution above an inclined wing depends strongly on Reynolds number (Birch *et al.*, 2004; Aona, *et al.*, 2008). Our analysis further indicates that Coriolis acceleration is equally important in the stable attachment of the LEV, because this acceleration is an indispensible kinematic condition for the stable attachment of spanwise flow with respect to a revolving wing. All these experiments support, however, the hypothesis that spanwise flow balances the formation of vorticity at the leading edge and drains it into the tip vortex (Maxworthy, 1979; Ellington *et al.*, 1996). The importance of *Ro*, and not *Re*, in determining LEV stability suggests further that vorticity transport in the large 'Ekman-like' separated flow region *behind* the LEV could be equally critical in maintaining this balance at low *Re,* compared to vorticity transport found *in* the LEV at high *Re*. We infer this from a prior study that suggests that the outward spiral flow within the core is *Re* dependent (Birch *et al.*, 2004), whereas those results as well as our own suggest that LEV stability is not. Further, a direct analogy between LEVs on swept and revolving wings does not seem to hold for equally shaped wings operating at equally low Reynolds numbers, because we did not observe stable LEVs nor force augmentation for swept fruit fly wings (Fig. 1, 2). In other experiments with high aspect ratio swept bird wings (*Apus apus*) a stable LEV was found (Videler *et al.*, 2004; Lentink *et al.*, 2007), but no significant force augmentation (lift coefficients lower than one) for $12{,}000 < Re < 77{,}000$ (Lentink *et al.*, 2007). This suggests that a direct analogy between LEVs on swept and revolving wings does not hold at higher Reynolds numbers either.

Link between Rossby number and 'quasi-steady' lift theory

This study supports an earlier notion that the aerodynamic force generation of insects might be considered 'quasi-steady', excluding the complications that occur during stroke reversal (Dickinson *et al.*, 1999; Sane and Dickinson, 2001; Usherwood and Ellington, 2002). Quasi-steadiness implies that the instantaneous value of the flow velocity is more important than its instantaneous rate of change for understanding and predicting the aerodynamic forces, in particular wing lift (Sane and Dickinson, 2001). Our theoretical framework supports this idea, since the 'quasi-steady' rotational accelerations, $\mathbf{a}_{\text{cen}}$ and $\mathbf{a}_{\text{cor}}$, are responsible for LEV stability, whereas the unsteady angular acceleration, $\mathbf{a}_{\text{ang}}$, is not. This is not to say that unsteadiness is not significant in insect flight. The translational reciprocating case resulted in an unstable LEV that still significantly augmented force, as found by Wang *et al.* (2004), but this force is less than that found for revolving wings (Fig. 6). Further, LEV stability is less important for insects that employ considerable smaller stroke amplitude than fruit flies. For example, unloaded hovering bees use a narrow stroke amplitude ($\Phi_0 = 0.78$ rad, compared to 1.2 for a fruit fly) resulting in a lower dimensionless stroke amplitude. Recent experiments indicate that bees depend more strongly on unsteady force augmentation at the start and end of the stroke (Altshuler *et al.*, 2005), at which point angular acceleration is maximal and the rotational accelerations are minimal. This implies that unsteady lift mechanisms such as added mass effects and wake capture (Dickinson *et al.*, 1999) become increasingly more significant, compared with 'quasi-steady' forces based on the stable LEV, when the dimensionless stroke amplitude decreases.

Lift augmentation at Reynolds numbers higher than 14,000

Our experiments ($110 < Re < 14{,}000$) and experiments of others on a propeller ($Re = 280.000$) and wind turbines (*Re* of order 10^6) suggests that lift augmentation is continuous in the inertial flow regime for Rossby numbers of order one. Ellington and Usherwood (2001) found, however, that revolving model hawk moth wings operating at $10{,}000 < Re < 50{,}000$ failed to produce high lift. The reason for this is unclear, and their findings for $Re = 10{,}000$ contrast ours at $Re = 14{,}000$

and the high force coefficients found for quail wings at $Re = 26{,}000$ by Usherwood and Ellington (2002). It could well be that airfoil shape plays a critical role in the apparent lift crisis for the thin and sharp model hawk moth-like wings at $10{,}000 < Re < 50{,}000$. Schmitz (1942) found such phenomenon for airfoils through wind tunnel experiments within this same range. He found that thin and sharp airfoils outperformed blunt and thick airfoils at low *Re* and *vice versa* at high *Re*. For these airfoils there exists a critical *Re* below which its lift decreases and its drag increases drastically. This is due to the presence of laminar separation bubbles and transitions to turbulent boundary layer flow that dominate airfoil performance at intermediate *Re*. This is relevant because the spinning wings tested by Ellington and Usherwood (2001) (at intermediate *Re*) featured thin and sharp, sub-critical, airfoils whereas the propeller (Himmelskamp, 1947) and wind turbine blades at high *Re* (Tangler, 2004) featured thick and blunt, super-critical airfoils, airfoils. Ellington and Usherwood (2001) tentatively conclude that the LEV is unstable on revolving wings at $Re >= 10{,}000$ due to a lack of spanwise flow that stabilizes the LEV. Spanwise flow visualization of Himmelskamp (1947) on a propeller at $Re = 280{,}000$ (Fig. 11) and visualizations of stable LEVs on wind turbine blades (Beom-Seok *et al.*, 2002), propeller fans (e.g. Simonich *et al.*, 1992) and ship screws (e.g. Kerwin, 1986) operating at similar angles of attack and *Ro*, but at higher *Re*, contradict this idea. Work of Hubel and co-workers (Hubel, 2006) shows that a model goose flapping in the intermediate Reynolds number regime can, indeed, generate a stable LEV during forward flight. We conclude therefore that there is significant evidence that LEV-based force augmentation could exist continuously from revolving fruit fly wings to wind turbine blades at low *Ro*, but more research on the influence of airfoil shape on LEV generation, stability and force augmentation in the intermediate $10{,}000 < Re < 100{,}000$ is needed.

Force augmentation of revolving wings in nature and technology

In summary, the single condition for LEV stability and maximal force augmentation appears to be a sufficiently low *Ro*. Thus, the use of LEVs to augment forces may be more widely distributed among swimming and flying animals than previously appreciated. In Fig. 12C, we show the results of a literature survey plotting *Ro* for hovering wings as a function of body mass. The distribution indicates that many large animals possess wings with a sufficiently low *Ro* to create stable LEVs (note that *Ro* at the all-important radius of gyration is roughly 50% lower than *Ro* calculated at the wing tip in Fig. 12C). This is not to suggest that all animals larger than insects can hover or create LEVs when flying at cruising speed, but that there is no aerodynamic reason why they could not make use of this mechanism during slow hovering flight or short-take off and landing when their advance ratio is small and *Ro* is of order one (E.g. see Fig. 10, spanwise flow decreases for higher advance ratios). LEVs, under low *Ro* conditions have indeed been found on the wings of bats during hovering flight (Muijres *et al.*, 2008). The elevated forces we measured at $Re = 14{,}000$, a value appropriate for hummingbirds, is consistent with the putative observation of LEVs on hummingbird (Altshuler *et al.*, 2004; Warrick *et al.*, 2005) and quail (Usherwood and Ellington, 2002) wings. Finally, Hubel and co-workers found a stable LEV near the base of a flapping goose model in forward flight (Hubel, 2006). The local Rossby number is much lower near the wing base, like on wind turbine blades (see also Lentink and Dickinson, 2008) and can therefore locally support a stable LEV, even at relatively high advance ratios.

Because Reynolds number and stroke amplitude are not critical features in LEV stability, we think that a LEV could be an efficient high-lift mechanism for slow hovering animals, small and big. Our experiments suggest that aerodynamic efficiency is maximal for smaller LEVs generated at lower angles of attack, at increasingly higher Reynolds number (Figs. 8, 9). Total hovering efficiency, however, depends not only on aerodynamic efficiency, but also on the efficiency of the muscles that drive the wing. During hovering, animal weight is balanced by vertical thrust, which is proportional to the product of lift coefficient, (flapping frequency)^2, and (stroke amplitude)^2. Noting that flapping frequency is confined to a narrow band for high muscle efficiency (McMahon, 1984), and that stroke amplitude is limited to 180° or less, a high maximum lift coefficient clearly helps to accommodate both the high vertical thrust needed to balance weight during hovering and the much lower thrust needed during cruising.

Our theoretical frame work represents air and water equally well. The pectoral fins of many swimming animals flap similar to the wings of flying animals, but not only for generating lift, also for generating drag to maneuver. Fig. 6 shows that revolving wings (unidirectional and reciprocating) not only generate more lift for their surface area, they also generate much more drag at very high angles of attack, well beyond 45°. For angles of attack above 45°, the attached leading and trailing edge vortex (LEV and TEV) on the model fly wings are surprisingly similar to the ones recently observed on the pectoral fin of a sun fish (Lauder and Madden in: Bandyopadhyay *et al.*, 2008). The Rossby number based on the single-wing aspect ratio of fish pectoral fins is often low. For 7 species described in literature we found $Ro = 2.5$ on average with *std*. 0.7 (references in appendix I), low enough values of Ro for stable LEVs. For completeness we also estimated an average Ro value of 3.7 for autorotating seeds (*std* 1.14 $n = 26$, references in appendix I). This suggests that a stable LEV could also explain the elevated lift forces found for these botanical structures (Azuma and Yasuda, 1989), We have recently tested this using three-dimensional DPIV and will report the results elsewhere. With respect to technology, we envision that micro air vehicles could more easily mimic nature and generate a stable LEV by simply adopting the only constraint for a stable LEV and force augmentation — revolving a wing continuously at low Rossby number, which is more efficient than flapping the same wing.

Acknowledgements

We gratefully acknowledge Will Dickson for help with the experimental setup, valuable suggestions and proof reading the manuscript and Andrew Straw for helping with the video set-up. We also thank Douglas Althshuler for valuable comments and lending his water proof force sensor. And we thank Ulrike Müller, Jim Usherwood, Mees Muller, John Dabiri and GertJan van Heijst for valuable comments. We acknowledge Koert Lindenburg for proof reading the manuscript and mathematical derivations. We thank Johan van Leeuwen for heartily support, encouragement and proof reading of the various versions of the manuscript. Finally DL wishes to thank Peter Bakker, Hester Bijl and Bas van Oudheusden for helping him obtain travel bursaries for this research.

Funding

This research is supported by travel bursaries of the Netherlands Organization for Scientific Research, the Journal of Experimental Biology and the J. M. Burgers centre for fluid dynamic research and NWO-ALW grant 817.02.012 to D. L. and a Grant from the National Science Foundation (IBN-0217229) and Packard Foundation (2001-17741A) to M.H.D.

Symbols

α	wing angle of attack
α_0	wing angle of attack amplitude
Φ_0	wing stroke amplitude (half the total stroke amplitude Φ)
ν	kinematic viscosity
ρ	fluid density
$\boldsymbol{\Omega}$	angular velocity of the rotating frame
$\boldsymbol{\Omega}_{\mathrm{stroke}}$	angular velocity of the rotating frame
$\dot{\boldsymbol{\Omega}}$	angular acceleration due to wing stroke
$\dot{\boldsymbol{\Omega}}_{\mathrm{stroke}}$	angular acceleration due to wing stroke
$\boldsymbol{\Omega}'$	angular velocity of the fluid separated from the fly wing

$\mathbf{a}_{\mathrm{ang}}$	angular acceleration
$\mathbf{a}_{\mathrm{cen}}$	centripetal acceleration
$\mathbf{a}_{\mathrm{Cor}}$	Coriolis acceleration
$\mathbf{a}_{\mathrm{inert}}$	acceleration with respect to inertial coordinate system
$\mathbf{a}_{\mathrm{loc}}$	acceleration with respect to local coordinate system
A^*	stroke amplitude
AR_{s}	single wing aspect ratio
AR	tip to tip wing aspect ratio
b	burst vortex, Fig. 4
b_{s}	single wing span
c	average wing chord length
C	correction factor wing aspect ratio data
C_{L}	lift coefficient
C_{D}	drag coefficient
C_{D0}	drag coefficient at zero lift
$\mathbf{D}_{\mathrm{chord}}$	chordwise drag force
Ek	Ekman number
$\mathbf{f}_{\mathrm{cen}}$	specific centripetal force (per unit of volume)
$\mathbf{f}_{\mathrm{Cor}}$	specific Coriolis force (per unit of volume)
J	advance ratio
$\mathbf{L}$	lift force
m	mass
n	number of experiments
r	magnitude of radius vector
$\mathbf{r}$	position of a fluid particle in the rotating frame
R	wing radius
R_{g}	wing radius of gyration
Re	Reynolds number
Re_{g}	Reynolds number at the radius of gyration
Ro	Rossby number
s	distance traveled in chord lengths
sb	spiral burst vortex, Fig. 4
std	standard deviation

S	single wing area
$\mathbf{u}_{\mathrm{loc}}$	velocity in local coordinate system
U_{g}	average velocity at the radius of gyration
V	velocity along wing radius
W	Weight
(x, y, z)	local coordinate system

Appendix I: Rossby numbers of animal wings from insects to birds.

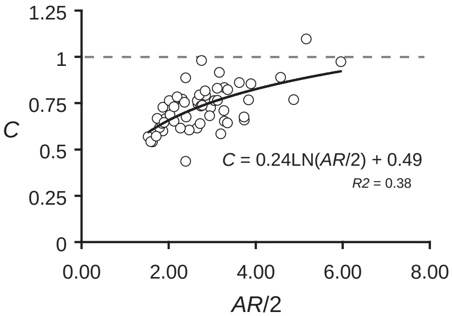

Fig. A1 | Rossby numbers had only to be corrected for insects and birds. For insects we made use of photos of insects with extended wings, which resulted in an accurate correction (yellow circles without outline in Fig. 12C). For the corrected bird values (blue circles without outline in Fig. 12C) we could not obtain such accurate photos and proceeded as follows: First, we obtained a large data set of aspect ratios based on the full wing span (Tennekes, 1997). Subsequently, we compared these values with the ones for which we also obtained an accurate value of the single-wing aspect ratio (Slater Museum, 2005-2006) and determined the required correction factor C. We correlated the correction factor C to the aspect ratio of the full wing divided by two, $AR/2$. This factor was used to estimate the single-wing aspect ratio of the remaining bird wings with a conservative extrapolation r value for albatrosses ($AR/2 \approx 7.5$) that is close to one.

Insect wing data:

Azuma A. (2006). *The biokinetics of flying and swimming*, AIAA Education series.

Ellington C. P. (1984). The aerodynamics of insect flight. I-VI. *Phil. Trans. R. Soc. Lond. B* **305,** 1-181.

Lehmann F. -O. and Dickinson M. H. (1998). The control of wing kinematics and flight forces in fruit flies (*Drosophila spp.*). *J. Exp. Biol.* **201,** 385-401.

Marden H.J. (1987). Maximum lift production during takeoff in flying animals. *J. Exp. Biol.* **130,** 235-258.

Hummingbird wing data:

Altshuler D. L. (2001). Ecophysiology of hummingbird flight along elevational gradients: An integrated approach. PhD. thesis *Univ. of Texas at Austin*.

Chai P. and Millard D. (1997). Flight and size constraints: hovering performance of large hummingbirds under maximal loading. *J. Exp. Biol.* **200,** 2757-2763.

Stiles F. G. Altshuler D. L. and Dudley R. (2005). Wing morphology and flight behaviour of some north american hummingbird species. *The Auk* **122,** 872-886.

Bat wing data:

Hartman F. A. (1963). Some flight mechanics of bats. *Ohio J. of Sc.* **53,** 59-65.

Jones G. Webb P. I. Sedgeley J. A. and O'Donnell C. F. J. (2003) Mysterious Mystacina: how the New Zealand short-tailed bat (*Mystacina tuberculata*) locates insect prey. *J. Exp. Biol.* **206,** 4209-4216.

Norberg U. M. Brooke A. P. and Trewhella W. J. (2000). Soaring and non-soaring bats of the family *pteropodidae* (flying foxes, *Pteropus spp.*): wing morphology and flight performance. *J. Exp. Biol.* **203**, 651-664.

Vaughan N. Parsons S. Barlow K. E. and Gannon M. R. (2004). Echolocation calls and wing morphology of bats from the west indies. *Acta Chiropterogica* **6,** 75-90.

Bird wing data:

Slater Museum (2005-2006). Online Wing collection of the Slater Museum of Natural History, Univ. of Puget Sound, http://www.ups.edu/x5662.xml (2005-2006).

Tennekes H. (1997). The simple science of flight, The MIT Press, Cambridge.

Fish pectoral fin data:

Hove J. R., O'Bryan L. M., Gordon, M. S., Webb, P. W. and Weihs D. (2001). Boxfishes (Teleostei: Ostraciidae) as a model system for fishes swimming with many fins: kinematics. *J. Exp. Biol.* **204**, 1459-1471.

Combes, S. A. and Daniel, T. L. (2001). Shape, flapping and flexion: wing and fin design for forward flight. *J. Exp. Biol.* **204**, 2073-2085.

Walker, J. A. and Westneat, M. W. (2002). Performance limits of labriform propulsion and correlates with fin shape and motion. *J. Exp. Biol.* **205**, 177-187.

Walker J.A. (2004). Dynamics of pectoral fin rowing in a fish with an extreme rowing stroke: the threespine stickleback (Gasterosteus aculeatus) *J. Exp. Biol.* **207**, 1925-1939.

Autorotating seed wing data:

Azuma, A. and Yasuda, K. (1989). Flight performance of rotary seeds. *J. Theor. Biol.* **138**, 23-53.

Yamada, T. and Suzuki, E. (1999). Comparative morphology and allometry of winged diaspores among the Asian Sterculiaceae. *J. Trop. Eco.* **15**, 619-635.

Appendix II: The relation between Ro, mass and Re

The Reynolds and Rossby number (based on wing radius; single-wing span) in hovering flight are given by:

$$Re_{\mathrm{g}} = \frac{\rho \overline{U}_{\mathrm{g}} c}{\mu}, \text{ and} \qquad \text{(II.1)}$$

$$Ro = AR_{\mathrm{s}} = \frac{b^2}{2S} = \frac{b}{2\bar{c}}. \tag{II.2}$$

Note that b is the wing span, S the wings surface area and AR_{s} the single-wing aspect ratio. Force equilibrium in hovering flight requires that the following relation holds:

$$W = \bar{L} \;\rightarrow\; \overline{C_{\mathrm{L}}}\,1/2\rho\overline{U_{\mathrm{g}}^2}S = mg, \tag{II.3}$$

where W is the weight, $\bar{L}$ the time-averaged lift, $\overline{C_{\mathrm{L}}}$ the time-averaged lift coefficient, m the mass and g the gravitational constant. We now approximate the time-averaged velocity with the r.m.s. time-averaged velocity which results in:

$$\overline{U_{\mathrm{g}}} \approx \sqrt{\overline{U_{\mathrm{g}}^2}} = \sqrt{\frac{mg}{\overline{C_{\mathrm{L}}}\,1/2\rho S}}. \tag{II.4}$$

Combining eqs. II.1, II.2 and II.4, we obtain the Reynolds number as a function of the total mass and the wingtip Rossby number for hovering flight:

$$Re_{\mathrm{g}} = \frac{\rho\overline{U_{\mathrm{g}}}c}{\mu} \approx \sqrt{\frac{mg}{\overline{C_{\mathrm{L}}}}\cdot\frac{\rho}{\mu^2}\cdot\frac{2c^2}{S}} = \sqrt{\frac{mg}{\overline{C_{\mathrm{L}}}}\cdot\frac{\rho}{\mu^2}\cdot\frac{1}{Ro}}. \tag{II.5}$$

We plotted Reynolds number isolines of hovering animal wings in figure 12C of the paper by assuming a time averaged lift coefficient of 1.5 for the full weight range from insects to birds. In doing so, we assume the animal is making use of a LEV and operates at a high lift coefficient of $C_{\mathrm{L}} = 1.5$. This approximation suffices for the Reynolds number of which the exact value is less relevant.

References

Altshuler, D., Dudley, R. and Ellington, C. P. (2004). Aerodynamic forces of revolving hummingbird wings and wing models. *J. Zool. Lond.* **264**, 327-332.

Altshuler, D. L., Dickson, W. B., Vance, J. T., Roberts, S. P. and Dickinson, M. H. (2005). Short-amplitude high-frequency wing strokes determine the aerodynamics of honeybee flight. *PNAS* **102**, 18213-18218.

Aono, H., Liang, F. and Liu, H. (2008). Near- and far-field aerodynamics in insect hovering flight: an integrated computational study. *J. Exp. Biol.* **211**, 239-257.

Azuma, A. and Yasuda, K. (1989). Flight performance of rotary seeds. *J. Theor. Biol.* **138**, 23-53.

Bandyopadhyay, P. R., Beal, D. N. and Menozzi, A. (2008). Biorobotic insights into how animals swim. *J. Exp. Biol.* **211**, *206-214.*

Baruh, H. (1999). *Analytical dynamics*. McGraw-Hill.

Beom-Seok, K., Jeong-Hwan, K., Koji, K., van Rooij, R. P. J. O. M. and Young-Ho L. (2002). 3D Numerical predictions of horizontal axis wind turbine power characteristics of the scaled Delft university T40/50 model. *Fifth JSME-KSME Fluids Engineering Conference*, Nagoya, Japan.

Birch, J. M., Dickinson, M. H. (2001). Spanwise flow and the attachment of the leading-edge vortex on insect wings. *Nature* **412,** 729-733.

Birch, J. M., Dickinson, M. H. (2003). The influence of wing–wake interactions on the production of aerodynamic forces in flapping flight. *J. Exp. Biol.* **206**, 2257-2272.

Birch, J. M., Dickson, W. B. and Dickinson, M. H. (2004) Force production and flow structure of the leading edge vortex on flapping wings at high and low reynolds numbers *J. Exp. Biol.* **207**, 1063-1072.

Dickinson, M. H. and Götz, K. G. (1993). Unsteady aerodynamic performance of model wings at low Reynolds numbers. *J. Exp. Biol.* **174**, 45-64.

Dickinson, M. H. (1994). The effects of wing rotation on unsteady aerodynamic performance at low Reynolds numbers. *J. Exp. Biol.* **192**, 179-206.

Dickinson, M. H., Lehmann, F. O. and Sane, S. P. (1999). Wing rotation and the aerodynamic basis of insect flight. *Science* **284**, 1954-1960.

Dickson, W. B. and Dickinson, M. H. (2004). The effect of advance ratio on the aerodynamics of revolving wings. J. Exp. Biol. **207**, 4269-4281.

Dumitrescu, H. and Cardos, V. (2003). Rotational effects on the boundary-layer flow in wind turbines. *AIAA Journal* **42**, 408-411.

Ellington C. P. (1984). The aerodynamics of insect flight I-VI. *Phil. Trans. R. Soc. Lond. B* **305**, 1-181.

Ellington C. P., Van den Berg C., Willmott A. P. and Thomas A. L. R. (1996). Leading-edge vortices in insect flight. *Nature* **384**, 626-630.

Ellington, C. P. and Usherwood, J. R. (2001). Lift and drag characteristics of rotary and flapping wings. in: *Fixed and flapping wing aerodynamics for micro air vehicle applications.* Ed. Mueller T.J., AIAA books.

Fry, S. N., Sayaman, R. and Dickinson, M. H. (2003). The aerodynamics of free-flight maneuvers in Drosophila. *Science* **300,** 495-498.

Greenwell D. I. (2002). Simple engineering model for delta-wing vortex breakdown. *J. Aircraft* **40**, 402-405.

Greitzer, E. M., Tan, C. S. and Graf, M. B. (2004). *Internal flow concepts and applications.* Cambridge University Press.

Himmelskamp, H. (1947). Profile investigations on a rotating airscrew. *Dissertation Göttingen 1945*, Reports and Translations No. 832.

Hubel, T. (2006). Untersuchungen zur instationären Aerodynamik an einem vogelähnlichen Flügelschlagmodell, PhD thesis, *TU Darmstadt, Fachbereich Biologie*.

Kerwin, J. E. (1986) Marine propellers. *Ann. rev. Fluid Mech.* **18,** 367-403.

Lentink, D., Müller, U. K., Stamhuis, E. J., de Kat, R., van Gestel, W., Veldhuis, L. L. M., Henningsson, P., Hedenström, A., Videler, J. J. and van Leeuwen, J. L. (2007). How swifts control their glide performance with morphing wings. *Nature* **446**, 1082-1085.

Lentink, D., Muijres, F. T., Donker-Duyvis, F. J. and van Leeuwen, J. L. (2008). Vortex-wake interactions of a flapping foil that models animal swimming and flight. *J. Exp. Biol.* **211**, 267-273.

Lentink, D. and Dickinson, M. H. (2008). Biofluiddynamic scaling of flapping, spinning and translating fins and wings. *J. Exp. Biol.*, submitted.

Lindenburg, C. (2004). Modelling of rotational augmentation based on engineering considerations and measurements. *European wind energy conference*, London.

Lu, Y., Shen, G. X. and Lai, G. J. (2006). Dual leading-edge vortices on flapping wings. *J. Exp. Biol.* **209**, 5005-5016.

Maxworthy, T. (1979). Experiments on the Weis-Fogh mechanism of lift generation by insects in hovering flight. Part 1. Dynamics of the 'fling'. *J. Fluid Mech.* **93**, 47-63.

McMahon, T. A. (1984) *Muscles, reflexes, and locomotion*. Princeton University Pres.

Miller, L. A. and Peskin, C. S. (2004). When vortices stick: an aerodynamic transition in tiny insect flight. *J. Exp. Biol.* **207**, 3073-3088.

Muijres, F. T., Johansson, L. C., Barfield, R., Wolf M., Spedding, G. R. and Hedenström, A. (2008). Leading-Edge Vortex Improves Lift in Slow-Flying Bats. *Science* **319**, 1250-1253.

Poelma, C., Dickson, W. B. and Dickinson, M. H. (2006). Time-resolved reconstruction of the full velocity field around a dynamically-scaled flapping wing. *Exp. Fluids* **41**, 213-225.

Ringuette, M., Milano, M. and Gharib, M. (2007). Role of the tip vortex in the force generation of low-aspect-ratio normal flat plates. *J. Fluid. Mech.* **581**, 453–468.

Rossby, C. G. (1936). On the momentum transfer at the sea surface. Part I Papers *Phys. Oceanogr. Meteorol* 3 no 3.

Ruijgrok, G. J. J. (1994). *Elements of airplane performance.* Delft University Press Delft.

Sane, S. P. and Dickinson, M. H. (2001). The control of flight force by a flapping wing: lift and drag production. *J Exp Biol* **204**, 2607-2626.

Schmitz, F. W. (1942). Aerodynamik des flugmodells, C.J.E. Volckmann Nachf. E. Wette, Berlin.

Schlichting, H. (1979) *Boundary-layer theory.* McGraw-Hill, 7th edition.

Simonich, J., McCormick, D. and Haas, R. (1992) Flow visualization of a prop-fan leading edge vortex at takeoff. *AIAA* **0386**.

Srygley, R. B. and Thomas, A. L. R. (2002). Unconventional lift-generating mechanisms in free-flying butterflies. *Nature* **420,** 660-664.

Stepniewski, W. Z. and Keys, C. N. (1984) *Rotary-wing aerodynamics.* Dover.

Sun, M. and WU, J. (2004) Large aerodynamic forces on a sweeping wing at low Reynolds number. *Acta Mechanica Sinica* **20**, 24-31.

Tangler, J. L. (2004). Insight into wind turbine stall and post-stall aerodynamics. *Wind Energy* **7**, 247-260.

Usherwood, J. R. and Ellington, C. P. (2002). The aerodynamics of revolving wings I-II. *J. Exp. Biol.* **205**, 1547-1576.

Van Den Berg, C. and Ellington, C. P. (1997). The three-dimensional leading-edge vortex of a 'hovering' model hawkmoth. *Philos. Trans. R. Soc. Lond. B Biol. Sci.* **352**, 329 -340.

Vanyo, J. P. (1993). *Rotating fluids in engineering and science.* Dover.

Videler, J. J., Stamhuis, E. J. and Povel, G. D. E. (2004) Leading-edge vortex lifts swifts. *Science* **306**, 1960-1962.

Wang, Z. J., Birch, J. M., Dickinson, M. H. (2004). Unsteady forces and flows in low Reynolds number hovering flight: two-dimensional computations vs robotic wing experiments *J. Exp. Biol.* **207**, 449-460

Wang, Z. J. (2008). Aerodynamic efficiency of flapping flight: analysis of a two-stroke model *J. Exp. Biol.* **211**, 234-238.

Warrick, D. R., Tobalske, B. W. and Powers, D. R. (2005). Aerodynamics of the hovering hummingbird. *Nature* **435**, 1094-1097.

Winter, H. (1936). Flow phenomena on plates and airfoils of short span. *NACA report 798.*

5 Swirling down to earth

5.1

A LEADING EDGE VORTEX PROLONGS DESCENT OF MAPLE SEEDS

David Lentink*, William B. Dickson, Johan L. van Leeuwen and Michael H. Dickinson

Like other autorotating seeds, swirling maple seeds descend slowly to the ground and can thus make more effective use of wind for dispersal[1-5]. As they descend, the autorotating seeds of maples and other trees generate exceptionally high lift forces for their wing area[6,7], but the mechanisms by which they attain this elevated performance is largely unknown. To find out how they achieve this aerodynamically, we measured the three-dimensional flow around dynamically scaled models of maple and hornbeam seeds. We show that maple seeds attain high lift because they generate a stable leading edge vortex (LEV), whereas the flow around the hornbeam seed is partially separated. Taking both seed weight and wing area into account for a wide range of gliding and spinning seeds[3,7-9], we find that maple seeds remain in the air more effectively than do both hornbeam and a variety of non-autorotating seeds. LEVs also explain the high lift generated by hovering insects[10-13], bats[14] and possibly, hummingbirds[15]. This suggests that the ability to generate LEVs represents a convergent aerodynamic solution in the evolution of flight performance in both animals and plants. The high performance aerodynamics of maple seeds could inspire the design of future turbine blades and autorotating vehicles[16,17].

Maples (*Acer*) are primary succession trees adapted to nutrient-poor habitats in temperate climates[18]. Like many other pioneer trees, maples rely on wind, updrafts and turbulent gusts to disperse their seeds over distances ranging from several meters to, on occasion, kilometers[4,5]. Maple seeds typically disperse under windy conditions and start to autorotate within one meter of detaching from the tree (Fig. 1a, c). Autorotation results from the heavy nut, and hence the seed's center of gravity, being located at the wing base[1-3,6,7]. The stable autorotation of maple and other rotary seeds depends on an intricate, non-linear, interplay between their three-dimensional inertial and aerodynamic properties, which is not fully understood[6,16,19]. The presumed function of autorotation is that it creates lift to prolong the descent of the seed. Detailed performance studies by Norberg[6] and Azuma and Yasuda[3,7] revealed that autorotating seeds are able to generate exceptionally high lift forces with their small, slow wings. The seed's capacity to generate lift is quantified by its mean lift coefficient which is typically well above one[3,7]. How autorotating seeds are able to attain such high lift coefficients is unknown[3]. Usherwood and Ellington[20] noted that both autorotating seeds and steadily revolving insect wings generate exceptional high lift. Insect wings and autorotating seeds operate at high angles of attack, well beyond the point (roughly beyond 15-20°) at which aircraft wings and helicopter blades abruptly loose lift or 'stall' during flight (Fig. 1d). Instead of stalling, insect wings generate a prominent leading edge vortex (LEV), which is known to be responsible for elevating both lift and drag[10-13,20,21]. Building upon these observations we hypothesized that autorotating seeds generate a LEV that enables them to generate high lift at high angles of attack during their descent.

Submitted

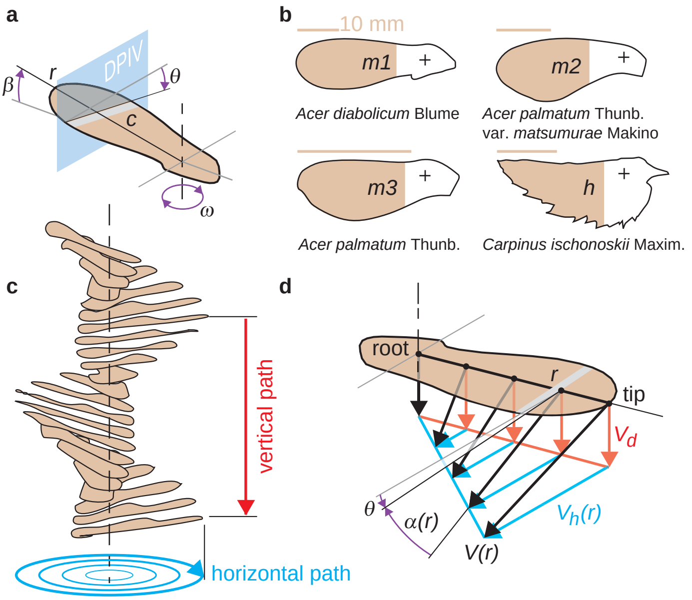

Figure 1 | Kinematics and morphology of all four autorotating seeds studied. a, Free flight parameters of autorotating seeds after Azuma and Yasuda[7]; local wing radius, *r*; local chord length, *c*; pitch angle, θ; cone angle, β; angular velocity, ω. One of up to 26 planes in which we measured the velocity field along the span using DPIV is indicated in blue. **b,** Planform and Latin names of the three maple seeds (*m1*, *m2*, *m3*) and hornbeam seed (*h*) studied, the brown area indicates the region for which we performed DPIV around the wing The plus sign indicates the center of gravity, which corresponds closely to the center of rotation[3,7,23]. **c,** Free flight sequence of an autorotating seed showing both the vertical (red) and horizontal, circular translation (blue) of a wing section during a full period. **d,** Due to the different horizontal path lengths travelled by subsequent spanwise wing sections (**c**), the wing's local geometric angle of attack is defined as the arctangent of descend speed, V_d, divided by horizontal speed, V_h. The effective aerodynamic angle of attack, α, is equal to geometric angle of attack minus the absolute value of the pitch angle (*m1*: -1.17°, *m2*: -1.39°; *m3*: -0.90°, *h*: -2.16° measured at 75% span and approximately constant along span (Azuma and Yasuda[7])); α starts at its minimum value at the tip and increases towards the base where it is 90°. (Note *V* is velocity and '(*r*)' indicates dependence of a variable on radius.)

To test if autorotating seeds generate a LEV we built a dynamically scaled model actuated by a robotic arm in a tank of mineral oil[22] (methods). We based the shape and kinematics of the model seeds on the shape (n = 1) and average free flight parameters (n = 20) of seeds from three species of maple (*Acer diabolicum* Blume; *m1*, *Acer palmatum* Thunb. var. *matsumurae* Makino; *m2*, *Acer palmatum* Thunb; *m3*) and one species of hornbeam (*Carpinus ischonoskii* Maxim; *h*) (Fig. 1b). All four of these seeds are known to generate exceptionally high lift[7,23]. The flight parameters and the ratio of inertial to viscous stress in the surrounding flow of the model seeds in oil were scaled such that they are identical to real seeds descending in air. This stress-ratio is measured by the Reynolds number and is of order 1000 for autorotating seeds[7]. We used stereo digital particle image velocimetry (DPIV) to measure the three-dimensional velocity field at

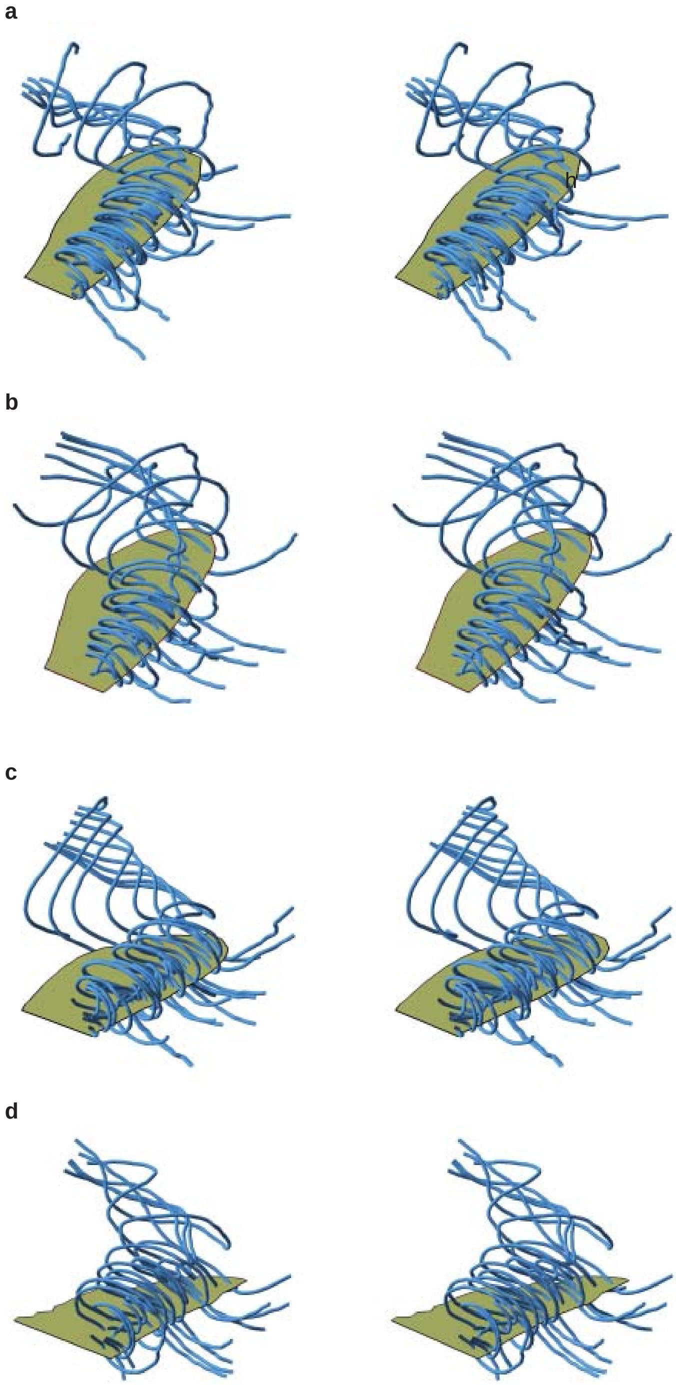

Figure 2 | Stereo images of the large leading edge vortex (LEV) measured for all four model seeds. a-d, Flow visualization of absolute (in lab frame) streamlines (shown in blue); calculated from the three-dimensional velocity field measured using DPIV. The models of the three maple seeds (**a**, *m1*; **b**, *m2*; **c**, *m3*) and the hornbeam seed (**d**, *h*) generate a LEV with significant spanwise flow that is connected to the tip vortex. The angle of attack of the seed increases from (**a**) to (**d**). Note that the seed spins clockwise (in all figures).

26 equally spaced spanwise slices starting at roughly 25% span (indicated in brown in Fig. 1b) and extending well beyond the wing tip so that we would captured the structure of the tip vortex as well. We combined all these slices to reconstruct the three-dimensional velocity field around the model seeds[24] (Fig. 2 and methods).

Our measurements show that all four model seeds generate a prominent LEV near the base, which is strikingly similar to LEVs generated by insect wings. The structure of the LEV depends not only on the wing shape and Reynolds number, but also on the wing's angle of attack. The angle of attack is maximal at the wing root (approx. 90°) and minimal at the wing tip due to the seeds radial velocity distribution (Fig. 1d). Based on prior free flight measurements[7,23] we calculated the angle of attack at the wing tip of all four seeds. It is lowest for maple seed *m1* (14°), highest for hornbeam

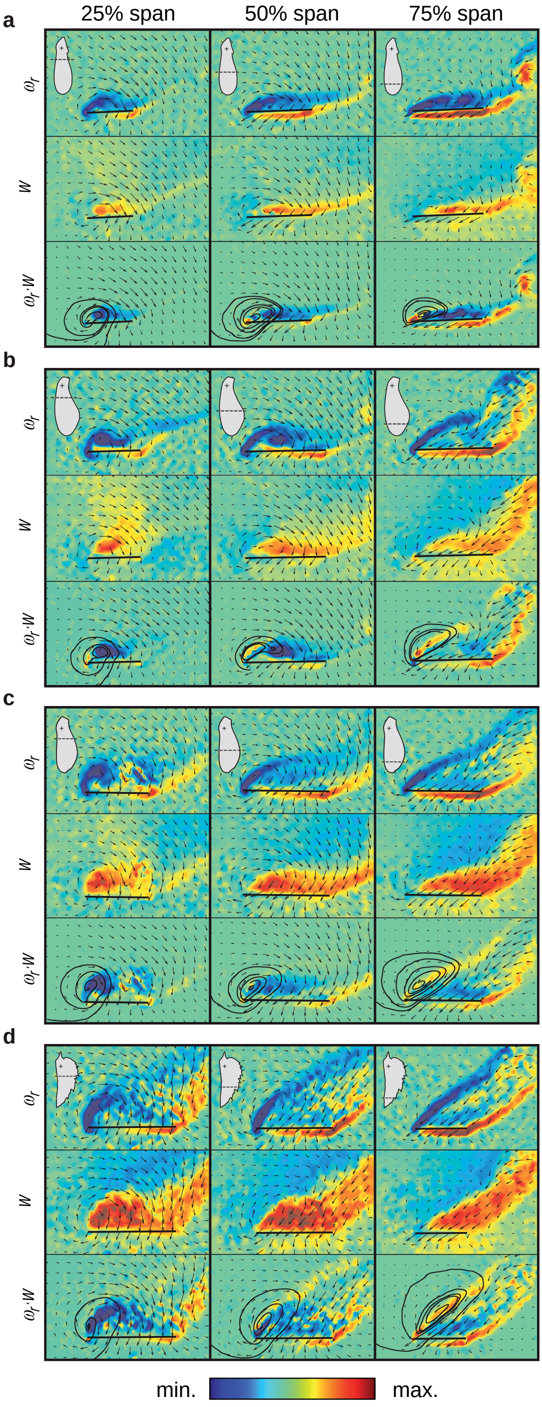

Figure 3 | The vorticity concentration that builds-up the LEV at the wing's base is drained by concentrated spanwise flow. a-d, Measured flow fields of seeds *m1* (**a**), *m2* (**b**), *m3* (**c**) and *h* (**d**) subsequently shown in the three columns of every block for three spanwise sections; 25%, 50% and 75% span. First row shows spanwise vorticity (ω_r) which builds up into a significant LEV at 25% span for all four seeds (color bar **a-d**: ±70; ±50; ±30; ±30 [s^{-1}]). Second row shows spanwise flow speed (w) which peaks at 25% span (color bar **a-d**: ±0.5; ±0.4; ±0.2; ±0.2 [$m\,s^{-1}$]). Third row shows spanwise transport of vorticity ($\omega_r \cdot w$), which peaks at 25% span (color bar **a-d**: ±13; ±8; ±3; ±3 [$m\,s^{-2}$]).

h (28°), with the other two maples seeds, *m2* (22°) and *m3* (25°), falling in between (methods). This qualitative trend can explain in part why the LEV of all three maple seeds (Fig. 2a-c) is relatively compact and well attached to the seed's surface, whereas the LEV generated by the hornbeam seed looks more separated (Fig. 2d). The LEV is most prominent near the base of the seed, at roughly 25% span, where there is a strong concentration of vorticity (first row Fig. 3a-d). Towards the tip (at 75% span), the LEV merges with the tip vortex, resulting in a long trail of vorticity in the seed's wake. The flow around the maple seeds re-attaches behind the LEV near the trailing edge, whereas the flow around the hornbeam seed is more separated at the wing tip and fails to re-attach. This difference in flow structure is also apparent in images of the three- and two-dimensional streamlines (Fig. 2 and last row Fig. 3a-d) and the vorticity plots (first row Fig. 3a-d).

How well does the flow structure around the seeds compare to those of insect wings? For insects operating at Reynolds numbers of order 1000, the stable attachment of the LEV depends partly on strong span-wise flow on top of the wing that drains vorticity from the LEV towards the wing tip vortex[11,25]. This process is a key feature, because it prevents the LEV from growing so large that it becomes unstable and separates. For all four seeds we find

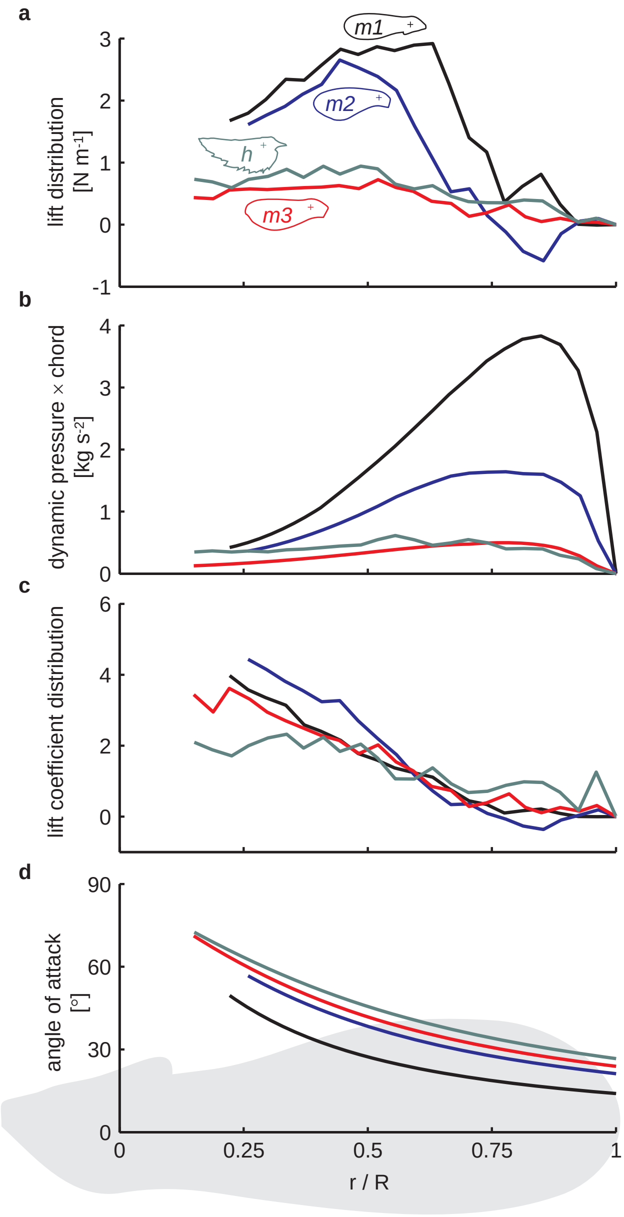

Figure 4 | The LEV induces exceptional high local lift coefficients near the wings base. a, Spanwise lift distribution. The wing's sectional lift is particularly low near the wing tip due to the presence of the tip vortex (*r*, local radius; *R*, wingtip radius; seed code, Fig. 1b). **b,** Product of sectional dynamic pressure and chord length. **c,** The wing's lift sectional coefficient (**a** divided by **b**), peaks near the wing's base (where a LEV is present) and it is minimal at the tip. **d,** The distribution of angle of attack with span. The high lift coefficients near the base of the wing (**c**) and the corresponding LEV result from the extremely high local angles of attack, well beyond 30°.

strong spanwise flow on top of the wing (second row Fig. 3a-d). The spanwise flow is concentrated in the LEV at 25% span, whereas it is smeared out towards the trailing edge at 50% span and convected into the wake and tip-vortex at 75% span. To test if the spanwise flow is sufficient to drain vorticity from the LEV of these model seeds, as found for insects LEVs, we computed the spanwise transport of vorticity (vorticity × spanwise flow speed) towards the wing tip (third row Fig. 3a-d). Vorticity transport is strong at 25% span, it is less prominently concentrated at 50% span and it is absent for *m2*, *m3* and *h* at 75% span where the LEV connects to the tip vortex. This suggests that the LEV structure of all four seeds is quite similar to that of insects[11,25].

We computed the seed's spanwise lift distribution using the area integral of measured vorticity around each wing section (methods, Fig. 4a). Sectional lift peaks near 40-60% span for maple seeds *m1* and *m2*, whereas it forms a wide plateau for maple seed *m3* and hornbeam seed *h*. The lift distribution is equal to the product of local chord length times sectional dynamic pressure and sectional lift coefficient (methods, Fig. 4b, c). We find that the spanwise lift variation of the maple seeds is significantly smaller than expected, because the product of sectional dynamic pressure and chord length peaks near the wing's tip (Fig. 4b), whereas the sectional lift coefficient peaks near the base (Fig. 4c), thus compensating each other. The sectional lift coefficient reaches values ranging from 2 for hornbeam to 4.5 for maple seeds. This increase in lift coefficient at the base is explained in part by the variation in angle of attack, which ranges from 30° to 70° at the base (Fig. 4d). The flow visualization in Fig. 2 and 3 indicates that the LEV is stably attached at the 25% span location where the sectional lift coefficients are greatest. This stability is noteworthy, given that the local angles of attack are well beyond the stall point for conventional aircraft wings and helicopter blades. Near the wing's base, the section lift coefficients are lowest for the hornbeam seed, which is operating at the highest local angles of attack off all four seeds. This high angle of attack at the base may explain why the hornbeam seed appears partially stalled (Fig. 4d). Our results (Fig. 4c, d) further suggest that previous estimates of local stall angle based on theoretical aerodynamic models[7] (20°) substantially underestimate actual wing performance. The resulting average lift coefficient of the four seeds increases with angle of attack: *m1*; 1.15, *m2*; 1.38, *m3*; 1.43, *h*; 1.67, which is computed using the blade element method and free flight data of Azuma and Yasuda[7]. The corresponding measured average lift coefficients, averaged over the brown areas in Fig. 1b, are 1.19, 1.17, 1.39 and 1.71. Although we find that the hornbeam seed is locally stalled, it generates the highest average lift coefficient.

How effectively do these autorotating seeds descend and how do they perform compared to other autorotating and gliding seeds? Assuming that the descent speed and nut mass of flying seeds are good choices for their local weather conditions and habitat, the tree can minimize the surface area of its seeds through optimizing aerodynamic efficacy. Minimizing surface area results in maximizing wing loading (weight divided by surface area). The lower surface area saves the tree both material and energy spent on seed dispersal, or alternatively it allows the tree to make and disperse more seeds. To compare aerodynamic performance across specimens, we computed for each seed a dimensionless descent factor, defined as seed weight divided by the product of wing area and the dynamic pressure due to descent speed (methods) (Fig. 5). A high descent factor indicates that for a seed's measured descent speed, mass, and wing area it exhibits a high aerodynamic efficacy, allowing it to use a relatively small wing operating at high loading. Descent factor is highest for maple *m1* and is subsequently lower for *m2*, *m3* and hornbeam *h*. The compact and well-attached LEV generated by the maple seeds corresponds to better aerodynamic efficacy than that of the partially stalled hornbeam seed (neglecting Reynolds number and morphology

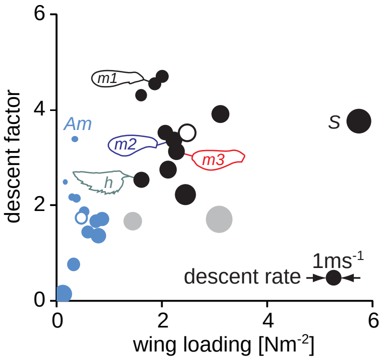

Figure 5 | Comparison of descent performance for various seeds. A dimensionless descent factor (see text) is plotted as a function of wing loading. The width of each point indicates descent speed. Autorotating seeds are shown in black; *S* is a four winged Santalaceae seed. The three maple seeds perform better than hornbeam seed. Ash and tulip tree seeds (plotted in grey) also autorotate, but spin along two major axes. Both descend similarly well as gliding seeds, plotted in blue. The gliding seed, *Alsomitra macrocarpa* (*Am*) has a fragile sail wing that enables it to descent particularly well at relatively high Reynolds numbers (c. 5000, roughly five times higher than maple and hornbeam seeds). The average descent factor of gliding seeds is, however, much lower than that of autorotating seeds (that spin along one axis). Average performance is indicated with open circles. (Based on flight data of Azuma and co-workers[3,7-9].)

effects). On average, the descent factor of autorotating seeds is 100% higher than that of gliding seeds, enabling them to descend only 50% faster at wing loadings (seed weight / wing area) that are 400% higher than those of gliding seeds. Although the success of wind dispersal depends critically on flight performance, it is unclear how these performance differences relate to possible differences in evolutionary success. We expect that differences in flight performance interact with various ecological and meteorological factors resulting in different niches for different descent strategies.

The high lift of LEVs is not only exploited by autorotating seeds during their descent, hovering insects[10-13,20,21], bats[14] and probably hummingbirds[15] utilize the same mechanism. This suggests that the use of LEVs represents a convergent aerodynamic solution in the evolution of high performance flight of both animals and plant seeds. Our findings further suggest that animals might generate a leading edge vortex not only during hovering flight, but also during forward flight, which closely resembles the flow conditions of autorotating seeds during their descent. The aerodynamics of autorotating seeds is also quite similar to that of wind turbines. Although turbine blades are more slender and operate at much higher Reynolds numbers than the wings of autorotating seeds, both extract energy from the incoming flow, and both generate exceptionally high lift near their base (hub) at similar normalized local radii (roughly at local radii / chord length ≤ 3). For wind turbines, Tangler[26] hypothesized that a large standing vortex might be responsible for lift augmentation near the hub. This is supported by computational fluid dynamic simulations[27]. Our experiments on seeds readily support this hypothesis for a Reynolds number of order 1000. Our finding of a strong LEV that is responsible for the high lift generated by autorotating seeds could therefore inspire the design of future turbine blades and autorotating vehicles[16,17].

Methods

Dynamically-scaled robot seed. Using a translating robotic arm immerged in a tank filled with mineral oil[22] (density = 830 kg m^{-3}; kinematic viscosity = 11.0×10^{-6} $m^2\,s^{-1}$) we dynamically-scaled the kinematics of four model autorotating seeds (Fig. 1b) such that their planer shape, Reynolds number, and flight parameters (e.g. descent speed and angle of attack) matched those of freely flying seeds. The free flight parameters of the seeds are described in Azuma and Yasuda[7] and their morphology in Azuma and Yasuda[7] and Yasuda and Azuma[23]. The angle of attack of the seeds is calculated based on the free flight data and by adding the negative pitch angle (close to -1° at 75% radius) to the positive local geometric angle of attack, see Fig. 1. In matching the morphology of the flat seeds, the model wings had no twist. The model wings were made from 1.5 mm thick transparent acrylic; such simple wing models have proven accurate in representing moderately cambered and corrugated insect wings at Reynolds numbers[12,20,22,25] similar to that used here for the four seeds (Fig. 1b). The distance between the wing's center of rotation and its tip was 130 mm for all model seeds to minimize wall effects, which we estimated to be within 1% of an infinite volume (Dickinson, *et al.*, 1999). We tilted the flight path 90° (horizontal) to enable the robot[22] to correctly translate and spin the seeds at their natural pitch and cone angle (Fig. 1a, Supplementary Fig.1).

Stereo DPIV flow measurement. We measured flow fields after two whole revolutions when the flow was steady and repeatable using the LaVision stereo DPIV software and hardware described in Poelma *et al.*[24]. The pitch of the resulting spiraling tip vortex is large, such that interactions with tip vortices shed beyond one revolution are small (e.g. see Fig. 9 in Azuma and Yasuda[7]). By repeating the DPIV measurements 10 times per spanwise section we were able to perform standard stereo ensemble correlation for every section (multipass: $1\times(64\times64)$ and $2\times(32\times32)$ each with 50% overlap) using DaVis 7.0, LaVision GmbH (Poelma *et al.*[24]). We measured flow fields at 24 to 26 spanwise sections that were separated by 5 mm. Using custom Matlab R2007a software and Tecplot 360 we processed data and build up the three dimensional velocity field. The spanwise velocity field sampling proved to be smooth enough for plotting the absolute (in lab frame) streamlines in Fig. 2 (view point & angle are identical in Fig. a-d, stereo angle offset is ±3.5 degrees). To obtain high-quality vorticity fields we calculated the gradient of the flow field in the spanwise sections for which we have good resolution measurements. Through integration of the vorticity field in every spanwise section we obtained the corresponding spanwise circulation. For this we used a vorticity cut-off value 5% higher than the highest vorticity noise found in the upstream flow field at the particular spanwise section. We then used circulation to calculate section lift = fluid density × section wing speed × net section circulation. Finally we calculated the wing section lift coefficient by dividing section lift by the product of dynamic pressure (½ × fluid density × section wing speed squared) and section chord length.

Calculation seed flight performance. Average lift coefficients were calculated using a blade element method similar to the one used for calculating the average lift coefficients of insect wings in forward flight[22], which takes into account that the seed's descent direction is parallel to its angular velocity vector. Finally, we calculated the aerodynamic descent performance of various seeds using a basic point mass performance analysis. This analysis provided a dimensionless descent factor, which was calculated as seed weight divided by the product of dynamic pressure (based on descent speed) and wing area, see supplementary equations (1).

Acknowledgements

All experiments were conducted in the Robofly facility at the California Institute of Technology. We thank Gerrit Elsinga, Jim Usherwood and GertJan van Heijst for valuable comments. Research was funded by NWO-ALW grant 817.02.012 to D. L. and J. L. v. L., and National Science Foundation grant (IBN-0217229) to M. H .D.

References

1. **Burrows F. M.** in *Seed Dispersal* (ed. Murray D.R.) 1-49 (Academic Press, San Diego, 1986).
2. **Niklas, K. J.** *Plant Biomechanics* (The Univ. of Chicago Press, Chicago, 1992).
3. **Azuma, A.** *The Biokinetics of Flying and Swimming* 2nd edn (AIAA Education Series, Reston, 2006).
4. **Nathan, R., Katul, G.G., Horn, H. S., Thomas, S. M., Oren, R., Avissar, R., Pacala, S.W., & Levin S. A.** Mechanisms of long-distance dispersal of seeds by wind. *Nature* **418**, 409-413 (2002).
5. **Nathan, R.** Long distance dispersal of plants. *Science* **11**, 786-788 (2006).
6. **Norberg, R. A.**, Autorotation, self-stability and structure of single-winged fruits and seeds (samaras) with comparative remarks on animal flight. *Biological Reviews* **48** 561-596 (1973).
7. **Azuma, A. & Yasuda K.** Flight performance of rotary seeds. *J. Theor. Biol.* **138** 23-53 (1989).
8. **Azuma, A. & Okuno, Y.** Flight of a Samara, Alsomitra macrocarpa. *J. Theor. Biol.* **129** 263-274 (1987).
9. **Minami, S. & Azuma, A.** Various flying modes of wind-dispersal seeds. *J. Theor. Biol.* **225** 1-14 (2003).
10. **Maxworthy, T.** Experiments on the Weis-Fogh mechanism of lift generation by insects in hovering flight. Part 1. Dynamics of the `fling'. *J. Fluid Mech.* **93** 47-63 (1979).
11. **Ellington, C. P., van den Berg, C., Willmott, A. P. & Thomas, A. L. R.** Leading-edge vortices in insect flight. *Nature* **384** 626 -630 (1996).
12. **Dickinson, M. H., Lehmann, F.-O. & Sane, S. P.** Wing rotation and the aerodynamic basis of insect flight. *Science* **284** 1954 -1960 (1999).
13. **Srygley, R. B. & Thomas, A. L. R.** Unconventional lift-generating mechanisms in free-flying butterflies. *Nature* **420** 660 -664 (2002).
14. **Muijres F. T., Johansson L. C., Barfield R., Wolf M., Spedding G. R. & Hedenström A.** Leading-Edge Vortex Improves Lift in Slow-Flying Bats. Science 319, 1250 -1253 (2008).
15. **Warrick, D. R., Tobalske, B. W. & Powers, D. R.** Aerodynamics of the hovering hummingbird. *Nature* **435** 1094-1097 (2005).
16. **Lugt, H. J.** Autorotation. *Ann. Rev. Fluid Mech.* **15** 123-147 (1985).
17. **Lorenz, R. D.** *Spinning Flight* (Springer, New York, 2006)
18. **Van der Pijl, L.** *Principles of Dispersal in Higher Plants* 3rd ed. (Springer-Verlag, Berlin, 1982).
19. **Seter, D. & Rosen A.** Stability of the vertical autorotation of a single-winged samara. *Transactions of the ASME* **59** 1000-1008 (1992).
20. **Usherwood, J. R. & Ellington, C. P.** The aerodynamics of revolving wings. I. Model hawkmoth wings. *J. Exp. Biol.* **205** 1547-1564 (2002).
21. **Dickinson, M. H. & Götz, K. G.** Unsteady aerodynamic performance of model wings at

low Reynolds numbers. *J. Exp. Biol.* **174** 45-64 (1993).
22. **Dickson, W. B. & Dickinson, M. H.** The effect of advance ratio on the aerodynamics of revolving wings. *J. Exp. Biol.* **207** 4269-4281 (2004).
23. **Yasuda, K. & Azuma, A.** The autorotation boundary in the flight of samaras. *J. Theor. Biol.* **185** 313-320 (1997).
24. **Poelma, C., Dickson, W. B. & Dickinson, M. H.** Time-resolved reconstruction of the full velocity field around a dynamically-scaled flapping wing. *Exp. Fluids* **41** 213-225 (2006).
25. **Birch, J. M., Dickson, W. B. & Dickinson, M. H.** Force production and flow structure of the leading edge vortex on flapping wings at high and low reynolds numbers. *J. Exp. Biol.* **207** 1063-1072 (2004).
26. **Tangler, J. L.** Insight into wind turbine stall and post-stall aerodynamics. *Wind Energy* 7 247-260 (2004).
27. **Beom-Seok, K., Jeong-Hwan, K., Koji, K., van Rooij, R. P. J. O. M. & Young-Ho L.** 3D Numerical predictions of horizontal axis wind turbine power characteristics of the scaled Delft university T40/50 model. *Fifth JSME-KSME Fluids Engineering Conference*, Nagoya, Japan (2002).

Supplementary Figure 1. *Robot model of a descending autorotating seed.*

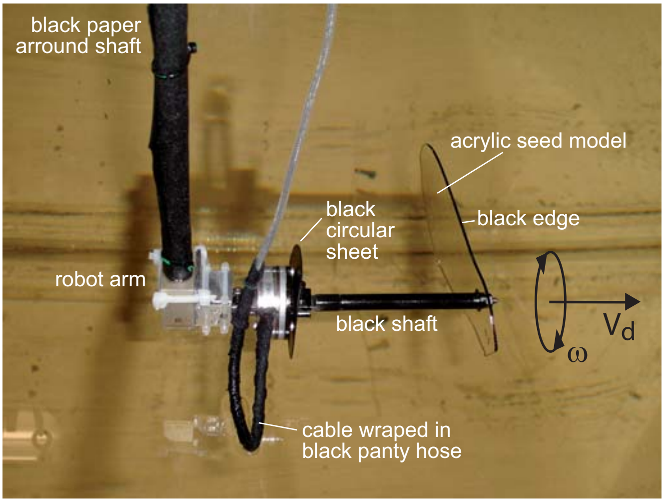

Robot. The robot seed consists of an acrylic seed model driven by a translating robot arm[1]. Our robot can only translate horizontally, thus to simulate the descending flight of the hornbeam and maple we tilted the flight path by 90°. The acrylic seed models were fixed to the shaft at their measured cone and pitch angle[2]. We revolved (ω; angular velocity) and translated (V_d; descent speed) the model seeds in oil such that they followed the same path at the same Reynolds number as seeds in air[2]. The model seed moves from left to right such that it flies in undisturbed oil; the wake of the seed hits the arm (and not *vice versa*).

DPIV. We measured the three-dimensional flow field using a stereo Digital Particle Image Velocimetry setup described previously[3]. The laser light sheet was oriented parallel to chord length, (close to the one shown) and was activated using an automated trigger. To minimize laser light reflections in our DPIV image, both the shaft and edges of the wings were painted black. In addition, we placed a black circular sheet in front to shield the robots knuckle, wrapped the sensor cable in black panty hose (Sheer Energy, Leggs), and wrapped a black sheet around the shaft of the robot arm.

References

1. **Dickson, W. B. & Dickinson, M. H.** The effect of advance ratio on the aerodynamics of revolving wings. *J. Exp. Biol.* **207** 4269-4281 (2004).
2. **Azuma, A. & Yasuda K.** Flight performance of rotary seeds. *J.Theor. Biol.* **138** 23-53 (1989).
3. **Poelma, C., Dickson, W. B. & Dickinson, M. H.** Time-resolved reconstruction of the full velocity field around a dynamically-scaled flapping wing. *Exp. Fluids* **41** 213-225 (2006).

Supplementary Equations 1. ***Derivation of the descent factor of seeds.***

We derive the descent factor of a seed, which measures its aerodynamic efficacy, using a basic point performance analysis[1] and the blade element method. The blade element method is applied similarly to the one used in calculating forward insect flight performance[2]. The vertical aerodynamic force generated by a seed counteracts its weight W. The vertical force distribution over the wing can be integrated along the span using small chord wise surface segments of chord wise length c and width dr at radial distance r (Fig. 1). The total vertical force F_V can be calculated as follows:

$$F_V = \int_0^R C_V(r)\cdot 1/2\,\rho\left(V_\text{d}^2+\omega^2 r^2\right)\cdot c(r)dr \quad , \tag{1}$$

in which C_V the vertical force coefficient, ρ the density, V_d the descent speed and ω the angular velocity and, finally, '(r)' indicates that the particular variable depends on radius. Noting that F_V is equal (in magnitude) to the seeds weight W, which is equal to mass m times gravity constant g, we can now define the average vertical force coefficient as follows:

$$C_{V,\text{ave}} = \frac{mg}{\int_0^R 1/2\,\rho\left(V_\text{d}^2+\omega^2 r^2\right)\cdot c(r)\,dr} = \frac{mg}{1/2\,\rho\left(V_\text{d}^2+\omega^2 R_\text{g}^2\right)S}\,, \tag{2}$$

in which R_g is the radius of gyration of the seeds wing. We now find the following expression for the surface area needed for a seed of given mass and descent rate in air ($\rho \approx 1.23$) on earth ($g \approx 9.81$):

$$S = \frac{2mg}{C_{V,\text{ave}}\,\rho\left(1+\dfrac{\omega^2 R_\text{g}^2}{V_\text{d}^2}\right)V_\text{d}^2} = \frac{2mg}{C_{V,\text{ave}}\,\rho\left(1+\dfrac{1}{k_\text{g}^2}\right)V_\text{d}^2}\,, \tag{3}$$

with the advance ratio k_g at the radius of gyration being:

$$k_g = \frac{V_d}{\omega R_g}. \qquad (4)$$

Based on Eq. 4 we can now infer the factors through which a seed can minimize its wing area. First it can increase its average vertical force coefficient $C_{V,ave}$ through optimizing wing morphology and the angle of attack of the wing (Ruijgrok, 1994). Angle of attack depends, however, directly on advance ratio k_g. (Fig. 1d) which therefore determines $C_{V,ave}$. We therefore include both $C_{V,ave}$ and k_g simultaneously in the descent factor *DF*:

$$DF = \left(1 + \frac{1}{k}\right) C_{V,ave}, \qquad (5)$$

which needs to be maximized for minimizing wing surface area at given mass *m* and descend speed V_d (Eq. 3.). To evaluate the aerodynamic efficacy of a seed we can now simply calculate its descent factor based on readily available field and lab data as:

$$DF = \frac{2mg}{\rho V_d^2 S}. \qquad (6)$$

This formula is derived from Equations 3 and 5. It also works for seeds that spin along two axes or simply glide; our analysis yields the same formula (Eq. 6.). For gliding seeds we consider the average descent speed and absolute average of forward speed. We then again find that aerodynamic efficacy is measured by a product of the average vertical force coefficient times a factor that captures the descent kinematics like the advance ratio does for autorotating seeds; the average glide ratio. Although one could think of extracting subtleties from the descent factor, such as the effect of cone angle and other kinematic parameters on needed wing surface area, we choose not to do so because here we are interested in the total aerodynamic efficacy of the seed. We therefore use Equation 6 to calculate and compare the total aerodynamic descent efficacy of several spinning and gliding seeds (see Fig. 5).

References

1. **Ruijgrok, G. J. J.** *Elements of airplane performance*. Delft University Press Delft (1994).
2. **Dickson, W. B. & Dickinson, M. H.** The effect of advance ratio on the aerodynamics of revolving wings. *J. Exp. Biol.* **207** 4269-4281 (2004).

6 Escape into thin air

6.1

TURNING ON A DIME

Ulrike K. Müller* and David Lentink

Scientists may think that insects are the masters of unconventional lift (*1–4*), but it seems that birds have caught on to the same trick, using it to outsmart their insect prey. On page 1960 of this issue, Videler *et al.* (*5*) report how swifts—agile aerial hunters that catch insects on the wing—produce unconventional lift: They use their wings to generate a so-called leading-edge vortex. Biologists first caught on to this vortex in 1996 when trying to explain how insects fly (*1*). Since then, this vortex has been observed again and again in flying insects (*2–4*). The new study reveals that a bird's wing also can generate this type of vortex (*5*).

A leading-edge vortex forms on the top of a wing when the angle between the wing and the oncoming air flow is large. The flow then separates from the wing at the leading edge and rolls up into a vortex. To form a leading-edge vortex at lower angles of attack, some wings have a sharp rather than blunt leading edge. To exploit this vortex, the flying animal needs to keep the vortex close to its wing. Insects and swifts have found different solutions to this problem. To stabilize the vortex, flying insects beat their wings rapidly (*1*), whereas gliding swifts sweep their wings backward (*5*). The leading-edge vortex spirals out toward the tip of the wing, adopting the shape of a tornado. Like a tornado, the air pressure in the core of the vortex is low, sucking the wing upward and sometimes forward (during flapping).

Swifts have scythe-shaped wings that consist of a long curved hand-wing, which is attached to the body by a short arm-wing. The hand-wing is composed of primary feathers, which form a sharp and swept-back leading edge. Both features help to generate and stabilize a leading-edge vortex. Videler *et al.* cast a model of a single swift wing in fast gliding posture and recorded the flow fields around the wing in a water tunnel using digital particle image velocimetry. (Flow patterns in water are the same as in air as long as the same Reynolds number is used.) They observed that a vortex forms on top of the wing close behind the wing's leading edge. This leading-edge vortex is robust against changes in flow speed and angle of attack—observations that agree well with those of other biologists studying the leading-edge vortices of insects. However, surprisingly, the swift wing produces such a vortex at angles of attack as small as 5°, compared with 25° to 45° typical for insects (*6*, *7*).

The achievements of aerospace engineers have inspired biologists to study the aerodynamics of flying animals. Engineers first discovered the extraordinary amount of lift that leading-edge vortices produce when they solved the problem of how to land supersonic fighter jets and passenger aircraft like the Concorde. Swept-back wings not only make supersonic flight possible, but also generate stable leading-edge vortices at high angles of attack. The resulting extra lift enables delta-wing aircraft to land safely despite their small wings, which are much smaller than those of conventional aircraft.

Science **306**, 1899 – 1900 (2004).

The swept wing of a swift generates a stable leading-edge vortex. Yet the exact role of this vortex in the swift's flight performance can only be inferred from observations of their flight. Swifts in flight turn on a dime while catching insects, a spectacular aerobatic display. Anybody observing swifts circling in a yard will notice that the birds hold their wings swept back during fast flight and swiftly change the wing sweep to execute tight turns (see the figure). Aerospace engineers converged on the same solution for their military aircraft, which have to perform optimally both during supersonic and subsonic flight (*8*). Pilots of fighter jets such as the F-14 Tomcat and the Tornado can choose between different wing sweeps for maximal dogfight and cruise performance (see figure 1).

The gliding flight of storks inspired the first airplane designs of Otto Lilienthal in the late 19th century. The benevolent flight characteristics of these slow and stately gliders invested airplane pioneers with the confidence to take to the skies. Swifts are radically different gliders from storks: They are nimble and fast. These attributes require the ability not only to generate large aerodynamic forces from unsteady lift mechanisms, but also to exercise exquisite control over these forces.

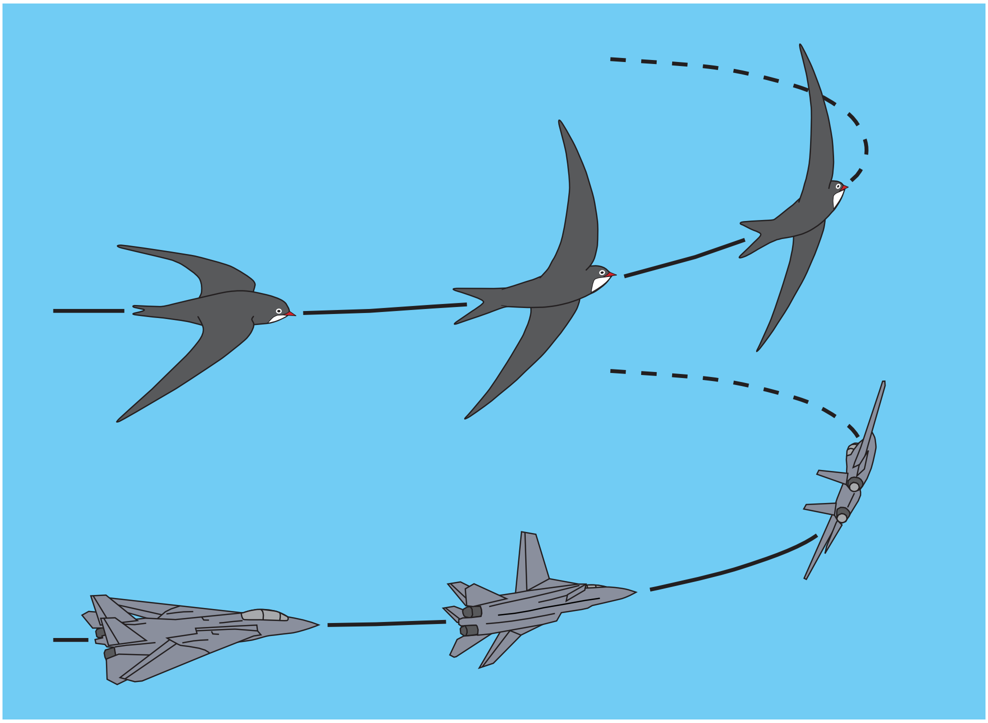

Figure 1 | On the wing. Swifts are aerial hunters, catching flying insects on the wing. To outmaneuver their agile prey, swifts are able to fly fast and to make very tight turns.To maximize flight speed as well as maneuverability, evolution and aeronautic engineering converged on the same solution—variable wing sweep. Swifts (top) and the Tomcat jet fighter (bottom) keep their wings swept back to reach high flight speeds. To execute tight turns, both flyers reduce their wing sweep.

The next challenge for Videler and his team is to elucidate how swifts use their variable wing sweep to gain direct control over leading-edge vortices in order to increase their flight performance. In the future, the swift's flight control might inspire a new generation of engineers to develop morphing microrobotic vehicles that can fly with the agility, efficiency, and short take-off and landing capabilities of insects and birds.

References

1. C. P. Ellington *et al.*, Nature **384**, 626 (1996).
2. M. H. Dickinson *et al.*, Science **284**, 1954 (1999).
3. R. B. Srygley, A. L. R. Thomas, Nature **420**, 660 (2004).
4. F. O. Lehmann, Naturwissenschaften **91**, 101 (2004).
5. J. J.Videler *et al.*, Science **306**, 1960 (2004).
6. J. R. Usherwood, C. P. Ellington, J. Exp. Biol. **205**, 1547 (2002).
7. S. P. Sane, M. H. Dickinson, J. Exp. Biol. **204**, 2607 (2001).
8. E. C. Polhamus, T. A. Toll, NASA TM 83121 (1981).

6.2

How swifts control their glide performance with morphing wings

David Lentink*, Ulrike K. Müller, Eize J. Stamhuis, Roeland. de Kat, Wouter van Gestel, Leo L.M. Veldhuis, Per Henningsson, Anders Hedenström, John J. Videler and Johan L. van Leeuwen

Gliding birds continually change the shape and size of their wings[1-6], presumably to exploit the profound effect of wing morphology on aerodynamic performance[7-9]. That birds should adjust wing sweep to suit glide speed has been predicted qualitatively by analytical glide models[2,10], which extrapolated the wing's performance envelope from aerodynamic theory. Here, we describe the aerodynamic and structural performance of actual swift wings, as measured in a wind tunnel, and on this basis build a semi-empirical glide model. By measuring inside and outside swifts' behavioural envelope, we show that choosing the most suitable sweep can halve sink speed or triple turning rate. Extended wings are superior for slow glides and turns; swept wings are superior for fast glides and turns. This superiority is due to better aerodynamic performance — with the exception of fast turns. Swept wings are less effective at generating lift while turning at high speeds, but can bear the extreme loads. Finally, our glide model predicts that cost-effective gliding occurs at speeds of 8-10 m s^{-1}, whereas agility-related figures of merit peak at 15 to 25 m s^{-1}. Swifts in fact roost at 8-10 m s^{-1} [11], thus our model can explain this choice for a resting behaviour[11,12]. Morphing not only adjusts birds' wing performance to the task at hand, but could also control the flight of future aircraft[7].

Bird wings lend themselves to morphing because they have an articulated skeleton under muscular control, and because the changing overlap between feathers allows continuous changes in wing shape and wing size. Gliding birds sweep their hand wings back at high flight speeds[1-5,13], and spread their wings in turns[4]. To test whether a bird's chosen wing geometry maximises its flight performance, biologists have focused on gliding flight[1-5,13], during which changes in wing geometry are not related to wing beat. Aerodynamic forces have been inferred from the behaviour of freely gliding birds[1,2,5,13]; lift and drag have also been measured directly on single bird wings fixed in one shape[14,15]. These approaches provide no information on morphing outside the bird's behavioural envelope and must be supplemented with aerodynamic theory in order to predict wing aerodynamic performance and bird glide performance[2,16,17].

Rather than estimating how wing geometry affects wing performance, we measured it in a wind tunnel. We chose the common swift (*Apus apus*), which spends most of its life on the wing, foraging, courting, migrating, and even roosting[11,12,18,19], and has a gliding repertoire to suit: soaring, gliding and 'flap-gliding'. Flap-gliding birds alternate flapping and gliding at 1-2 second intervals[11,19], matching the speeds of flapping and gliding episodes[20]. With speed approximately constant, glides can be approximated as 'equilibrium gliding', which encompasses turns and straight glides (turns with infinite radius) (Fig. 1; Methods). During this steady state, flight performance can be deduced from four readily measured parameters: aerodynamic lift, drag, body mass, and flight velocity (Fig. 1b). These determine the swift's glide path, convention-

Nature **446**, 1082 – 1085 (2007).

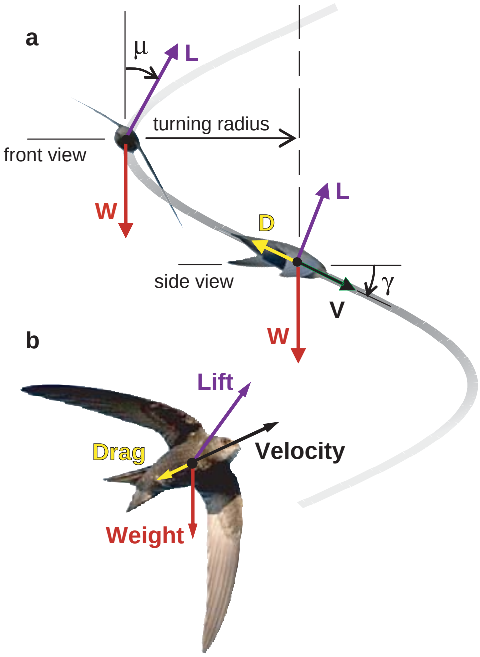

Figure 1 | Equilibrium gliding along a helical path. (a) Turning swifts glide at a constant glide speed, whereas glide velocity **V** changes direction along a helical path (grey ribbon) inclined downward at glide angle γ. To turn without sideslip, swifts incline sideways at bank angle μ. Glide angle is determined by cos μ component of lift/drag; the sin μ component of lift provides the centripetal force required for turning. (b) Main forces acting on a swift gliding at a given velocity.

ally described by glide angle, turning radius, and bank angle[21]. Glide path and velocity determine bird glide performance.

Aerodynamic force is proportional to force coefficient × wing area × square of glide speed[21]. Swifts control force coefficient by altering wing shape, angle of attack, and speed. Increasing sweep angle from 5° (fully extended) to 50° (Fig. 2a) decreases wing area *and* shape (i.e. aspect ratio) by roughly a third (Fig. 2b,c). We quantified how variable sweep affects wing aerodynamics by measuring lift and drag on 15 wing pairs in the Delft Low Turbulence wind tunnel (see Methods).

Our experiments show that variable sweep enlarges the aerodynamic performance envelope of swift wings. At a given glide speed, the polars of lift *vs.* drag coefficient (Fig. 2d) for individual sweep angles build up to a much wider enveloping polar: swept wings contribute low drag coefficients at low angles of attack; extended wings contribute high lift coefficients at high angles of attack. The effects of wing shape are "amplified" by wing area (Fig. 2e plots the same data as polars of speed-specific lift and drag[22], i.e. lift coefficient × wing area *vs.* drag coefficient × wing area). The decrease in wing area with increasing sweep further enlarges the enveloping polar for a given glide speed, further widening the performance gap between fixed-shape and morphing wings.

The enveloping polar changes with glide speed (Fig. 2f). With increasing speed, the polar at first maintains its shape and shifts to lower drag values[10,23] because drag coefficient scales with speed to a power less than two at low angles of attack, when flow separation is minimal[24]. Beyond 15 m s^{-1}, the enveloping polar breaks off at lower and lower speed-specific lift values because less swept wings break under the extreme loads; only the more swept wings are left to build up the enveloping polar.

To demonstrate how morphing wings can affect gliding, we translated the above measures of wings' aerodynamics into swift's flight-dynamics — our six figures of merit (see Supplementary Equations 1). Three flight-cost related indices are: (1) *glide distance* (expressed as max. glide ratio[21]), (2) *glide duration*[21], (3) *turn angle* for a given height loss. By maximising distance or time spent gliding, birds reduce energy expenditure while foraging and roosting. Three indices are agility-related: pursuits and escapes require (4) fast turns (high *angular velocity*[21]) with (5) a high *path curvature*[21]; while (6) high *horizontal speed* (horizontal component of glide velocity) helps to avoid drift in strong winds. Our discussion of performance maxima ignores combinations of sweep and glide speed that cause diving (glide angles > 45°, Fig 1.).

Extended wings provide the best glide performance. Five of the six indices (Fig. 3a,b,d-f) reach an absolute maximum with extended wings — characteristic of gliders in general. The cost-related maxima occur between 8 and 15 m s^{-1}. At 10 m s^{-1}, within this optimal speed range, choosing extended over swept wings triples all three turning indices (Supplementary Figure 2). Nevertheless, swifts sometimes choose higher glide speeds[11,18].

During straight glides at higher-than-optimal speeds, high sweep improves aerodynamic wing performance. Consider Figure 3a: at lower-than-optimal speeds (left of highest peak), extended wings deliver superior glide ratios. As speed increases beyond the optimum, the lines of constant sweep cross, and glide ratio is higher for swept wings. At 20 m s^{-1}, for example, a sweep angle of 50° yields a 70% improvement over extended wings, whereas at speeds below 10 m s^{-1}, extended wings improve glide ratio by as much as 50%. The second cost-related index, glide duration, behaves similarly (Fig. 3b). Unsurprisingly, 'horizontal speed' is the only index that peaks at high glide speeds (Fig. 3c). Although not sensitive to sweep angle at low glide speeds, horizontal speed increases with increasing sweep above 20 m s^{-1}. These results confirm predictions that swept wings improve glide performance at high speed[2,6].

Swept wings can bear higher loads during fast turns. Whereas, during straight gliding at constant speed, the wings bear a load necessarily equal to the bird's mass × 1g, centripetal acceleration increases the load during equilibrium turns. If the bird were to maximise aerodynamic wing performance, it should choose low sweep and low speed: the superior lift force of extended wings is desirable at any speed, in theory[16]. Consistent with this prediction, our measure-

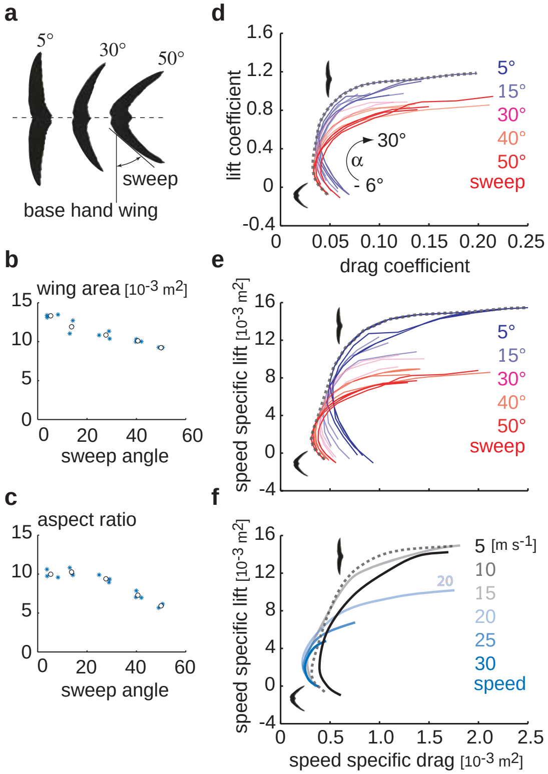

Figure 2 | Morphing swift wings can generate higher lift and lower drag than wings with a fixed geometry. (a) Adjusting sweep angle alters (b) wing area and (c) aspect ratio. Individual wings *, average per sweep o. (d) The enveloping polar (grey dashed line) spans a wider range of lift and drag coefficients than the polar for any one sweep (fine coloured lines) (angles of attack α -6° to +30°); glide speed 10 m s^{-1}. (e) The combined effect of wing shape *and* size (speed-specific lift and drag[22]) further enlarges the enveloping polar. (f) Increasing glide speed shifts enveloping polars left and decreases maximum speed-specific lift.

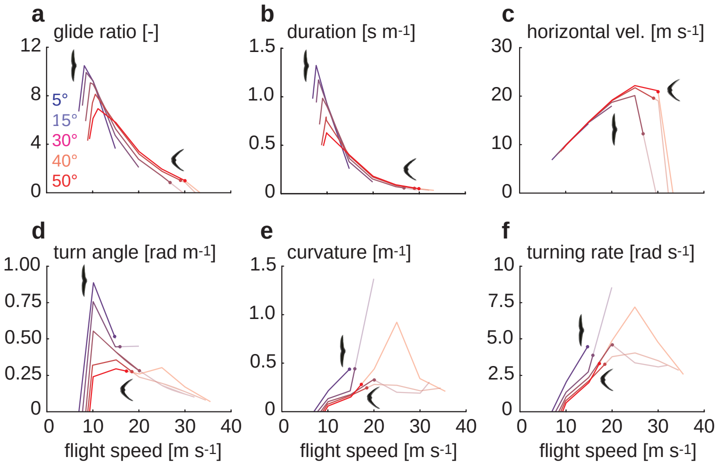

Figure 3 | Morphing improves glide performance of swifts. Performance indices (a)-(f) for a range of sweep angles (coloured lines) and flight speeds (X axis). Absolute performance maxima occur at low speeds and sweeps in all indices but (c). In two of three straight-flight indices (top row), low sweep delivers superior performance at low speeds while high sweep is superior at high speeds. During turning (bottom row), no cross-over from low to high sweep occurs during gliding. Solid lines: glide angle < 45°; dot: glide angle = 45°, no dot: wing fails before 45° is reached; faded lines: glide angle >45°.

ment-based turning indices show no clear cross-overs from low to high sweeps at glide angles below 45° (Fig. 3d-f). Dive performance (glide angle > 45°) is severely limited during high-speed turns due to high loads. We measured loads of up to six times the bird's weight (Fig. 4 bottom), and observed two types of structural failure: one extended-wing specimen bent to the point of breaking at $15\ \mathrm{m\,s^{-1}}$; another started vibrating violently at 15 and $20\ \mathrm{m\,s^{-1}}$, which ultimately led to failure at the bone. Swept wings don't "flutter", and they avoid static failure by bending and twisting under lift-loads (Fig. 4 top), which reduces effective angle of attack at the handwing and thereby caps aerodynamic load. Such phenomena are not captured by theoretical or experimental studies using rigid wing models[25].

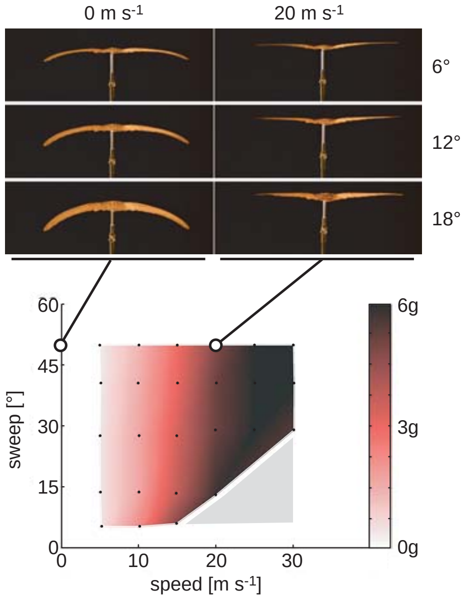

Figure 4 | Morphing maintains wing structural integrity at high glide speeds. Bottom: during fast glides, swift wings experience considerable loads (expressed as multiples of g; grey: no measurements). Top: swept wings bend and twist under load to a lower angle of attack (rear view; sweep 50°; α 6°, 12°, 18°).

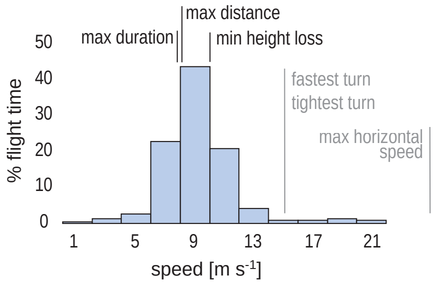

Figure 5 | Swifts roost at glide speeds that minimise energy expenditure. Five of six predicted performance maxima occur within the most commonly observed range of flight speeds during roosting[11]: two of three agility-related maxima (grey), and all cost-related maxima (black), which cluster around swifts' preferred roosting speed of 9 m s^{-1}.

High sweep maximises high-speed glide performance, but not by creating strong leading edge vortices (LEVs). LEVs have been observed over model swift wings, and have been proposed to boost lift[25]. Our flow visualisations on real wings confirm the presence of LEVs at high sweep angles (≥ 30°) (Supplementary Table 1). However, our force measurements at speeds of 5 to 30 m s^{-1} show that swept wings *always* generated less lift than extended wings. Extra lift from LEVs does not compensate for lift lost to the concomitant drop in wing area and aspect ratio (Fig. 2d,e), and to load-induced wing deformations at high speeds (Fig. 4 top). Rather than by increasing lift, sweep improves gliding by decreasing drag.

Our glide model predicts performance-maximising glide speeds that agree with observations of swift behavioural choices. Glide speeds are readily observable in the field and therefore serve well to validate our semi-empirical glide model. Our model predicts different optimal gliding speeds for maximising agility (15 to 25 m s^{-1}) *vs.* cost-effectiveness (8-10 m s^{-1}). The only glide behaviour on which free-flight data have been published is roosting[11,12,18], for which we expect that flight-cost considerations outweigh agility[11,12]. Radar measurements[11] show that roosting swifts indeed flap-glide at speeds centred around 8-10 m s^{-1} (Fig. 5). This agreement of model predictions and field observations validates the analytical step from wing aerodynamic to bird glide performance.

The modification of glide performance achieved by morphing is comparable to the differences between bird species with widely different wing shapes and flight behaviours[15]. Swifts can adjust their wings' maximum lift coefficients between 0.8 and 1.1, which is similar to the full range from thrush (0.8) to nighthawk (1.15) found by Withers[15] for extended wings. Therefore, extended wing geometry alone might not be enough to justly evaluate bird gliding performance[8,15]. Birds with an aerial life style, such as swifts, face a wide range of tasks with sometimes conflicting performance goals. To match wing shape to the task at hand, morphing provides birds with a suite of wing geometries to choose from.

Supplementary Information and a Full Protocol accompany the paper.

Supplementary Figure 1: body drag measurements. Supplementary Figure 2: statistics for performance indices. Supplementary Table 1: results of tuft flow visualisation. Supplementary Equations 1: derivation of equations of motion and construction of Figure 3.

Acknowledgements

Swifts were supplied by Vogelopvang Woudenberg, Fugelpits Moddergat, Fugelhelling Ureterp, Vogelopvang De Strandloper Bergen, Vogelasiel De Wulp Den Haag, Vogelasiel Haarlem, Vogelasiel Naarden,Vogelopvang Someren. Jean-François Cornuet (front-view, Fig. 1a) and Ran

Schols (side-view Fig. 1a; Fig. 1b) kindly provided swift photographs. Niek Verhagen, Johan Bäckman and Jan Becking helped with background research. Eric Karruppannan, Dick Bongers, Leo Molenwijk, Loek Boermans, Stefan Bernardy, and Henk Schipper helped with the experimental set-up. Florian Muijres and Ronald Petit helped with the experiments. Thomas Weber and Stephen Deban critically read the manuscript. Otto Berg carefully improved many versions of the manuscript. U. K. M. is funded by NWO, and A. H. by Carl Trygger's Foundation.

References

1. Rosén, M. & Hedenström, A. Gliding flight in a jackdaw. *J. Exp. Biol.* **204**,1153-1166 (2001).
2. Tucker, V.A. Gliding birds: the effect of variable wing span. *J. Exp. Biol.* **133**, 33-58 (1987).
3. Pennycuick, C.J. Gliding flight of the fulmar petrel. *J. Exp. Biol.* **37**, 330-338 (1960).
4. Newman, B.G. Soaring and gliding flight of the black vulture. *J. Exp. Biol.* **35**, 280-285 (1958).
5. Pennycuick, C.J. Wind-tunnel study of gliding flight in the pigeon *Columba livia*. *J. Exp. Biol.* **49**, 509-26 (1968).
6. Müller, U.K. & Lentink, D. Turning on a dime. *Science* **306**, 899-1900 (2004).
7. Weiss P. Wings of change: shape-shifting aircraft ply future skyways. *Science News* **164** (23), 359 (2003).
8. Rayner, J.M.V. Form and Function in avian flight. In *Current Ornithology* Vol. 5, ed. R.F. Johnston. Plenum Press New York (1988).
9. Hoerner S.F. & Borst, H.V. *Fluid-dynamic lift*. Published by L.A. Hoerner, Bakersfield (1985).
10. Azuma A. *The Biokinetics of Flying and Swimming*. AIAA Education Series, Reston, 2nd edition (2006).
11. Bäckman, J. & Alerstam, T. Confronting the winds: orientation and flight behaviour of roosting swifts, *Apus apus*. *Proc. R. Soc. B* **268**, 1081-1087 (2001).
12. Bruderer, B. & Weitnauer, E. Radarbeobachtungen über Zug und Nachtflüge des Mauerseglers (*Apus apus*). *Rev. Suisse Zool.* **79**, 1190–1200 (1972).
13. Parrott, G.C. Areodynamics of gliding flight of a black vulture *Coragyps atratus*. *J. Exp. Biol.* **53**, 363-374 (1970).
14. Nachtigall, W. Der Taubenflügel in Gleitflugstellung: geometrische Kenngrössen der Flügelprofile und Luftkrafterzeugung. *J. Orn.* **120**, 30-40 (1979).
15. Withers, P.C. An aerodynamic analysis of bird wings as fixed aerofoils. *J. Exp. Biol.* **90**, 143-162 (1981).
16. Thomas, A.L.R.. The flight of birds that have wings and tails: variable geometry expands the envelope of flight performance. *J. theor. Biol.* **183**, 237-245 (1996).
17. Tucker, V.A. & Parrott, G.C. Aerodynamics of gliding flight in a falcon and other birds. *J. Exp. Biol.* **52**, 345-367 (1970).
18. Bäckman, J. & Alerstam, T. Harmonic oscillatory orientation relative to the wind in nocturnal roosting flights of the swift *Apus apus*. *J. Exp. Biol.* **205**, 905-910 (2002).
19. Lack, D. *Swifts in a tower*. Methuen London (1956).
20. Pennycuick, C.J. Flight of auks (Alcidae) and other Northern sea birds compared with Southern Procellariiformes: ornithodolite observations. *J. Exp. Biol.* **128**, 335-347 (1987).
21. Ruijgrok, G.J.J. *Elements of airplane performance*. Delft University Press Delft (1994).
22. Vogel, S. *Life in moving fluids*. Princeton University Press Princeton, 2nd edition (1994).
23. Schmitz, F.W. Aerodynamik des Flugmodells. Verlag CJE Volckmann Nachf. Berlin (1942).

24. Schlichting, H. *Boundary layer theory*. McGraw-Hill Book Company New York, 7th edition (1979).
25. Videler, J.J., Stamhuis, E.J. & Povel, G.D.E. Leading-edge vortex lifts swifts. *Science* **306**, 1960-1962 (2004).
26. Hedenström, A. & Rosén, M. Predator versus prey: on aerial hunting and escape strategies in birds. *Behav. Ecol.* **12**, 150-156 (2001).
27. Veldhuis, L.L.M. *Configuration and propulsion aerodynamics research in the Low Speed Aerodynamics laboratory* (in Dutch). Internal Report LSW 93-1, Faculty of Aerospace Engineering, Delft University of Technology Delft (1993).
28. Bird, J.D. Tuft-grid surveys at low speeds for delta wings. *NASA Technical Note* D-5045 (1969).
29. Pennycuick, C.J., Alerstam, T. & Hedenström, A. A new low-turbulence windtunnel for bird flight experiments at Lund University, Sweden. *J. Exp. Biol.* **200**, 1441-1449 (1997).
30. Glutz von Blozheim, U.N. & Bauer, K.M. *Handbuch der Vögel Mitteleuropas*. Akademischer Verlag Wiesbaden (1980).

Methods / Full protocol

To determine how morphing wings affect bird flight, we built a semi-empirical model that translates wing performance into swift glide performance. Glide performance is determined by the lift- and drag contributions of wings, body, and tail, and by the bird's weight.

Animals. In spring 2005, we received from eight Dutch bird sanctuaries 35 adult swifts that had died after having been brought in. We selected 15 swifts based on their wings and general state, neglecting a 2% sex-specific variation in wing length[1].

Wing preparation. To study the influence of morphing on wing aerodynamic and structural performance, we separated 15 wing pairs from the body at the shoulder joint and manually extended them onto templates for 5 fixed sweep angles (5°, 15°, 30°, 40°, 50°; between wrist and proximal half of leading edge) (Fig. 2a). Manually extending wings reliably reproduces wing shape during gliding[2]. Wing pairs were frozen, freeze-dried, then glued together to form a continuous wing surface. Freeze-drying changes the mechanical properties of biological tissues, yet yields better specimens than freshly dead material[4].

Wing mounting. The wings were mounted onto the sting of the balance system and placed in a wind tunnel. By measuring aerodynamic forces with the body removed, we were able to reduce the dimensionality of the parameter space by excluding body posture, body angle of incidence, tail spread, tail angle of incidence, amongst others. This enabled us to gather a uniquely large data set on the aerodynamics of bird wings, which is focused on accurately determining the influence on wing morphing on the wings aerodynamic performance. With this approach we likely overestimate induced drag[5] because the wings are closer together by 34 mm (body diameter). We also ignore any effect of wing dihedral angle and we ignore the effect of the body on the wings' lift and drag, which has been shown to be small[6].

Wind tunnel tests. We used the Delft Low Turbulence Wind Tunnel[7] with an octogonal test section of 1.80 × 1.25 m (turbulence levels ≤ 0.025% until 40 m s^{-1}). We designed a balance system with a resolution of 40,000 steps to measure lift and drag at air speeds between 5 and 30 m s^{-1} (Reynolds number 12,000-77,000) with an accuracy of at least 3% (Ohaus SP402). This speed range encompasses loads up to six times the swift's body weight. We calibrated the balance with a 5 × 5 matrix of weights over the full lift and drag range to account for the system's small non-linearity. Each force value was sampled at 5 Hz for 10 s at each angle of attack α (0° → +30° → -6° → 0°; step size 1.5°, precision < 0.5°). Data from up- and down-leg of the α cycle were pooled because hysteresis was negligible below stall. Measurements were corrected for aerodynamic forces of the sting, and for changes in the wings' centre of mass with α. To confirm that a leading edge vortex is present not only on model, but also on our real swift wings, we used tuft visualisation, a simple and established method in aeronautic engineering[8].

Lift-drag polar of swifts. We built the total lift-drag polar of the swift from the wing lift and drag and body drag, measured in the Lund windtunnel[9] (see Supplementary Figure 1). Wing polars were built up from force measurements across a range of glide speeds (5-30 m s^{-1}), sweeps (5°-50°) and angles of attack α (-6° to 30°), excluding high αs at which the wing stalls — stall was assumed to have occurred when mean lift flattened off and instantaneous lift suddenly became variable. We calculated lift and drag coefficients to quantify the effect of changes in wing shape. To account for the effects of wing area, we further calculated so-called speed-specific lift and drag[10], which are strictly speaking dynamic-pressure-specific lift and drag and better known in aeronautic engineering as lift- and drag area. We measured an average body drag coefficient[5] of 0.26 for a frontal area of 913 mm^2 (Supplementary Figure 1).

Calculation of glide path. To evaluate the correct part of the total polar that the bird can use, we used a body weight of 43 g[1] to calculate glide paths. By solving for the unknown glide path parameters glide angle γ, bank angle μ, and turn radius R (Fig. 1), we obtained equations of motion that contain only measurable quantities - body mass m and weight W, flight speed V, lift L and drag D (supplementary Equations 1):

$$\begin{pmatrix} \gamma \\ \mu \\ R \end{pmatrix} = \begin{pmatrix} \arcsin\left(\dfrac{D}{W}\right) \\ \arccos\left(\dfrac{\sqrt{W^2 - D^2}}{L}\right) \\ \dfrac{mV^2}{W^2}\left(\dfrac{W^2 - D^2}{\sqrt{L^2 + D^2 - W^2}}\right) \end{pmatrix} \tag{1}$$

We then determined all possible helicoidal glide paths[5] (assuming a constant glide speed and no side slip). Note that straight gliding flight is a special case of turning with infinite turning radius.

Calculation of performance maxima. We assessed how morphing wings affect swift glide performance using three straight-glide and three turning-related figures of merit (Fig. 3): (1) max. glide distance[5]: $\max(1/\tan(\gamma))$ (= maximal glide ratio), (2) max. glide duration[5]: $\max(1/(V \sin\gamma))$, (3) max. turning angle for a given height loss: $\max(1/(R \tan\gamma))$, (4) max. angular velocity in a turn[5]: $\max(V\cos\gamma / R)$, (5) max. curvature of the turn path[5]: $\max(1/R)$, (6) max. horizontal component of the flight speed): $\max(V\cos\gamma)$ (see also Supplementary Equations 1). We limited the performance analysis by two criteria. First, our calculations were only valid for non-zero turning radii, when the swift does not purely roll around its body axis. Second, values were calculated, but ignored in the search for performance maxima, when the swift dives (glide angle $\gamma > 45°$). We linearly interpolated the force coefficients of the two adjacent polars to calculate the 45° dive-angle cut-off speed, straight flight performance maxima, and minimum and maximum flight speeds. Finally, we averaged performance indices per sweep angle to construct Figure 3 (Supplementary Figure 2).

Sensitivity analysis. We tested the sensitivity of the optimal sweep configuration (for a given performance maximum) to weight, drag, and lift. Changing body weight (±23%), body drag coefficient (–100%,+200%), or tail lift coefficient (± 20% tail contribution of wing lift) did not shift the performance maximum to a different sweep increment. Our experiments resolves sweep in discrete increments of 10-15°.

Accuracy of roost speed prediction. Air density at the average roosting height[11,12] (1700 m) is unknown. We therefore used air density at sea level (1.201 ± 0.005 kg m^{-3}, measured in the Delft wind tunnel), leading to a maximum underestimate of 9% in the predicted optimal speed. However, roosting flight speed does not correlate strongly with altitude (Anders Hedenström, unpublished observation).

References

1. Glutz von Blozheim, U.N. & Bauer, K.M. *Handbuch der Vögel Mitteleuropas*. Akademischer Verlag Wiesbaden (1980).
2. Hedenström, A. & Rosén, M. Predator versus prey: on aerial hunting and escape strategies in birds. *Behav. Ecol.* **12**, 150-156 (2001).
4. Nachtigall W. *Warum die Vögel fliegen*. Rasch und Röhring Hamburg (1985).
5. Ruijgrok, G.J.J. *Elements of airplane performance*. Delft University Press Delft (1994).
6. Hoerner S.F. *Fluid-dynamic drag*. Published by L.A. Hoerner, Bakersfield (1965).
7. Veldhuis, L.L.M. *Configuration and propulsion aerodynamics research in the Low Speed Aerodynamics laboratory* (in Dutch). Review of project 90-LR-5-S, 1993, Internal Report LSW 93-1, Faculty of Aerospace Engineering, Delft University of Technology Delft (1993).
8. Bird, J.D. Tuft-grid surveys at low speeds for delta wings. *NASA Technical Note* D-5045 (1969).
9. Pennycuick, C.J., Alerstam, T. & Hedenström, A. A new low-turbulence windtunnel for bird flight experiments at Lund University, Sweden. *J. Exp. Biol.* **200**, 1441-1449 (1997).
10. Vogel, S. *Life in moving fluids*. Princeton University Press Princeton, 2nd edition (1994).
11. Bäckman, J. & Alerstam, T. Confronting the winds: orientation and flight behaviour of roosting swifts, *Apus apus*. *Proc. R. Soc. B* **268**, 1081-1087 (2001).
12. Bäckman, J. & Alerstam, T. Harmonic oscillatory orientation relative to the wind in nocturnal roosting flights of the swift *Apus apus*. *J. Exp. Biol.* **205**, 905-910 (2002).

Supplementary table 1. *Leading edge vortex visualisation.*

sweep [°]	speed [m s^{-1}]	angle of attack
15	10	no LEV
15	20	no LEV
30	10	≥14°
30	20	no LEV
40	10	≥14°
40	20	≥13°
50	10	≥11°
50	20	≥14°

We performed tuft-based flow visualisation (see Methods) to determine whether a leading edge vortex (LEV) is present on swift wings. We found LEVs at sweep angles of 30° and greater at sufficiently high angles of attack of 11, 13 or 14° or greater, depending on sweep angle and air speed. Note that the geometric angle of attack at which lift is zero[1] is defined as 'zero aerodynamic angle of attack'.

Reference

1. Ruijgrok, G.J.J. *Elements of airplane performance*. Delft University Press Delft (1994).

Supplementary Figure 1.

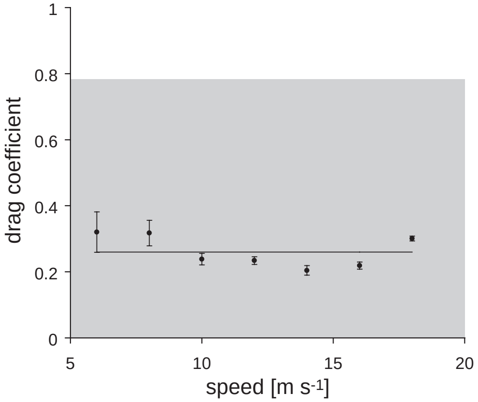

Body drag measurements in the Lund wind tunnel.

The body drag measurements were performed in the wind tunnel at Lund University. We averaged body drag (•) over the speed range of 6-18 m s^{-1} and used the mean (0.26) in our swift glide model (bars indicate standard error of the mean and the line the mean drag coefficient). The gray area shows the body-drag range of our sensitivity analysis (–100%,+200% mean value).

Supplementary Figure 2.

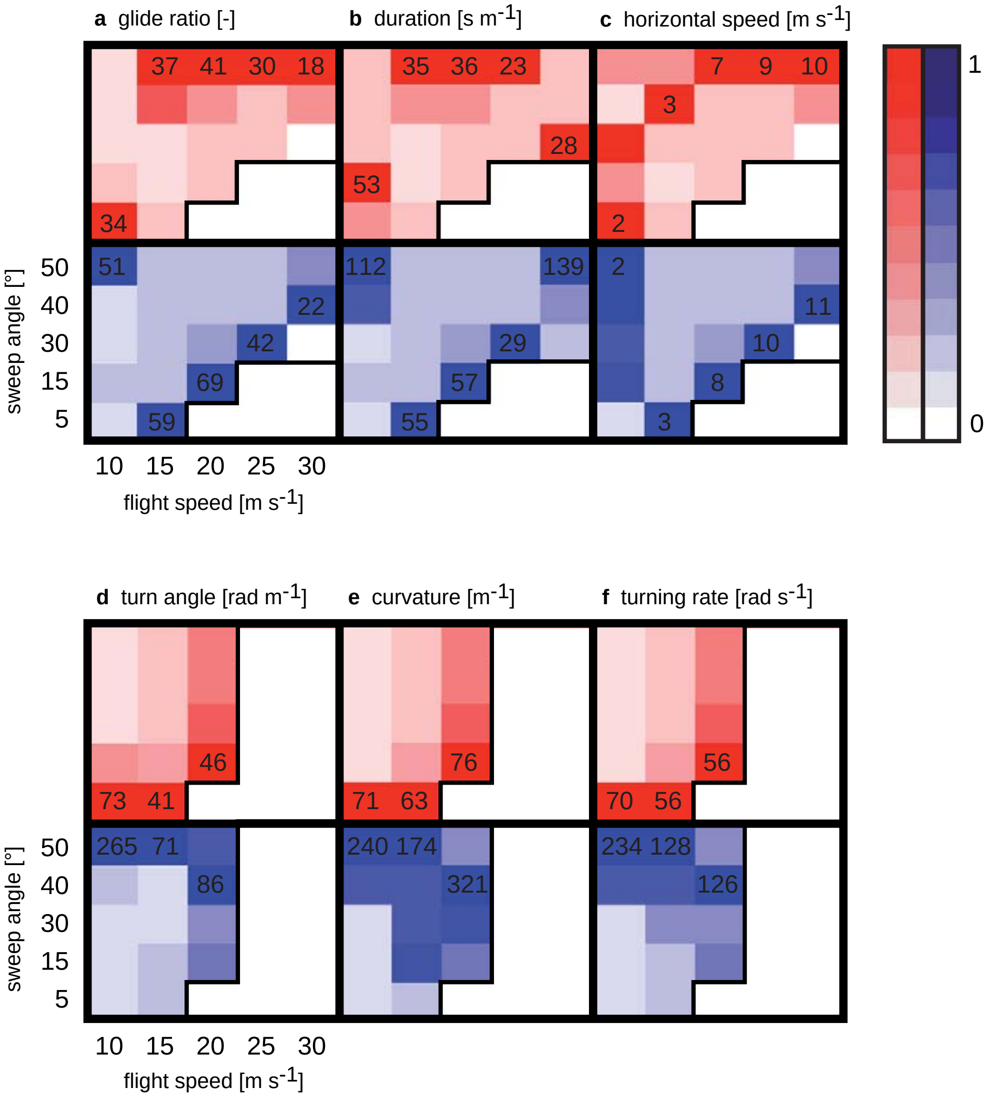

Statistical independence of glide performance differences due to morphing

To test statistical independence between the differences in performance due to different sweeps, we performed a Rank analysis. We calculated average performance for each sweep angle and glide speed (n = 3, or n = 2 if a wing broke), as shown in Figure 3. Here (a-f) we present the corresponding Rank test to check for all six performance indices that the performance values for different sweep angles at a given glide speed are mutually independent. Note that we performed a Rank test for the speeds for which we obtained polars within the flight range of swifts (10, 15, 20, 25 and 30 m s^{-1}). Red represents the probability (p) that maximum performance at optimal sweep is statistically different from performances at sub-optimal sweep angles. Blue represents the probability (p) that minimum performance at the least-suitable sweep is statistically different from performances at other sweep angles. (Note for n = 3, $p_{min} = 1/10$ for independent data and for n = 2, $p_{min} = 1/3$). For the maxima and minima the probability is 1.0 because the value is compared with itself. The maximum percentage drop in performance (min-max) / max × 100% is indicated by the number in the red squares, maximum performance increase (max-min)/min × 100% is indicated in the blue squares. Note that glide distance and duration peak below 10 m s^{-1} and that duration already shows a cross-over at 10 m s^{-1} (Fig. 3b). White boxed areas represent glide angles > 45° and sweep-speed combinations for which we could not obtain measurements due to wing failure (Fig. 4).

Supplementary Equations 1.

Equations of motion of a swift gliding along a helicoidal path.

Based on Newton's second law of motion, and assuming a constant glide speed and no slip turn, the helicoidal glide path of a swift (Fig. 1) is described by[1]:

$$\begin{pmatrix} -D + W\sin\gamma \\ L\sin\mu \\ -L\cos\mu + W\cos\gamma \end{pmatrix} = \begin{pmatrix} 0 \\ mV^2/R\cos^2(\gamma) \\ 0 \end{pmatrix}. \tag{1}$$

A turning swift experiences gravitational attraction, represented by its weight *W*, and centripetal acceleration, represented by the non-zero right-hand term in equation 1. By solving equation 1 for the unknown glide path parameters (glide angle γ, bank angle μ, and turn radius *R*) we obtain equations of motion that contain only measurable quantities – body mass *m* and weight *W*, flight speed *V*, lift *L* and drag *D*:

$$\begin{pmatrix} \gamma \\ \mu \\ R \end{pmatrix} = \begin{pmatrix} \arcsin\left(\frac{D}{W}\right) \\ \arccos\left(\frac{\sqrt{W^2 - D^2}}{L}\right) \\ \frac{mV^2}{W^2}\left(\frac{W^2 - D^2}{\sqrt{L^2 + D^2 - W^2}}\right) \end{pmatrix}. \tag{2}$$

Plotting figures of merit.

We defined six figures of merit (see methods and full protocol) that measure agility *vs*. energy efficiency during helicoidal gliding. Four of these indices are used in aircraft performance and design studies[1-6]: max. glide distance[1], max. glide duration[1], max. angular velocity[1] and max. curvature[1]. Max. duration and max. curvature are the inverse of the more commonly used indices[1-6] min. sink speed and min. turning radius. The latter is inconveniently infinite at minimum glide speed. Inversion facilitates graphic representation of the turning indices, identification of cross-over regions for the straight glides, and comparison of the indices — all six reach a maximum, and none a minimum, at maximum performance.

References

1. Ruijgrok, G.J.J. *Elements of airplane performance*. Delft University Press Delft (1994).
2. Stengel, R. *Flight Dynamics*. Princeton University Press Princeton(2004).
3. Vinh, N. *Flight Mechanics of High-Performance Aircraft*. Cambridge University Press Cambridge (1993).
4. Howe, D. *Aircraft Conceptual Design Synthesis*. John Wiley & Sons London (2000).
5. Thomas, F. *Fundamentals of Sailplane Design*. College Park Press College Park (1999).
6. Torenbeek, E. *Synthesis of Subsonic Airplane Design*. Kluwer Academic Press Dordrecht (1996).

7 Synthesis

7.1

BIOFLUIDDYNAMICS AS AN INSPIRATION FOR DESIGN

David Lentink

The locomotion of many macroscopic organisms that swim or fly depends on fins or wings. The swimming and flying animals and plant seeds that I study here create vortices with their fins and wings that are shed in a wake. These vortices have their own dynamics, which the organisms have to cope with to move effectively through their surrounding fluid. The aim of this thesis is, therefore, to explore how the swimming and flight apparatus of organisms is constrained by vortex dynamics. I focus on how principal morphological and kinematic parameters of fins and wings co-determine leading edge vortex stability and vortex wake periodicity, which mediate fluid force augmentation and forecast horizon respectively. The principal findings of this exploration will serve as an inspiration for the design of new micro air vehicles. These studies were carried out using a number of increasingly realistic swimming and flight models that represent swimming fish and flying insects, autorotating seeds and swifts: From a two-dimensional flapping foil in a soap film tunnel to freeze-dried swift wings in a wind tunnel.

In the following sections I will first synthesize our findings into five main biofluiddynamic conclusions: (1) Symmetric and periodic flapping mediates asymmetric and chaotic vortex wakes. (2) Rotational accelerations stabilize leading edge vortices on revolving wings. (3) Leading edge vortices augment lift in both animal and plant flight. (4) Wing morphing drastically improves glide performance. (5) Flapping wings are less efficient than spinning and translating wings.

Subsequently I will synthesize conclusions 2 and 4 in the bio-inspired design of two new micro air vehicles: (1) RoboSwift, which can morph its wings like a swift, and (2) DelFly, which can flap its wing like an insect (Fig. 1).

Finally, I will present an outlook in which I describe the design of a new experiment based on conclusion 2 and 5: Is wing slenderness optimized for power efficiency in hummingbirds? The results of this experiment can provide new insight in the functional morphology of hummingbirds, and will serve as inspiration for designing more efficient hovering micro air vehicles.

Biofluiddynamic conclusions

Conclusion 1 | *Symmetric and periodic flapping mediates asymmetric and chaotic vortex wakes.*
The wings and fins of swimming and flying animals are commonly modeled as two-dimensional flapping foils. In several computer simulations the vortex wakes of these flapping foils have been found to become asymmetric and even chaotic (Lewin and Haj-Hariri, 2003; Lentink and

Based on a submitted manuscript

Gerritsma, 2003; Blondeaux *et al.*, 2005; Alben and Chelley, 2005; Iima, 2007). The vortex wake interacts with the foil and can therefore influence the force it generates. Vortex wake asymmetries induce asymmetric angles of attack of the foil, which can result in a non-zero time-averaged lift force on the foil. Similarly, chaotic vortex wakes can induce chaotic forces, which have a limited forecast horizon (Lorenz, 1963). It is, however, unclear to which extent chaotic vortex wakes exist, and how asymmetric and chaotic vortex wakes could be relevant for animals.

Our extensive experiments with a two-dimensional flapping foil in a soap film tunnel confirm earlier findings of asymmetric vortex wakes (e.g. Lewin and Haj-Hariri, 2003). More significantly, we show for the first time experimentally that chaotic vortex wakes exist and that they occur in abundance. These chaotic wakes occur predominantly under close-to-hover conditions, whereas the vortex wakes are periodic under conditions at which animals prefer to cruise and obtain high efficiency (0.2 < Strouhal number < 0.4) (Triantafyllou *et al.*, 1993, Taylor *et al.*, 2003). Our two-dimensional model predicts therefore that swimming and flying animals cope with chaotic vortex-wake interactions when they transition between cruising and hovering. Swimming and flying animals could potentially either avoid or exploit asymmetric and chaotic vortex-wake interactions by tuning their morphology and kinematics. Based on the present findings we formulated two new hypotheses: (1) Fish that primarily depend on their caudal fin for propulsion might try to avoid asymmetric vortex wake interactions that could induce net turning moments that complicate swimming straight-on. (2) Butterflies and moths might exploit chaotic vortex-wake interactions that result in chaotic forces that can make their flight path erratic, making them hard to catch. [*Chapter 3*]

A three-dimensional analysis using more realistic animal models is needed to determine to what degree fish fins and insect wings can actually generate asymmetric and chaotic vortex wakes and fluid forces. One important difference between two- and three-dimensional flapping foils that could affect vortex wake periodicity is leading edge vortex stability. The stability of the leading edge vortex determines when it is shed in the wake during the stroke cycle, which influences vortex wake interactions. Our experiments confirm that the leading edge vortex is unstable on two-dimensional flapping foils (Dickinson and Götz, 1993; Dickinson, 1994), whereas it is known to be stably attached to three-dimensional flapping foils such as insect wings (Maxworthy, 1979; Ellington *et al.*, 1996; Dickinson *et al.*, 1999).

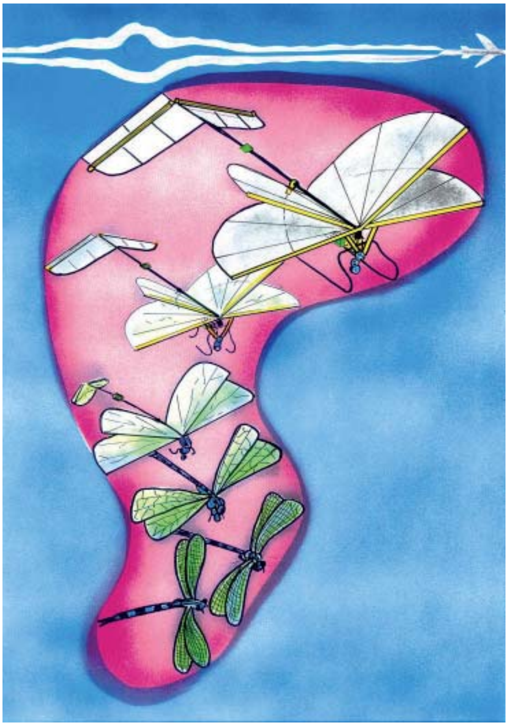

Fig. 1 | Artist impression of the bio-inspired design of DelFly, a micro air vehicle with flapping wings.

Conclusion 2 | *Rotational accelerations stabilize leading edge vortices on revolving wings.* Hovering insects can generate exceptionally high lift with a leading edge vortex that rests stably on their wings (Maxworthy, 1979; Ellington *et al.*, 1996; Dickinson *et al.*, 1999). Why and under which conditions this vortex is stable is still unclear. One hypothesis is that the mechanism that stabilizes the leading edge vortex on flapping insect wings is analogous to the mechanism that stabilizes similar vortices on the swept wings of aircraft (Ellington *et al.*, 1996). Another hypothesis is that the tip vortex generated by stubby insect wings stabilizes the leading edge vortex (Birch and Dickinson, 2001).

Our experiments with a robotic fruit fly wing show that the leading edge vortex is unstable on translating fly wings, irrespective of wing sweep and the tip vortex it generates. This result contradicts both existing hypotheses. We further observed, like others (Dickinson *et al.*, 1999; Usherwood and Ellington, 2002), that the leading edge vortex is stable on both flapping *and* spinning fly wings. Our subsequent theoretical analysis of leading edge vortex stability shows that not the reciprocating motion, but the revolving motion of flapping insect wings, their propeller-like swing, stabilizes the leading edge vortex. The analysis further shows that this stabilization should continue to exist at larger scales. Our experiments confirm this for fruit fly, house fly and hummingbird scale. For these scales we compared leading edge vortex stability on a reciprocating translating fly wing, which generated an unstable vortex, versus a reciprocating revolving fly wing, which generated a stable vortex.

Our theory and experiments show that the stability of the leading edge vortex is mediated by the centripetal and Coriolis acceleration in the flow close to the wing's surface. The vortex is stabilized when the convective flow acceleration, induced by the velocity of the wing, has the same order of magnitude as the centripetal and Coriolis accelerations, induced by the angular velocity of the wing. For hovering flight, the relative magnitude of these accelerations is represented by the Rossby number at the wingtip Ro, which must be of order one, 'close to one', for leading edge vortex stability. The Rossby number was first derived for studying geophysical flows under the influence of the earth's rotation by Rossby (1936).

For hovering flight, the Rossby number is calculated as the radial distance between the tip of the wing and its center of rotation R, divided by the average width of the wing, the chord length c; $Ro = R/c$. This radial distance R is finite and equal to the radius of animal wings that revolve around the joint that connects them to the body. For such fins and wings the Rossby number is equivalent to single wing aspect ratio, R/c, a measure of wing slenderness. Wing slenderness should therefore be low, of order one, to sustain a stable leading edge vortex over the whole wing and maximize lift augmentation. Low wing aspect ratio not only increases lift augmentation, through a prominent stable leading edge vortex, it also increases the drag associated with the prominent wingtip vortex. The drag associated with the wingtip vortex is disproportionally high for very stubby wings with aspect ratios below one (e.g. Winter, 1936), which diminishes efficiency. In summary, we find that the single condition for LEV stability resulting in maximal force augmentation at reasonable efficiency appears to be a Rossby number between 1 and 5. The Rossby number of the stubby fruit fly wing in our experiments is comfortably in the middle of this range at 2.9.

To determine if other animals can potentially also exploit the lift augmentation of stable leading edge vortices we calculated their Rossby number. We found data on more than 300 animal species. For these species we found an average Rossby number of 3.1 for insects, 3.7 for hummingbirds, 3.2 for other birds, 3.3 for bats and 2.5 for the pectoral fins of fish (which also revolve around their base), which all fall close to the 2.9 of fruit flies. This suggests that many animals could potentially generate a stable leading edge vortex during near hover conditions (such as vertical take-off and landing). This prediction is confirmed by findings of stable leading edge vortices in insects (Maxworthy, 1979; Ellington *et al.*, 1996), birds (Hubel, 2006), bats (Muijres *et al.*, 2008) and sun fish (Lauder and Madden in: Bandyopadhyay *et al.*, 2008). [*Chapter 2 & 4*]

Interestingly the average Rossby number of autorotating 'helicopter' seeds is 3.7, which suggests that even plant seeds might generate a stable leading edge vortex during wind dispersal.

Conclusion 3 | *Leading edge vortices augment lift in both animal and plant flight.*

During wind dispersal, autorotating seeds generate much higher lift than predicted by theory (Azuma and Yasuda, 1989). Our analysis of leading edge vortex stability on fly wings suggests that autorotating seeds augment their lift with a stable leading edge vortex that rests on their wing.

To test this prediction, we measured the three-dimensional flow field generated by dynamically scaled models of maple and hornbeam seeds that are actuated by a robot arm. The measured flow fields revealed that these autorotating seeds indeed generate a large stable leading edge vortex and corresponding exceptionally high lift. The lift augmentation of the leading edge vortex allows autorotating seeds to obtain longer airtimes for their relatively small wings. Smaller wings save material and energy spend on seed dispersal, or alternatively, it allows a tree to disperse more seeds. The finding of a stable leading edge vortex on autorotating seeds suggests that this vortex represents a convergent aerodynamic solution in the evolution of flight performance in both plants and animals. [*Chapter 5*]

Not all wings of organisms that are known to generate stable leading edge vortices revolve around their base as do autorotating seeds and insects. The common swift can also generate a stable leading edge vortex on its hand wing by sweeping its wing backwards during gliding, which is thought to boost lift (Videler *et al.*, 2004). Actual lift measurements have, however, not been carried out.

Conclusion 4 | *Wing morphing drastically improves glide performance.*

Like many other birds common swifts continually change the shape and size of their wings while gliding (Newman, 1958; Pennycuick, 1960; Pennycuick, 1968; Tucker, 1987; Rosén and Hedenström, 2001). Their morphing wing consists of an arm and hand wing that can be seen in action whenever they change the sweep of their wings from fully extended to swept back and *vice versa*. To what degree wing morphing improves the glide performance of birds has not yet been quantified through aerodynamic measurements inside *and* outside the behavioral envelope of birds (Tucker, 1987; Azuma, 2006).

Our measurements on freeze-dried swift wings show that the main function of wing morphing during gliding flight is not the generation of a stable leading edge vortex to boost lift. The swept back wings with a stably attached leading edge vortex (on the hand wing) actually generate less lift than the fully extended wings without a leading edge vortex. Instead we found that the function of wing sweep is to match wing shape and surface area to suit glide speed such that glide performance is maximized. Morphing can increase glide distance by 60%, glide duration by 100% and turning performance up to 300%. Minimal energy expenditure is obtained with fully extended wings at low speeds, but at higher speeds swept wings outperform extended wings. The measurements on morphing swift wings show that wing morphing can significantly broaden the

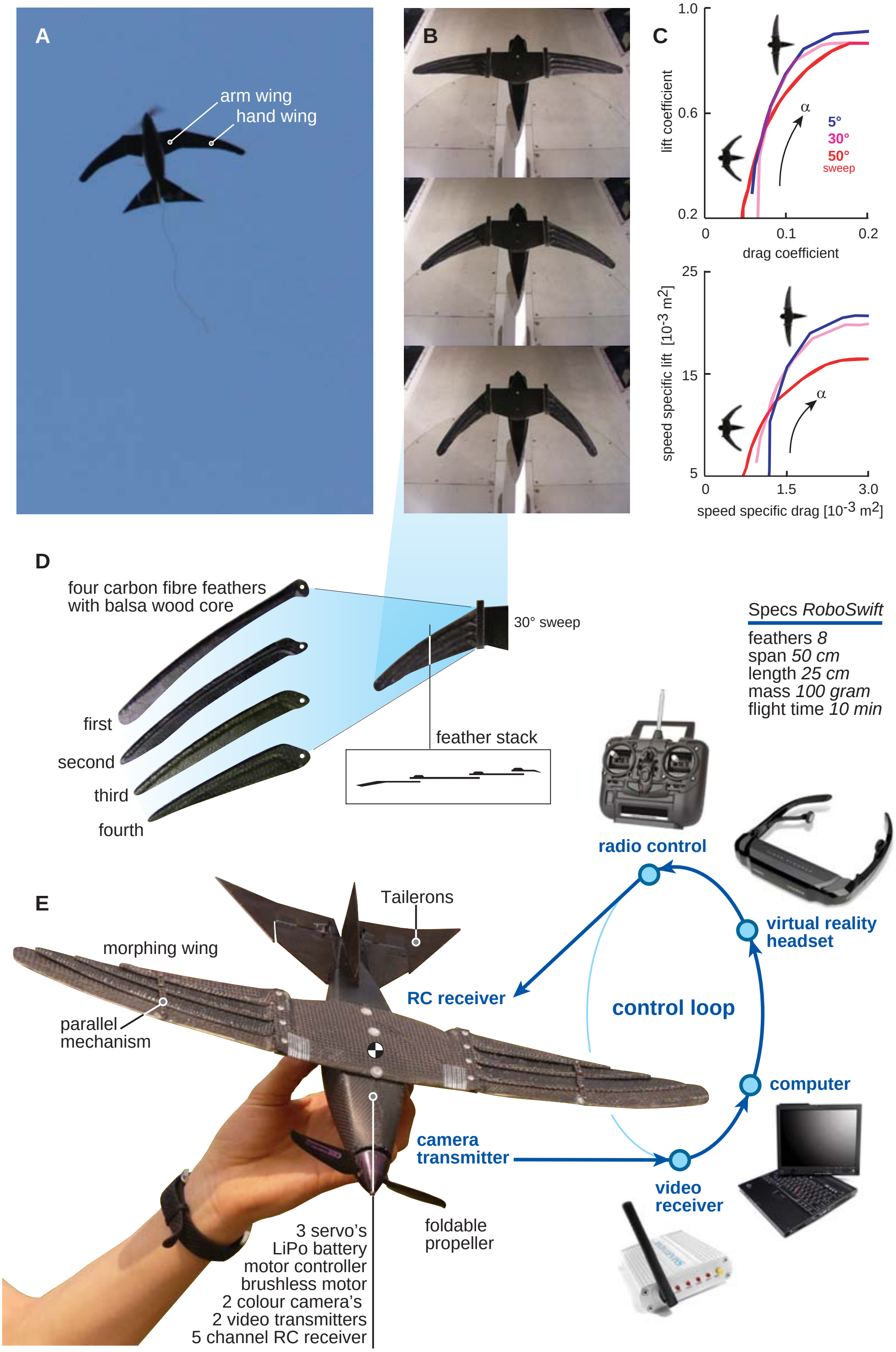
A
arm wing
hand wing
B
C
1.0
0.6
0.2
lift coefficient
0
0.1
0.2
drag coefficient
α
5°
30°
50°
sweep
25
15
5
speed specific lift [10^{-3} m^2]
0
1.5
3.0
speed specific drag [10^{-3} m^2]
α
D
four carbon fibre feathers
with balsa wood core
first
second
third
fourth
30° sweep
feather stack
Specs *RoboSwift*
feathers *8*
span *50 cm*
length *25 cm*
mass *100 gram*
flight time *10 min*
E
morphing wing
Tailerons
parallel
mechanism
RC receiver
camera
transmitter
3 servo's
LiPo battery
motor controller
brushless motor
2 colour camera's
2 video transmitters
5 channel RC receiver
foldable
propeller
radio control
virtual reality
headset
control loop
computer
video
receiver

flight performance envelope of gliding birds. This finding supports the idea that wing morphing could also broaden the performance envelope of flapping birds (discussed in Tobalske, 2007).

The extended performance envelope of morphing wings has been recognized by aerospace engineers who attempt to design more efficient aircraft inspired by bird flight. Our quantification of the increased glide performance of swifts through the use of morphing wings supports this bio-inspired design idea. However, the morphological complexity of bird wings is beyond reach of current engineering design capabilities, especially at the much larger scale of commercial airplanes. Therefore we need simpler morphing mechanisms for airplanes. Perhaps the best scale for development of such technology is the scale of birds, at which it is a proven concept and we can study it in detail to find inspiration for design. [*Chapter 6*]

Our extensive glide performance analysis of swift wings illustrates that a simple analysis, based on lift and drag alone, is not sufficient for evaluating the efficacy of generating a leading edge vortex. This raises the question how efficient translating versus spinning versus flapping wings generate lift.

Conclusion 5 | *Flapping wings are less efficient than spinning and translating wings.*

Surprisingly, the efficiency of flapping, spinning and translating wings has never been compared before in a single experiment. A strong motivation for many engineers to develop flapping millimeter sized air vehicles (Fearing *et al.*, 2000), is the idea that flapping wings might be more effective than translating and spinning wings at the scale of insects.

We tested this idea for hovering fly wings from hummingbird scale to fruit fly scale. In our experiments we determined how effective fly wings generate lift by measuring the drag they produce and the power they consume to generate this lift. Our experiments show that flapping fly wings are less efficient aerodynamically than translating fly wings, only at fruit fly scale do they perform equally poorly. Spinning fly wings are up to a factor two more efficient than flapping

Fig. 2 | RoboSwift, a morphing micro air vehicle inspired by the common swift. (A) In flight demonstration of wing morphing of the hand wing at wind force 5-6 (Photo: Johan van Leeuwen). (B) Carbon fiber wind tunnel model with wing sweeps of 5°, 30° and 50° (wing sweep is measured at the leading edge of the hand wing). (C) These (preliminary) lift-drag polars are made by measuring lift and drag at 10 m/s at angles of attack α that range roughly from 0°-30° and subsequently connecting the lift-drag values. Top, the lift-drag coefficient polars show that RoboSwift can indeed decrease drag with swept wings at low angles of attack and increases lift with extended wings at high angles of attack, but not as much as found for swifts. Top, the speed specific lift and drag polar is obtained by multiplying the lift-drag coefficient polars by the actual wing area of the wings when it is swept versus un-swept. This shows that the difference in wing area significantly broadens the lift-drag envelope of RoboSwift, as found for swifts. (D) The morphing wing is built up with four artificial 'primary feathers' built from carbon fiber and balsa wood. These feathers rest on top of each other, form a feather stack, and can slide controlled with respect to each other using a coupled parallel mechanism. (E) System overview of RoboSwift. Most of the components are enclosed in the fuselage, made out of carbon fiber, like the wing. These components form a control loop, which includes a pilot, with equipment on the ground. The morphing mechanism is enclosed in the arm wing, except for the parallel mechanism. The parallel mechanism simplifies the actuation of the wing; only the first feather is actuated by a servo motor, the others follow. The current in-flight control variables of RoboSwift are; (1) the sweep of its morphing wings, (2) excursion of the two flaps that build up the taileron, (3) the number of revolutions per minute of the propeller. (Photo RoboSwift: Eddy van der Weijden.)

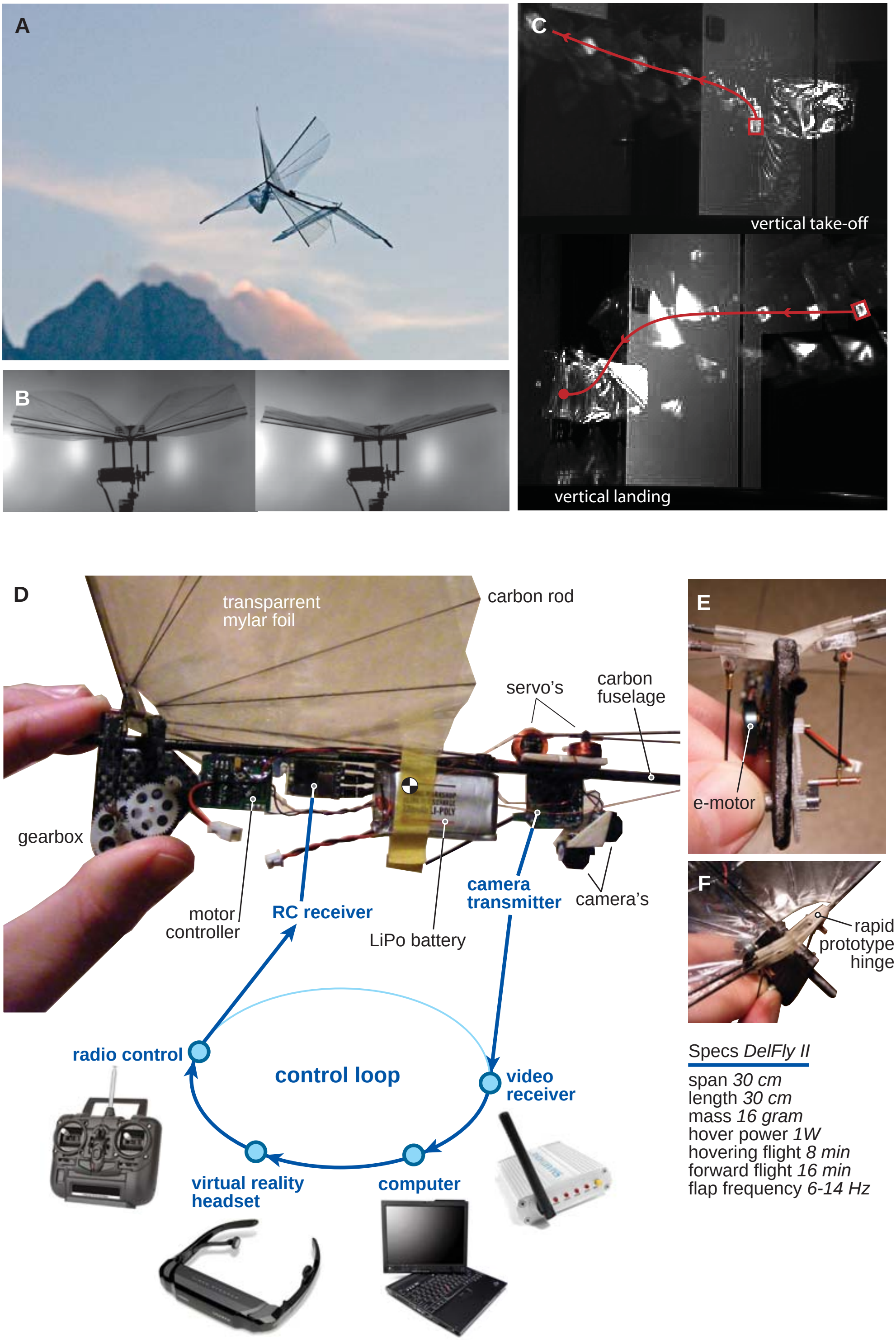
A
B
C
vertical take-off
vertical landing
D
transparrent mylar foil
carbon rod
servo's
carbon fuselage
gearbox
motor controller
RC receiver
LiPo battery
camera transmitter
camera's
radio control
control loop
video receiver
virtual reality headset
computer
E
e-motor
F
rapid prototype hinge
Specs *DelFly II*
span *30 cm*
length *30 cm*
mass *16 gram*
hover power *1W*
hovering flight *8 min*
forward flight *16 min*
flap frequency *6-14 Hz*

and translating fly wings. Flapping wings do generate much more lift than translating wings, but spinning wings generate similar high lift most efficiently. The reason for similar lift between flapping and spinning fly wings is that both revolve and can, therefore, sustain a stable leading edge vortex at a Rossby number close to one. The lower aerodynamic efficiency of flapping versus spinning wings is due to energy losses that correspond with accelerating and decelerating the flow continuously. Another explanation is that a spinning wing can operate continuously at an optimal angle of attack, whereas the angle of attack of a flapping wing necessarily varies. [*Chapter 4*]

Currently engineers try to copy the flapping motion of insect wings to augment the lift of their micro air vehicles with a leading edge vortex. To maximize efficiency such micro air vehicles should only copy the low Rossby numbers of insect wings, and revolve wings continuously. In practice this implies designing stubbier rotor blades such that they can operate at much higher angles of attack, and sustain a stable leading edge vortex that augments lift, at the cost of drag. Which blade aspect ratio results in maximal hover performance is, however, unknown.

From biofluiddynamics to bio-inspired design

Synthesis 1 | *Bio-inspired design of a morphing micro air vehicle*

The extended performance and control envelope of morphing bird wings is an attractive design concept for efficient and agile micro air vehicles (Lind *et al.*, 2004). Morphing wings not only have the potential to make micro air vehicles more effective, they also have the potential to make a micro air vehicle less conspicuous during surveillance missions in combination with a bird-like silhouette. This mission perspective and the aerodynamic analysis of morphing swift wings provided the inspiration for me to initiate the RoboSwift project. Roboswift flies passively stable and has a fixed arm wing to which a morphing hand wing is attached, Fig. 2A.

The morphing hand wing of RoboSwift consists of four feathers that can slide over each other like real feathers. This allows the hand wing to be swept back and forth. The hand wing area is maximal when fully extended and roughly 25% less fully swept back, with a maximal feather overlap, shown for the wind tunnel model in Fig. 2B. Lift and drag measurements in the wind tunnel show that the morphing wings of Roboswift indeed widen the lift-drag envelope significantly, similar to swifts, Fig. 2C. Swifts possess, however, more shape-effective morphing wings than RoboSwift, because they can generate even higher lift coefficients and lower drag

Fig. 3 | DelFly, a flapping micro air vehicle inspired by insect flight. (A) DelFly in flight in Garmisch-Partenkirchen (the Bavarian Alps, Germany). Note the considerable wing deformation of the slack wings. (B) The wing deformation of DelFly at stroke reversal when wing speed is minimal and wing acceleration maximal. Shown is wing deformation in air (left) versus near-vacuum (right). (C) Combined video frames of DelFly demonstrate its vertical take-off and landing capabilities. The bright square is the Lithium-Polymer battery pack. (Based on a movie made by Bart Remes.) (D) System overview of DelFly, which is constructed mostly out of carbon fiber components covered with transparent Mylar foil. The on-board components are fixed unprotected to the carbon fuselage. The on-board components form a control loop, which includes a pilot and equipment on the ground. The current in-flight control variables of DelFly are (1) the flapping frequency of the wings, (2) the elevator excursion of the horizontal stabilizer, (3) the rudder excursion of the vertical stabilizer. (E) Symmetric flap mechanism driven by an electric brushless motor. (F) Rapid prototype hinge.

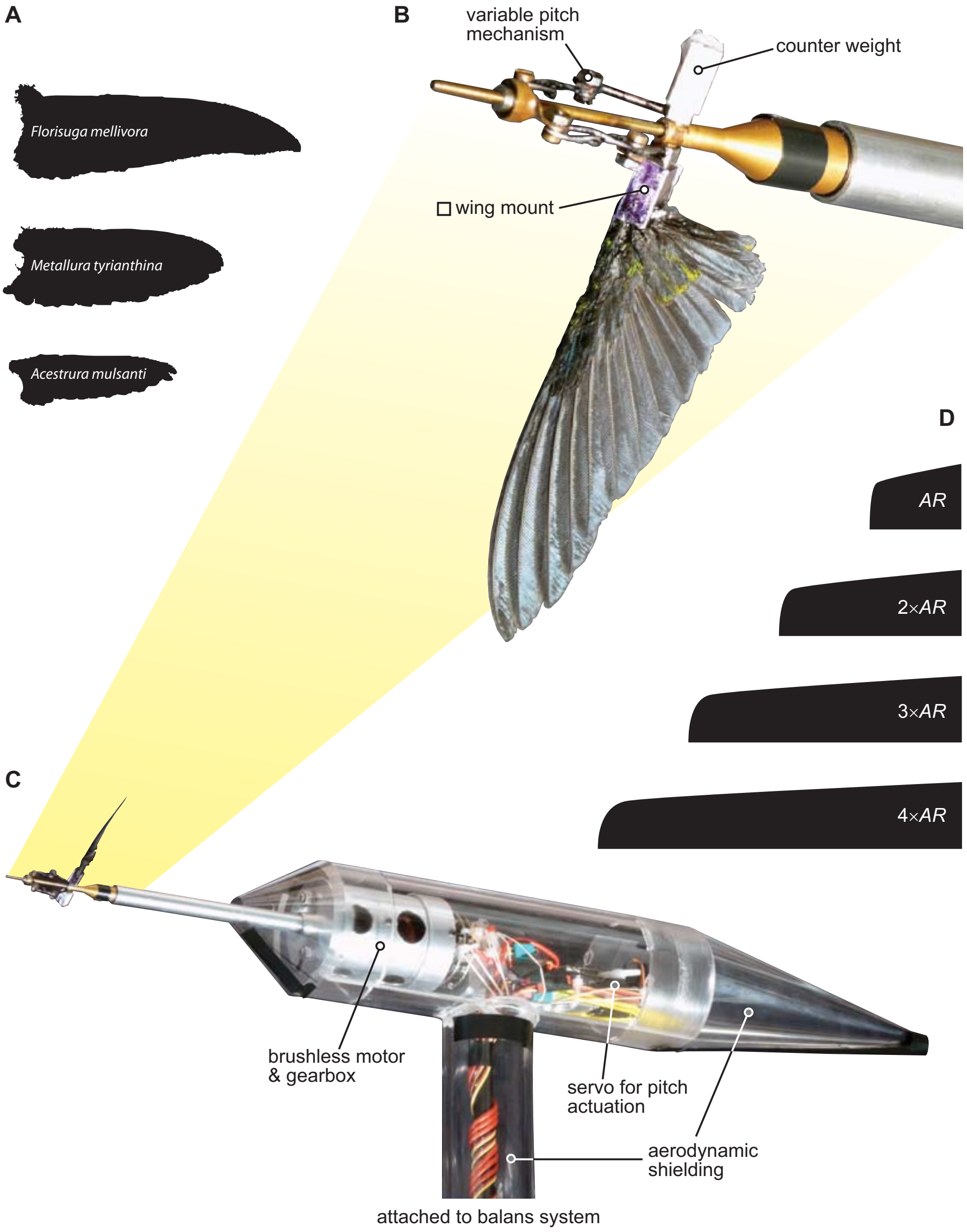

Fig. 4 | Spinner setup for testing the aerodynamic performance of spinning hummingbird wings. (A) Wing planform of three of more than 40 hummingbird wings that we plan to test. (B) Miniature variable pitch mechanism with a mounted hummingbird wing. (C) Aerodynamically shielded driving mechanism of the spinner setup, which is connected to a sensitive (1/1000 of a gram) lift-drag balance system. The spinner system itself is placed in a large transparent box, such that drafts in the lab cannot affect the lift and drag measurements. (D) Illustration of a series of model wings with variable aspect-ratio. Such a series of model wings will be used to determine if hummingbird wings have a close-to optimal wing aspect ratio. (photos spinner setup: Henk Schipper) coefficients with their morphing wings. Roboswift is nevertheless an impressive flyer with its simple morphing wings. It uses only four primary feathers to morph its hand wing compared to eleven in the swift, Fig. 2D. The morphing capabilities of RoboSwift have been demonstrated during free flight tests in turbulent weather at wind force 5-6.

There are two reasons why the feathers that build up the morphing wing remain stably packed together during flight (1) The spar (shaft) of every feather is placed near the leading edge of the feather, which prevents individual feathers from fluttering, and (2), Every feather rests on top of the feather in front of it, which enables the feathers to push against each other such that the wing closes under positive loading. The feather design is based on a real swift wing, as is the sharp leading edge of the first primary feather of the hand wing. Surprisingly this sharp leading edge turned out to be essential for good stall characteristics of RoboSwift's fully extended wing; it could not fly without it. This shows how flight tests with a mechanical swift model can also provide new insight into the aerodynamics of real swifts.

An overview of the RoboSwift system design and a short specification are given in Fig. 2E. Roboswift is powered by a quiet electric motor that drives a foldable propeller. The foldable propeller allows roboswift to glide efficiently in between powered flights. The RoboSwift design and its rationale are further described in Lentink *et al.* (2008a).

Synthesis 2 | *Bio-inspired design of a flapping micro air vehicle*

Insects are inspirational 'flight machines'; they can take off and land vertically, fly both fast and hover, are agile, maneuverable and they accomplish this at an impressively small scale. One reason why I studied the aerodynamics of insect flight is to better understand how the design of micro air vehicles can be inspired by insect flight (Pornsin-Sirirak *et al.*, 2001; Wood, 2008). Our experiments show that the lift and drag generated by flapping fly wings is scalable from fruit fly scale to hummingbird scale. This scalability implies that, once we know the lift and drag of a flapping wing, we can easily obtain values for other scales. These values can be obtained using scaling laws for aerodynamic force and power, using the assumption that the shape of the wing tip path and the flight path remains unchanged during scaling. The structural design of micro air vehicles can also be scaled using scaling laws. Using all these scaling laws iteratively, the smallest possible flapping micro air vehicle can be sized based on commercially available components such as motors, batteries, radio receivers and actuators.

Based on the insight that insect flight is scalable, I initiated the DelFly project. DelFly is a passively stable, camera-equipped, flapping micro air vehicle that can fly fast and hover. The design is inspired both by an existing rubber-powered toy with flapping wings, the Luna, and the scalability of flapping wing aerodynamics as found for insects, Fig. 1. The single wing aspect ratio of DelFly was kept low (1.6) inspired by the low Rossby number condition for leading edge vortex stability on fly wings. DelFly is extremely lightweight for its size (low wing loading), which makes it susceptible for gusts, it flies therefore primarily indoors. The DelFly was demonstrated in 2005 at a micro air vehicle conference in Garmisch-Partenkirchen, Fig. 3A. The aero elastic wings were made from thin Mylar film and carbon fiber stiffeners.

In a follow-up design project, DelFly was scaled down from 35 cm to 28 cm wingspan and its motor and drive train where improved, which resulted in DelFly II. To determine to what extent aerodynamic and inertial forces deform the slack flapping wings, we compared the wings deformation for hover conditions in both air and vacuum. The high-speed video images reveal that inertial force is dominated by aerodynamic force, which deforms the wing throughout the stroke cycle. We further determined that the deformable wings of DelFly II can indeed generate up to twice as much lift as translating wings, as found for insects. Power measurements, under near-vacuum conditions, further show that roughly half of DelFly II's power is needed just to accelerate the drive train and wings; DelFly II is therefore not very efficient. DelFly II is nevertheless an impressive flyer as it can take-off and land vertically many times in a row, like insects can, Fig. 3C. DelFly II has two onboard cameras that can be used to fly it beyond line of sight using a virtual reality headset, Fig. 3D. The design details are shown in Figure 3D-F and include flight performance specifications.

The initial DelFly design has been scaled down further to 10 cm wing span in the lab of Yoshiyuki Kawamura (Kawamura *et al.*, 2008). This tiny design is the first successfully flying insect-sized flapping micro air vehicle. The design of DelFly and its rationale are further described in Lentink *et al.* (2008b).

Outlook | *Is wing slenderness optimized for power efficiency in hummingbirds?*

In order to design a really efficient hovering micro air vehicle with spinning wings, we still need to know which wing slenderness (aspect ratio) will result in the highest efficiency. For the currently commercially available components, hummingbird scale is the smallest feasible scale for such a vehicle. Not only do hummingbirds fly at the smallest feasible scale, they are perhaps also the most impressive and efficient hovering animals that exist. To test how efficiently hummingbird wings actually generate lift, we would need to measure their lift and drag. Fortunately Douglas Altshuler (UC Riverside) shares my interest and through his contacts we obtained over 40 Colombian hummingbird wings of various sizes, illustrated in Fig. 4A. For these experiments we developed a spinner to measure both lift and drag (Usherwood and Ellington, 2002), Fig. 4B, C. Spinning and flapping wings mediate leading edge vortex stability through the same mechanism. This makes tests with spinning wings the simplest relevant experiment for our aims. In a future experiment we want to test the available range of real hummingbird wings and compare these with tests of model hummingbird wings with various aspect ratios, Fig. 4D. These new experiments can give us insight in the aerodynamic adaptations of hummingbird wings and hopefully inspiration for the future design of more efficient hovering micro air vehicles

Acknowledgements

Steven Prins, Ulrike Müller, Sander Kranenbarg and Johan van Leeuwen critically read several versions of the manuscript.

My research is the result of fruitful collaborations with scientists, and students from various universities and countries. I am grateful for their help, inspiration and friendship that made this research possible. The research synthesized here has been supported by NWO-ALW grant 817.02.012. Please find my extended acknowledgements at the end of this thesis.

My bio-inspired design projects RoboSwift and DelFly are the result of a collaboration with (among others) Michel van Tooren, Rick Ruijsink, Christophe de Wagter, and students Stefan Jongerius, Stan Kosman and Bart Remes, at TU Delft, and Maarten van Dijk at van Dijk Pultrusion products. The work on RoboSwift is supported by the Dutch National Police Force and the work on DelFly is supported by TNO Defence, Security, and Safety.

The hummingbird project presented here is a collaboration with Douglas Altshuler at UC Riverside and students Jan Wouter Kruyt and Elsa Quicazán.

References

Alben, S. and Shelley, M. (2005). Coherent locomotion as an attracting state for a free flapping body, *PNAS* **102**, 11163-11166.

Azuma, A. and Yasuda, K. (1989). Flight performance of rotary seeds. *J. Theor. Biol.* **138**, 23-53.

Azuma, A. (2006). *The Biokinetics of Flying and Swimming.* AIAA Education Series, Reston, 2nd edition.

Bandyopadhyay, P. R., Beal, D. N. and Menozzi, A. (2008). Biorobotic insights into how animals swim. *J. Exp. Biol.* **211**, 206-214.

Birch J. M., Dickinson, M. H. (2001). Spanwise flow and the attachment of the leading-edge vortex on insect wings. *Nature* **412,** 729-733.

Blondeaux, P., Guglielmini, L. and Triantafyllou, M. S. (2005). Chaotic flow generated by an oscillating foil. *AIAA J.* **43**, 918-922.

Dickinson, M. H. and Götz, K. G. (1993). Unsteady aerodynamic performance of model wings at low Reynolds numbers. *J. Exp. Biol.* **174**, 45-64.

Dickinson, M. H. (1994). The effects of wing rotation on unsteady aerodynamic performance at low Reynolds numbers. *J. Exp. Biol.* **192**, 179-206.

Dickinson, M. H., Lehmann, F. O. and Sane, S. P. (1999). Wing rotation and the aerodynamic basis of insect flight. *Science* **284**, 1954-1960.

Ellington, C. P., Van den Berg, C., Willmott, A. P. and Thomas, A. L. R. (1996). Leading-edge vortices in insect flight. *Nature* **384**, 626-630.

Hubel, T. (2006). Untersuchungen zur instationären Aerodynamik an einem vogelähnlichen Flügelschlagmodell, PhD thesis, *TU Darmstadt, Fachbereich Biologie*.

Fearing, R. S., Chiang, K. H., Dickinson, M. H., Pick, D. L., Sitti, M. and Yan J. (2000). Wing transmission for a micromechanical flying insect. *IEEE Int. Conf. on Robotics and Automation.*

Iima, M. (2007). A two-dimensional aerodynamic model of freely flying insects. *J. Theor. Biol.* **247**, 657-671.

Kawamura, Y., Souda, S. Nishimoto, S. and Ellington, C. P. (2008). Clapping-wing Micro Air Vehicle of Insect Size, in *Bio-mechanisms of Swimming and Flying* Ed. Kato, N. and Kamimura, S., Springer Verlag.

Lentink, D. and Gerritsma, M. I. (2003). Influence of airfoil shape on performance in insect flight. *AIAA* 2003-3447.

Lentink, D., van der Veen, T. S., and Kosman, S. (2008a). Aerodynamic performance of a mechanical bird with a morphing wing composed out of artificial feathers. *In preparation.*

Lentink, D., Jongerius, S. R. and Bradshaw, N. L. (2008b). The scalable design of flapping micro air vehicles inspired by insect flight. *Will appear in a Springer-Verlag book on insects and robotics.*

Lewin, G. C. and Haj-Hariri, H. (2003). Modelling thrust generation of a two-dimensional heaving airfoil in a viscous flow. *J. Fluid Mech.* **492**, 339-362.

Lind, R., Abdulrahim, M., Boothe, K. and Ifju, P. (2004). Morphing for flight control of micro air vehicles. European Micro Air Vehicle Conference, Braunschweig, Germany.

Lorenz, E. N. (1963). Deterministic nonperiodic flow. *J. Atmos. Sci.* **20**, 130-141.

Maxworthy, T. (1979). Experiments on the Weis-Fogh mechanism of lift generation by insects in hovering flight. Part 1. Dynamics of the ‘fling’. *J. Fluid Mech.* **93**, 47-63.

Muijres, F. T., Johansson, L. C., Barfield, R., Wolf, M., Spedding, G. R. and Hedenström, A. (2008). Leading-edge vortex improves lift in slow-flying bats. *Science* **319**, 1250-1253.

Newman, B. G. (1958). Soaring and gliding flight of the black vulture. *J. Exp. Biol.* **35**, 280-285.

Pennycuick, C. J. (1960). Gliding flight of the fulmar petrel. *J. Exp. Biol.* **37**, 330-338.

Pennycuick, C. J. (1968). Wind-tunnel study of gliding flight in the pigeon Columba livia. *J. Exp. Biol.* **49**, 509-526.

Pornsin-Sirirak, T. N., Tai, Y. C., Ho, C. H. and Keenon, M. (2001). Microbat-a palm-sized electrically powered omithopter. *NASA/JPL Workshop on Biomorphic Robotics*, Pasadena, USA.

Rosén, M. and Hedenström, A. (2001). Gliding flight in a jackdaw. *J. Exp. Biol.* **204**, 1153-1166.

Rossby, C. G. (1936). On the momentum transfer at the sea surface. Part I Papers *Phys. Oceanogr. Meteorol.* 3 no 3.

Taylor, G. K., Nudds, R. L. and Thomas, A. L. R. (2003). Flying and swimming animals cruise at a Strouhal number tuned for high power efficiency. *Nature* **425**, 707-711.

Tobalske, B. W. (2007). Biomechanics of bird flight. *J. Exp. Biol.* **210**, 3135-3146.

Triantafyllou, G. S., Triantafyllou, M. S. and Grosenbaugh, M. A. (1993). Optimal thrust development in oscillating foils with application to fish propulsion. *J. Fluid Struc.* **7**, 205–224.

Tucker, V. A. (1987). Gliding birds: the effect of variable wing span. *J. Exp. Biol.* **133**, 33-58.

Usherwood, J. R. and Ellington, C. P. (2002). The aerodynamics of revolving wings I-II. *J. Exp. Biol.* **205**, 1547-1576.

Videler, J. J., Stamhuis, E. J. and Povel, G. D. E. (2004). Leading-edge vortex lifts swifts. *Science* **306**, 1960-1962.

Winter, H. (1936). Flow phenomena on plates and airfoils of short span. NACA report 798.

Wood R. J. (2008). The first takeoff of a biologically-inspired at-scale robotic insect. *IEEE Trans. on Robotics* **24**, 341-347.

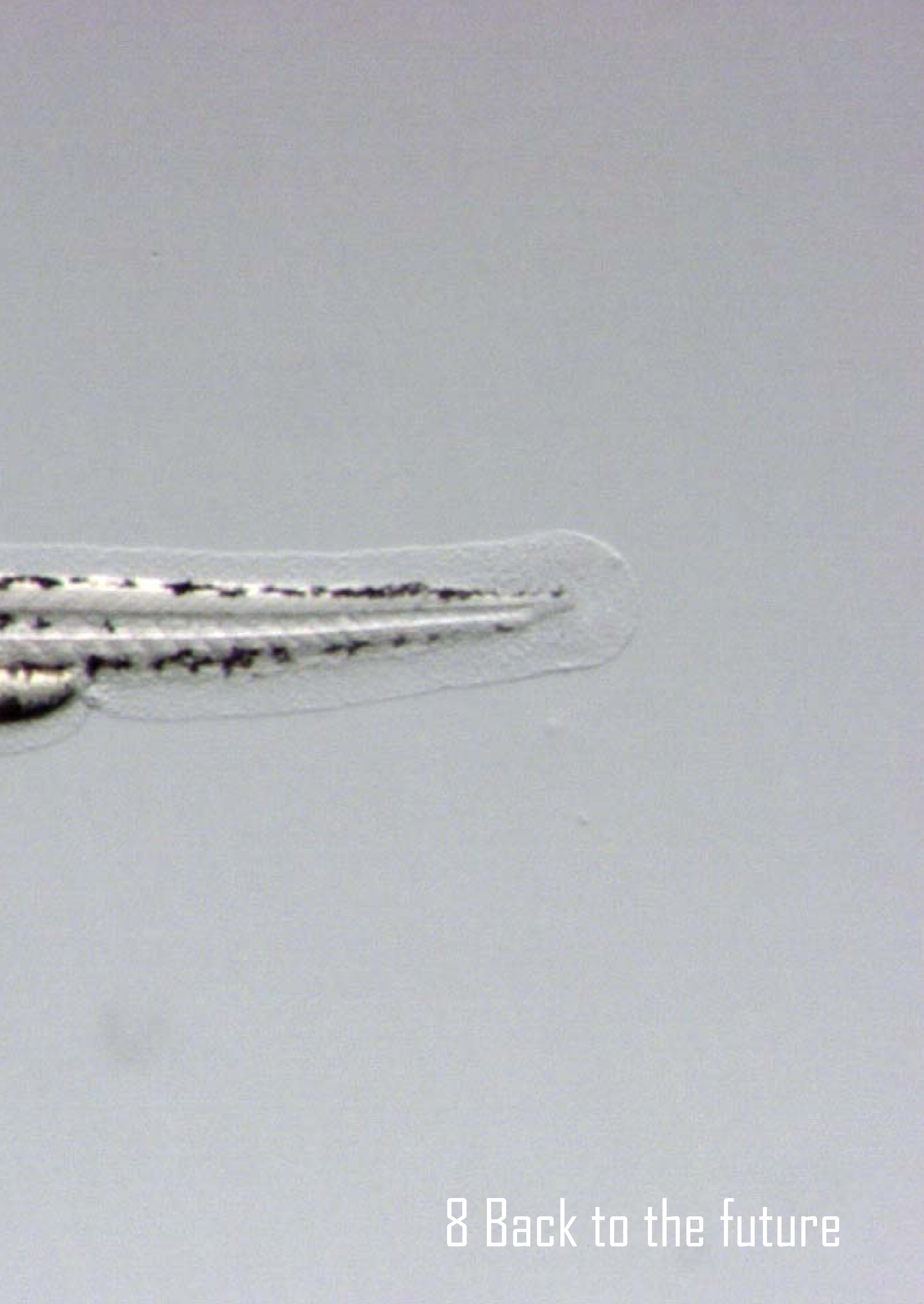

8 Back to the future

8.1

QUANTIFYING THE DEVELOPMENT OF ZEBRA FISH SWIMMING PERFORMANCE

David Lentink*, Gijs de Rue, Ebraheem Fontaine and Johan L. van Leeuwen

What is the hydrodynamic efficiency of swimming fish, and how does it develop from the larval to adult stage? We developed a whole array of improved techniques and experimental facilities that can provide an answer to this question if they are used in gear: a fish wheel, an automated fish tracker and a dynamically scaled robot fish. Here we will illustrate the design of these three newly developed techniques for NWO-ALW grant 817.02.012: Lentink, D., Müller, U.K., Dickson, W.B., Breedveld, P., Liu, H., van Heijst, G.J.F., Dickinson, M.H. and van Leeuwen, J.L. (2007). Vortex dynamic strategies in animal swimming and flight.

Filming fish in a bend

To determine how efficient zebra fish swim as a function of speed and age, we first need to study how they swim. For this we need a swimming facility with high quality flow of which the speed can be manipulated accurately. The size range of zebra fish is roughly 4 - 40 mm from the larval to adult stage (Reynolds number 30 to 30000), Fig. 1A. The main challenge for designing a zebra fish swimming facility is that zebra fish swim at speeds for which the velocity profile in small water tunnels (pipes) can be almost parabolic. Such a velocity profile corresponds with significant background vorticity that infers with the flow measurements (particle image velocimetry), Fig. 1B. Further, at the low speed and small diameters of water tunnels that best suit experiments with small fish, the laminar velocity profile is unstable and can transition from laminar to turbulent flow, which is undesirable. To resolve both problems, we designed a fish wheel consisting of a spinning, wheel-shaped, horizontal fish tank, Fig. 1C: First there is no laminar-turbulent flow transition as soon as the tank has spun-up and is in rest. Second there is almost no velocity gradient over the tank width if the wheel radius is large enough, Fig. 1B. Further, the small remaining velocity gradient can be calculated analytically and subtracted from the measurements. We designed the wheel such that its Rossby number (wheel radius divided by fish length) is of order 100 (larvae) to 10 (adult). These high values ensure that the centripetal and Coriolis accelerations in the spinning tank are negligible compared to convective accelerations.

The fish wheel consists of a narrow transparent tank for larvae and juvenile zebra fish (shown) and a wider tank for adults (not shown). The high-speed camera and laser sheet for particle image velocimetry are fixed with respect to each other and can be translated vertically as a whole. The fish wheel itself can be translated horizontally with respect to the camera using a X-Y table, and the angle of the fish wheel can be controlled using a servo motor. In this way we can always get the fish in focus. In a water tunnel fish like to swim in the boundary layer close to the wall to save energy. In a fish wheel it actually costs more energy to swim close to the wall, which will motivate fish to swim close to the center line. The 'test section' of the fish wheel with the laser and camera is shown in Fig. 1D.

Based on published work and an accepted proposal

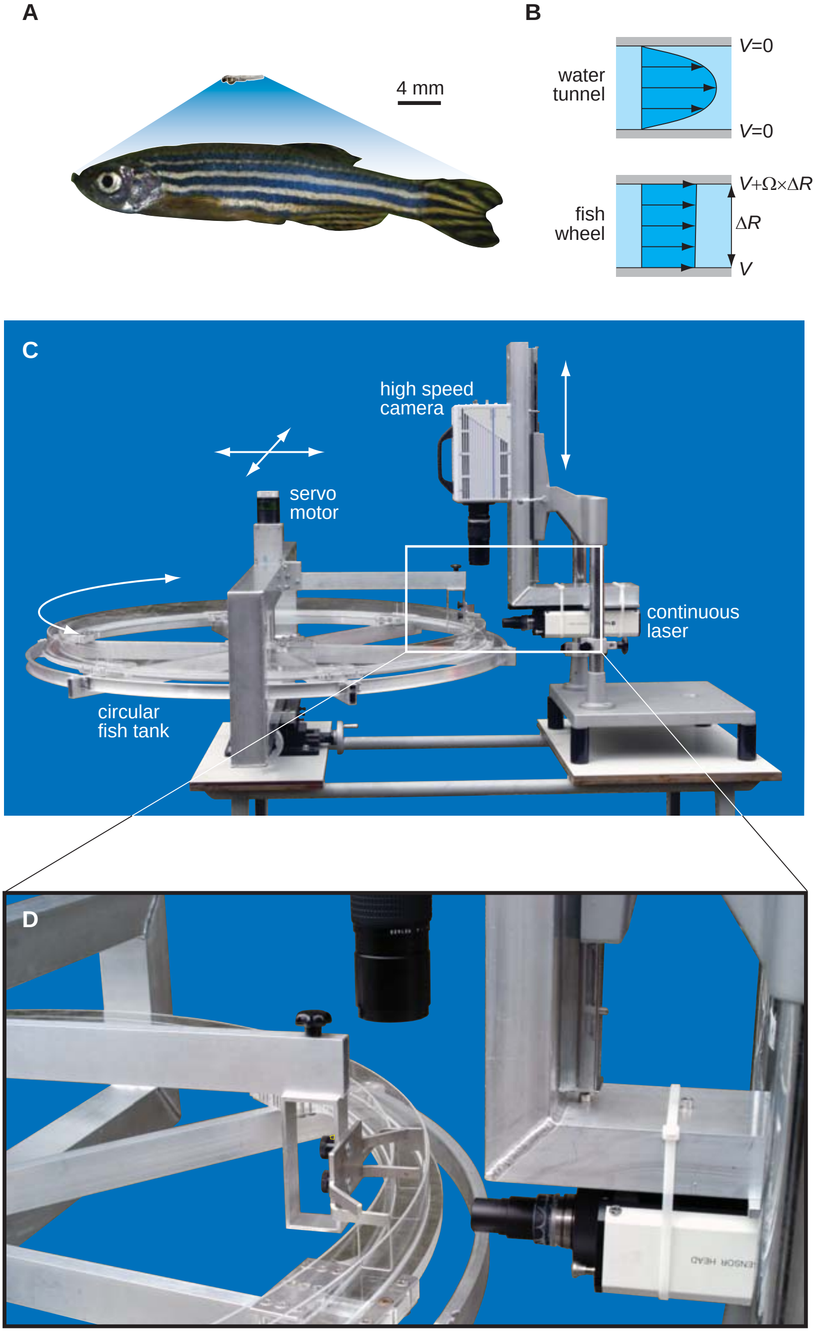

Fig. 1 | Fish wheel designed for studying zebra fish swimming from larvae to adult. (Photos: Henk Schipper)

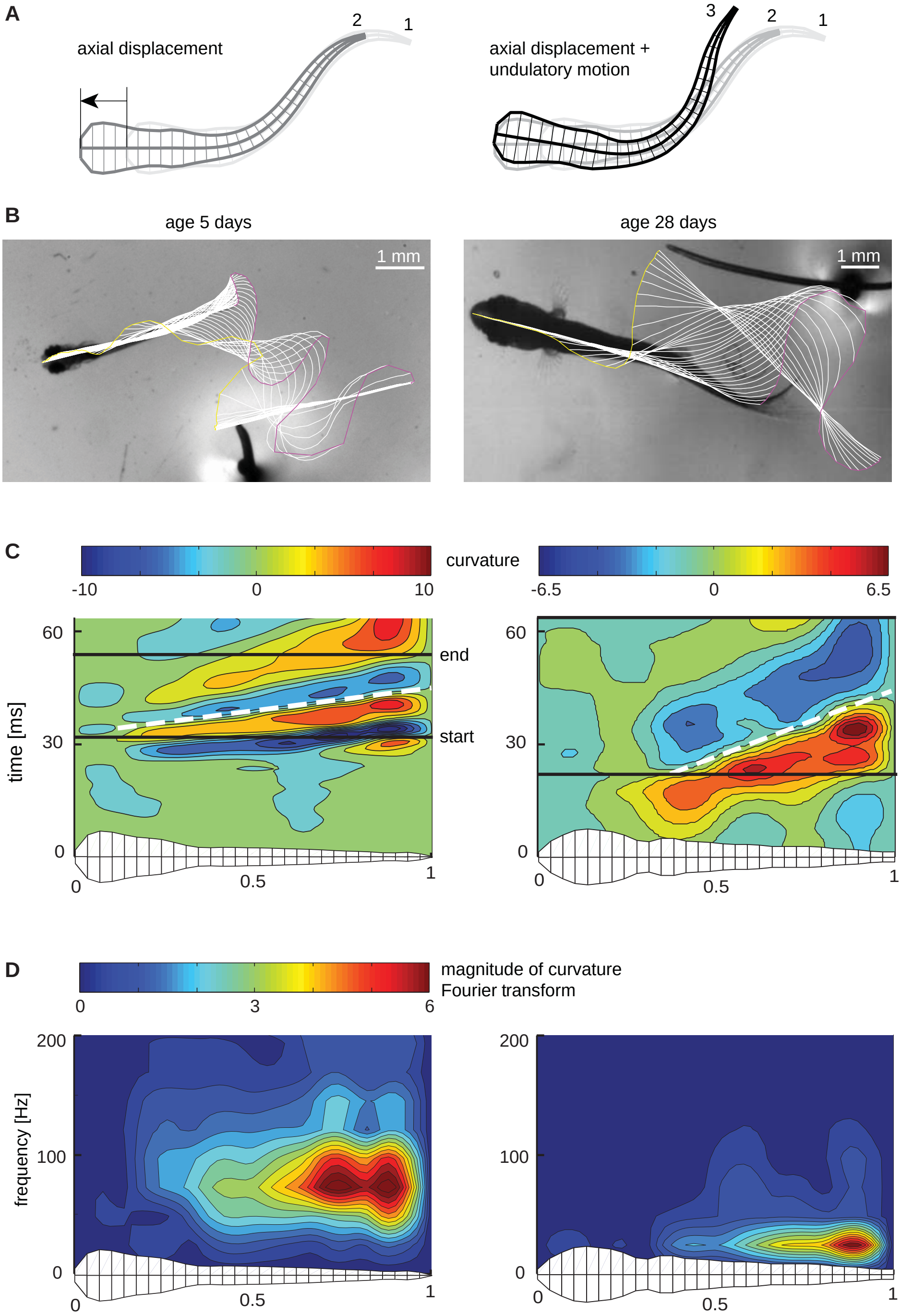

Fig. 2 | Automated fish tracking and kinematics processing. (Video frames fish: Ansa Wasim)

Fish start swimming automatically in a fish wheel because of an optomotor response that enables them to stabilize their position relatively to a stationary background in a running flow. To make use of this optomotor response we have made the fish tank transparent. The fish wheel designed by Bainbridge (1958) shows that fish wheels work well, and that we have actually reinvented the fish wheel. [**Bainbridge, R. and Brown, R. H. J.** (1958). An Apparatus for the Study of the Locomotion of Fish. *J. Exp. Biol.* **35**, 134-137.]

Automated fish tracking

To obtain a statistically sound data set on zebra fish swimming kinematics as a function of speed and age we need to film and track many zebra fish. For this we developed an automated, high-throughput, fish tracker that can extract the body wave kinematics time-efficiently. The tracker is robust to partial occlusions and can track both larvae and adults reliably. The tracker consists of a fish model which is derived semi-automatically from an individual image of the swimming sequence. In the subsequent image this model is first translated and then bended such that the overlap between fish and model is again maximal, which yields both displacements and body wave data, Fig. 2A. The automatically derived body wave kinematics, the midlines, can then be plotted and analyzed, Fig. 2B (white line, midlines; blue line, tail path; yellow line, snout path). Using the midlines we can not only calculate the angular velocity distribution of the body, but also how body curvature varies along the body in time, Fig. 2C. The magnitude of curvature Fourier transform gives us the distributed body-wave frequency of the fish, Fig. 2D. Further information can be found in **Fontaine, E., Lentink, D., Kranenbarg, S., Müller, U. K. van Leeuwen, J. L., Barr, A. H. and Burdick, J. W.** (2008). Automated visual tracking for studying the ontogeny of zebrafish swimming. *J. Exp. Biol.* **211**, 1305-1316.

Ω3 the fatty fish robot

To determine the hydrodynamic efficiency of swimming fish we need to integrate the hydrodynamic power distribution along the body. The power distribution is calculated as bending moment times angular velocity distribution. We can obtain the angular velocity distribution along the body with the automated fish tracker, but measuring the bending moment distribution *in vivo* is an open challenge. Therefore we designed a dynamically scaled robotic model of a zebra fish in an oil tank facility instead. This robot fish, Ω 3, allows us to replay the swimming kinematics of actual zebra fish and measure the corresponding bending moments along its body simultaneously. For this we use strain gauges between the servomotors that actuate the robot. The drive train of the robot is designed such that it can accommodate plastic shells that represent the body shape of both adult and larval zebra fish, Fig. 3.

Three times is out

In summary we will use our equipment in three subsequent steps to determine the hydrodynamic efficiency of zebra fish. First the fish wheel will yield high quality flow fields and movies of body kinematics of zebra fish as a function of both speed and age. Second the automated fish tracker will efficiently yield a dataset with a high enough number of samples to be statistically sound. And finally the fish robot will yield the bending moment distributions and hence the net hydrodynamic power needed to evaluate zebra fish swimming efficiency as a function of both speed and age. In subsequent steps we hope to vary the kinematics of the robot fish to determine to which degree zebra fish maximize their hydrodynamic swimming performance.

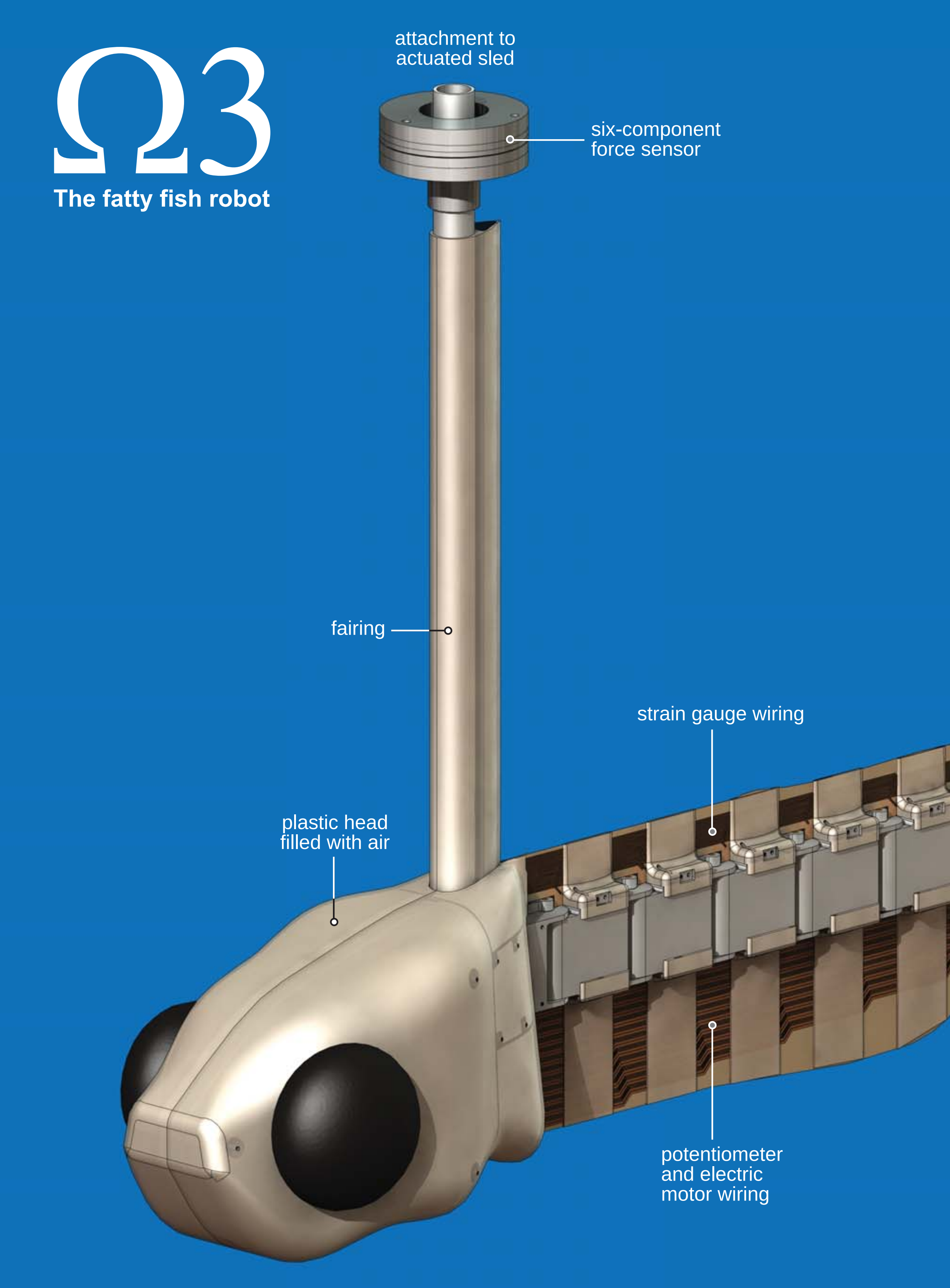

Fig. 3 | Dynamically scaled robot model of a zebra fish larvae.

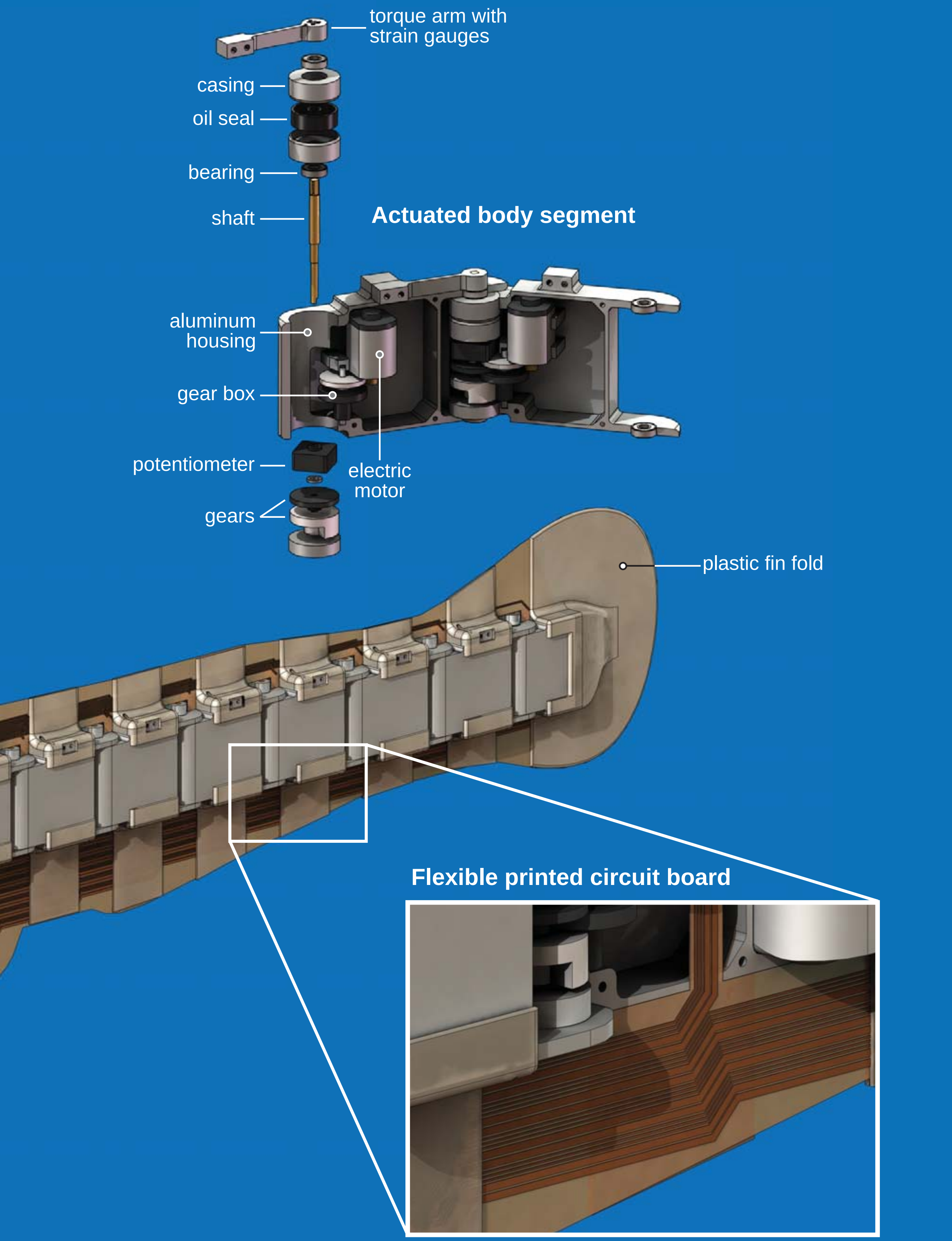

Actuated body segment

Flexible printed circuit board

9 Thanks to my wingmen

9.1

AFFILIATION OF CO-AUTHORS

David Lentink

Michael H. Dickinson
Department of Bioengineering, California Institute of Technology, Pasadena, California 91125,
USA.

William B. Dickson
Department of Bioengineering, California Institute of Technology, Pasadena, California 91125,
USA.

Frits J. Donker-Duyvis
Faculty of Aerospace Engineering, Delft University of Technology, 2600 GB Delft,
the Netherlands.

Ebraheem Fontaine
Mechanical Engineering, California Institute of Technology, Pasadena, CA 91125,
USA.

Wouter van Gestel
Experimental Zoology Group, Wageningen University, 6709 PG Wageningen,
the Netherlands.

Anders Hedenström
Department of Theoretical Ecology, Lund University, Ecology Building, SE 223 62 Lund,
Sweden.

GertJan F. van Heijst
Department of Physics, Eindhoven University of Technology, 5600MB Eindhoven,
the Netherlands.

Per Henningsson
Department of Theoretical Ecology, Lund University, Ecology Building, SE 223 62 Lund,
Sweden.

Roeland de Kat
Department of Aerospace Engineering, Delft University of Technology, 2629 HS Delft,
the Netherlands.

Johan L. van Leeuwen
Experimental Zoology Group, Wageningen University, 6709 PG Wageningen,
the Netherlands.

Florian T. Muijres
1) Department of Experimental Zoology, Wageningen University, 6709 PG Wageningen,
the Netherlands.
2) Department of Theoretical Ecology, Lund University, Ecology Building, S-223 62 Lund,
Sweden.
3) Faculty of Aerospace Engineering, Delft University of Technology, 2600 GB Delft,
the Netherlands.

Ulrike K. Müller
Experimental Zoology Group, Wageningen University, 6709 PG Wageningen,
the Netherlands.

Gijs de Rue
1) Experimental Zoology Group, Wageningen University, 6709 PG Wageningen,
the Netherlands.
2) Faculty of Aerospace Engineering, Delft University of Technology, 2600 GB Delft,
the Netherlands.

Eize J. Stamhuis
Department of Marine Biology, Groningen University, 9750 AA, Haren,
the Netherlands.

Leo L. M. Veldhuis
Department of Aerospace Engineering, Delft University of Technology, 2629 HS Delft,
the Netherlands.

John J. Videler
1) Department of Marine Biology, Groningen University, 9750 AA, Haren,
the Netherlands.
2) Institute of Biology, Leiden University, 2300 RA Leiden,
the Netherlands.

9.2

ACKNOWLEDGEMENTS

David Lentink

In October 2004 my PhD study finally kick-started, because I decided to move from my alma mater Delft University of Technology to the Experimental Zoology group at Wageningen University headed by Johan van Leeuwen. Johan, when we first met at SEB Edinburgh in 2004 you friendly 'ordered' me to not call you 'professor', but 'Johan'. A very pleasant culture shock, because I was used to receiving orders from professors in Delft, but not to call them by their first name. I really enjoyed our scientific discussion that day, and the conversations that I had with your group members at that meeting. This is why I came to Wageningen when you invited me, and up until the end of my PhD study it has been a very positive and enabling experience. Every PhD student struggles to learn the skills needed to become a successful scientists, your trust in me and your friendly and patient support throughout the past four years have helped me enormously. I had a great time in your inspiring and motivating lab. I feel extremely lucky that you built up an incredible support team around me in which you and my two co-promoters, Michael Dickinson and GertJan van Heijst provided a life-lasting inspiration for doing science. Michael, your willingness to welcome a stranger in your impressive lab, a candy store for enthusiastic students, is inspirational in itself. Thank you for all your help, patience, scientific input, great lab meetings and seemingly endless time and effort to help me to better communicate science – it was super helpful. GertJan, ever since I learned about your vortex dynamic lab early 1999, the work from your lab has inspired me. I love vortices like everyone in your lab seems to do, which makes me feel at home in Eindhoven. Thank you for the very pleasant and inspiring discussions in Eindhoven. With every visit I learned a lot and, as Michael and Johan, you made a vital contribution to my development as a scientist.

Just before I moved to Wageningen University they had a slogan "Wake up in Wageningen". In Wageningen I definitely woke up, and for this very pleasant experience I want to thank my dear colleague and friend Ulrike. In the first week Ulrike and I wrote a Science perspective on leading edge vortices generated by swifts, which provided literally a swift start towards chapter six of this thesis. Ulrike what a great time did we have, first as colleagues helping each other out with doing research, later also as friends going out for dinner after work many, many times. Thank you (and Otto) for all your advice, help and warm friendship, which is perhaps best illustrated by our cozy sitting area in our office with tea, chocolate and cookies.

Mees, when I first came to Wageningen I was welcomed with Balkan hospitality in your house to enjoy many cozy, hours lasting, dinners with great courses, music and good wine, which compelled me to eat many things I had not eaten before. I enjoyed every single dish and together with you and Celine I had many pleasant evenings. I much appreciated our scientific discussions and the many hours of help you gave me and my students to develop new experimental setups. Your creativity in doing biomechanics research, dedication to help students and hospitality are admirable.

The workshop rocks, Eric, not only because you like to play your guitar whenever you can, but also because you and Evert helped me and my students out designing and building all our setups. They proved to be amazing setups, I really enjoyed working with you both and I am very proud of what we accomplished as a team. Thank you for being there for me and caring about my research, even beyond office hours, and most importantly, your friendship.

Henk, you placed almost all orders for every single part I or a student of me needed to build our setups. To stick to our tight schedule we always pressed for ordering quick and asked many times if our ordered goods finally arrived. Your help, enthusiasm and ideas are much appreciated, together with Eric and Ulrike you really stood out in supporting my PhD research.

Will, you not only helped me out enormously with my experiments with RoboFly at Caltech, we also had many great discussions about our work and interests. What I perhaps appreciated even more was your friendship in helping me finding my way around on campus; man did I enjoy our Friday afternoon beers after work! You are by far the most impressive mathematician I ever met, not only great at math, also an ace experimentalist and one of the nicest guys I ever met, thanks for crossing my path!

Jos and Sander, thank you both for helping and advising my students many times with the design and building of our various experimental setups, and for the many useful comments on my manuscripts. Jos, I want to thank you especially for spending even a couple of free weekends to construct our soap film tunnel such that it became both a great and affordable setup.

I thank all my colleagues, collaborators and fellow scientists for their support, enthusiasm and friendship! I would like to thank in particular: Mark (& Elles), Coen, Patricia, Wouter, Arie, Nand, Annemarie, Hilda, Karen, Talitha and Ansa, in the experimental zoology group. Joop, Prescilla, Carla, Mark and Beja in the Cell Biology and Immunology group. Amber, Doug, Andrew, Jasper, Gaby, Gwyneth, Alice, Hiroki, Michael and Mark in the Dickinson lab, Ebraheem in the Burdick lab, and Mike in the machine shop at Caltech. Eize and John at Groningen University. Anders and Per at the Animal Flight lab of Lund University. Michel, Adriaan, Dick, Bob, Leo, Frits, Herman, Christophe, Jochem, Bart, Olaf and Christiaan at aerospace engineering, TU Delft. Paul and Martijn at mechanical engineering, TU Delft. Tom and Bert at University of Washington. Hao at Chiba University. Rick (Ruijsink Dynamic Engineering, now at TU Delft) for supporting both the DelFly and RoboSwift project. Eric and Frank (TNO) for supporting DelFly. Maarten (van Dijk Pultrusion products) and Gerard and Eddy (KLPD) for supporting RoboSwift. Finally I would like to thank the press officers Bouke and Jack at Wageningen University for teaching me how to communicate with the media, it was a real pleasure.

Dear MSc. and BSc. students, thank you for your much appreciated enthusiasm and help with realizing my research and design projects, I hope you enjoy reading this thesis. You all contributed a lot to my research and my development as a tutor and scientist. A few students stood out, in particular Florian, Stefan, Gijs, Roeland, Jan Wouter, Elsa, Stan and Tjibbe, but many more contributed, thanks! I would also like to credit the complete DelFly and RoboSwift student teams for their work, the teams can be found on www.delfly.nl and www.roboswift.nl. Although not directly part of this thesis work, I would like to thank the Galatea student team for their enthusiasm for designing and building bio-inspired under water vehicles with our group: www.galatea-project.nl.

Further, I would like to acknowledge my dear colleagues at the Franeker Institute of Fluid Mechanics. Gerrit and Ferry, thanks for being my friends and the many dinners and drinks we enjoyed. I had a lot of fun working on Agora Aerodynamika with you both; our continued long distance friendship is much appreciated.

I owe a big thank you to all my friends for having time for me, the many dinners, parties and trips to cultural events or a local bar. You all made my time as a PhD student so much more enjoyable. Special thanks go to Steven, Koen and Renier, old friends from the good old days in Delft, and my new friends in Wageningen, Simone, Guido, Marlies and Miriam.

Finally I would like to thank my my girlfriend Suzanne, parents Wim and Roos and brother Samuel for their love, patience and support. I am sure I forgot to name many of my other friends and colleagues, not only is there only so much space for acknowledgements, the real thing that counts is the nice time we had together, and be assured that I much appreciated your friendship and contribution in the past years, thanks!

9.3

CURRICULUM VITAE

David Lentink

David Lentink was born on the 9th of March in 1975 in Doetinchem, the Netherlands. During his youth he was a member of the free flight model airplane club of Ebele Schouwstra in Enschede where he learned to design and build model airplanes. This hobby made him admire flying animals. His high school education started out at LBO level after which he worked himself up from MAVO, HAVO to HTS aeronautics (one year), which allowed him to start at the faculty of aerospace engineering at the Technical University of Delft in 1995. During his study in Delft he developed several additional activities: From initiating new student lab courses on airplane design and fluid mechanics to organizing monthly cabaret performances of talents that he scouted with friends at several Dutch cabaret festivals. He also organized a reunion for the famous national Cameretten cabaret festival that started in 1966 in Delft. In 2000 he made a study trip to biomechanics labs in Saarbrücken, Braunschweig, Lund, Cambridge and Groningen to find a suitable graduation topic in the field of biofluidmechanics. For this trip he was awarded a Shell Travel Bursary. He ended up doing his MSc. thesis work on computational fluid dynamic simulations of insect flight with Marc Gerritsma, Henk Tennekes and Bas van Oudheusden. He earned a BSc. and MSc. in aerospace engineering in 2003. For his novel fluid mechanic lab course he received the professor Dobbinga award from the faculty of aerospace engineering. For his AIAA paper on insect aerodynamics he received the best fluid dynamic AIAA paper award of 2003.

In 2004 David wrote an NWO-ALW proposal (260kE) for studying insect flight, which was awarded in 2005, unfortunately too late to be able to continue his research in Delft, as he already worked full-time as a PhD student in Wageningen. In Wageningen he worked in the Experimental Zoology group headed by Johan van Leeuwen who supervised him together with Michael Dickinson (Caltech) and GertJan van Heijst (TUE). During his PhD research he spent a total of 9 months in the Dickinson lab at Caltech where he studied the aerodynamics of insect and autorotating seed flight using robot models in an oil tank (supported by travel funds from NWO and J. Exp. Biol.). He wrote a second NWO-ALW grant for comparing the fluid dynamics of fish swimming and insect flight (270kE), for supporting his PhD work, which was granted in 2007. Based in Wageningen, he used his research results to initiate and tutor the DelFly (a flapping micro plane) and RoboSwift (a morphing micro plane) bio-inspired design projects in Delft for BSc. aerospace engineering students. The student-tutor teams received several prizes (most exotic MAV prize 2005, Best Dutch aerospace innovation 2005, and best teamwork TU Delft 2006) and received much national and international media attention (e.g. New Scientist, Discovery Channel and BBC). The DelFly and RoboSwift designs have been on display in several museums, among which the Brandenburger Tor in Berlin and Science Museum in London.

David received several awards for his PhD research; the Elsevier Young Scientist Award of the Society for Experimental Biology (2005), the best PhD presentation award of the BeNeLux

Zoology conference (2005) and WIAS science day (2007), the Bolk prize from the Netherlands Society for Anatomy (2008), and the publication prize of the WIAS graduate school (2008) for his research on morphing swift wings, which was featured on the cover of Nature in 2007. During his PhD study he attended many international conferences and workshops on biomechanics, fluid dynamics and bio-inspired design and gave invited presentations. During his PhD he reviewed for four international scientific journals (PNAS, J. Exp. Biol., J. Theor. Biol & Exp. Fluids). Every research chapter in this thesis has been submitted to or published in an international scientific journal.

Starting in October 2008 David will work as an assistant professor at the Experimental Zoology Group of Wageningen University. In 2009 David will work for a year as a post-doctoral fellow studying bird flight at the Concord field station of Harvard University, during which he will be affiliated with both Harvard and Wageningen University.

9.4

Publication list

David Lentink

Published journal papers

Fontaine, E., *Lentink, D.*, Kranenbarg, S., Müller, U.K., van Leeuwen, J.L. Barr, A.H. and Burdick, J.W. (2008). Automated visual tracking for studying the ontogeny of zebrafish swimming. *J. Exp. Biol.* 211, 1305 – 1316.

Bos, F.M., *Lentink, D.*, van Oudheusden B.W. and Bijl H. (2008). Influence of wing kinematics on aerodynamic performance in hovering insect flight. *J. Fluid Mech.* 594, 341 – 368.

***Lentink, D.*, Muijres, F.T., Donker-Duyvis, F.J. and van Leeuwen, J.L.** (2008). Vortex-wake interactions of a flapping foil that models animal swimming and flight. *J. Exp. Biol.* 211, 267 – 273. (special issue).

***Lentink, D.*, Müller, U.K., Stamhuis, E.J., de Kat, R. van Gestel, W.,Veldhuis, L.L.M., Henningsson, P., Hedenström, A. Videler, J.J. and van Leeuwen, J.L.** (2007). How swifts control their glide performance with morphing wings. *Nature* 446, 1082 – 1085.

Muijres, F.T. and *Lentink, D.* [*corresponding author*] (2007). Wake visualization of a heaving and pitching foil in a soap film. *Exp. Fluids* 43, 665 – 673. (special issue).

Müller, U.K. and *Lentink, D.* (2004). Turning on a Dime, *Science* 306, 1899 – 1900.

Book chapter

***Lentink, D.*, Jongerius, S.R. and Bradshaw, N.L.** (2008, under review). The scalable design of flapping micro air vehicles inspired by insect flight. *To appear in a Springer book on insects and robotics.*

Submitted journal manuscripts

***Lentink, D.*, Dickson, W.B., van Leeuwen, J.L. and Dickinson, M.H.** (2008). A leading edge vortex prolongs descent of maple seeds.

***Lentink, D.*, Muijres, F.T. van Heijst G.J.F. and van Leeuwen J.L.** (2008). Symmetrically and periodically flapping foils mediate chaotic vortex-wake interactions.

***Lentink, D.* and Dickinson, M.H.** (2008). Biofluidmechanic scaling of flapping, spinning and translating fins and wings.

***Lentink, D.* and Dickinson, M.H.** (2008). Rotational accelerations stabilize leading edge vortices on revolving fly wings.

Awarded conference publications

Lentink, D. **and Dickinson, M.H.** (2005).“Structure stability and strength of leading edge vortices in insect flight”, SEB conference, Barcelona. *SEB Elsevier Young Scientist of the year award.*

Lentink, D. **and Gerritsma, M.I.** (2003). “Influence of airfoil shape on performance in insect flight”, presented at the 33th AIAA Fluid Dynamics conference, Orlando Florida; AIAA 2003-3447. *Best AIAA fluid mechanics paper award 2003.*

9.5

WIAS TSP

David Lentink

WIAS Graduate School Training and Supervision Program

Education & training 2004-2008	*ECTS*
WIAS introduction course and philosophy & ethics course	**3.0**
Conferences, seminars and presentations | among others (28 meetings; 6×poster & 27×oral): — World Congress of Biomechanics 2006 (oral presentation). — Annual meeting Society for Integrative and Comparative Biology 2007 (oral & poster presentation). — Flying Insects and Robots symposium 2007 (oral presentation and flight demonstration).	**50.1**
Disciplinary and interdisciplinary courses | among others: — Advanced turbulence, J.M. Burgerscentrum. — Biofluiddynamics, J.M. Burgerscentrum. — DTU summer school “Complex motion in fluids”, Denmark.	**9.0**
Professional skills | among others: — Wrote NWO-ALW proposal ”Optimal Aerodynamic Strategies in Insect Flight” (granted, started 2005). — Wrote NWO-ALW proposal “Vortex Dynamic Strategies in Animal Swimming and Flight” (granted, started 2007). — Wrote KLPD RoboSwift proposal (granted, started 2007).	**26.4**
Didactic skills | among others: — Lectured on biofluiddynamics in biomechanics course at Wageningen University. — Lectured on micro air vehicle design in bio-inspired design course at TU Delft. — Tutored three student projects: www.delfly.nl | www.roboswift.nl | www.galatea-project.nl. — Supervised 7 BSc. and 6 MSc. projects and theses.	**49.3**

Management skills	**12.0**
— Organizer & principle investigator swift project (Wageningen University, Groningen University, TU Delft, Lund University & Leiden University).	
Organization seminars	**0.4**
— Bio-inspired design seminar at Wageningen University (RoboSwift project).	
Total (1 ECTS credit equals 28 h study load)	**150**

9.6

PHOTO CREDIT

The copyright of the photos shown below, and elsewhere in this thesis, is property of the indicated authors

© Dickinson lab, Caltech.

© Henk schipper, Wageningen University.

© Johan L. van Leeuwen

© Johan L. van Leeuwen

© Jaap Oldenkamp

© Anette Linnea Rasmussen | Dreamstime.com

© Frans Koomen

© team DelFly

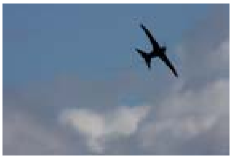

© Johan L. van Leeuwen

© Jean Francois Cornuet

© Henk schipper, Wageningen University.

Please note that the credits of images used in the figures of chapters 1-8 can be found in the figure legends or the acknowledgements of those chapters. Further note that the credits of the cover photos can be found in the list above.

9.7

SAMENVATTING

David Lentink

Vele organismen moeten zich voortbewegen door water en lucht (aangeduid met ‘vloeistof’ in de stromingsleer) om te overleven en zich voort te planten. De ontwikkeling van individuele organismen en de evolutie van hun soort wordt vormgegeven door de fysische interactie tussen het organisme en de vloeistof. Een karakteristieke eigenschap van vele macroscopisch grote dieren die zich voortbewegen door vloeistof is het ontstaan van wervels; draaikolken in water en lucht. Deze wervels worden vlak langs het lichaam gecreëerd terwijl het lichaam wordt voortbewogen met behulp van spier- of zwaartekracht. Nadat deze wervels zijn afgeschud vormen zij tezamen een zog; een spoor van wervels achtergelaten in de vloeistof. Het bestuderen van de dynamica van vloeistoffen door de dynamica van deze wervels te beschouwen wordt bemoeilijkt door de inherente complexiteit van de mogelijke wervelinteracties. Wervels kunnen zich niet alleen zelfstandig voortbewegen in een vloeistof, vaak interacteren zij onderling en met het organisme waardoor complexe stromingsfenomenen kunnen ontstaan die cruciaal zijn voor ons begrip van zwemmen en vliegen.

Dit onderzoek richt zich op twee stromingsfenomen die van belang zijn voor de voortbewegingsprestatie van een aantal organismen. Het eerste fenomeen is de stabiliteit van voorrandwervels. Deze tornado-achtige wervels zijn geobserveerd boven flapperende insectenvleugels, waarop zij parallel aan de voorrand stabiel blijven liggen. Deze stabiele voorrandwervel versterkt de lift dusdanig dat zij een belangrijke verklaring vormen voor de uitzonderlijke vliegprestaties van insecten. Hier onderzoek ik waarom deze voorrandwervels stabiel aan insectenvleugels blijven plakken. Het tweede fenomeen is de periodiciteit van het wervelzog. Afhankelijk van de condities, kan het wervelzog, afgeschud door een organisme, gestructureerd en voorspelbaar zijn of chaotisch. Ondanks dat de stroming van vloeistoffen deterministisch is, wordt deze als zij chaotisch is ultragevoelig voor minuscule verstoringen. Deze chaos kan er voor zorgen dat de vloeistofkrachten slecht voorspelbaar worden. Hier beschrijf ik het optreden van chaotische wervelinteracties in biologische relevante modellen in het licht van de mogelijke consequenties van deze chaos voor de neurale controle van de voortbeweging.

Deze studies zijn uitgevoerd met behulp van modellen van zwemmende vissen, vliegende insecten, autoroterende plantenzaden en vogels. De stromingspatronen en krachten zijn bepaald met behulp van de volgende modellen die in toenemende mate een realistische benadering geven van het organisme: Een flapperende vin/vleugel in een zeepfilm tunnel, een dynamisch geschaalde driedimensionale robot die zowel de vleugelmodellen van vliegen als autoroterende planten zaden kan voortbewegen in een tank met olie, en ten slotte gevriesdroogde vleugels van gierzwaluwen in een windtunnel. De metingen werden ontworpen en geïnterpreteerd met behulp van dimensie-analyse: dimensieloze parameters die aangeven welke versnellingen en schuif- en drukspanningen in de vloeistof de stroming domineren, als functie van de morfologische en kinematische variabelen die de stroming induceren. Deze analyse heeft geresulteerd in een overzicht van de relevante parameterruimte van deze biologische stromingen rondom translerende, roterende en flapperende vleugels en vinnen. Op basis van deze aanpak is het ons gelukt om aan te tonen dat: (1) Symmetrisch en periodiek flapperende vleugels zowel asymmetrische als chaotische wervelzoggen kunnen voortbrengen. (2) Acceleraties geïnduceerd door rotatie er voor zorgen dat de voorrandwervel stabiel blijft liggen op de draaiende vleugels, zowel continue als flapperend, van insecten en andere organismen. (3) Stabiele voorrandwervels de lift sterk verhogen van zowel vliegende dieren als autoroterende planten zaden. (4) De actieve vleugelvervorming 'morphing' van vogels tijdens de zweefvlucht de vliegprestaties drastisch verhogen. (5) Flapperende insectenvleugels minder efficiënt zijn dan spinnende en translerende insectenvleugels.

Deze inverse ontwerpanalyse van de voortbeweging van organismen in vloeistoffen heeft ons geholpen om twee nieuwe microvliegtuigjes te ontwerpen, te bouwen en uiteindelijke te laten vliegen. We hebben een flapperend vliegtuigje (DelFly) en een vliegtuigje met actief vervormende vleugels (RoboSwift) uitontwikkeld tot daadwerkelijk functionerende demonstratiemodellen. Dit illustreert dat de methodes en vondsten die hier worden gepresenteerd direct kunnen resulteren in vernieuwende technologische producten.

Research schools
This research has been carried out within the WIAS graduate school and J.M. Burgerscentrum for Fluid Mechanics.

Funding research
NWO-ALW grant 817.02.012.

Funding bio-inspired design
Dutch National Police Force and TNO Defence, Security, and Safety.